Water, heat and salt cycles over the South China sea, from seasonal to interannual variability : a closed budget and high-resolution ocean modelling approach

Bich Ngoc Trinh

THÈSE

En vue de l'obtention du

DOCTORAT DE L'UNIVERSITÉ DE TOULOUSE

Délivré par : *l'Université Toulouse 3 Paul Sabatier (UT3 Paul Sabatier)*

Présentée et soutenue le *09/12/2020* **par :**

Bich Ngoc TRINH

Cycles de l'eau, de la chaleur et du sel dans la Mer de Chine Méridionale, de la variation saisonnière à la variabilité interannuelle: modélisation océanique à haute résolution et à bilan fermé

JURY

Christophe MENKES	ENTROPIE	Rapporteur
Vincent ECHEVIN	LOCEAN	Rapporteur
Thanh NGO-DUC	USTH	Rapporteur
Rosemary MORROW	LEGOS	Présidente du jury/Examinatrice
Sylvain OUILLON	LEGOS, USTH	Invité
Caroline ULSES	LEGOS	Co-directrice de thèse
Marine HERRMANN	LEGOS	Directrice de thèse

École doctorale et spécialité :
SDU2E : Océan, Atmosphère, Climat

Unité de Recherche :
Laboratoire d'études en géophysique et océanographie spatiales (UMR5566)

Directeur(s) de Thèse :
Marine Herrmann et *Caroline Ulses*

Rapporteurs :
Christophe Menkes, *Vincent Echevin* et *Thanh Ngo-Duc*

Remerciements

Tout d'abord, je tiens à remercier profondément ma directrice de thèse, Marine Herrmann (directrice de recherche de l'IRD), de m'avoir proposé ce sujet de thèse à la fois ambitieux et très intéressant. Je lui suis reconnaissante pour le temps qu'elle m'a accordé, son encouragement, son soutien et sa sympathie tout au long de ce projet.

Je souhaite également remercier ma co-directrice de thèse, Caroline Ulses (chargée de recherche du LEGOS), pour sa disponibilité, ses qualités scientifiques et sa gentillesse. Merci d'avoir toujours été à l'écoute et merci de m'avoir beaucoup appris sur le modèle biogéochimique.

Cette thèse n'aurait jamais vu le jour sans le soutien des personnes du groupe SIROCCO (LEGOS). Je remercie chaleureusement Patrick Marsaleix, Claude Estournel, Thomas Duhaut et Cyril Nguyen pour leurs implications, non seulement dans l'aspect technique mais aussi dans l'orientation scientifique du projet. J'ai beaucoup apprécié l'accueil chaleureux qu'ils m'ont réservé et l'ambiance très conviviale au sein du groupe.

Un grand merci à Kipp Shearman (Origon State University, États-Unis), à Benoît Tranchant (CLS Toulouse), à Joseph Montoya (Schmidt Ocean Institut, États-Unis) et à Vĩnh (Institute of Marine Environment and Resources, Vietnam) pour des précieuses données qu'ils m'ont si généreusement partagées afin de valider le modèle.

J'adresse mes sincères remerciements à l'équipe informatique du Laboratoire d'Aérologie (cluster Nuwa) : Didier Gazen, Laurent Cabanas, Jeremy Leclercq et à Kien (l'ingénieur en charge du cluster Hilo), pour leur soutien d'une grande compétence et leurs disponibilités à chaque fois j'ai rencontré des difficultés.

Je désire en outre remercier l'Insitut de Recherche pour le Développement (IRD) et le Consortium USTH, pour les supports financiers que j'ai reçu pendant mes quatre années de doctorat.

La thèse, c'est aussi des échanges et des rencontres. J'ai une pensée particulière pour mes amis doctorants au LEGOS. Un grand merci à Violaine et Thai pour leur soutien tout au long de cette thèse. Violaine, merci pour tes conseils et le soutien que tu m'as apporté jusqu'au jour de ma soutenance. Tu resteras ma coloc préférée des conférences.

Thai, merci pour tes codes Matlab et pour les heures que tu passais à discuter des problèmes de calcul avec moi. Merci également à anh Đa, Việt, Tùng, Thái em, Hạnh pour les repas au midi et les pauses café pleines d'humour. Je n'oublierai jamais votre gentillesse et vous souhaite beaucoup de succès pour le futur.

Je voudrais remercier mes collègues du département Eau, Environnement, Océanographie de l'Université de Science et Technologie de Hanoi (USTH). Merci beaucoup Sylvain Ouillon, directeur du département, pour ton soutien et ta relecture de l'article. Merci Thu, Lê Anh, Tú, Hợi pour avoir accepté de me remplacer lorsque je partais travailler sur ma thèse à Toulouse. Merci Philippe pour tes conseils et tes petites plantes.

J'embrasse mes copains de l'INSA : Vanessa, Lisou, Laura, Feida, Guillaume, Emeric, Nga - avec qui j'ai passé des moments magnifiques de retrouvailles. Merci Chantal, ta maison fleurie à Saint Lary est un de mes plus beaux souvenirs de France. Merci Nguyệt, ma meilleure copine.

De gros câlins et plein de bisous à tous les membres de ma famille. Merci à ma mère Thủy, mon père Giao, mon frère Kiên, ma belle-mère Hồng pour leurs encouragements et soutiens inconditionnels pendant tout ce temps.

Enfin, merci Hà. Sans toi je ne serais jamais parvenue au bout de ce chemin.

Contents

List of figures

List of tables

Résumé

La dynamique océanique en Mer de Chine Méridionale (SCS pour “South China Sea”) joue un rôle important à l'échelle locale pour le système climatique régional, mais aussi pour la circulation océanique et le climat à l'échelle globale. Les eaux de surface de la circulation thermohaline globale transitent en effet de l'océan Pacifique à l'océan Indien à travers la SCS par plusieurs détroits (“South China Sea Throughflow”, SCSTF), et sont modifiées de manière significative au cours de ce transit. La dynamique océanique gouverne en outre le transport et le mélange des composants des écosystèmes marins planctoniques, et influence donc les écosystèmes marins. L'objectif central de cette thèse est de contribuer à la compréhension de la dynamique océanique en SCS et de ses interactions avec les autres compartiments du système régional, en s’intéressant au fonctionnement et à la variabilité des bilans hydrique, thermique et halin, avec pour perspective d’étudier leur impact sur les écosystèmes planctoniques pélagiques.

Pour cela, une configuration à haute résolution d'un modèle océanique régional couplé physique-biogéochimie couvrant la SCS et où les bilans sont rigoureusement fermés a été développée pour réaliser des simulations sur la période récente 2009-2018.

Nous montrons d'abord, par comparaison aux données satellitaires et observations in-situ, la capacité de notre simulation physique à reproduire les caractéristiques de surface des masses d'eau et de la circulation, ainsi que la distribution thermohaline verticale, aux échelles climatologiques, saisonnière et interannuelle.

Nous examinons ensuite la moyenne climatologique et le cycle saisonnier de toutes les composantes impliquées dans les bilans d'eau, de chaleur et de sel en SCS : variations internes et flux latéraux, atmosphériques et fluviaux. Les apports d'eau et de sel sont principalement liés aux flux latéraux d'eau du Pacifique par le détroit de Luzon. La moitié de ces apports s’écoule par le détroit de Mindoro vers la mer de Sulu, un quart par le détroit de Taiwan vers la mer de Chine orientale et un quart par le détroit de Karimata vers la mer de Java. Le gain de chaleur provient principalement de l'entrée latérale à Luzon (~¾) et de l'apport atmosphérique (~¼), et s’écoule de manière équivalente par les détroits de Mindoro, Taïwan et Karimata. Sur la période étudiée, la SCS stocke respectivement 0,3% et 2,5% des apports totaux de sel et de chaleur (le volume ne varie

pas significativement). Le cycle saisonnier des bilans hydrique et halin est principalement gouverné par le flux d'eau latéral, tandis que celui du bilan thermique est principalement régi par le flux de chaleur atmosphérique.
A l'échelle interannuelle, les flux d'eau, de chaleur et de sel à travers les détroits de Luzon et de Mindoro sont fortement corrélés et présentent la plus forte variabilité de tous les transports aux détroits, ainsi que des corrélations élevées avec ENSO (El Niño Southern Oscillation) et la PDO (Pacific Decadal Oscillation). Le flux atmosphérique annuel d'eau régit la variabilité interannuelle du bilan hydrique en SCS : une variation de l'apport atmosphérique d'eau douce induit une variation équivalente du débit sortant latéral, de sorte que le volume de la SCS varie très peu à l'échelle interannuelle. Le bilan salin en SCS est piloté au premier ordre par la variabilité interannuelle du flux d'eau latéral, puis par la salinité des eaux entrantes/sortantes. La variabilité interannuelle du bilan thermique est pilotée d'abord par le flux thermique latéral net, lui-même piloté par la variabilité de la température des eaux sortantes/entrantes, puis par la variabilité du flux d'eau latéral et du flux thermique de surface. Les bilans d’eau et de sel ainsi que le SCSTF sont fortement affectés par ENSO et la PDO, alors que le bilan thermique n'est affecté que par ENSO.

Mots clés : South China Sea ; Bilans d’eau, de la chaleur et du sel ; Modélisation ; Modèle à budget fermé haute résolution

Abstract

The South China Sea (SCS) ocean dynamics play an important role at the local scale for the regional climate system, but also in global ocean circulation and climate. Surface waters of the global thermohaline circulation indeed transit from the Pacific to the Indian Oceans across the SCS through several interocean straits (the South China Sea Throughflow, SCSTF), and are significantly modified during this transit. Ocean dynamics moreover influences the SCS marine life through its role in the transport and mixing of the pelagic planktonic ecosystems' components. The general objective of this thesis is to contribute to the understanding of the SCS ocean dynamics and of their interactions with the other compartments of the regional system, by focusing on the functioning and variability of the SCS water, heat and salt budgets with the perspective to study their impact on the pelagic planktonic ecosystems. For that, a high resolution (4 km) configuration of a regional physical-biogeochemical ocean model covering the SCS with rigorously closed budgets is developed and used to perform and analyze simulations over the recent period 2009 – 2018.

We first show by comparison with available satellite data and in-situ observations the ability of our physical simulation to reproduce the surface water masses and circulation characteristics as well as thermohaline vertical distribution, at the climatological, seasonal and interannual scales.

We then examine the climatological average and seasonal cycle of all components involved in the water volume, heat and salt budgets over the SCS: internal variations and lateral, atmospheric and river fluxes. Water and salt inputs to the SCS are mostly related to the lateral inflow of Pacific water through the Luzon strait. About ½ of those inputs is released through the Mindoro strait to the Sulu sea, ¼ through the Taiwan strait to the East China Sea and ¼ through the Karimata strait to the Java Sea. Heat gain mostly comes for the Luzon lateral input (~ ¾) and from the atmosphere (~¼), and is equivalently released through the Mindoro, Taiwan and Karimata straits. Over the studied period, the SCS stores respectively 0.3% and 2.5% of the total salt and heat inputs. The seasonal cycle of water and salt budgets is mainly driven by the net lateral water flux through

interocean straits, whereas the seasonal cycle of heat budget is mainly governed by the atmospheric heat flux.

On the interannual time scale, water, heat and salt fluxes at Luzon and Mindoro straits are highly correlated together and show the strongest variability of all straits' transports, and high correlations with ENSO (El Niño Southern Oscillation) and PDO (Pacific Decadal Oscillation). The annual atmospheric water flux governs the interannual variability of SCS water budget: a variation of annual atmospheric freshwater input induces a mirror variation of lateral outflow so that the SCS volume hardly varies at the interannual scale. The SCS salt budget is regulated at the first order by the interannual variability of net lateral water flux, then by the salinity of the in/outflowing interocean waters. In particular, we show that the recent SCS saltening was mainly induced by the increase in the inflow of salty Pacific water which compensated a deficit of rainfall freshwater over the area. The heat budget interannual variability is driven first by the total lateral heat flux, itself driven by the variability of the temperature of the out/inflowing waters, then by the variability of the lateral water flux and surface heat flux. Water and salt budgets as well as the SCSTF are strongly affected by ENSO and PDO, whereas the heat budget is only affected by ENSO

Key words: South China Sea; Water, heat and salt budgets; Modeling; High resolution closed-budget model

Introduction générale

La Mer de Chine Méridionale (SCS pour South China Sea) est la plus grande mer semi-fermée du Pacifique tropical occidental, non seulement pour son immense superficie ($3,5*10^6$ km^2) mais aussi pour son rôle important dans la géopolitique, l'économie et l'environnement de la région d'Asie de l'Est. La SCS est le principal lien entre l'Océan Indien et l'Océan Pacifique, avec des lignes maritimes reliant le Moyen-Orient, l'Europe et l'Asie de l'Est. 25% du transport maritime mondial passe par la SCS (Organisation mondiale du commerce 2017), avec une valeur commerciale de 3,37 trillions de dollars par an. En outre, une grande partie du commerce mondial de l'énergie passe par la SCS, ce qui en fait une mer extrêmement importante au sens géopolitique du terme. Plus de 10 millions de barils de pétrole brut sont expédiés chaque jour par le détroit de Malacca - les voies maritimes les plus fréquentées au monde. Géographiquement, la SCS est située dans régions en plein croissance sur le plan économique : il est bordé par la Chine et Taïwan au nord, par le Vietnam, la Thaïlande et le Cambodge à l'ouest, par la Malaisie, le Singapour, l'Indonésie et le Brunei au sud et par les Philippines à l'est (Figure 1). Cette région affiche un taux de croissance moyen pondéré du PIB de 5,2 %, contre 3,2 % de la moyenne mondiale en 2017. Selon la Banque mondiale, en 2019, cette région de l'Asie de l'Est et du Pacifique représentait 30 % des 7,67 milliards d'habitants de la planète et 30 % du PIB mondial (production intérieure brute) de 87 698 milliards de dollars.

La SCS est également riche en biodiversité et est définie comme l'un des grands écosystèmes marins (LME) au climat tropical dans le monde (Ng and Tan 2000). La SCS possède un écosystème unique et abrite des milliers d'espèces et d'organismes, allant des récifs coralliens aux mangroves, en passant par les herbiers marins, les poissons et les plantes. Plus de 450 espèces de coraux ont été recensées aux Philippines. Selon les estimations de Talaue-McManus (2000), environ 2 millions d'hectares de mangroves, soit 12 % du total mondial, sont situés dans les pays limitrophes du LME de la SCS. Randall et Lim (1999) ont établi une liste de poissons marins dans la SCS avec un total de 3365 espèces dans 263 familles. Les riches ressources biologiques marines de la SCS ont fait de cette zone l'une des plus grandes zones de pêche au monde. En 2015, on estime que plus de la moitié des navires de pêche du monde opéraient dans la région et que la SCS

fournissait 12 % des prises mondiales de poissons (Polling 2019). Les activités de pêche, qui emploient officiellement environ 3,7 millions de personnes dans la région de la SCS et officieusement beaucoup plus, représentent une source importante de revenus et de nourriture. Toutefois, la surexploitation des ressources halieutiques régionales a fait baisser les stocks totaux de 70 à 95 % depuis les années 1950, et les taux de capture ont diminué de 66 à 75 % au cours des 20 dernières années.

Les régions côtières de la SCS sont parmi les plus densément peuplées au monde, avec une densité moyenne de 154 habitants/km^2. Dans certaines régions comme les deltas vietnamiens et le sud de la Chine, cette densité dépasse 1000 habitants/km^2 (Shah et al. 2018). La survie de millions de personnes dans cette région dépend fortement des activités liées aux ressources océaniques telles que la pêche, l'exploitation pétrolière, la mariculture, le tourisme et le commerce. Les communautés côtières sont également les plus vulnérables aux phénomènes météorologiques extrêmes qui frappent la région (typhons, surcôtes de tempête, inondations et sécheresses). Goh et Chan (2010) ont estimé que de 1965 à 2005, environ 10 cyclones tropicaux ont frappé la SCS chaque année, causant de graves dommages humains et matériels. Le changement climatique - par le biais de phénomènes météorologiques violents, d'ondes de tempête, de l'élévation du niveau de la mer, d'inondations et de sécheresses - devient une préoccupation majeure pour tous les pays de la région. Au début de 2020, le delta du Mékong au Vietnam, qui produit plus de la moitié du riz vietnamien, a été frappé par des sécheresses extrêmes - estimées les pires du siècle - après un déficit prolongé en précipitations combiné à l'intrusion d'eau salée. L'augmentation de la consommation d'eau et du stockage de l'eau dans les barrages en amont du Mékong est également considérée comme l'une des principales causes de sécheresse dans les zones en aval du Mékong (Hung B.V 2017).

Le développement économique rapide et la croissance démographique dans la zone côtière s'accompagnent de pollution et de contamination. Les déchets d'origines domestique industrielle, agricole et aquacole, ainsi que les sédiments et les déchets solides sont les principaux polluants d'origine terrestre qui affectent les zones côtières (Heileman 2009, Fortes 2006). Les concentrations élevées de nutriments rejetés chaque

année dans le milieu aquatique par les activités industrielles et agricoles, si elles ne sont pas réduites de manière significative, transformeront les eaux côtières du bassin sud du SCS en une zone eutrophe (Talaue-McManus 2000). Des changements majeurs de la turbidité et des niveaux de sédiments en suspension ont été observés dans la plupart des zones côtières, entraînant des modifications de la biodiversité des communautés benthiques (PNUE 2005). Selon Naess (1999), des activités telles que la déforestation extensive dans de nombreux bassins versants, l'exploitation forestière, l'exploitation minière et le développement urbain ont entraîné l'augmentation des niveaux de solides en suspension dans les zones côtières.

Comprendre et prévoir la réponse du système régional couplé atmosphère-océan-continent en SCS aux facteurs de variabilité à différentes échelles et de différentes origines constitue donc un défi scientifique et socio-économique majeur. La circulation océanique est un élément clé du système régional couplé. En pilotant le transport et le mélange des nutriments et des composants de l'écosystème planctonique, qui constitue la base de la chaîne trophique marine, elle joue en outre un rôle essentiel dans le fonctionnement et la variabilité des écosystèmes marins. L'amélioration de notre connaissance du fonctionnement et de la variabilité des processus à différentes échelles impliqués dans la dynamique océanique de la SCS, de leurs interactions avec les compartiments atmosphériques et continentaux du système climatique, et de leur influence sur l'écosystème planctonique pélagique est essentielle pour une meilleure compréhension de l'ensemble du système climatique régional de l'Asie du Sud-Est.

Cette question est la motivation principale de cette thèse de doctorat : les objectifs sont d'étudier le rôle de la dynamique de la SCS dans le climat régional, sa connexion avec les milieux environnants et sa réponse aux différents facteurs de variabilité, des échelles de temps saisonnières à interannuelles. Pour cela, nous étudions d'abord sur les bilans hydrique, thermique et salin de la SCS, en examinant la contribution de la dynamique océanique et des autres compartiments du système climatique régional. L'étape suivante consiste à examiner la réponse de l'écosystème planctonique pélagique et des cycles du carbone et de l'azote associés à ces facteurs de variabilité.

La structure de ce manuscrit de thèse est la suivante. Le chapitre 1 dresse une revue des connaissances actuelles sur la géographie physique de la SCS ainsi que sur les facteurs de forçage atmosphériques et continentaux (fluviaux) qui y influencent la dynamique océanique. Les caractéristiques générales de la dynamique océanique et des écosystèmes biogéochimiques/planctoniques de cette région sont également présentées. Les objectifs détaillés de ce doctorat sont présentés à la fin du chapitre 1. Dans le chapitre 2, nous décrivons notre méthodologie ainsi que les observations et les outils numériques utilisés au cours de ce doctorat. Le réalisme des résultats de la simulation utilisé pour notre analyse est évalué par comparaison aux données satellitaires et aux observations in-situ dans le chapitre 3. Nous présentons au chapitre 4 notre analyse des bilans hydrique, thermique et salin sur l'ensemble de la zone aux échelles climatologique et saisonnière. Leur variabilité interannuelle et leurs réponses aux phénomènes climatiques (ENSO et PDO) sont examinées au chapitre 5. Les conclusions finales et les perspectives sont présentées au chapitre 6. Les travaux préliminaires concernant la mise en œuvre et la validation des simulations couplées physique-biogéochimie sur la SCS sont présentés en annexe.

General introduction (Context)

The South China Sea (SCS) is the largest sea body in the tropical Western Pacific, not only for its huge area ($3.5*10^6$ km^2) but also for its important role in geopolitics, economy and environment of the East Asian region. The SCS is the main link between the Indian Ocean and the Pacific Ocean, connecting the Middle East, Europe, and East Asia with shipping lines. 25% of the world's shipping passes through the SCS (World Trade Organization, 2017), with a 3.37 trillion dollars trade value per year. In addition, a big portion of world energy trade passes through the SCS, making this area an extremely significant body of water in a geopolitical sense. Over 10 million barrels of crude oil are shipped a day through the strait of Malacca – the most heavily traveled shipping channels in the world. Geographically, the SCS is situated in one of the most economically emerging regions in the world: it is bordered by China and Taiwan in the North, by Vietnam, Thailand, and Cambodia in the West, by Malaysia, Singapore, Indonesia and Brunei in the South and by the Philippines in the East (Figure 1). This fast-growing region shows a weighted average GDP growth rate of 5.2% compared to 3.2% of the world average in 2017. According to the World Bank, in 2019, this region of East Asia & Pacific accounted for 30% of the 7.67 billion world population, and 30% of the $87.698 trillion world GDP (Gross Domestic Production).

Figure 1: The political map of the South China Sea. Image source: Asian art museum (https://education.asianart.org/)

The SCS is also rich in biodiversity and is defined as one of the Large Marine Ecosystems (LME) with tropical climate in the world (Ng and Tan 2000). The SCS has a unique ecosystem and is home to thousands of species and organisms, ranging from coral reefs, mangroves, seagrasses, fishes and plants. Over 450 coral species have been recorded from the Philippines. Estimates of Talaue-McManus (2000) suggest that approximately 2 million ha of mangrove forest, or 12% of the world total, are located in the countries bordering the SCS LME. Randall and Lim (1999) established a list of marine fishes in the SCS with a total of 3365 species in 263 families. The rich marine biological resources of the SCS have made this area one of the largest fishing grounds in the world. In 2015, more than half of the fishing vessels in the world were estimated to operate in the region and the SCS accounted for 12% of global fish catch (Polling 2019). Fishing activities, officially employing around 3.7 million people over the SCS region and unofficially many more, remain a significant source of revenue and food. However, the overexploitation of

regional fish resources has decreased the total stocks by 70-95% since the 1950s, and catch rates have declined by 66 - 75% over the last 20 years.

Coastal regions of the SCS are among the most densely populated areas in the world, with an average density of 154 habitants/km^2. In some regions such as Vietnamese deltas and southern China, this number exceeds 1000 habitants/km^2 (Shah et al. 2018). Livelihood of millions of people in this area depends strongly on activities related to ocean resources such as fisheries, oil exploitation, mariculture, tourism and trade. Coastal communities are also the most vulnerable to extreme weather events that hit the region (typhoons, storm surges, floods and droughts). Goh and Chan (2010) estimated that from 1965 to 2005, approximately 10 tropical cyclones each year hit the SCS, causing serious damages to human lives and properties over the impacted regions. Climate change - through severe weather, storm surges, sea level rise, floods and droughts - becomes a big concern of all countries over the area. In early 2020, the Vietnam Mekong delta, which produces more than half of Vietnam's rice, was hit by extreme droughts - estimated the worst of the century - after a prolonged lack of rainfall combined with salty water intrusion. The increase of water consumption and storage of water in upstream dams on the Mekong is considered as one of the main causes of droughts in Mekong downstream zones (Hung B.V 2017).

This rapid economic development and population growth in the coastal zone come with pollution. Wastes from domestic and industrial sources, agricultural and aquaculture, as well as sediments and solid wastes are the major land-based pollutants affecting coastal areas (Heileman 2009, Fortes 2006). High concentrations of nutrients rejected from industrial and agricultural activities into the aquatic environment each year, if not reduced significantly, will change the coastal water over SCS southern basin into an eutrophic zone (Talaue-McManus 2000). Major changes in turbidity and levels of suspended sediment have been observed in most coastal zones, causing changes in biodiversity of benthic communities (UNEP 2005). According to Naess (1999), activities such as extensive deforestation in many watersheds, logging, mining, and urban development have led to the increase of suspended solids levels over coastal areas.

It is therefore a strong scientific and socio-economic challenge to understand and forecast the response of the SCS regional coupled atmosphere-ocean-continent system to factors of variability at different scales and from different origins. The ocean circulation is a key component of this regional system. By driving the transport and mixing of nutrients and components of the planktonic ecosystem, which forms the base of the marine food web, it moreover plays an essential role in marine life. Improving our knowledge of the functioning and variability of processes at different scales involved in the SCS ocean dynamics, of their interactions with the atmospheric and continental compartments of the climate system, and of their influence on the planktonic pelagic ecosystem is essential for a deeper understanding of the whole Southeast Asian regional climate system.

This question is the main motivation of this PhD thesis: the objectives are to study the role of the SCS ocean dynamics in the regional climate, its connection with surrounding environments and its responses to factors of variability from the seasonal to the interannual time scales. For that, we first focus on the SCS water, heat and salt budgets, examining the contribution of ocean dynamics and of the other compartments of the regional climate system. The next step is to examine the answer of the planktonic pelagic ecosystem and of the related carbon and nitrogen cycles to those factors of variability.

The structure of the thesis manuscript is as follows. Chapter 1 gives an overview of the current knowledge on the SCS's physical geography as well as the atmospheric and continental (riverine) forcing factors that influence the SCS dynamics. General characteristics of ocean dynamics and biogeochemical/ planktonic ecosystems over this region are also presented. The detailed objectives of this PhD are presented at the end of Chapter 1. In Chapter 2, we describe our methodology as well as the observation data and numerical tools used during this PhD. The realism of the simulation outputs is evaluated by comparison with observational datasets in Chapter 3. We present in Chapter 4 our analysis of the water, heat and salt budgets over the whole studied zone at the climatological and seasonal scales. Their interannual variability and response to climate phenomena (ENSO and PDO) are examined in Chapter 5. Final conclusions and perspectives are given in Chapter 6. Preliminary work concerning the implementation and

validation of coupled physical-biogeochemical simulations over the SCS is presented in the Appendix.

Chapter I: Introduction - Context and objectives

This chapter presents a literature review on the current knowledge about the South China Sea (SCS): geographical characteristics, different kinds of forcing affecting the zone, governing hydrodynamic processes and currents. The second part of this chapter details the existing knowledge on the volume, heat and salt fluxes exchanged through interocean straits connecting the SCS with the surrounding oceans and seas, known as the South China Sea Throughflow (SCSTF, Qu et al. 2005). Finally, we present the detailed scientific questions of the thesis.

I.1. Physical geography of the South China Sea

The South China Sea (SCS) is a tropical marginal sea situated in Southeast Asia, extending from the Tropic of Cancer to the equator, across over 25° of latitude (2.5°S to 23°N) and over 20° of longitude (from 99°E to 121°E, Figure I.1). With an area of about 3.6 million km^2, the SCS is the largest marginal sea in the world (Sverdrup et al. 1942). The topography of the SCS is illustrated in Figure I.1. The SCS is bounded by the Asian continent on the Northwest and by a series of islands on the Southeast, from Taiwan, Luzon and Palawan on the East to Borneo and Sumatra on the South. The SCS basin has an average water depth of 1140 m and includes broad continental shelves, a continental slope and a deep basin in the central part of the SCS. The shallow shelf (with depth < 100m), covers about 47% of the total SCS area (1.6 million km^2) and is more developed on the northern and southern sides of the basin. In the North, the shelf starts in Taiwan, extends until Hainan with a mean width of 100 km then covers the whole Gulf of Tonkin. The entire southwestern part of the basin including the Gulf of Thailand is shallow shelf. The Sunda Shelf, with its width exceeding 300 km, is one of the largest shelves in the world. Numerous submarine deltas off the Pearl river and other rivers exist on the northern shelf as well as in the Sunda Shelf in the south (Pinxian et al. 2014). The continuity of the northern and southern shelves is disrupted by the steep continental slope near central Vietnam. The continental slope covers 38% of the SCS area. The western and southern slopes are occupied by the Hoang Sa (Paracel) islands and the Truong Sa (Spratly) islands, respectively. These two later form the two major groups of islands in the

SCS. Covering 15% of the SCS area, the deep basin has a maximum water depth of about 5500 m with an abyssal plain with depth average of 4300 m.

The South China Sea is connected with other seas and oceans through several straits (marked in red in Figure I.1). The Luzon strait, between Taiwan and the Philippines – the biggest and deepest channel of the zone - connects the SCS with the Pacific Ocean. It has a depth of more than 3000 m and a width of about 300 km. On the north, the Taiwan strait connecting the SCS with the East China Sea, is about 160 km wide and about 70 m of depth. The SCS is connected with the Sulu Sea on the southeast through the Mindoro strait (sill depth of ~420 m) and Balabac strait. In the southern basin, the SCS exchanges water with the Java Sea and Andaman Sea (Indian Ocean) through respectively the Karimata and Malacca straits. Except the Luzon and Mindoro straits, other channels' water depths are shallower than 100 m. Malacca strait is the narrowest strait (only 30 km).

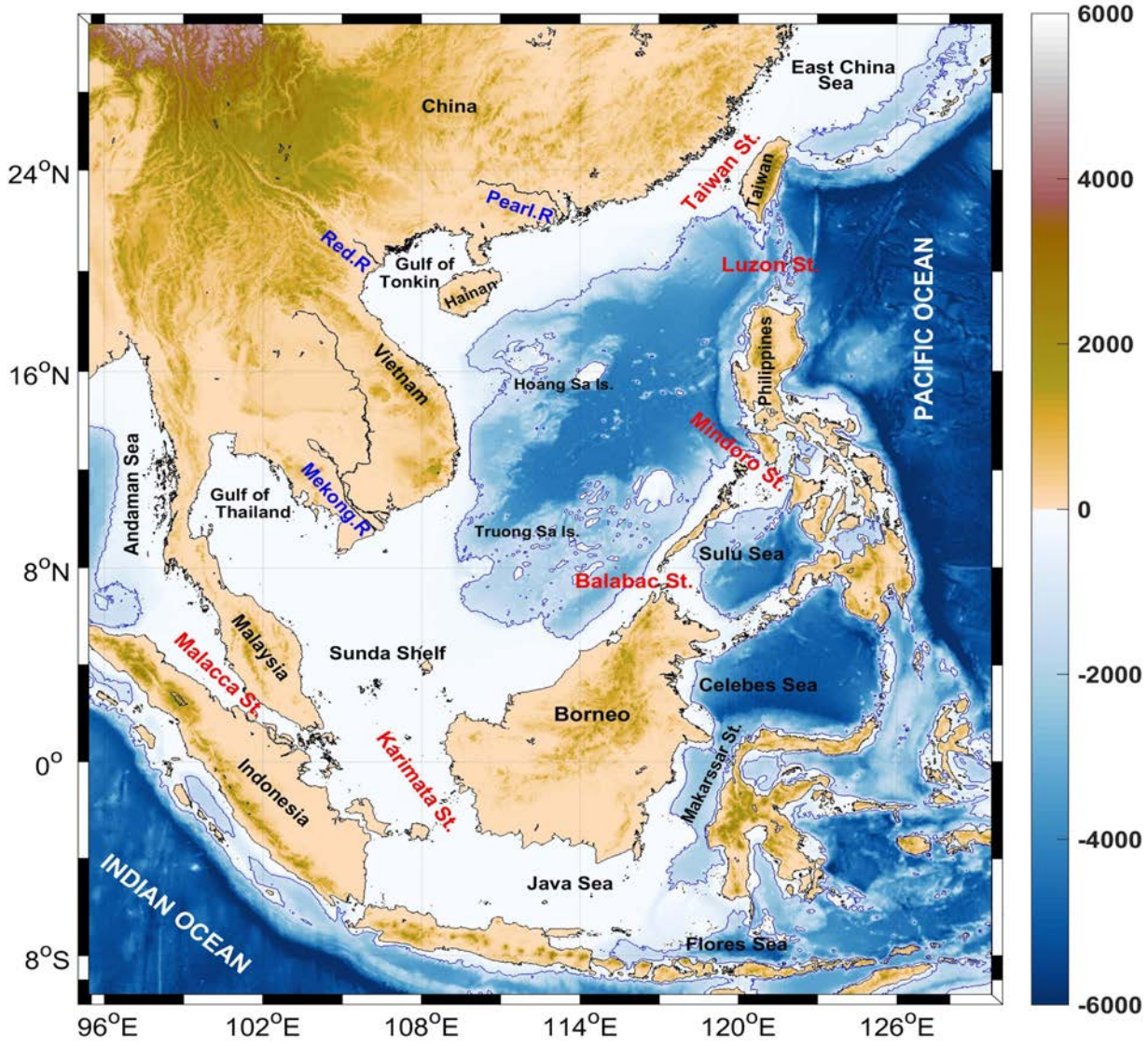

Figure I.1: Physical geography of the SCS area with bathymetry data (in meters) released by the General Bathymetric Chart of the Oceans (GEBCO) 2020, a product of the Nippon Foundation GEBCO Seabed 2030 project, available from https://www.gebco.net). The blue contours indicate the 1000 m isobath.

I.2. Atmospheric forcing

I.2.1. The monsoon wind system

Located between the land masses of Asia and Australia, the SCS resides at the center of the Asian - Australian monsoon and joins four monsoon subsystems: the subtropical East Asian monsoon, the tropical Indian monsoon, the western North Pacific monsoon, and the Australian monsoon. Because of its special geographic location and unique monsoon

characteristics, the SCS is an ideal case study of the monsoon system and has become one of the foci of monsoon research (Park and Choi, 2016).

The monsoon principle can be summarized as follows. The equatorial pressure trough moves seasonally according to the position of the sun, crossing the equator twice a year. In the boreal summer a low develops over the continent in prolongation of the equatorial pressure trough, while in the boreal winter a high is formed over the continent, belonging to the subtropical high. Between the high and the low the monsoons develop (Wyrtki, 1961).

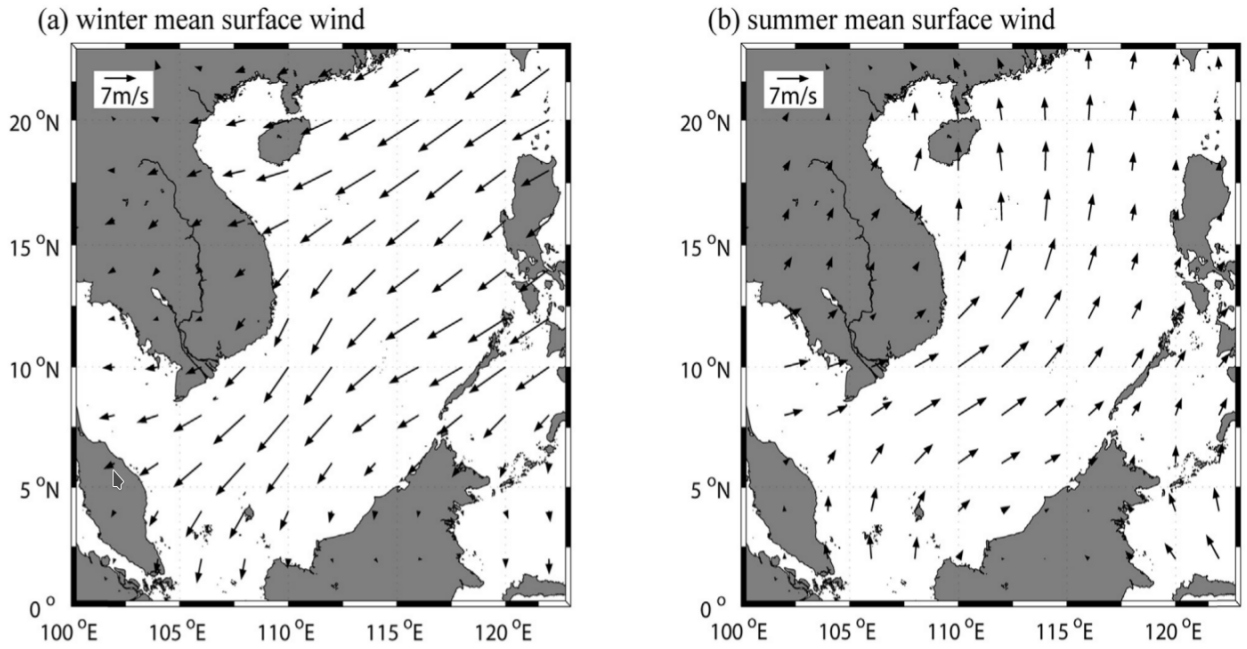

Figure I.2: Surface wind over the SCS region averaged in (a) winter and in (b) summer derived from NOAA-CIRES 20th C Reanalysis, version 2 (20CRv2), period 1871 to 2010 (extracted from Park and Choi, 2016). Winter monsoon months are calculated from December to February, summer monsoon months are from June to August.

Every year, the SCS experiences two monsoons, winter and summer (Wyrtki. 1961). Unlike the Indian monsoon, in the SCS, the winter monsoon exceeds the summer monsoon in strength and in time duration on a yearly basis. During the winter monsoon season, a northeast (NE) wind blows over the SCS (Figure I.2a) as a result of the Siberian high-pressure system located over the East Asian continent, thus cold and dry. The winter monsoon pattern is fully developed in January and lasts nearly 6 months (around mid-October to mid-April). The most intense NE wind is observed at Taiwan, Luzon strait and

Southeast of Vietnam (10-13 m/s), whereas the weakest NE wind speed is recorded over the Thailand Gulf (5 - 6 m/s), probably due to the shadowing effect of the southern Vietnam land mass.

During the summer monsoon season, a southwest (SW) wind blows over the SCS (Figure I.2b), originating from the Southern Pacific and Indian Ocean, thus warm and humid. The summer monsoon pattern is fully developed in July and August and lasts nearly 4 months (around mid-May to mid-September). The SW wind speed reaches the maximum (about 9 m/s) off southern Vietnam and becomes weakest off the Thailand Peninsula, Borneo and near Luzon island under the shadowing effects of land.

The transition periods are spring (April - May) and autumn (September - October). In spring, the system of the northeast winds over the SCS and the Philippines collapses, and the south monsoon blows over the whole of SCS. In autumn, northeast winds first develop in September over waters around Taiwan and southern China, whereas in the other parts of the region the south monsoon loses slightly in strength. In October the equatorial trough begins to move rapidly southwards, weaker SW to W wind blows over the southern SCS whereas a strong NE wind prevails in the northern SCS.

This strong seasonal variation of the atmospheric circulation induces a corresponding variation of the oceanic circulation that will be discussed in section I.3.

I.2.2. Atmospheric heat and freshwater fluxes

Atmospheric heat and freshwater fluxes are major forcing factors for the ocean thermohaline circulation. The net atmospheric heat flux is the sum of four terms: the incoming short waves solar radiation, the outgoing sensible heat flux, latent heat flux, and long-wave radiation. The map of the annual mean net atmospheric heat flux over the global ocean (Figure I.3a) shows the SCS locating in the area of strong positive heat flux along the equator (black box in Figure I.3a).

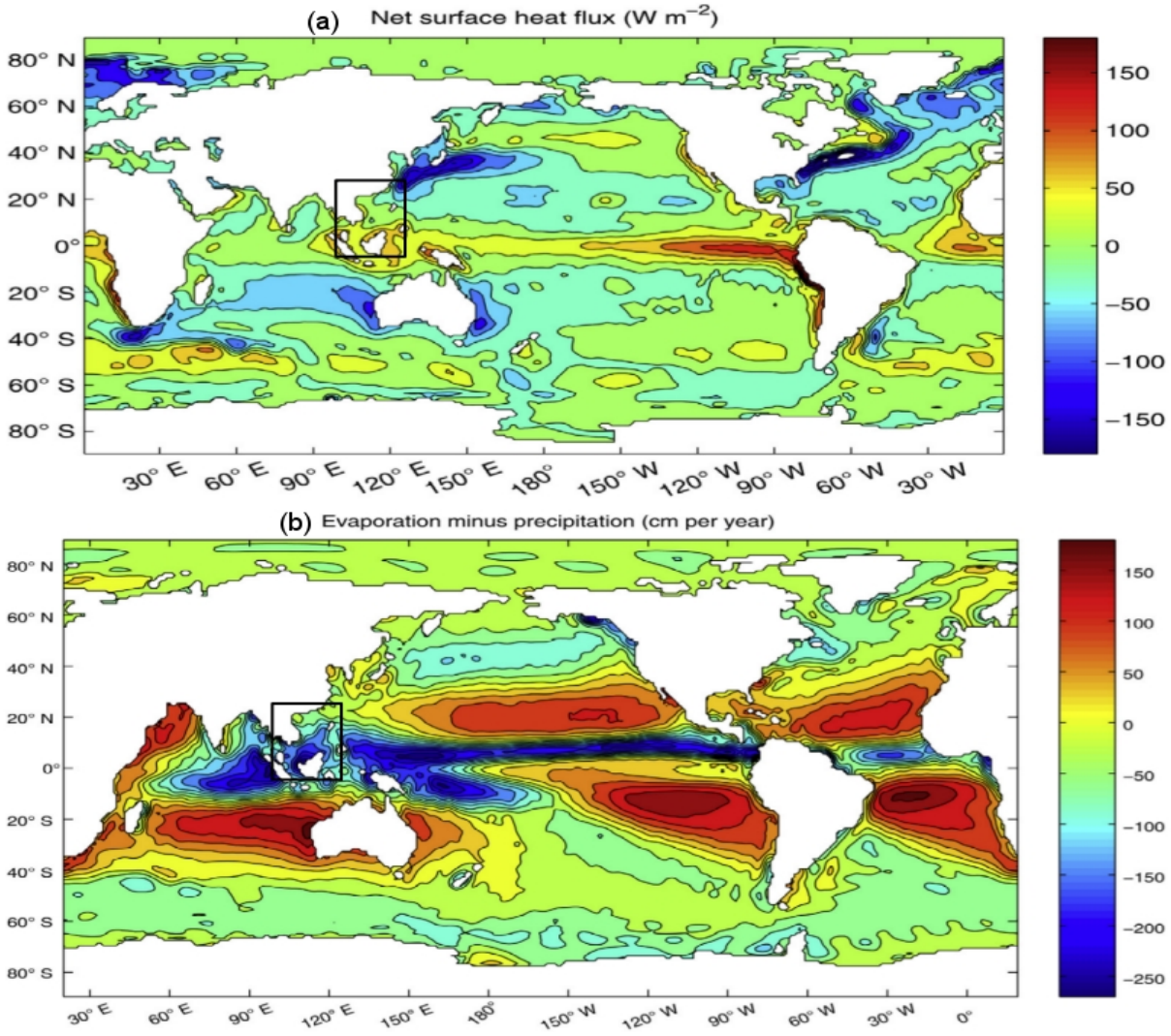

Figure I.3: Global maps of (a) net annual mean atmospheric heat flux and (b) net annual mean atmospheric freshwater flux to the ocean, based on NCEP - NCAR data (1979 - 2010). Image modified from study of Huang (2015). The black box indicates the SCS zone.

Situated in the tropical Western Pacific Ocean, the yearly averaged air to sea heat flux is positive almost the whole SCS, except the northern basin, with a strong spatial variability: the northern basin receives less heat than the southern basin. The estimates from observations (23 W m^{-2}, Oberhuber 1988; 30 W m^{-2}, Yang et al. 1999; 49 W m^{-2}, Yu and Weller 2007) and numerical studies (17 W m^{-2}, Qu et al. 2004; 19 W m^{-2}, Fang et al. 2009; 51 W m^{-2}, Wang Yan et al. 2019) of the atmospheric net heat flux into the SCS varies from one study to another, from ~15 to ~50 W/m^2. All estimates show that the net heat flux over the SCS is positive, corresponding to a net heat gain from the atmosphere. The seasonal

distribution of atmospheric heat flux from European Centre for Medium Range Weather Forecasts (ECMWF, Figure I.4a, b) operational forecasts shows that in summer, all the basin receives heat, with stronger gain over at the northern SCS. In winter, the northern SCS loses heat to the atmosphere while the southern SCS continues to receive heat (Figure I.4b).

Several studies provided estimates of the atmospheric and continental contributions to the SCS water and heat budgets.

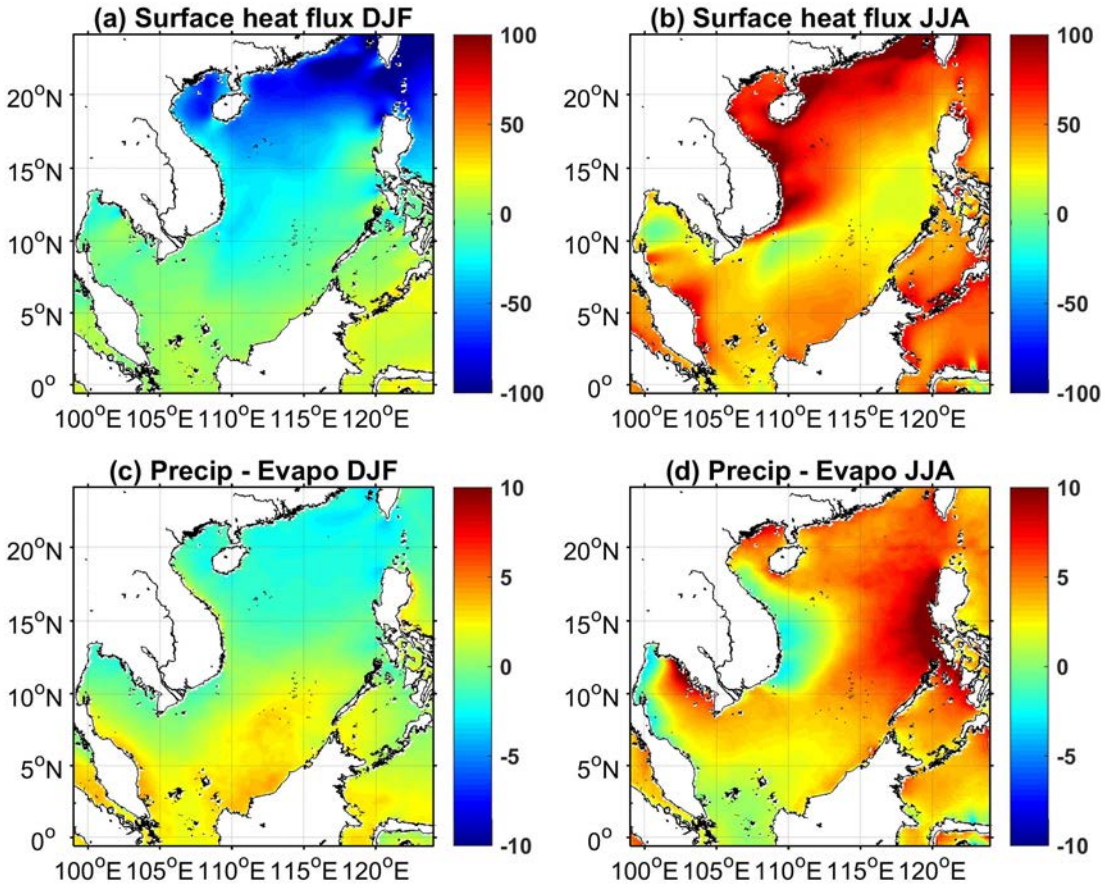

Figure I.4: SCS seasonal maps of net atmospheric heat flux (in W/m^2) and freshwater flux (in mm/day) averaged in (a, c) winter and in (b, d) summer from ECMWF dataset (2009 -2018).

The net atmospheric freshwater flux corresponds to the difference between the gain from precipitation and loss from evaporation. Evaporation provides moisture in the atmosphere, and brings heat from the low-latitude ocean to the atmosphere. Water vapor in the atmosphere eventually condenses and releases the latent heat content, returning to the oceans or land as precipitation. Freshwater flux through the air–sea interface plays an

essential role in regulating the hydrological cycle in the ocean, especially in controlling salinity distribution in the oceans. The global map of the annual mean atmospheric net freshwater flux is presented in Figure I.3b. Strong evaporation occurs in the subtropics and the western boundary current system in both hemispheres. Strong precipitation zones include the equatorial Pacific and Atlantic Oceans and the Northeastern Indian ocean. In the SCS zone (black box in Figure I.3b) we also observe a strong spatial variability of annual mean precipitation and evaporation: in the northern SCS, evaporation exceeds precipitation whereas precipitation dominates in the southern SCS. Several studies have attempted to estimate the annual mean value of the net atmospheric freshwater flux using both observations and numerical methods, providing estimates varying from ~1.5 to ~ 2.5 mm/day.

All studies found that the SCS overall gains freshwater, with precipitation exceeding evaporation. Qu et al. (2006), in examining the CMAP (Climate Prediction Center Merged Analysis of Precipitation), GPCP (Global Precipitation Climatology Project), TRMM (Tropical Rain Measuring Mission) precipitation data and NCEP (National Center for Environmental Prediction) Reanalysis product, estimated that the SCS net air to sea freshwater flux is about 0.1 Sv, equivalent to 2.5 mm/day (averaged over the SCS area of $3.5*10^{12}$ m^2). Da (2018) obtained a value of 1.8 mm/day by using the NCEP CFSR (Climate Forecast System Reanalysis) data for the period 1994 - 2001. Using numerical models, Qu et al. (2006), Fang et al. (2009) obtained a yearly average of total freshwater flux over the whole SCS respectively of 0.08 Sv (period 1950 - 2003) and 0.06 Sv (period 1982 - 2003), equivalent to 2 mm/day and 1.5 mm/day. This freshwater gain from the atmosphere makes the surface salinity of the SCS much fresher than neighboring sea and oceans (averaged SSS ~33.2 psu over SCS and ~34.2 psu over Pacific Ocean, Qu et al. 2009).

The seasonal distribution of freshwater flux shows considerable latitudinal variations. In winter, when the cold and dry northeast monsoon blows, evaporation dominates precipitation in most of the basin (Lau and Yang 1997, Figure I.4c), with stronger evaporation in the northern basin than in the southern basin. In summer, with the onset of the summer monsoon, precipitation dominates in most of SCS (Figure I.4d). A seasonal

zonal variation is also revealed by Wang et al. 2009: due to orographic effect, it rains more in winter in the southwestern SCS around Borneo and in summer in the eastern part along the Philippines coasts (Figure I.4c, d).

In a long-term average, the heat and freshwater gains of the SCS from the atmosphere are balanced by horizontal advection through interocean straits, following Qu et al. (2006) and Fang et al. (2009).

I.2.3. Tropical cyclones

The Northwest Pacific is the most active basin on the planet in terms of tropical cyclones (TC) with ~⅓ of all TC activity. TCs are large-scale destructive natural hazards that cause serious ecological and human damages. The SCS, a subregion of the Northwest Pacific is one of the areas most often frequented by TCs (Figure I.5).

Following Goh and Chan (2010), from 1965 to 2005, there were approximately 10 TCs each year in the SCS. Most TCs pass through the Philippines and make landfall in southern China and Vietnam. There are two kinds of TCs in the SCS: those locally formed in the SCS (local TCs, 40%) and those crossing the SCS (nonlocal TCs, 60%). Most local TCs are less intense and harder to predict than nonlocal TCs, as they have a relatively short time to develop before making landfall (Wu et al. 2020). Previous statistical studies show that about 98% of the TCs form from May to December in the SCS (Wang et al. 2007). Heavy winds and rainfall from TCs lead not only to severe disasters (such as storm surges and flooding) but also strongly affect the primary production (Menkes et al. 2016, Lin 2012), the momentum, heat and water exchanges between the ocean and the atmosphere (Vincent et al. 2012, 2013), thus the water, heat and salt budgets over the whole SCS area.

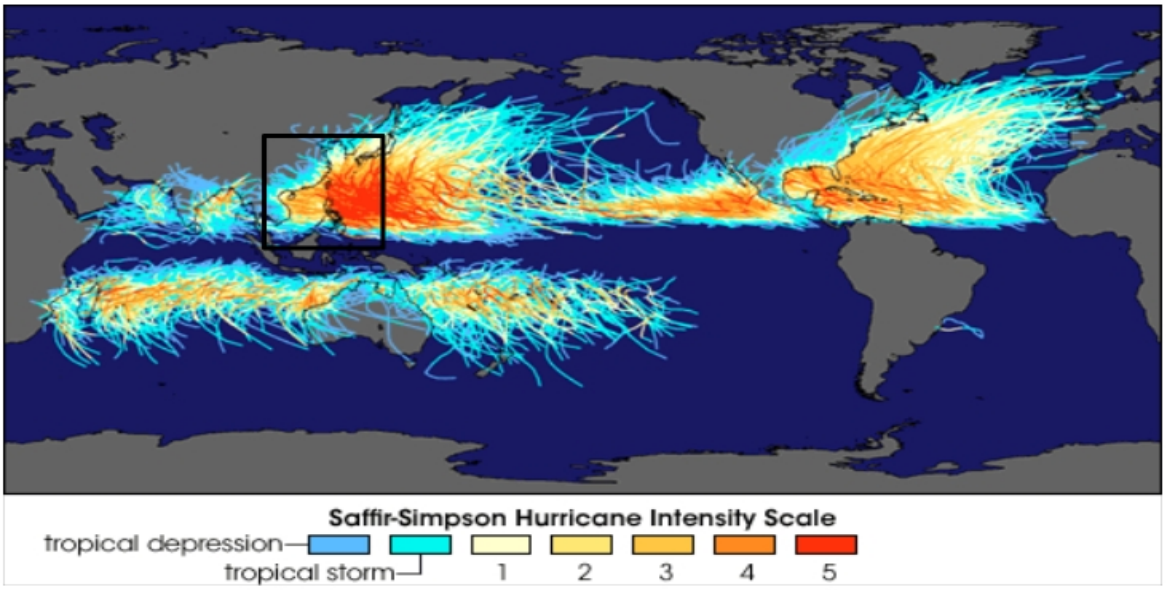

Figure I.5: TCs tracks over 150 years on the globe, with Saffir - Simpson Hurricane Intensity Scale (image from NASA Earth Observatory (https://earthobservatory.nasa.gov). The black box indicates the Northwest Pacific and SCS zone.

I.2.4. Climate phenomena

The SCS climate is strongly affected by several climate phenomena: the El Niño Southern Oscillation (ENSO), the Pacific Decadal Oscillation (PDO), the Indian Ocean Dipole (IOD) at interannual and interdecadal time scales and the Madden Julian Oscillation (MJO) at intraseasonal time scale.

ENSO

ENSO is one of the most important climate phenomena on Earth due to its ability to change the global atmospheric circulation, which in turn, influences temperature and precipitation across the globe. ENSO is a coupled climate phenomenon as it involves changes in both the ocean and the atmosphere. ENSO includes three phases: the two opposite phases “El Niño” and “La Niña”; between these two states is the Neutral phase.

+ El Niño (warm phase) corresponds to: a warming of the ocean surface in the central and eastern tropical Pacific Ocean, where the sea surface temperature (SST) is higher than the average value, inducing a cyclonic zonal circulation over the Pacific (Figure I.6a). Precipitation tends to reduce the tropical Western Pacific and increase over the tropical Pacific Ocean. Surface winds that normally blow

from east to west (easterly winds) along the equator, weaken or even start blowing in the other direction. Monsoon winds over East Asia are also reduced (Wang et al. 1999).

+ La Niña (cool phase): opposite to the El Niño event, La Niña occurs with a cooling of the ocean surface in the central and eastern tropical Pacific Ocean (Figure I.6b). Rainfall increases over the tropical Western Pacific while it decreases over the central tropical Pacific Ocean. Normal easterly winds become stronger. The East Asia monsoon is strengthened during this event (Neelin and Latif 1998).

+ Neutral: during this phase the SST of the tropical Pacific is generally close to the average. It is noteworthy that in certain moments, the ocean looks like that it is in El Niño or La Niña state, but the atmospheric conditions are not coming along (and vice versa), we are still in the neutral phase.

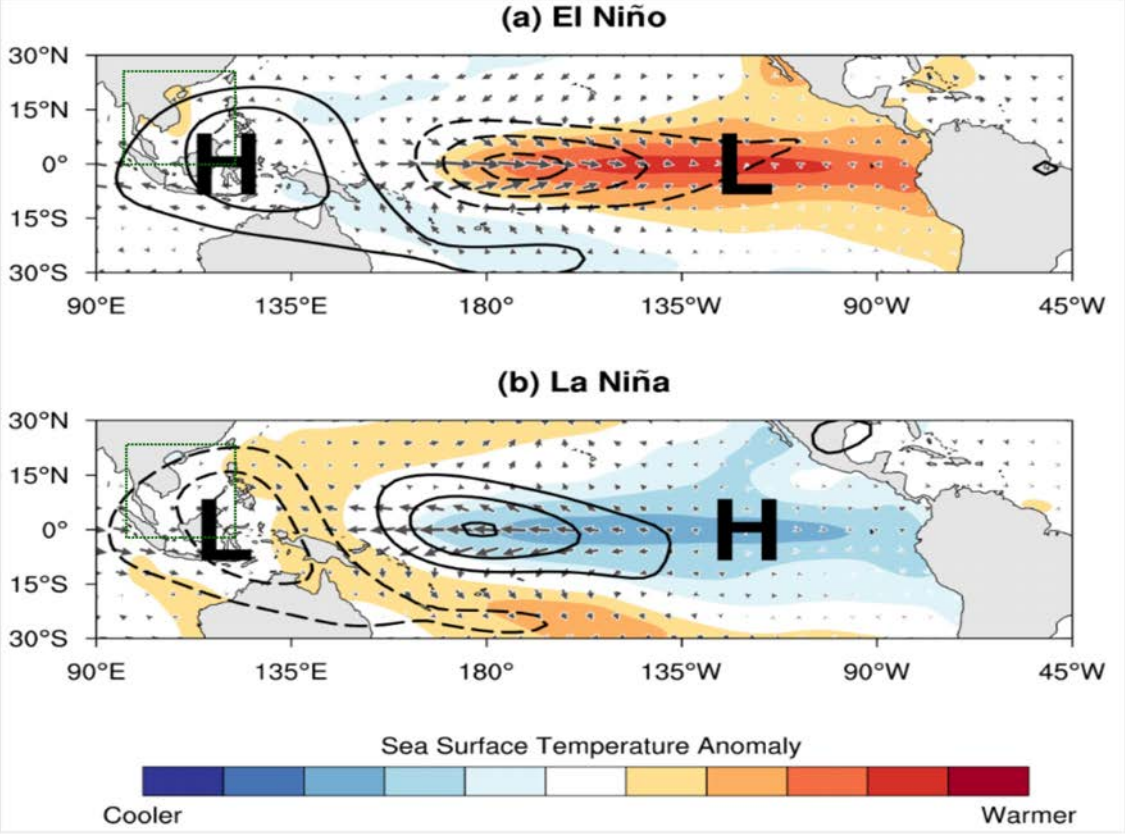

Figure I.6: Winds and SST anomaly during (a) El Niño event and (b) La Niña event. The green box indicates the SCS zone. Modified from original image on Weather Works website (https://weatherworksinc.com).

Historically, ENSO occurs every three to seven years, and lasts for one or two years. Several studies have investigated the impacts of ENSO on the climate and hydrodynamical processes of the SCS. The SCS summer monsoon is strongly influenced by ENSO: it is weakened/ strengthened by the El Niño/La Niña years, with a later/sooner onset (Lau and Yang 1997, Chou et al. 2003, Zhou et Chan 2007, Liu et al. 2012). Since the SCS monsoon is one of the important subsystems of the East Asian monsoon, ENSO also certainly has impacts on the SCS winter monsoon, however there are much less studies on the relation between ENSO and the SCS winter monsoon. Following Wang and He (2012), the winter East Asian monsoon is weakened/strengthened during El Niño/La Niña years. Studies about ENSO related interannual variability of other climate parameters over the SCS zone such as precipitation (Juneng and Tangang 2005, Räsänen and Kummu 2013, Räsänen et al. 2016), cyclone frequency occurrences (Camargo and Sobel 2005; Wu et al. 2005), and surface winds (Huynh et al. 2016) have been also conducted.

ENSO has also a significant influence on the SCS ocean circulation, including the interocean fluxes. Wang.Y et al. (2006) found that the interannual variations of the SCS upper layer currents are highly correlated with ENSO while anomalous SCS circulation has been observed over El Niño events: both the winter basin-wide cyclonic gyre and the summer double gyres weaken. According to Qu et al. (2004), Wang.Y et al. (2006) and Liu et al. (2008), the intrusion of Pacific water into the SCS through the Luzon strait tends to be higher/lower during El Niño/La Niña years. The SCS SST anomaly and SLA (Sea Level Anomaly) during ENSO events are the target of several studies (Wang et al. 2006, Tan et al. 2016, Peng et al. 2013, Rong et al. 2007). In general, the SCS SST is warmer (cooler) during El Niño (La Niña) events and reaches a maximum (minimum) approximately 3 - 6 months after SST anomalies peak in the tropical Pacific (Klein et al. 1999). The SCS SST can be influenced by El Niño through atmospheric forcing: anomalous Walker circulation modulates the SST through surface heat fluxes (Klein et al. 1999, Wang et al. 2000, Tan et al. 2016). On the other hand, the variations of the SCS SST anomalies are modulated by the ENSO-induced ocean dynamical processes: the El Niño signal is conveyed into the SCS through the Luzon strait (Qu et al. 2004) and Mindoro strait (Liu et al. 2011). EOF analysis of the low-pass filtered sea level anomalies of Rong

et al. (2007) revealed that observed sea level shows a good correspondence with ENSO. The mean sea level anomalies are negative during El Niño years and positive during La Niña years.

ENSO also impacts local processes as coastal upwellings: Da et al. (2019) found a high significant correlation between the strength of the upwelling that develops in summer along Southern Vietnam and ENSO, with a lag time of 3 - 13 months.

PDO

In the North Pacific, the atmosphere and the ocean display a trend of covariance with a period of about 20 years. This variability is called the Pacific Decadal Oscillation (PDO), and was discovered by Steven R. Hare while studying salmon production pattern results in 1997. The PDO is often described as a long-lived El Niño-like pattern of Pacific climate variability (Zhang et al. 1997). The PDO index value is defined by the leading pattern (EOF) of SST anomalies in the North Pacific basin (typically, polewards of 20°N, Mantua et al. 1997). There are two phases of PDO:

+ A warm phase (positive values of PDO index) corresponds with below averaged sea level pressures in the North Pacific, anomalously cool SSTs in central and western North Pacific and anomalously warm SST in the eastern North Pacific, in the central and eastern tropical Pacific (Figure I.7).
+ A cool phase (negative values of PDO index): opposite to the warm phase, with above average sea level pressures in the North Pacific, warm SST anomalies in the central and western North Pacific and cool SST anomalies along the eastern North Pacific in the central and eastern tropical Pacific.

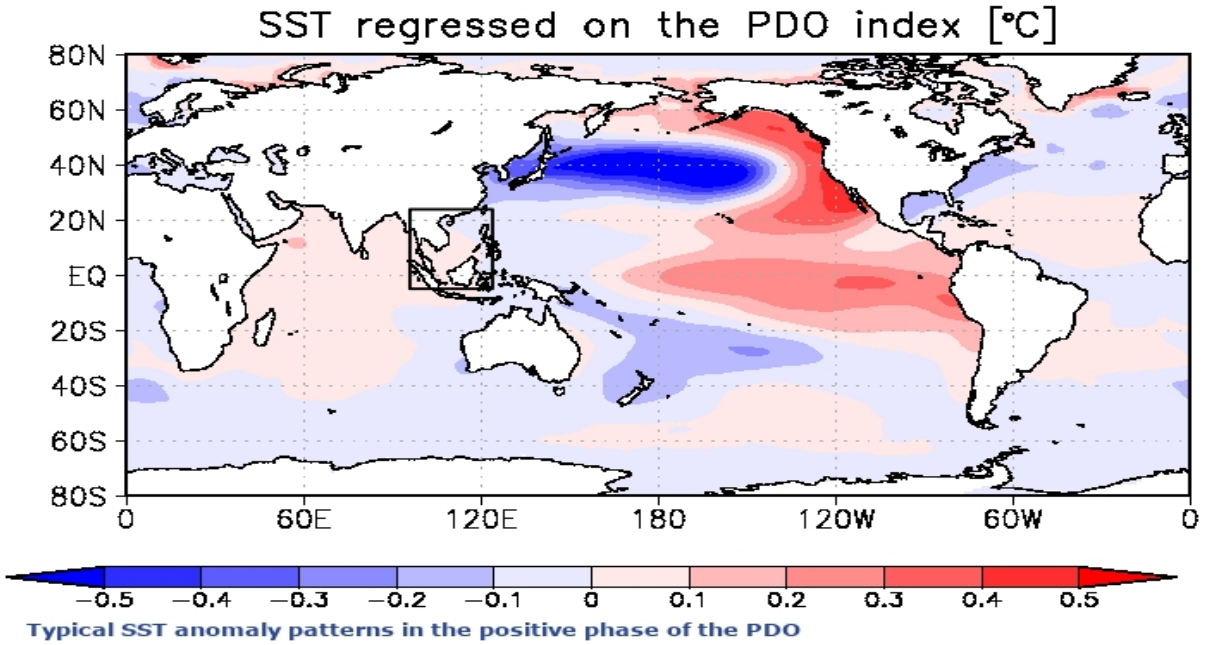

Figure I.7: Distribution of monthly SST anomalies (based on COBE-SST) linearly regressed on the PDO index in the positive phase of PDO. The black box represents the SCS zone. Image source: Japan Meteorological Agency (https://ds.data.jma.go.jp).

The largest distinction between PDO and ENSO is their timescales: the PDO persists from 20 to 30 years, while typical ENSO events last for 6 to 18 months. As a marginal sea of the Western Pacific, the SCS is considerably impacted by the SST oscillations related to PDO in the North Pacific. SLA of the southern and eastern SCS are negatively correlated with PDO (Han et al. 2008, Soumya et al. 2015). PDO also has a major effect on the Sea Surface Salinity (SSS) of the SCS as during the positive PDO phase, the precipitation over the zone is reduced (Zeng et al. 2018).

IOD

The Indian Ocean Dipole (IOD) is a coupled ocean - atmospheric phenomenon, like ENSO but in the Indian Ocean. It is defined by the SST difference between two regions : the western pole in the Arabian Sea (Western Indian Ocean) and the eastern pole in the Eastern Indian Ocean (off Sumatra, south of Indonesia). Positive IOD is characterized by positive SST anomalies over the Western Indian Ocean and negative SST anomalies off Sumatra and vice versa. IOD has a major impact on the Indian Ocean monsoon onset and precipitation rate over India, eastern South Africa, southern Australia and Indonesia

(Saji et al. 1999, Ashok et al. 2001). This phenomenon also influences the onset of the SCS summer monsoon in neutral ENSO years (Yuan et al. 2008) and the interannual variation of SLA in the southern SCS (Soumya et al. 2015).

MJO

The Madden and Julian Oscillation (MJO) corresponds to 30–60 days quasi-periodic oscillations in the whole tropical ocean and global atmosphere, which are regarded as main features of atmospheric low-frequency changes (Madden and Julian, 1971, 1972, 1994). Unlike standing patterns like ENSO, PDO or IOD, the MJO is a zonally moving pattern at approximately 4 to 8 m/s, through the warm parts of Indian Ocean to the Pacific Ocean. The MJO influences precipitation in several regions around the globe, including the Asian monsoon region (Lawrence and Webster 2002, Wu et al. 2018, Liu et al. 2020). The MJO contributes to about 10% of the intra-seasonal anomalous precipitations over the Southern China Continent in summer (Zhang et al. 2009). Isoguchi and Kawamura (2006), in investigating the relation of SCS oceanic phenomena and MJO, has found that MJO-related wind fields can intensify the summer monsoon, induce a surface cooling in the center basin and phytoplankton blooms off the South Vietnam coast in specific summers.

I.3. River discharges

Under the prevailing monsoonal climate, South East Asia watersheds receive very high rainwater input, with average annual precipitation over 1000 mm. Fang et al. (2009) deduced from the land discharges relation of Perry et al. (1996) a yearly river discharge over the SCS of 0.051 Sv. Although the volume of river discharges into the ocean is small compared to the whole SCS volume, they can have large scale impacts due to the large-scale circulation which advects freshwater masses hundreds of kilometers from the river mouth (Gan et al. 2009). Contributions of river inputs into the SCS are indeed considerable and provide freshwater, sediments and nutrients into the coastal waters, thus affect the water masses and dynamics by modifying the salinity, and impact the coastal ecosystem and biomass. The major rivers draining into the SCS are the tributaries of the Pearl river (south of China), the Red river (north of Vietnam) and the Mekong river (south of Vietnam)

(Figure I.1). Table I.1 summarizes the general information on the three major rivers into the SCS.

River	Area (10^3 m^3)	Length (km)	Max Elev. (m)	Ann. Prec. (mm)	Water Disch. (km^3/year)	Sed. Disch. (Mt/year)	Delta area (10^3 km^2)
Pearl	440	2100	1800	1600 - 2300	300	70	41
Red	150	1100	2200	1120	120	130	14
Mekong	810	4400	5400	1300	500	160	93

Table I.1: Features of the three major rivers into the SCS: Catchment area, River length, Maximal elevation, Annual precipitation, Water discharges, Sediment discharges (Mt = million tons), Delta area. Data collected from Wang et al. (2011, 2012).

The monthly climatological river runoff of the three rivers presented in Figure I.8 shows a high seasonal variability. High discharge periods of the three rivers coincide with the SCS summer monsoon (from Spring to Autumn) while the low discharge periods are recorded when SCS winter monsoon prevails. The ratio between the maximal et minimal values of the river freshwater discharges can go up to 8 for the Pearl river, and even more for the Red and Mekong rivers (more than 10). Among the rivers emptying into the SCS, Mekong is the biggest one regarding the catchment area and water discharges (twice bigger than the Pearl river, five times bigger than the Red river), as well as in term of sediment discharges (respectively twice and three times bigger than the Pear and Red rivers).

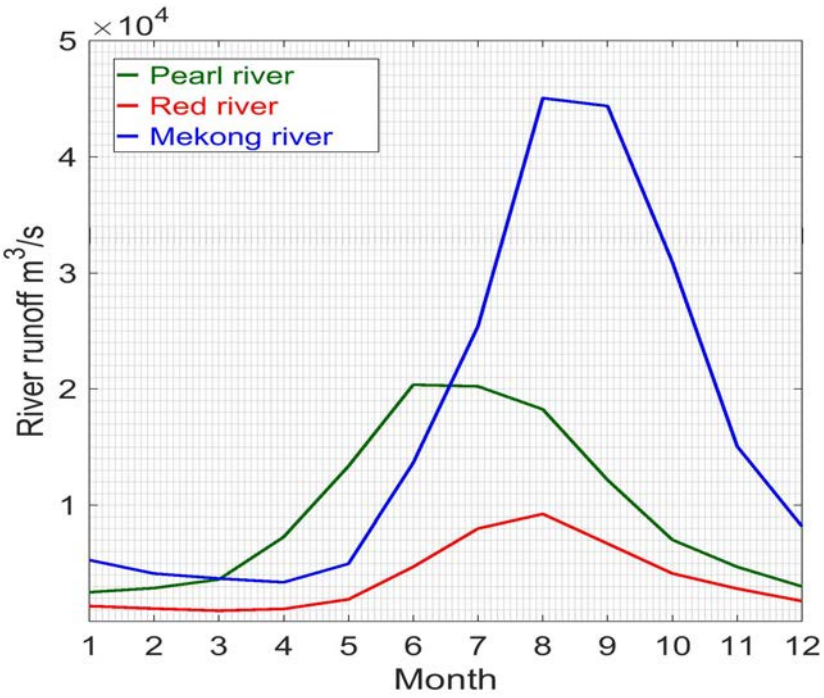

Figure I.8: Climatology river runoff (in m^3/s) of the three major rivers of the SCS; data issued from CLS (Collecte Localisation Satellites, INDESO project, Tranchant et al. 2016) for the Pearl and Mekong rivers and from the National Hydro-Meteorological Service (NHMS) of Vietnam for the Red river.

Together with the major rivers, small mountainous rivers in Taiwan, in islands of the southern SCS margin and along the Vietnam coast provide high supplies in sediments to the SCS: Liu et al. (2008) estimated the total sediment discharges from small Taiwanese rivers at more than 300 Mt/year, comparable to the discharge from large rivers. These voluminous river sediment discharges were responsible for the development of mega deltas and extensive continental shelves that feature the South and East China Seas (see section I.1.1).

The SCS - one of the richest fishing grounds in the world, receives large amounts of nutrients from river discharge that support productivity. Because the weak Coriolis force allows direct across-shelf movement of tropical and subtropical river plumes, the proportion of nutrients reaching the open ocean from rivers such as the South East Asia rivers tend to be the most important (Sharples et al. 2016). In addition to carbon, rivers export nitrogen, phosphorus and silica which are the key potentially limiting nutrients required for phytoplankton growth. Thus, riverine nutrients not only impact the primary

productivity but also contribute to regulating the long-term biological productivity of the ocean and the ocean carbon storage (Jickells et al. 2017). Despite the importance of riverine nutrient concentrations on the ocean biogeochemical characteristics, in-situ monitoring nutrient data over major rivers of the SCS are still scarce.

Since recent decades, scientists have observed a strong decrease in the water and sediment river discharges into the SCS, mainly due to the anthropogenic activities such as dam construction, excess groundwater extraction and deconstruction of coastal ecosystems (Saito et al. 2007, Le et al. 2007, Wang et al. 2011, Vinh et al. 2014). It is thus important to study the interannual to long term effect of the changing river runoff (not only from major rivers but also from smaller rivers) to the thermohaline and biogeochemical characteristics of the SCS, and its contribution to the water, heat and salinity budgets and marine ecosystems over the basin.

Rivers	NH_3-N	TN	DIN	DON	PN	TP	DIP	SiO_2
Pearl[(a), (b)]	2.94	3.17	1.59	0.44	0.003	0.27	0.02	-
Mekong[(c)]	0.41	-	0.45	-	-	0.13	-	19.29
Red[(d)]	0.17	-	0.75	-	-	0.03	-	3.53

(a) In-situ data from Tong et al. 2015, period 2006 - 2012
(b) In-situ data from Lu et al. 2009, period 2005 - 2006
(c) In-situ data from the National Hydro-Meteorological Service (NHMS) of Vietnam, period 2013 - 2017
(d) In-situ data from Institute of Natural Products of Chemistry (INPC), Vietnam Academy of Sciences and Technologies (VAST)

Table I.2: Concentration (in mg/L) of ammonium (NH_3-N), Total Nitrogen (TN), Dissolved Inorganic Nitrogen (DIN), Particulate Nitrogen (PN), Total Phosphorus (TP), Dissolved Inorganic Phosphorus (DIP) and SiO_2 of major rivers.

Table I.2 resumes information on nutrient concentrations of major rivers collected from different sources and studies. Like other tropical rivers, these rivers discharge relatively high concentrations of nutrients. Highest nutrient concentrations are observed at the Pearl River. Following Tong et al. (2015), the sources of nutrients flowing into the seas could be

generally divided into non-point sources (such as agriculture diffuses) and point sources (such as industrial and sewage sources). To feed the growing population in the region, more grains are planted and more animal-derived products are required. The increased nutrient discharges from agriculture, wastewater and industrial emissions caused by the urbanization and industrialization also increased nutrient inputs to the rivers and coastal waters. The numerical study of Qu and Kroeze (2011) suggested that between 1970 and 2000 the dissolved nitrogen and phosphorus export to the Chinese coastal water increased significantly, while the export of other nutrients changed less.

In the southern basin, the nutrient discharge of the Mekong river into the SCS has much reduced in recent years, due to dam construction. According to Baran et al. (2015), the number of dams in the Mekong basin is expected to increase from 16 in the year 2000 to between 77 and 136 by 2030. Following the same study, these dams retain and accumulate sediments and nutrients in their reservoirs; as such planned dam development is expected to result in a 60 to 96% reduction in sediment flow to downstream Mekong waters. This loss of sediments and nutrients will have a serious negative impact on aquatic habitats and coastal zone ecology, as well as on water productivity, fish production, and ultimately on food security.

I.4. Ocean dynamics characteristics

I.4.1. SCS circulation

As explained above, the SCS is subjected to forcings of different scales and origins, and its circulation is regulated by a combination of factors: the geometry of the zone, the connection with the Western Pacific Ocean and Indian Ocean and a strong variability of atmospheric forcings, from the daily to the seasonal and interannual scales (Shaw and Chao 1994, Metzger and Hurlburt 1996, Gan et al. 2006). In this section we present a short overview on our current knowledge of the SCS multi-layer circulation.

I.4.1.1. Surface and subsurface circulation

Earliest studies on the SCS surface circulation were carried out in 1950s, 1960s by Dale (1956) and Wyrtki (1961) using observational data deduced from ship drift data and prevailing wind data. They all pointed out that the monsoon winds are the main factor driving the SCS surface circulation. Since then, several studies on the SCS surface circulation have been conducted, broadening our understanding on this subject. Wyrtki (1961), Xu (1982), Shaw and Chao (1994), Chu and Li (2000), Fang et al. (2002) all agreed on a reversal surface circulation in response to the monsoon winds reversal. In winter, strong northeasterly monsoon winds generate a cyclonic surface circulation over the whole basin with subbasin cyclonic gyres in both northern and southern parts of the SCS (Figure I.9a). In summer, relatively weaker southwesterly monsoon winds blow over the region, leading to a structure with a cyclonic gyre in the North and an anticyclonic gyre in the South (Figure I.9b, Qu 2000, Gan et al. 2016).

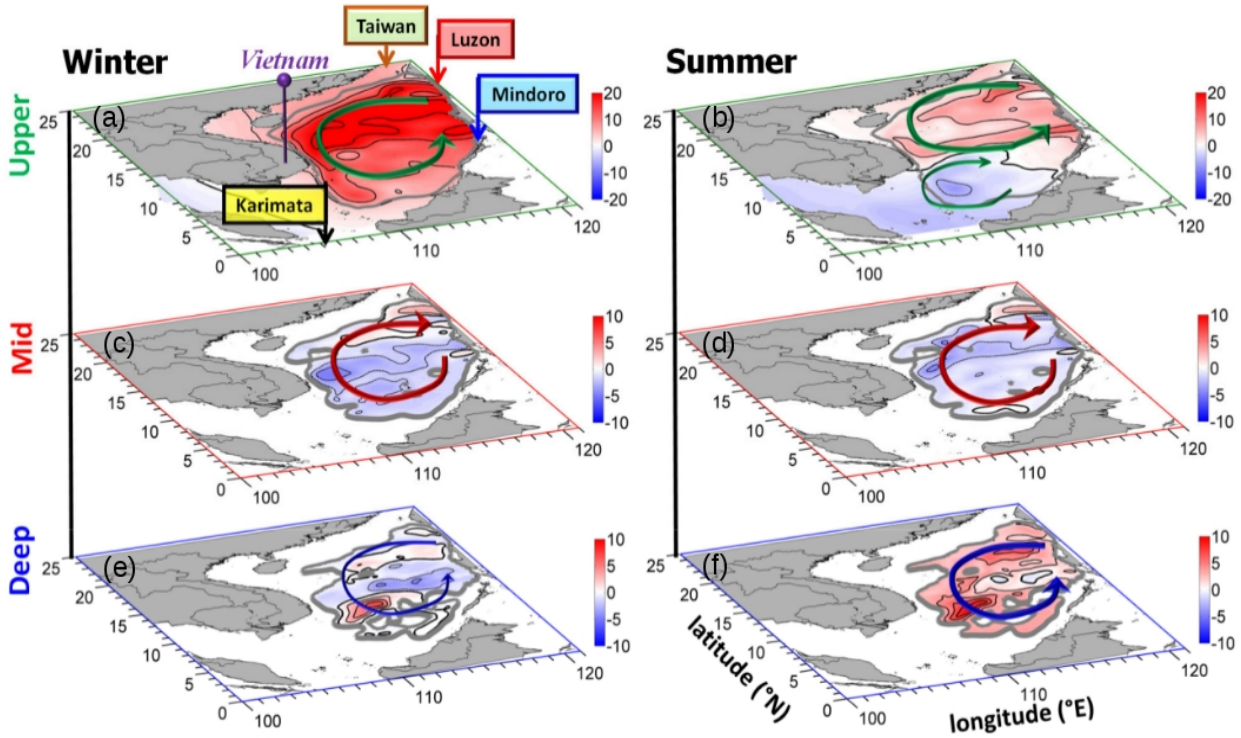

Figure I.9: Seasonal SCS circulation in different layers: (a, b) Upper layer (<750 m, c, d), intermediate layer (750 - 1500 m, e,f), deep layer (>1500 m) in winter (left) and in summer (right). Shade colors indicate the simulated barotropic stream functions (Sv). The circles represent the mean circulation in each layer. Adapted from: Gan et al. (2016).

The subsurface layer (100 - 500 m of depth) circulation is similar to the surface circulation, except that the former is more persistent than the latter since it is not submitted to the direct influence of wind stress (Xu 1982, Zhu et al. 2019). In terms of dynamics, unlike the surface layer, primarily characterized by a wind driven circulation, the subsurface circulation forcing is a mixture of wind stress curl effect (Ekman pumping) and geostrophic effect. Using hydrodynamic data, Li and Qu (2006) confirmed a cyclonic circulation in the subsurface layer. In seasonal scale, Qu (2000) revealed, from the dynamic height chart at 100 m depth, two cyclonic eddies named West Luzon eddy in winter and East Vietnam eddy in summer (see “Eddies and upwelling” below). Their existence reinforces the hypothesis of basin scale cyclonic circulation in the subsurface layer. In summer, the subbasin circulation is cyclonic in the northern SCS and anticyclonic in the southern SCS (Zhu et al. 2017). The year-round intrusion of Pacific water into the SCS through the Luzon strait in the upper 500 m (Tian et al. 2006, Zhang et al. 2015) plays a significant role in the SCS circulation in the upper layer: this westward flow maintains the cyclonic circulation in the northern SCS basin in summer even though the southwest monsoon prevails over the whole basin.

1.4.1.2. Intermediate and deep layer circulation

In the intermediate layer (500 - 1700 m depth), the SCS circulation - deduced from hydrographic data (Gan et al. 2016) and geographic current velocities (Zhu et al. 2017) - is considered to be anticyclonic on average. Previous work suggests that the intermediate layer circulation is characterized by a relatively steady flow pattern, dominated by local gyres and eddies. Most numerical studies show an anticyclonic circulation in yearly mean and in winter (Yuan 2002, Xu and Oey 2014), but results differ in summer: Gan et al. (2016) found a basin wide anticyclonic circulation in both winter and summer (Figure I.8c, d) while Wei et al. (2016) obtained in the southwestern SCS a subbasin cyclonic gyre in winter and a subbasin anticyclonic gyre in summer.

In the deep layer (> 1700 m), limited observations of Wang (1986) and Li and Qu (2006) inferred a possible cyclonic circulation. Later, Qu et al. (2006), Wang.G et al. (2011), Gan et al. (2016), Lan et al. (2015) and Zhu et al. (2017) obtained the same result: a strong inward flow from the Western Pacific enters the SCS basin through Luzon strait, turns northwestward then southwestward off the southern China continental slope, intensifies along the southwestern end of the deep basin, and eventually forms a basin scale cyclonic circulation (Figure I.8e, f).

It is important to note that due to the lack of in situ observations, the intermediate and deep layer circulation within the SCS basin, especially its seasonal variability, stays relatively poorly known until now. In recent years, several numerical studies and geostrophic analyses support the concept proposed by Yuan et al. (2002) of a sandwiched vertical circulation of the SCS basin: cyclonic circulations in the upper and deep layers separated by an anticyclonic circulation in the intermediate layer (Xu and Oey 2004, Gan et al. 2016, Zhu et al. 2017). This alternating cyclonic - anticyclonic circulation would be induced to the alternating inflow - outflow vertical distribution of the water fluxes at Luzon strait, that will be detailed in section I.4.2.1.

1.4.1.3. Kuroshio intrusion and Luzon strait transport

The Kuroshio current is the western boundary current of the North Pacific subtropical gyre. The Kuroshio originates from the North Equatorial Current (NEC), which bifurcates at the east coast of Luzon (Philippines) into the southward flowing Minadao Current (MC) and the northward Kuroshio current (Nitani et al. 1972), forming the so-called NMK current system shown in Figure I.10.

As the Kuroshio flows northward passing the Luzon Strait, its path makes a slight detour intruding into the SCS with only a small fraction actually entering the interior, mostly during winter (dashed black line, Figure I.10). According to the overview of Hu et al. (2000), different types of the Kuroshio intrusion into the SCS occur: Kuroshio direct branch, Kuroshio Current Loop (KCL), Kuroshio extension and Anticyclonic rings. As explained above, this intrusion acts against the effect of the northeastward summer monsoon wind and contributes to maintain a cyclonic circulation in the northern SCS in summer. The Kuroshio intrusion contributes the most to the Luzon strait transport (LST) - the Western Pacific water masses entering the SCS through Luzon strait. Kuroshio intrusion into the SCS is seasonally varying. Historical hydrographic data (Wyrtki 1961, Qu 2000, Xue et al. 2004) as well as numerical studies (Qu et al. 2004, Metzger and Hurlburt 1996, Hsin et al. 2012) showed similar seasonal cycle: the LST is larger in winter and smaller in summer under the influences of the seasonal reversing monsoon. On an interannual time scale, the LST from the Pacific into the SCS tends to be higher during El Niño years and lower during La Niña years, and play a key role in conveying the ENSO signal from the Pacific into the SCS (Qu et al. 2004, Liu et al. 2008). Estimates of the Kuroshio intrusion or LST, by observation and numerical methods, are detailed in the section I.4.2.2.

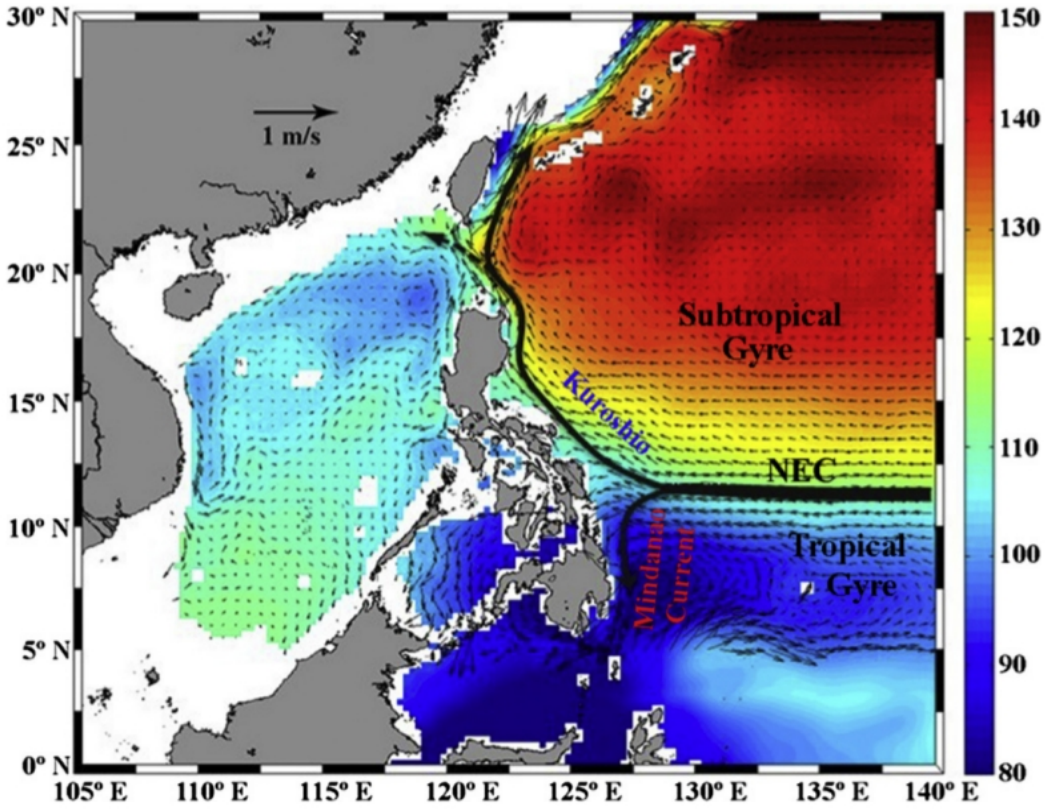

Figure I.10: The NMK current system, including the North Equatorial Current (NEC) - solid black line, the southward Mindanao Current (MC) and the northward Kuroshio. Shading colors represent the Mean Absolute Dynamic Topography (ADT, units: cm). Image source: Nan et al. 2015.

I.4.1.4. Eddies and upwelling

An important feature of the SCS ocean dynamics is the development of seasonal mesoscale eddies and upwelling. Most eddies are generated in the SCS deep basin over key regions such as the southwest of Taiwan, west of Luzon and southeast of Vietnam (Figure I.11a). These eddies were observed from both hydrodynamic data (Chu and Lu 1998) and altimetry data (Shaw et al. 1999, Wang et al. 2003). Two cyclonic mesoscales eddies were particularly studied: the West Luzon eddy and the East Vietnam eddy (Shaw et al. 1996, Qu 2000, Wang et al. 2003, Chen et al. 2011). In winter, the West Luzon cold eddy occurs several kilometers offshore at about 18°N – 118°E northwest of Luzon. It first appears in November, reaches its maximum in January – February then decays in May – June. In summer, the East Vietnam eddy develops in summer (June – August) at about 14°N – 110°E and becomes strongest at the end of season (October – November) with prevailing summer monsoon winds. Dynamical considerations suggested that both local

wind stress curl and basin-scale circulation participate in the formation of these eddies (Qu 2000). Eddies have profound effects on chlorophyll distribution (He et al. 2016), primary productivity (Lin et al. 2010, Loick et al. 2007), SST and wind variability (Chow and Liu 2012). Li et al. (1998) showed that eddies originating from the Kuroshio current could transport water of different properties from the Pacific into the SCS. Therefore, eddies play an important role in the exchange of water, heat and salt between the Pacific and the SCS via Luzon Strait.

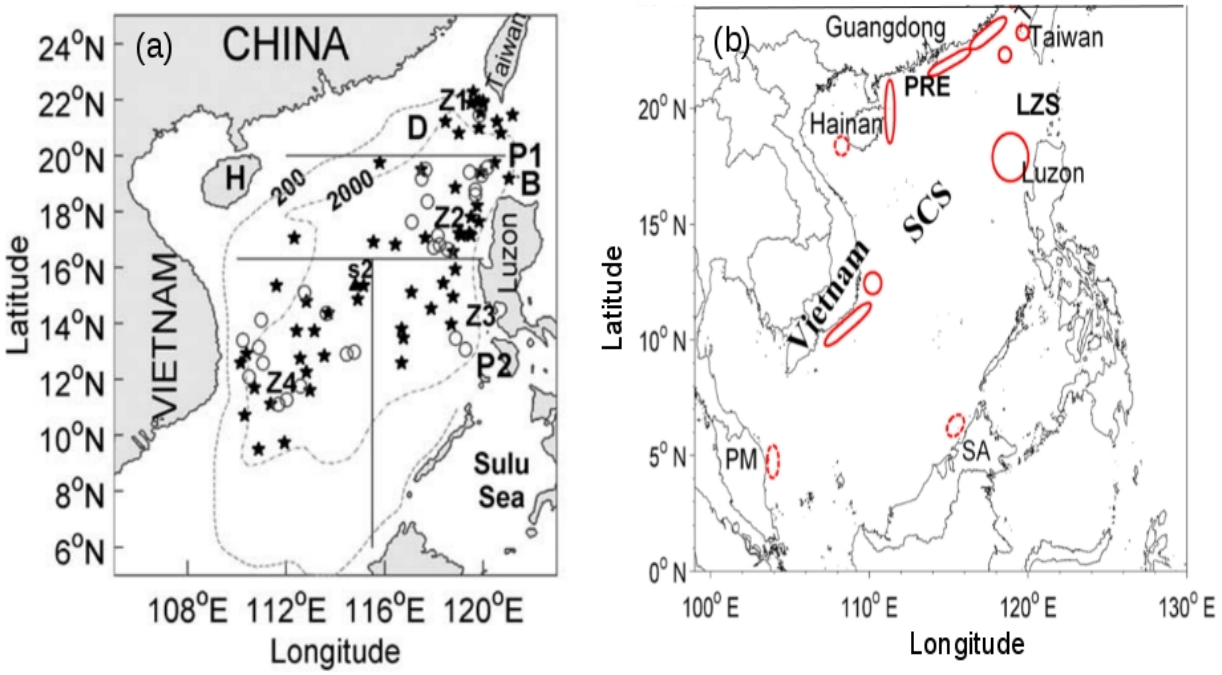

Figure I.11: (a) Positions of eddies identified by altimetry during the period 1993 – 2000 (○: cyclonic eddies, ⋆: anticyclonic eddies). Adapted from Wang et al. (2003); (b) Distribution of upwelling zone over the SCS (red zone). Adapted from Hu and Wang (2016). PRE=Pearl River Estuaries; LZS = Luzon Strait.

Associated with those two eddies, two coastal upwellings occur off the southern coast of Vietnam in summer (Southern Vietnam Upwelling SVU) and off the Luzon island in winter (Western Luzon Upwelling WZU, Figure I.11b). Upwelling is defined as an upward movement of seawater, with vertical speeds ranging from about 10^{-6} to 10^{-4} m/s (Hu et al. 2016), and large amounts of nutrients lifted from the deep up to the shallow and surface layers. With relatively high chlorophyll concentrations and low SST (Figure I.12a, b), upwellings play a very important role in primary and secondary productivity (they are

generally important fishing zones) as well as in atmosphere – ocean CO2 exchange and carbon recycling (McGregor et al. 2007). Xie et al. (2007) found that the surface cooling over the SVU could also reduce precipitation here, thus could influence the atmospheric freshwater flux. The cooling and saltening of the surface layer induced by upwelling might also affect the heat and salt circulation over the SCS and exchanges with neighbouring seas and oceans.

Several studies have been performed to investigate the upwelling dynamics in the SCS (Wyrtki 1961; Shaw et al. 1996, Xu 1982, Fang et al. 2002, Kuo et al. 2000, Xie et al. 2003, 2007, Wang.G et al. 2006, Dippner et al. 2007, Hein 2008, Chen et al. 2012, Da et al. 2019). The principal mechanisms for generating the upwelling phenomenon include the alongshore wind and wind stress curl, which are the controlling factors of upwelling dynamics. Those studies moreover suggested that topography (widened shelf, shelf break, cape, or canyon), tide (tidal mixing, internal tide), stratification, background flow and chaotic variability also play important roles in modulating those upwellings.

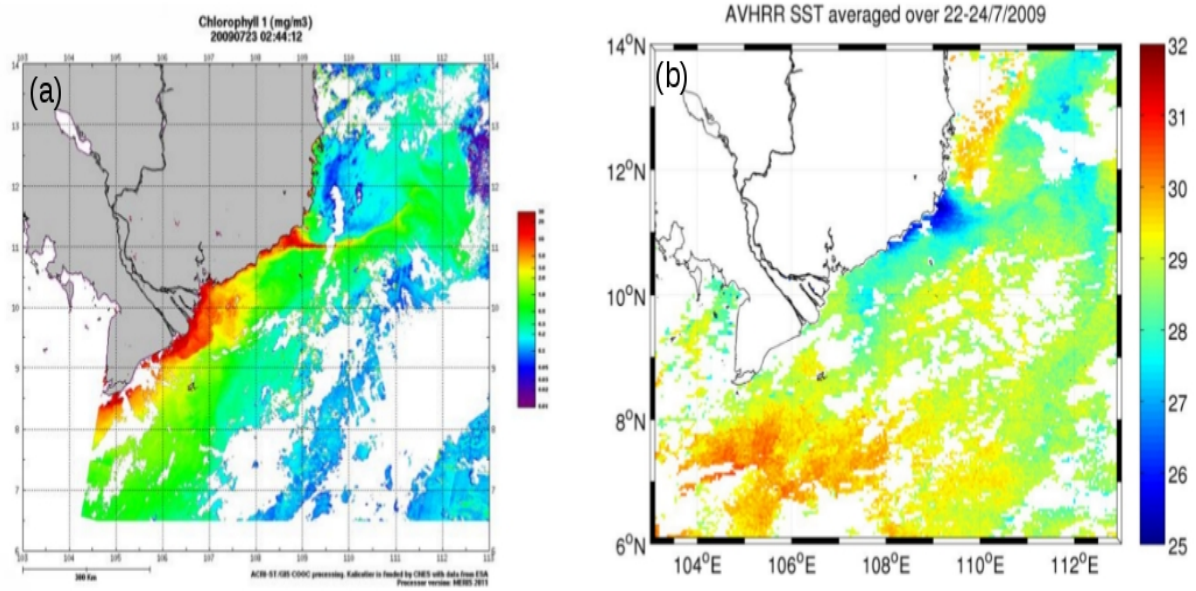

Figure I.12: SVU zone with high Chl a concentration (a) and low SST (b) from satellite observation (MERIS Chlorophyll surface concentration map on 23 July 2009 and AVHRR SST map averaged over 22 – 24 July 2009). From: Da (2018).

I.4.2. The South China Sea Throughflow (SCSTF)

I.4.2.1. Overview of the SCSTF

The SCS plays an important role in global ocean circulation and climate, connecting the Pacific and Indian Oceans (Qu et al. 2005, Tozuka et al. 2007). The SCS is indeed connected with surrounding oceans and seas by several straits (Figure I.1, red lines). The Luzon strait – the largest and deepest interocean strait of the zone – is the main pathway of seawater from the Pacific Ocean into the SCS (Wyrtki, 1961). Besides, the SCS exchanges seawater with the East China Sea through the Taiwan strait, with the Sulu Sea through the straits of Balabac and Mindoro, with the Java Sea and Andaman Sea (Indian Ocean) through Karimata and Malacca straits. Except the Luzon and Mindoro straits whose sills are respectively 3000 m and 400 m deep, the other straits are shallower than 100 m (Figure I.1). Based on numerical studies, satellite observations and long-term wind data analyses, Qu et al. (2005) and Yu et al. (2007) revealed a circulation where Pacific Ocean water masses enter the SCS through the Luzon strait and leave the basin through the Taiwan strait, Karimata strait and Mindoro strait, forming the South China Sea Throughflow (SCSTF) (Figure I.13).

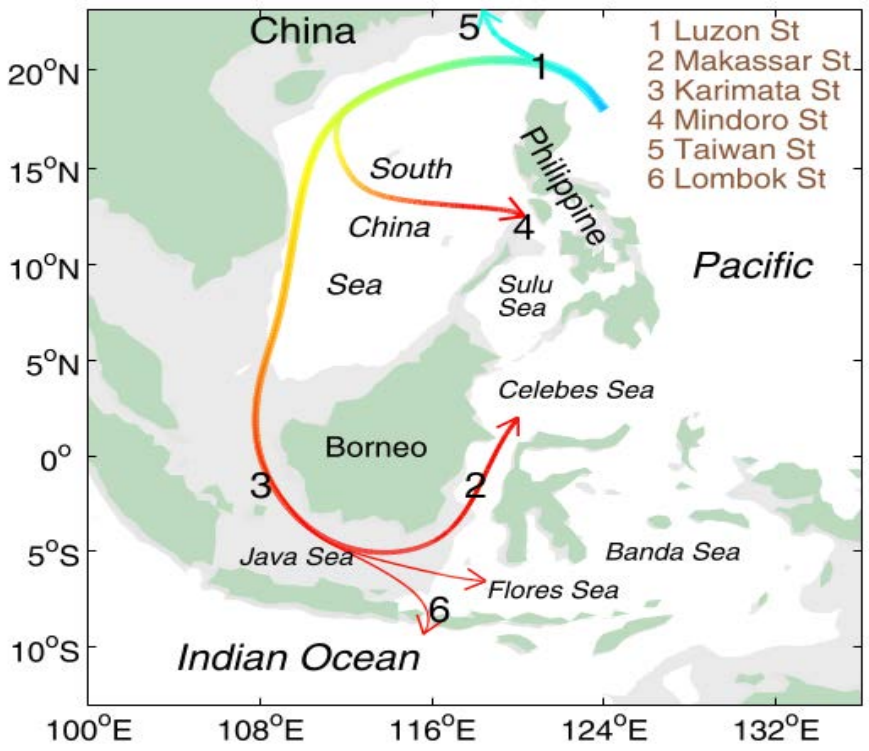

Figure I.13: A schematic diagram of the SCSTF. Image source: Qu et al. (2005)

Estimates of volume, heat and salt transports at the straits were performed based on in-

situ and satellite observations detailed in the next section and in Table I.3 below (Fang et al. 1991, Chu and Li 2000, Chung et al. 2001, Wang Y.H et al. 2003, Tian et al. 2006, Yuan et al. 2008b, Yang et al. 2010, Fang et al. 2010, Qu and Song 2009, Sprintall et al. 2012, Susanto et al. 2013). However, those estimates remain limited in space and time. Numerical modeling is a relevant tool to address this question, complementing in-situ and satellite measurements that cannot simultaneously access all the components of the whole water, heat and salt cycles and their interactions. Several modeling studies based on an integrated approach taking into account all terms of the water, heat and/or salt budgets were performed and are also detailed below. Many of them focused on water fluxes. Yaremchuk et al. (2009) provided estimates of upper volume transport at Luzon, Taiwan, Mindoro and Karimata straits issued from a reduced – gravity model. Wang et al. (2009), using a 1/6° resolution model, evaluated the seawater fluxes through all interocean straits of the SCS. In both studies, the inflow at Luzon was considered to be balanced by the outflows at other straits, and the contribution from the atmosphere and rivers was not discussed. Later, Liu et al. (2011), Hsin et al. (2012), Tozuka et al. (2014), Wei et al. (2016) with higher resolution numerical models provided estimates of the SCS interocean volume transports, but models configurations and assumptions did not allow to rigorously close the water budget. Besides the volume transport, other studies also estimated heat and salt fluxes. Qu et al. (2004) studied the whole depth volume transports through three straits of SCS (Luzon, Mindoro and Sunda Shelf) and the upper heat budget of the zone, revealing that the surface heat flux is the primary heating process. However, their numerical study was carried out with a closed Taiwan strait and a shallower Mindoro strait than reality, the inflow at Luzon was balanced by outflows at Mindoro and Sunda Shelf straits, and the river heat flux was neglected in the heat balance. Qu et al. (2006), using a 0.1° resolution model, estimated the total volume, heat and freshwater transport of the SCSTF, deducing surface heat and freshwater transports respectively from the difference between the inflowing and outflowing temperature and salinity. Fang et al. (2005, 2009) were the first to evaluate transports through all interocean straits of the SCS, including Balabac and Malacca straits, using 1/6° resolution simulations. They estimated the climatological average and monthly seasonal cycle of seawater volume and heat transports. They however assumed that lateral outflows exactly compensate the lateral

inflows. Using the same method, Wang Yan et al. (2019) used 7 km resolution numerical outputs to estimate the water, heat and salt fluxes through four main straits of the SCSTF for the period 2004 – 2014.

Almost all numerical studies focused on the climatological yearly average (over the whole studied period) and the climatological seasonal cycle of these fluxes. The interannual variations of SCSTF volume, heat and salt transports are less studied and mostly focused on the LST. According to Qu et al. (2004) and Wang. D et al. (2006), the interannual variability of the LST is mainly modulated by the large-scale wind stress in the western and central equatorial Pacific. Qu et al. (2004), using results from a global ocean circulation model for the period 1982 – 1998, revealed that the LST contains a strong ENSO signal: its value became stronger in El Niño years, and weaker in La Niña years. Wang.D et al. (2006) suggested the same results while evaluating the relationship between LST (calculated by the Island Rule, Godfrey 1989, from ocean data assimilation SODA over the period 1982 – 1998) and ENSO. Qu et al. (2006), through model output analysis on the period 1950 – 2003 on the upper layer heat budgets, confirmed the hypothesis that the SCS played the role of heat capacitor, storing heat in El Niño years and releasing heat in La Niña years. Yu and Qu (2013), using 62 – year – hindcast outputs (1950 – 2011) from the eddy-resolving ocean general circulation model OFES, revealed that the upper 745 m LST (and in general the SCSTF) has a strong connection with the PDO. Studies on interannual transports through other straits of the SCSTF are still limited, although the contributions of these transports are not negligible.

Concerning the vertical distribution of fluxes in the water column, several studies revealed alternating inflow/outflow of the yearly average vertical volume transport of Luzon strait. Qu et al. (2004), Hsin et al. (2012), Nan et al. (2013, 2015), Liu and Gan (2017), using numerical methods, found the same vertical structure of volume transport crossing the Luzon strait: the flow is a westward (inflow) in the upper and deep layers, and eastward (outflow) in between (Figure I.14). Li and Qu (2006), using dissolved oxygen distribution data from the World Ocean Atlas (WOA, 2001), also confirmed this sandwiched structure in vertical transports at Luzon. The vertical structure of fluxes through other straits are much less studied.

In the next section we review in detail the existing estimates of the SCSTF in terms of water, heat and salt transports from both observational and numerical methods.

I.4.2.2. Previous estimates

A summary of lateral volume, heat and salt transport published estimates at different interocean straits of the SCS is presented in Table I.3. Volume transport in-situ measurements are more numerous for the Luzon and Taiwan straits than for Karimata and Mindoro straits, and no direct measurements are available at Balabac and Malacca straits.

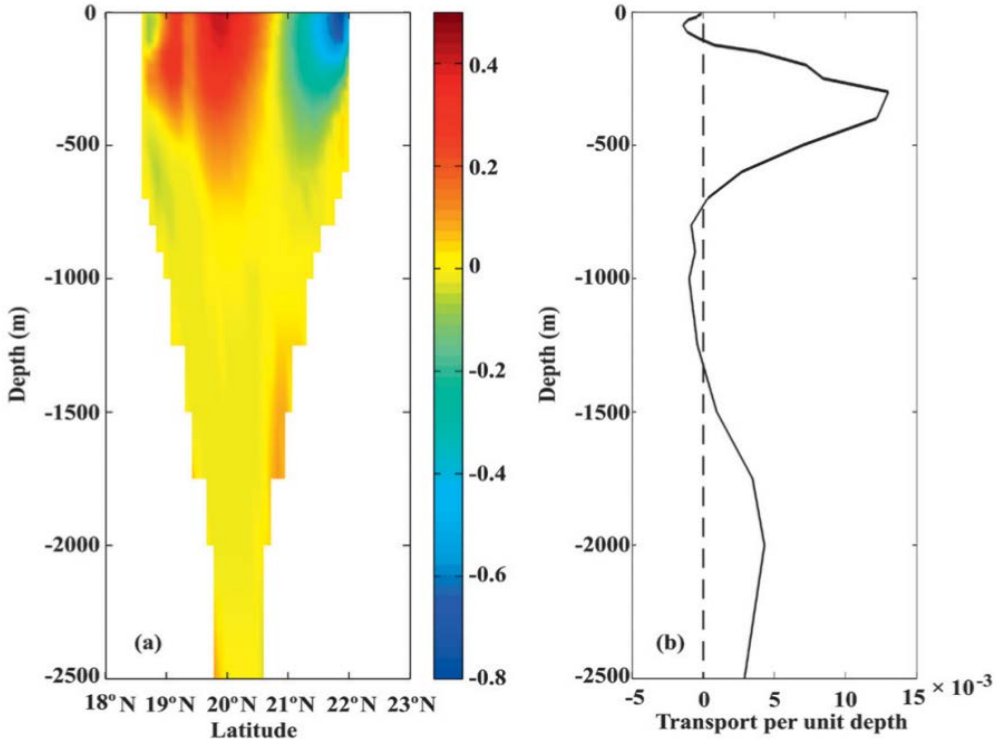

Figure I.14: (a) Annual mean zonal vertical velocity along a south-north transect at 120.75°E (m/s) and (b) vertical distribution of the LST (Sv/m) issued from a numerical study of Nan et al. (2013). The positive (negative) values represent inflow (outflow) currents. Image source: Nan et al. (2013).

Volume transport

The climatological and seasonal volume transport from the Western Pacific to the SCS through the Luzon strait (Luzon strait transport, or LST) was first estimated by Wyrtki

(1961) using hydrodynamic data. The author evaluated an average westward LST of 0.5 Sv for the upper layer (0-175 m). Since then, there have been several attempts to evaluate the LST. Estimates were first built from in-situ measurements. Converting temperature profiles from the World Ocean Atlas (WOA 1994) into dynamic heights, Qu (2000) obtained a yearly averaged LST estimate of 3.0 Sv for the upper layer (0-400 m). Chu and Li (2000) applied a P-vector calculation method on the United States Navy's temperature and salinity dataset over the period 1930-1997 and estimated an annual mean intrusion of 6.5 Sv from the Pacific Ocean into the SCS. Several observational studies revealed a year-round inflow LST, with a winter maximum and a summer minimum. Qu (2000) measured the strongest LST in January-February (5.3 Sv) and the minimum LST in June-July (0.2 Sv). Rong et al. (2007) deduced from the SODA (Simple Ocean Data Assimilation) global reanalysis dataset over 1958-2004 a maximum LST in December (3.1 Sv) and a minimum in May (0.74 Sv). Yuan et al. (2008), using NCEP wind data and hydrographic data obtained from August to September 1994, provided a full-depth inflow LST of 3.5 Sv. Other observations rather suggested alternating flows at Luzon Strait throughout the year, with a winter inflow and a summer outflow. Wyrtki (1961) observed, for the upper 175 m, inflow in winter (2.75 Sv) and outflow in summer (2.75 Sv). Tian et al. (2006) used current observations and hydrographic data collected from a campaign in October 2005 and obtained a 6±3 Sv westward LST. Yang et al. (2010) obtained a net eastward flow of 5.5 Sv from field measurements in July 2007. Given the complex bathymetry and current conditions at the Luzon area, it is difficult to obtain exact estimates of LST year-round, and numerical methods allow to complement in-situ observations. Several models have been used to quantify the LST, providing various results, due to differences in model configurations (studied period, grid and resolution, number of vertical layers, parameterisations, forcings, etc). The yearly average value of LST net inflow estimated by numerical studies listed in Table I.3 is 4.00 Sv, and values range from 2.4-2.9 Sv (Xue et al. 2004, Qu et al. 2004, Yaremchuk et al. 2009, Tokuza et al. 2014) to 4.0-5.6 Sv (Metzger and Hurlburt 1996, Fang et al. 2005, 2009, Tokuka et al. 2009, Wang et al. 2009, Liu et al. 2011, Hsin et al. 2012, Xu and Malanotte-Rizzoli 2013, Wei et al. 2016, Wang Yan et al. 2019). Despite the large range in annual estimates, most numerical model simulated a westward LST all year round with a winter maximum and summer minimum

(Metzger and Hurlburt 1996, Chu and Li 2000, Qu et al. 2004, Yu and Qu 2013, Fang et al. 2005, Yaremchuk et al. 2009, Liu et al. 2011, Xu and Malanotte-Rizzoli 2013, Wang Yan et al. 2019). Some studies examined the vertical distribution of LST, revealing a typical “sandwiched” structure, with inflows in the upper and deep layers, and outflow in the intermediate layer (Chen and Huang 1996, Yuan 2002, Qu et al. 2004, Li and Qu 2006, Fang et al. 2009, Hsin et al. 2012, Nan et al. 2013, 2015, Liu and Gan 2017). Analyses of vertical transport at other channels are still scarce.

At the Taiwan strait, all observational and modeling methods found a net northward outflow the whole year, with a summer maximum and a winter minimum (Fang et al. 1991, Chung et al. 2001, Wang et al. 2003, Wu and Hsin 2005, Fang et al. 2005, 2009, Rong et al. 2007, Yaremchuk et al. 2009, Xue et al. 2004, Zhang et al. 2014, Liu et al. 2011, Wang Yan et al. 2019). Fang et al. (1991) estimated a 2 Sv annual outflow at Taiwan strait by analyzing historical current meters data obtained in the 1980s. ADCP and CTD data of Chung et al. (2001) gave values of 2.0 Sv (May 1999) and 2.2 Sv (August 1999). Wang et al. (2003) found an annual mean outflow of 1.8 Sv using shipboard ADCP measurements over 1999-2001. Numerical estimates of yearly outflow range from 0.45 Sv (Fang et al. 2005) to 2.6 Sv (Hsin et al. 2012).

Estimates for the Mindoro strait are less numerous (Wang et al. 2009), but all observations and modeling studies suggested an average outflow to the Sulu Sea. Qu and Song (2009) used remotely-sensed SSH and ocean-bottom-pressure to estimate a 2.4 Sv yearly outflow. Using in-situ data from moored ADCP deployed from 2007 to 2009, Sprintall et al. (2012) obtained a very small value of Mindoro outflow (0.1 Sv), that they explained by the strong 2008 La Niña event. Numerical outflow estimations at this strait also fluctuate, from 0.1 Sv (Tozuka et al. 2014) to 2.6 Sv (Wei et al. 2016). Sprintall et al. (2012) field survey suggested a seasonal cycle with a net inflow from April to October and a net outflow from November to March, consistent with numerical results of Wei et al. (2016). In contrast, most of modelling studies (Fang et al. 2005, 2009, Yaremchuk et al. 2009, Liu et al. 2011, Xu and Malanotte-Rizzoli 2013, Wang Yan et al. 2019) found a net outflow all year round at Mindoro strait, with intense fluxes in autumn-winter and weaker fluxes in

spring-summer. It is noteworthy that the transect chosen in numerical and in-situ studies are not always at the same position and could lead to different results.

In the eastern region, studies on seawater flows through the Balabac strait provided contradictory results. Wang et al. (2009), Liu et al. (2011), Hsin et al. (2012), Tozuka et al. (2014) found a yearly net inflow with yearly average values varying from 0.01 Sv to 0.8 Sv. Fang et al. (2005, 2009) suggested a year-round outflow (with an annual average of 0.61 Sv and 0.41 Sv respectively). Observations by Wyrtki (1961) suggested an inflow in February and June and an outflow in August and September for the surface layer.

In the southern basin, all observational and modeling methods found a net southward outflow on a yearly average at the Karimata strait. Previous numerical studies provide a 1.1 Sv average yearly net outflow through the Karimata strait, and the seasonal cycle of the Karimata volume transport shows an inflow in late spring – summer and an outflow the rest of the year (Fang et al. 2003, Xue et al. 2004, Yaremchuk et al. 2009, Liu et al. 2011, Xu and Malanotte-Rizzoli 2013, He et al. 2015, Wei et al. 2016, Rong et al. 2007, Wang Yan et al. 2019). Fang et al. (2010) and Susanto et al. (2013) used ADCP measurements to provide outflow estimates of respectively 3.6±0.8 Sv (January – February 2008) and 0.5±1.9 Sv (from December 2007 to November 2008). Those measurements were continued until June 2015, and used by Wang Yan et al. (2019) to build a new estimate of 0.74 Sv for the period 2009-2014. Several net outflow estimates from numerical models were also computed at this strait, ranging from 0.18 to 2.30 Sv (Fang et al. 2005, Yaremchuk et al. 2009, Wang et al. 2009, Metzger et al. 2010, Tozuka et al. 2007, 2009, 2014, Liu et al. 2011, Xu and Malanotte-Rizzoli 2013, Daryaboy et al. 2016, Wei et al. 2016, Wang Yan et al. 2019).

At the Malacca strait, Daryaboy et al. (2016) computed from the SODA dataset a 0.13 Sv average net outflow. Numerical studies of Fang et al. (2005, 2009), Metzger et al. (2010), Liu et al. (2011) and Daryaboy et al. (2016) estimated a yearly average net outflow at this channel ranging from 0.08 Sv to 0.27 Sv. Most studies proposed a year–round outflow at this strait, while Daryaboy et al. (2016) found an outflow from November to April and an inflow from May to October. Some numerical studies analysed the seawater fluxes through Sunda Shelf (SS) strait, which is the sum of Karimata and Malacca outflows, obtaining

outflow estimates varying from 0.5 to 1.7 Sv (Qu et al. 2004, Wang et al. 2009, Hsin et al. 2012, He et al. 2015).

	Method / Analysed period	Luzon	Taiwan	Mindoro	Balabac	Karimata	Malacca
Metzger and Hurlburt (1996)	Model, NLOM (Reduced gravity 1.5 layer) 1/2° latitude 45/64° longitude 1982-1983	4.4±2.5 Sv					
Qu et al. (2004)	Model MOM2.0 1/4° 1982 – 1998	2.4 Sv		-0.7 Sv		-1.7 Sv (Sunda Shelf transport = sum of Karimata and Malacca)	
Xue et al. (2004)	Model POM 9-12km 20 yrs climato	2 Sv					
Wu and Hsin (2005)	Model, EAMS 1/8° 1999-2003		-1.09 Sv				
Fang et al. (2005)	Model, GFDL MOM2.0 1/6° 10yrs climato	4.37 Sv 0.411 PW	-0.45 Sv -0.048 PW	-1.77 Sv -0.171 PW	-0.61 Sv -0.067 PW	-1.32 Sv -0.147 PW	-0.22 Sv -0.025 PW
Tozuka et al. (2007)	Model, MOM3.0 0.4° 10yrs climato	3.6 Sv	-1.8 Sv	-0.4 Sv		-1.4 Sv	
Fang et al. (2009)	Model, MOM2.0 1/6° 1982-2003	4.80 Sv 0.373 PW	-1.71 Sv -0.153 PW	-1.35 Sv -0.111 PW	-0.41 Sv -0.039 PW	-1.16 Sv -0.113 PW	-0.16 Sv -0.016 PW

		169.91 Gg/s	-60.16 Gg/s	-47.11 Gg/s	-14.10 Gg/s	-39.27 Gg/s	-5.30 Gg/s
Yaremchuk et al. (2009)	Model,Reduced gravity $4^{1/2}$-layer 0.5° Upper 750 m	2.4±0.6 Sv	-0.6±0.5 Sv	-1.5±0.4 Sv		-0.3±0.5 Sv	
Tozuka et al. (2009)	Model MOM3.0 0.4°- 2° 1980-2006	4.4 Sv 0.35 PW				-1.6 Sv -0.19 PW	
Wang et al. (2009)	Model HYCOM 1/6° (30 yrs climato run)	4.5 Sv	-2.3 Sv	-1.7 Sv	0.01 Sv	-0.5 Sv (Sunda Shelf transport)	
Metzger et al. (2010)	Model HYCOM 1/12° 2003-2006					-0.6 Sv	-0.08 Sv
Liu et al. (2010)	Model MOM4p0d 1/10°-2° 1995-1999		-1.88±0.32 Sv -0.20 ± 0.03 PW				
Liu et al. (2011)	Model, BRAN 0.1° - 2° 1993-2008	4.81 Sv	-1.44 Sv	-2.27 Sv	0.01 Sv	-1.42 Sv	-0.27 Sv
Xu and Malanotte-Rizzoli (2013)	Model MITgcm/ -FVCOM 2°/5-18-50km 1960s/1990s	5.6 Sv		-2.0 Sv		-1.4 Sv	
Hsin et al. (2012)	Model, EAMS 1/8° 2002-2008	4.0±5.1 Sv	-2.6 Sv	-0.9 Sv	0.1 Sv	-0.8 Sv	

Zhang et al. (2014)	Model, 2D barotropic 1/10°-1/30° 2005 – 2008		-0.78±1.29 Sv				
Tozuka et al. (2014)	Coupled model UTCM 0.4°-2° OGCM T42 AGCM 160 yrs climato	2.9 Sv	-1.5 Sv	-0.1 Sv	0.8 Sv	-2.3 Sv	
He et al. (2015)	Model, BRAN 0.1° 1996-2006					-1.6 Sv	
Daryaboy et al. (2016)	Model, ROMS 9-50 km 10 yrs climato Observations SODA dataset					-0.18 Sv -0.018 PW -5.7 Gg/s -0.29 Sv -0.029 PW -11.9 Gg/s	-0.14 Sv -0.014 PW -4.3 Gg/s -0.13 Sv -0.013 PW -4.1 Gg/s
Wei et al. (2016)	Model, POM/ATOP 0.1°x0.1° 2004-2012	4.9 Sv	-1.1 Sv	-2.6 Sv		-0.7 Sv	
Wang Yan et al. (2019)	Model, GL-Ba008 dataset (HYCOM) 7km 2004-2014 Observations ADCP 11/2008-06/2015	4.67 Sv 0.261 PW 164.97 Gg/s	-1.6 Sv -0.148 PW -54.38 Gg/s	-2.13 Sv -0.135 PW -74.41 Gg/s		-0.5 Sv -0.051 PW -16.57 Gg/s -0.74 Sv (mean)	

Wrytki (1961)	Observations Dynamics method (1909-1957) Upper 175m	0.5 Sv					
Qu (2000)	Observations Dynamics method (WOA1994) Upper 400 m	3.0 Sv					
Chu and Li (2000)	Observations GDEM/MOODS dataset 1930-1997	6.5 Sv					
Tian et al. (2006)	Observations LADCP/CTD (Oct 2005)	6.0±3.0 Sv					
Yuan et al. (2008)	Observations NCEP/ hydrographic dataset (Aug-Sep 1994)	3.5 Sv					
Yang et al. (2010)	Observations LADCP/CTD (Jul 2007)	-5.5 Sv					
Fang et al. (1991)	Observations Current meters 1980s		-2 Sv				

Chung et al. (2001)	Observations ADCP/CTD (May, Aug 1999)		-2.0 Sv (May) -2.2 Sv (Aug)				
Wang et al. (2003)	Observations ADCP (1999-2001)		-1.8 Sv				
Fang et al. (2010)	Observations ADCP Jan-Feb 2008					-3.6±0.8 Sv -0.36±0.08 PW -120±30 Gg/s	
Susanto et al. (2013)	Observations ADCP Dec 2007-Nov 2008					-0.5±1.9 Sv -0.05±0.22 PW	
Qu and Song (2009)	Observations SSH & OBP data (2004-2007)			-2.4 Sv			
Sprintall et al. (2012)	Observations Mooring ADCP (2008)			-0.07 Sv			

Table I.3: Synthesis of volume, heat and salt transports (in Sv, PW and Gg/s respectively) through SCS straits obtained from previous numerical and observation studies. Positive = inflow and negative = outflow.

Heat transport

The heat and salt transports of the SCSTF have been much less studied than the water volume fluxes. Fang et al. (2005, 2009) and Wang Yan et al. (2019) however quantified the mean value and seasonal cycle of heat and salt fluxes through all of the interocean straits of the SCS. Heat fluxes over four main straits (Luzon, Taiwan, Karimata, Mindoro) were also calculated by Tozuka et al. (2009). They all suggested that the SCS receives heat from the Western Pacific Ocean through the Luzon strait and releases heat through the Taiwan, Mindoro, Karimata and Malacca straits, with numerically-estimated heat inflows through the Luzon strait varying between 0.261 PW and 0.411 PW. In a seasonal cycle, the SCS receives heat almost throughout the year from the Western Pacific. The heat inflow reaches a peak in boreal winter, weakens in summer, and could even be negative in May – June (Fang et al. 2005, Wang Yan et al. 2019). Heat outflow estimates at the Taiwan strait range from 0.048 PW to 0.2 PW (Fang et al. 2005, 2009, Wang Yan et al. 2019, Liu et al. 2010). The seasonal cycle differs from each study. Fang et al. (2005) suggested heat outflow in spring-summer and heat inflow in autumn-winter, whereas Wang Yan et al. (2019) and Liu et al. (2010) found a year-round heat outflow through Taiwan strait, with a maximum heat loss in summer and a minimum heat loss in winter. At Mindoro strait, the annual average heat outflow estimated by Fang et al. (2005, 2009) and Wang Yan et al. (2019) varies between 0.111 and 0.171 PW, with an annual cycle of heat flux characterized by a year-round outflow, larger in winter and weaker in summer. At the Balabac strait, yearly average heat flow was found eastward (outflow) in the studies of Fang et al. (2005, 2009) but westward in the study of Tozuka et al. (2009). Fang et al. (2005) found a year-round heat outflow through this section. At the Karimata strait, heat flows out of the SCS basin on a yearly average with numerical estimates varying from 0.051 PW (Wang Yan et al. 2019) to 0.19 PW (Tozuka et al. 2009). Fang et al. (2010) and Susanto et al. (2013) deduced from observations a southward heat outflow of 0.36±0.08 PW for January – February 2008 and of 0.05±0.22 PW for a longer period (December 2007 to November 2008). Estimates from SODA dat60sset of Daryaboy et al. (2016) gave an average heat outflow of 0.029 PW. Both observational and numerical studies found a summer heat inflow and a winter heat outflow at this strait. Through Malacca strait, the annual heat flux is an outflow as suggested by numerical studies of Fang et al. (2005,

0.025 PW), Fang et al. (2009, 0.016 PW) and (Daryaboy et al. 2016, 0.014 PW by model, 0.013 PW by SODA dataset). Fang et al. (2009) obtained a heat outflow at this channel all year long, while Dayaboy et al. (2016) found an outflow in winter and an inflow in summer.

Salt transport

Similarly to water and heat transports, the salt transport within the SCS zone includes a salt inflow from the Western Pacific through Luzon strait, and salt outflows through Taiwan, Mindoro, Karimata, Malacca and Balabac straits, estimated respectively at 169.91 Gg/s, 60.16 Gg/s, 47.11 Gg/s, 39.27 Gg/s, 5.30 Gg/s and 14.10 Gg/s over the period 1982 – 2003 (Fang et al. 2009). Wang Yan et al. (2019) focused on the 4 main straits of the SCSTF and evaluated for the period 2004 – 2014 a salt inflow of 164.97 Gg/s at Luzon and salt outflows of respectively 54.38 Gg/s, 74.41 Gg/s and 16.57 Gg/s at Taiwan, Mindoro, Karimata straits. They obtained a salt flux seasonal cycle similar to water flux cycle: inflow (outflow) all year round at Luzon (Taiwan, Mindoro) strait and alternating inflow (outflow) at Karimata strait for boreal summer (winter). ADCP measurements in January – February 2008 at Karimata strait gave a salt outflow of 120±30 Gg/s (Fang et al. 2010). Daryaboy et al. (2016) obtained through model study salt outflows of only 5.7 Gg/s and 4.3 Gg/s through Karimata and Malacca sections, consistently with their estimates from SODA dataset (11.9 Gg/s and 4.1 Gg/s respectively). They observed for both channels a summer salt inflow and a winter salt outflow.

I.4.3. Thermohaline structure

I.4.3.1. Surface characteristics and mixed layer depth

The temperature and salinity patterns of the SCS are strongly influenced by the alternating seasonal monsoons and the exchanges of water masses with the Western Pacific, Indian Ocean and surrounding seas (the SCSTF, sea above).

Seasonal averages of SST, SSS and Mixed Layer Depth (MLD) (Figure I.15) over the SCS zone reveal a strong spatial and seasonal variability. In winter, under the influences of NE monsoon associated with cold and dry atmospheric fluxes (see I.2.1) and the

intrusion of the Kuroshio into the SCS (see section 1.4.1), the northern SCS basin has lower SST and higher SSS compared to the southern basin. The strong dry and cold NE monsoon generates an intense western boundary current flowing southward along the continental slope, transporting cold and salty water to the south of the SCS and generating a cold and salty tongue in the southern basin and a temperature - salinity gradient over the SCS (Figure I.15a, b). Lowest SST zones are the Chinese southern coasts and the Gulf of Tonkin, whereas highest SST is observed in the southeast basin and over the Gulf of Thailand. SSS is maximum in the northern part and minimum in the Gulf of Thailand. In terms of MLD, we also observe a north - south gradient in winter, with higher MLD in the northern SCS (~80 m). SST, SSS and MLD ranges in winter are large, respectively at about 10-12°C, 3 - 4 psu and 50-70 m.

In summer, the SCS SST is relatively uniform, with minor variations over the whole basin (~2 °C, Figure I.15d). The warm and humid SW summer monsoon coming from the Southern Pacific and Indian Ocean associated with warmer atmospheric heat fluxes are the principal factors that increase the SST over the basin. Lowest SST are observed at the northern boundary (Chinese coasts), around Hainan island and the SVU while highest SST zones are located over the Gulf of Tonkin, Gulf of Thailand and southeastern boundary. Similarly, the SSS in summer becomes more homogeneous than in winter, with variations between 1.5 - 2 psu. The deep basin zones have higher SSS than coastal zones, partly due to strong freshwater discharges in summer. We also observe higher salinity along the central Vietnam coast due to upwelling. With a warmer and fresher upper layer, the SCS basin is much more stratified in summer, leading to a shallower MLD barely exceeding 40 m. The thickest MLD zone is no longer the northern basin but the southern basin, with around 40-50 m of depth at the center of eddies.

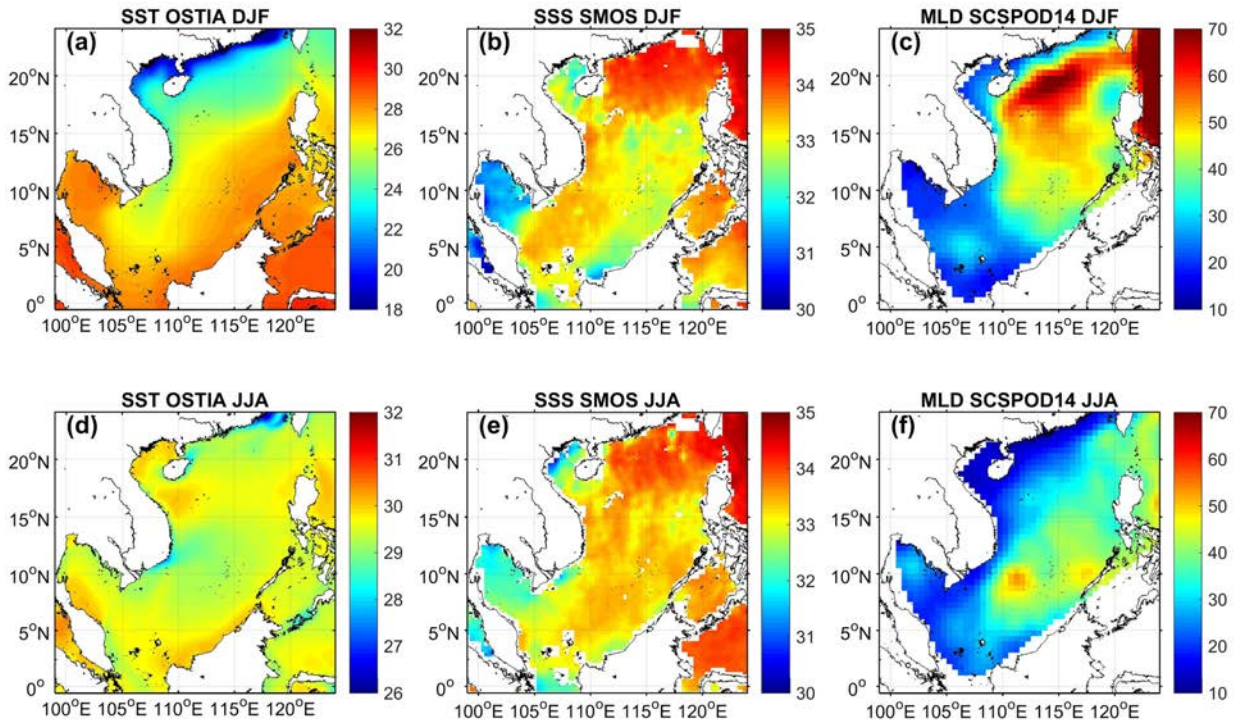

Figure I.15: Maps of winter (December - February DJF) and summer (June - August JJA) averaged SST (°C), SSS (psu) and MLD (m) over the SCS, derived respectively from reanalyzed satellite data OSTIA, SMOS and the SCSPOD14 in-situ gridded dataset built by Zeng et al. (2016a).

At the interannual scale, characteristics of the surface layer water masses thermocline in the SCS are significantly modulated by the sea surface buoyancy and momentum fluxes and exhibit a close relationship with large - scale climate phenomena such as ENSO or PDO. El Niño events weaken monsoon in both winter and summer over the SCS which leads to weakened ocean heat loss to the atmosphere and weakened advection of cold water from the northeast of the SCS, hence higher SST in the SCS. Several studies have also revealed a surface warming trend over the SCS in recent decades (Fang et al. 2006, Park and Choi. 2016, Xiao et al. 2019, Yu et al. 2019), reflecting a regional footprint of global warming. Potential mechanisms driving this warming trend could be attributed to the influences of ENSO (Yu et al. 2019), surface heat fluxes (Wang et al. 2016), and the South China Sea Throughflow (Thompson et al. 2017). Concerning the SSS, Zeng et al. (2014, 2016b, 2018) reported that after a surface freshening trend over 20 years (1993 - 2012) with the lowest SSS recorded in 2012, the SSS of the zone increased from late 2012 to 2017. These authors suggested that these subsurface salinity variations revealed a PDO - like signal, with a freshening during the negative PDO phase, and saltening during

the positive PDO phase. Following Zeng et al. (2014, 2018), the increase (decrease) of rainfall, together with weaker (stronger) intrusions of Kuroshio than normal during negative (positive) PDO phases would be the possible mechanisms inducing modulating the freshening (saltening) over the surface SCS.

I.4.3.2. Vertical structure

The characteristics of SCS water masses are essentially determined by the water exchanges through different straits, the air - sea heat and freshwater exchanges, the hydrodynamic regime and river discharges. The main factor influencing the structure of SCS water masses is the water exchange with the Western Pacific through the Luzon strait. Qu (2000), Liu and Gan (2017) indeed revealed that the origin of SCS water masses can be traced back to the Western Pacific. Figure I.16 shows the comparison between the average temperature and salinity profiles deduced from ARGO floats data in the middle of SCS deep basin (red box, 13°N - 15°N, 113°E - 115°E) and in the Western Pacific (blue box, 20°N - 22°N, 122°E - 124°E). The vertical water structure in the deep basin of the SCS is similar to the one of the Western Pacific, yet with differences due to the SCS local processes (ocean advection, mixing, air - sea fluxes, etc). The Western Pacific water is colder at the surface layer, but warmer in the subsurface layer (100 - 600 m) than the SCS water. In terms of salinity, water from the Western Pacific is saltier in the upper layer (0 - 450 m) but fresher in the intermediate layer (500 - 1200 m), compared to the SCS water. These observations are consistent with results of Zeng et al. (2016), using SCS Physical Oceanographic Dataset (SCSPOD14) and World Ocean Atlas 2013 (WOA13).

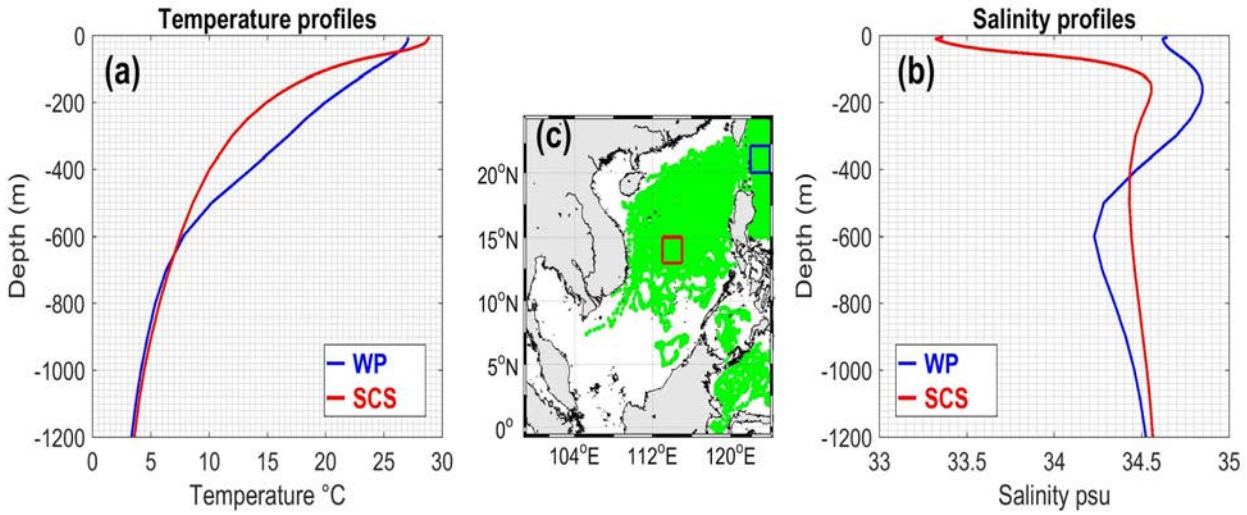

Figure I.16: (a) Temperature and (b) salinity profiles from ARGO floats averaged over the period 2009 - 2018 (c) in the Western Pacific (blue box) and inside the SCS (red box).

Da (2018), through SCSPOD14 analysis, found similar shape for the deep water mean profiles at the western Luzon Strait, Central Vietnam and western Mindoro Strait, meaning that the deep SCS basin water is quite well mixed. Da (2018) moreover showed that coastal and shelf waters exhibit distinctive properties from those in the deep basin due to the impacts of atmospheric forcing, coastal upwelling, river plumes, etc. In particular, the Gulf of Tonkin and Gulf of Thailand, due to their shallowness and freshwater input from big rivers, have fresher waters than other parts of the SCS. For the upper layer, the Tonkin and Thailand Gulfs show respectively the coolest and warmest water.

I.4.4. Tides

Tidal wave characteristics in the SCS are mainly modulated by the tidal wave propagation from the Pacific Ocean and the Indian Ocean. The Pacific Ocean tides spread into the SCS through the Luzon Strait and the Celebes Sea, whereas the Indian Ocean tides influence the SCS through the Andaman and Flores Seas. Following Fang et al. (1999) and Zu et al. (2008), barotropic tides (semidiurnal and diurnal) propagate into the SCS mainly through the Luzon strait but the tidal frequency, wavelengths and amplitude are strongly modified by local SCS geometry and bottom topography (Jan et al. 2007, Zu et al. 2008). After passing through the Luzon strait, a small part of this barotropic tide enters the Gulf of Tonkin, the rest continues to flow toward the southwest. After the tidal wave

reaches the Sunda Shelf edge, a part of it turns into the Gulf of Thailand and another part spreads southwards to the Sunda Shelf end and Java Sea (Phan et al. 2019).

Tidal constituents	***Tidal descriptions***	***Periods (h)***
M2	Semi - diurnal principal lunar	12.42
S2	Semi - diurnal principal solar	12.00
K1	Diurnal luni - solar	23.93
O1	Diurnal principal lunar	25.82

Table I.4: Description and periods of main tidal constituents in the SCS.

Wyrtki (1961) identified four main tidal constituents in the SCS: M2, S2, K1, O1 (see Table I.4). Figure I.17 represents the geographical distribution of tidal types over the SCS (Phan et al. 2019). The SCS is one of the few regions on the earth where diurnal tides dominate semi - diurnal tides. The Gulf of Tonkin, Gulf of Thailand, areas between Sumatra and Borneo and southwest of Luzon strait are regions where pure diurnal tide prevails. Mixed tides prevail in southern China, along the northwest coast of Borneo, the southwest of Thailand and over the continental shelf of the Mekong Delta. Studies of Zu et al. (2008) and Phan et al. (2019) indicated stronger variations of tidal amplitude over the shallow shelves, the Tonkin and Thailand Gulfs compared to homogeneous tidal amplitude in the deep basin.

Tidal currents and breaking tide-induced internal waves play a crucial role in the ocean mixing at all depths and thus participate to drive the ocean circulation and the transformation of water masses (Stewart 2008). With half of the SCS area covered by shallow shelves together with huge river discharges (Mekong, Pearl and Red rivers) flowing into the basin from wide deltas, the tidal forcing is particularly important in the SCS (Li.Z et al. 2006; Wolanski et al. 1998, Mao et al. 2004). In shallow seas, barotropic tidal currents are indeed amplified, tidal mixing is particularly strong and can strongly affect the

coastal sediment transport and mixing in the river mouths (Piton et al. 2020). In the deep basin, the interaction between barotropic tides and rough topography of the SCS generates baroclinic (internal) tides. The internal waves that originate from the Luzon Strait on the eastern margin of the SCS are the oceans' most powerful known internal waves (Alford et al. 2015), and numerical studies showed that tidal mixing generated from the dissipation of internal tides in Luzon strait and SCS plays a key dynamic role in controlling water mass properties and deep circulation features in the SCS (Wang et al. 2017). Therefore, it is essential to take into account the tidal parameters and baroclinic tidal effects in ocean models used for the study of this region.

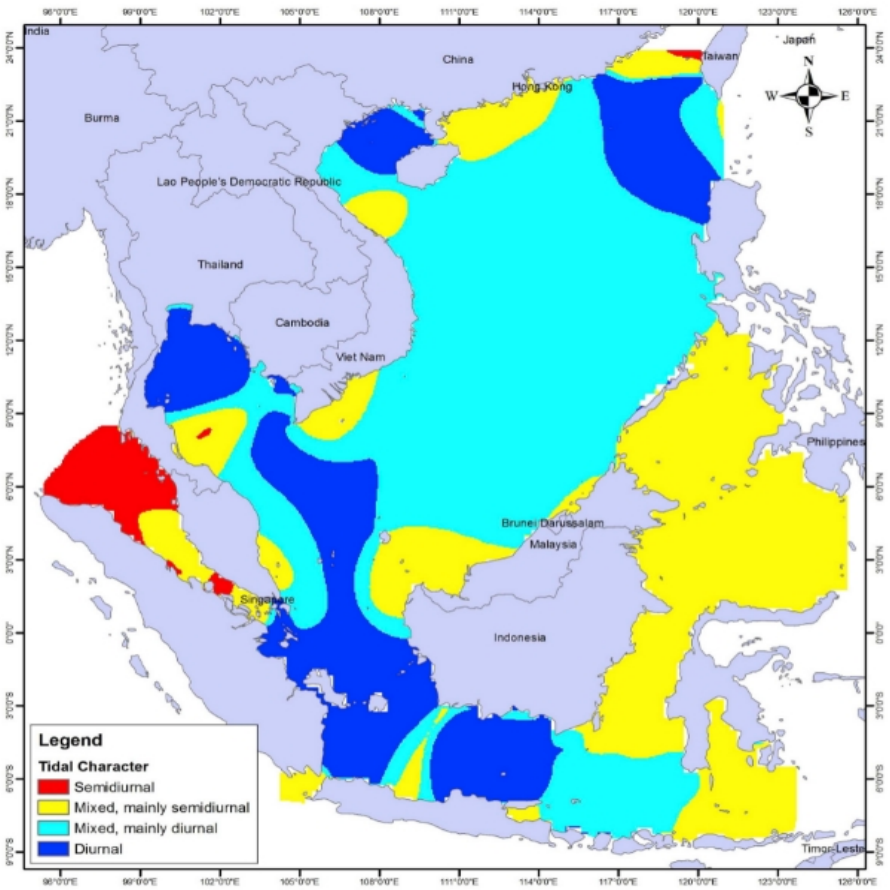

Figure I.17: Geographical distribution of tidal characteristics over the SCS. Image source: Phan et al. 2019.

I.5. Biogeochemistry and pelagic ecosystem of the SCS

The biogeochemical conditions and marine ecosystems in the SCS are subjected to strong climate forcing as well as anthropogenic impacts. As the SCS is bordered by the

world's most densely populated coastal communities, changes in these ecosystems may threaten the livelihood of a large population of humans over the region. Therefore, it is important to study the functioning and variability of planktonic ecosystems - the first level in the ocean food web. Ocean dynamics, by mixing and transporting nutrients and the other compartments of the planktonic ecosystems, are major factors of spatial and temporal variability for those ecosystems. Previous studies revealed that the biogeochemistry and ecosystems in the SCS are sensitive to atmospheric forcing, land-to-ocean fluxes and the Kuroshio intrusion (Liu et al. 2002, Tang et al. 2004, Liu and Chai. 2009, Du et al. 2013, Liu. K et al. 2014, Zhang et al. 2016). Since biogeochemical in-situ measurements are limited over the domain, numerical models and satellite observations are widely used to investigate the seasonal and interannual variability of the SCS planktonic ecosystem. Studies based on satellite remote sensing data of Suhung et al. 2008 and Yu.Y et al. (2019) showed that the Chl-a levels reached their maximum in winter and minimum in summer over most of the SCS, except southeast of Vietnam where the surface Chla becomes maximum in summer and minimum in winter (Figure I.18). The monsoon winds and SST were the most important factors impacting the distribution and variability of surface Chl-a along with other associated and influential environmental drivers, e.g., wind stress curl, frontal activity, and sea level anomalies (Liu et al. 2013, Yu.Y et al. 2019). Liu et al. (2002), using a coupled physical/biogeochemical model together with shipboard data and the CZCS-SeaWiFs satellite data, revealed a strong seasonality of surface chlorophyll in the SCS in monsoon-driven upwelling regions, with maximum concentrations developing northwest of Luzon in winter and off the east coast of Vietnam in summer (Figure I.18). Wang et al. (2010) indicated that the winter phytoplankton bloom off the northwest of Luzon is primarily induced by both Ekman pumping-driven upwelling and upper mixed layer entrainment. Over the southern Vietnamese coasts in summer, the wind stress curl and cyclonic eddies induce the so-called SVU (see I.4.1), which brings nutrients to the surface waters, leading to a phytoplankton bloom in this region (Tang et al. 2004, Da et al. 2019).

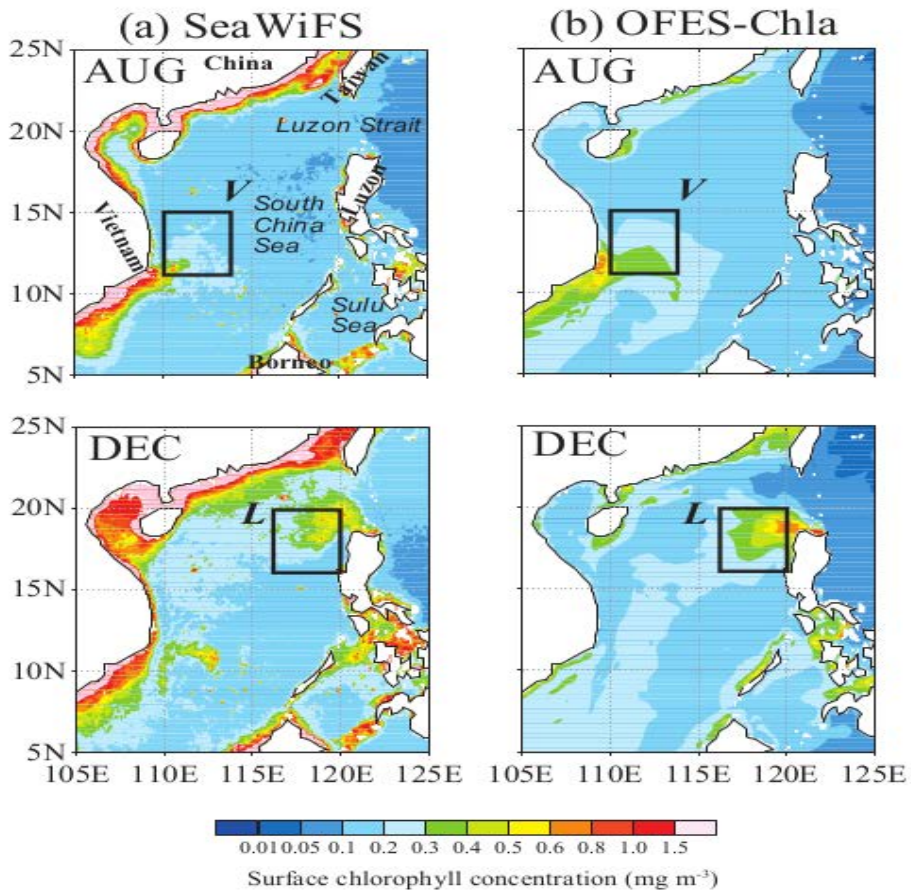

Figure I.18: The surface chlorophyll concentration in August and December averaged over 2000 - 2007 issued from (a) SeaWiFs satellite observations and (b) OFES model. Two black zones V and L indicate respectively the two maximum Chla zones: offshore east Vietnam and northwest Luzon. Image sources: Sasai et al. (2013).

On an interannual time scale, physical processes (monsoon winds, SST, ocean circulation) in the SCS are strongly affected by large-scale climate phenomena (ENSO, PDO, IDO). The changes in physical conditions also influence biology. Following Zhao and Tang (2007) and Jing et al. (2011), the unusually high SST, weak wind stress, and weak Ekman pumping during El Niño years lead to a decrease in nutrients supply, resulting in low chlorophyll concentrations. The case study in summer 2007 of Liu. X et al. (2012) showed that a positive IOD and La Niña event strengthened the southwest monsoon over the SCS, thus increasing the upwelling and the phytoplankton bloom off the South Vietnam coast.

Several studies focused on the impact of mesoscale eddies on the phytoplankton

distribution (Ning et al. 2008, Chen et al. 2007, Gou et al. 2015). These studies revealed that the cyclonic eddies were associated with abundance of nutrients, chlorophyll, phytoplankton and zooplankton while the anticyclonic eddies depressed the biogeochemical cycles with low chlorophyll and primary productions.

Observations on vertical distributions of Chla and nutrients in the water column of the SCS are still limited. However, some previous in-situ measurements issued from the SouthEast Asian Time-series Study (SEATS) program (Liu et al. 2002, Wong et al. 2007, Liu and Chai 2009) and ARGO Bio floats (Zhang et al. 2016) could widen our understanding on this topic. In the vertical structure of Chl-a, high Chl-a concentrations appear in the subsurface layer, so-called subsurface Chl-a maximum (SCM, Cullen 2015). In the SCS, the SCM is observed at different depths, depending on the season. Liu et al. (2002) observed a deeper SCM at 75 m in September 1998 and a shallower at 40–50 m at the same site (18.0°N, 118.5°E) in January 1999 in the northern SCS. Observations at SEATS point presented in Liu and Chai (2009) showed that in winter, the depth of SCM is slightly lower (50 - 60 m) than in summer (70 - 80 m), but the intensity of SCM is higher in winter (0.7 mg/m^3) than in summer (0.4 mg/m^3, Figure I.19a, d). One-dimensional physical-biogeochemical coupled model studies of Gong et al (2014) showed that wind speed can change the intensity of the SCM in winter and summer, but has a minor effect on its depth.

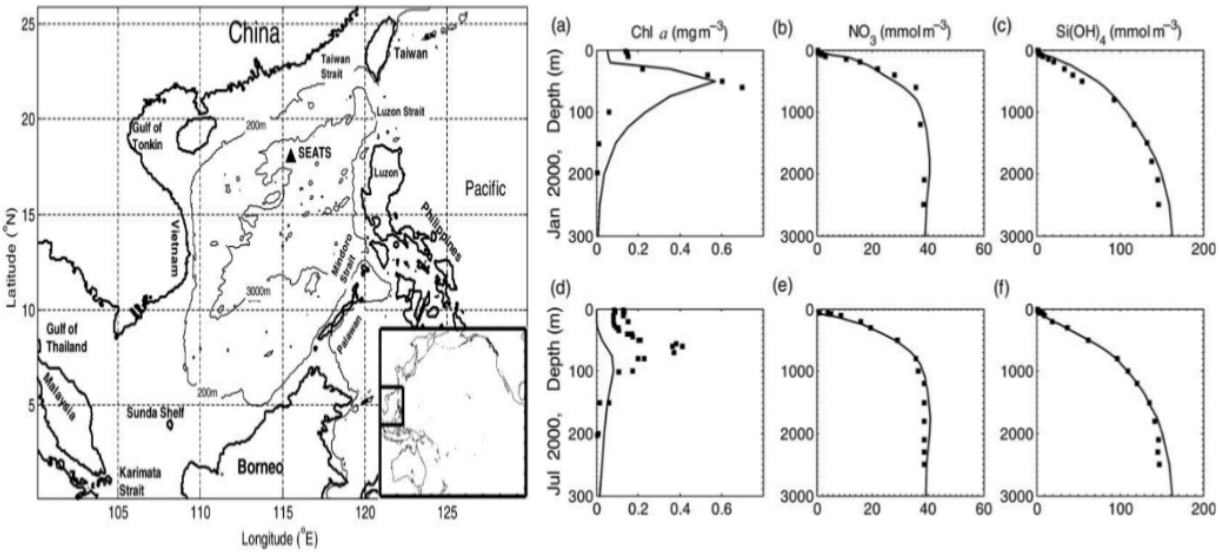

Figure I.19: Position of SEATS monitoring (left, triangular point) and in-situ profiles (right, black dots) at SEATS in January 2000 and July 2000 of Chla (a,d), nitrate (b,d) and silicate (c,d). Images source: Liu and Chai (2009).

Observations at SEATS point in January and July 2000 of Liu and Chai (2009) revealed a weak seasonal variation in the vertical structure of nutrients (Figure I.19b, c, e, f). Profiles of nitrate in the upper 200 m from ARGO bio floats over the period September 2014 - August 2015 of Zhang et al. (2016) showed a stronger surface nitrate concentration in winter than in other seasons. Strong northeast monsoon winds and the surface cooling in winter deepen the mixed layer (ML) and weaken the stratification, enhancing the vertical convection and bringing more nutrients to the surface layer (Wang et al. 2010, Duan et al. 2012). By contrast, summer surface warming strengthens the stratification, potentially preventing upward transport of nutrients (Duan et al. 2012). According to Gan et al. (2006) and Chou et al. (2007), the nutrient concentration over the continental shelf is much higher than in the open sea and generally peaks during summer due to river runoff and coastal upwelling.

Following Liu. K et al. 2014, the deep-inflow of the Kuroshio intrusion into the SCS through the Luzon strait controls the basin wide upwelling and nutrient supply, thus the phytoplankton growth. In winter, the SCS also receives additional nutrient supply from the East China Sea through the Taiwan strait when the China Coast Current flows southward. In other words, the SCSTF plays an important role in the nutrient dynamics of the region.

I.6. Scientific questions and objectives of the thesis

The general objective of this PhD thesis is to contribute to improve the knowledge of ocean dynamics over the SCS and of their variability from the seasonal to interannual time scales, of their impact on the SCS physical functioning at the regional scale and on its contribution to the regional climate system, and of their impact on the planktonic pelagic ecosystems.

Given the importance of the SCSTF in the global and regional ocean circulation and climate, it is essential to precisely estimate and monitor this interocean transport in terms of water, heat and salt exchanges. This is made complicated by the complex topography in the region. Moreover, lateral transports involved in the regional cycle of water, heat and salt interact with the other atmospheric and continental components of this regional cycle. An accurate and exhaustive understanding of the SCSTF and of its role in the regional ocean circulations and climate thus requires to understand and quantify the lateral interocean fluxes, as well as the contributions of atmospheric and continental fluxes in the SCS water, heat and salt budgets, and the interactions between those fluxes. Even though our understanding of water, heat and salt transports through the SCS area increased considerably in recent years, we still lack information to have a global picture of the water, heat and salt budgets for the whole area, especially to clarify the contributions of atmosphere and river fluxes. In particular the numerical studies cited above made the assumption that the SCS is at equilibrium over the studied periods, i.e. that all the water, heat and salt that enters the basin leaves it, and used this assumption to estimate atmosphere and rivers contributions. Though this assumption allows to close the budget at the first order, it is not realistic since it does not account for possible internal variations and trends in the water, heat and salt contents of the SCS. Yet Zeng et al. (2014, 2018), using in situ measurements and satellite data, for example evidenced a freshening of the SCS from 2010 to 2012 followed by a saltening, suggesting an interannual variability in salt and/or water mass content. Moreover, very few studies examined jointly the water, heat and salt budgets, which is however necessary to provide consistent estimates of all the terms involved in those budgets and of their variability. Last, their resolution did not allow to fully represent the (sub)mesoscale structures involved in the SCS circulation.

Our main and first detailed scientific objective is therefore to improve our understanding of the circulation and transformation of water masses in the SCS at the climatological, interannual and seasonal time scales and of the role of the SCSTF, by examining in details the variability of the SCS water, heat and salt budgets, quantifying in particular the contributions of lateral advection, surface atmospheric and rivers forcings and internal mixing. This scientific question is associated with a methodological requirement, which is to develop a high-resolution model able to represent processes at all scales, including external forcing, tides, mesoscale and small scale dynamics, involved in the functioning and variability of the SCS circulation and SCSTF, and where all budgets are rigorously closed at all time scales. These scientific and methodological questions constitute the main part of the work done during this PhD thesis and presented in the main body of this document.

Our second objective is to examine, understand and quantify the impacts of ocean dynamics and of their variability at different scales on the SCS planktonic pelagic ecosystems: how does the composition of the SCS planktonic ecosystem vary spatially and temporally, what is its role in terms of carbon and nitrogen cycles, at the regional but also local scales? To answer these questions, our goal is to develop a high resolution coupled physical - biogeochemical configuration over the studied zone. These scientific and methodological questions were addressed during the final part of this PhD thesis, and will need further development and analysis. This part of this PhD work is therefore presented at the end of this document.

The structure of this manuscript is as follows:

Chapter II describes the hydrodynamical model SYMPHONIE used for this study, the SCS high resolution configuration as well as the datasets used for atmospheric, rivers and open boundaries forcing conditions. Observational data (in-situ measurements and satellite dataset) used for model validation are presented. Computational methods used for fluxes and budgets analysis and for statistical diagnostics are also detailed.

Chapter III presents the evaluation of the performances of the physical model SYMPHONIE over the studied area and period, based on the comparison of the model outputs with satellite and in-situ observations. Surface water masses and ocean

circulation characteristics and vertical structures of water masses are examined, at the seasonal and interannual time scales.

Chapter IV provides updated and consistent estimates and analysis of all the terms involved in the SCS volume, heat and salt budgets: lateral, atmospheric and river fluxes, and internal variations, focusing on the climatological average and seasonal cycle.

Chapter V presents estimates of volume, heat and salt budgets over the SCS on an interannual timescale and identifies which factors drive the interannual variability of these budgets. The mechanisms controlling the SCS saltening observed over the recent periods are examined. The impacts of large-scale climate phenomenon (ENSO, PDO) on these budgets are discussed.

Chapter VI summarizes the main results and findings obtained during this study and discusses the preliminary results obtained from the coupling biogeochemical simulations. Remaining questions to be explored in future research are also discussed.

Chapter II: Material & Methods

In this chapter we firstly describe the hydrodynamic ocean model SYMPHONIE, the configuration and forcing elements used in this study. We then detail the satellite observations and in-situ data employed for model validation as well as the climate indexes used for the analysis of simulation results. Finally, we present the biogeochemical model Eco3m-S and parameters used for the preliminary physical/ biogeochemical coupled simulation.

II.1. The hydrodynamic ocean model SYMPHONIE

SYMPHONIE is a 3-D hydrostatic ocean circulation model developed by the Sirocco group (LEGOS, CNES, CNRS, IRD, Université de Toulouse, France) (Marsaleix et al. 2008, 2009, 2012). The SYMPHONIE model has been used and validated in various studies whose subjects covered a wide range of regions and processes: the formation and variability of shelf and open sea dense waters (Herrmann and Somot 2008, Herrmann et al. 2008, Ulses et al. 2008a, b, Waldman et al. 2016; Estournel et al. 2016), internal waves and wave-current interactions (Auclair et al. 2011, Michaud et al. 2011, Marsaleix et al, 2019), radioactive elements propagation over the Japanese coastal zone (Estournel et al. 2012, Masumoto et al. 2012).

The simulations presented in this study are performed using the SYMPHONIE model on a new study zone: the SCS. The later marginal sea exhibits similar characteristics with the Mediterranean Sea: (i) both seas are surrounded by land with high density of population, (ii) they all possess the average depth of 1200 – 1500 m with shallow coastal shelves and deep areas of more than 4000 m, (iii) they are semi-enclosed seas connected to different Oceans (the Atlantic Ocean for the Mediterranean Sea, the Pacific and Indian Oceans for the SCS) through narrow straits. Given the high performance of the SYMPHONIE model on various Mediterranean hydrodynamical studies, it is therefore relevant to choose this model to carry out the study on the “Asian Mediterranean Sea” - the SCS.

II.1.1. The governing equation

SYMPHONIE is a free surface model using the energy conserving finite difference as numerical model, as detailed in Marsaleix et al. (2008). We use a version of the model which is built based on the Navier–Stokes primitive equations under the hydrostatic equilibrium hypothesis, incompressibility hypothesis and Boussinesq approximations. The equations are based on six state variables: three velocity components (*u, v, w*), the temperature *T*, the salinity *S* and the sea surface elevation *η*.

Given the Cartesian coordinate system, the origin O corresponds to the rest level of the sea surface; Ox and Oy are the horizontal axes and Oz is the vertical ascending axis, the velocity components *u*, *v* and *w* (following respectively Ox, Oy and Oz axes) are determined via the continuity and momentum equations:

$$\frac{\delta u}{\delta x} + \frac{\delta v}{\delta y} + \frac{\delta w}{\delta z} = 0 \qquad \text{(Eq. II.1.1)}$$

$$\frac{\delta u}{\delta t} + \frac{\delta uu}{\delta x} + \frac{\delta uv}{\delta y} + \frac{\delta uw}{\delta z} - fv = \frac{-1}{\rho_0}\frac{\delta p}{\delta y} + \nu\Delta^2 v + \frac{\delta}{\delta z}\left(K_m \frac{\delta v}{\delta z}\right) \qquad \text{(Eq. II.1.2)}$$

$$\frac{\delta v}{\delta t} + \frac{\delta uv}{\delta x} + \frac{\delta vv}{\delta y} + \frac{\delta wv}{\delta z} + fu = \frac{-1}{\rho_0}\frac{\delta p}{\delta y} + \nu\Delta^2 v + \frac{\delta}{\delta z}\left(K_m \frac{\delta v}{\delta z}\right) \qquad \text{(Eq. II.1.3)}$$

where *f* is the Coriolis parameter, ρ_0 the reference water density, *p* the pressure, *v* the kinematic viscosity, Δ^2 the horizontal squared Laplacian operator, K_m the vertical coefficient of eddy diffusivity is determined by the turbulence closure scheme (detailed below).

The vertical pressure gradient is computed using the hydrostatic hypothesis:

$$p(z) = \int_z^\eta g\rho\partial z \qquad \text{(Eq. II.1.4)}$$

where g is the acceleration due to gravity, ρ the density, and η the free surface elevation anomaly derived from the depth-averaged component of the current:

$\left(\underline{u,v}\right) = \frac{1}{H}\int_{-h}^{\eta}(u,v)\partial z$ by:

$$\frac{\delta \eta}{\delta t} + \frac{\delta}{\delta x}\left(H\underline{u}\right) + \frac{\delta}{\delta y}\left(H\underline{v}\right) = 0 \qquad \text{(Eq. II.1.5)}$$

in which H = h + η is the sum of the water column thickness at rest (bathymetry) h and the free surface elevation anomaly η.

Temperature T and salinity S variations are calculated from the conservation equations:

$$\frac{\delta T}{\delta t} + \frac{\delta uT}{\delta x} + \frac{\delta vT}{\delta y} + \frac{\delta wT}{\delta z} = \frac{\delta}{\delta z}\left(K_h \frac{\delta T}{\delta z}\right) + \frac{1}{\rho_0 C_p}\frac{\delta I_s}{\delta z} + \frac{\delta F_x^T}{\delta x} + \frac{\delta F_y^T}{\delta y} \quad \text{(Eq. II.1.6)}$$

$$\frac{\delta S}{\delta t} + \frac{\delta uS}{\delta x} + \frac{\delta vS}{\delta y} + \frac{\delta wS}{\delta z} = \frac{\delta}{\delta z}\left(K_h \frac{\delta S}{\delta z}\right) + \frac{\delta F_x^S}{\delta x} + \frac{\delta F_y^S}{\delta y} \quad \text{(Eq. II.1.7)}$$

where I_s is the radiative solar forcing, C_p the water heat capacity and $F_{x,y}^{T,S}$ the diffusion fluxes for temperature and salinity. The density is deduced from the non-linear state equation (Jackett et al. 2006) using *T*, *S*, and *p* variables. The vertical eddy diffusivity coefficient K_h for temperature and salinity tracers is computed by the turbulence closure scheme detailed here after.

II.1.2. Turbulence closure scheme

The K-epsilon turbulence closure scheme with the implementation described in Michaud et al. (2012) is used to determine the vertical eddy diffusivity coefficients (K_h and K_m). Following Gaspar et al. (1990), K_h and K_m are expressed by:

$$K_h = \sqrt{2E_k} l_k S_h \quad \text{(Eq. II.1.8)}$$

$$K_m = \sqrt{2E_k} l_k S_m \quad \text{(Eq. II.1.9)}$$

where E_k is the turbulent energy, l_k the mixing length depending on the eddy's dimension, S_h and S_m are respectively the stability factors.

The kinetic energy equation is deduced from the momentum equation:

$$\frac{\delta E_k}{\delta t} + \frac{\delta uE_k}{\delta x} + \frac{\delta vE_k}{\delta y} + \frac{\delta wE_k}{\delta z} = K_m\left[\left(\frac{\delta u}{\delta z}\right)^2 + \left(\frac{\delta v}{\delta z}\right)^2\right] + \frac{\delta}{\delta z}\left(K_m \frac{\delta E_k}{\delta z}\right) + \frac{g}{\rho_0} K_m \frac{\delta \rho}{\delta z} - \epsilon$$

(Eq. II.1.10)

where ε is the dissipation rate of the turbulent energy kinetic E_k, expressed as:

$$\epsilon = \frac{c_0^3 E_k^{\frac{3}{2}}}{l_k} \quad \text{(Eq. II.1.11)}$$

with c_0 an empirical constant

The mixing length l_k corresponds to the equilibrium between kinetic energy and the Brunt-Väisälä frequency N:

$$l_k = \frac{\sqrt{2E_k}}{N} \quad \text{(Eq. II.1.12)}$$

The stability factors S_h, S_m depend on E_k and ε, following Burchard and Bolding (2001):

$$\frac{dEk}{dt} = \frac{\delta}{\delta z}\left(K_m \frac{\delta Ek}{\delta z}\right) + P + B \quad \text{(Eq. II.1.13)}$$

$$\frac{d\epsilon}{dt} = \frac{\delta}{\delta z}\left(\frac{K_m}{\sigma_k}\frac{\delta E_k}{\delta z}\right) + \frac{\epsilon}{E_k}(c_1 P + c_3 P - c_2 \epsilon) \quad \text{(Eq. II.1.14)}$$

where c_1, c_2, c_3 stand for calibration constants described in Canuto et al. (2001), σ_k is the Schmidt number for dissipation, P the production of turbulent kinetic energy and B the buoyancy flux. The parameter P and B is expressed as:

$$P = K_m \left[\left(\frac{\delta u}{\delta z}\right)^2 + \left(\frac{\delta v}{\delta z}\right)^2\right] \quad \text{(Eq. II.1.15)}$$

$$B = \frac{g}{\rho} K_h \frac{\delta \rho}{\delta z} \quad \text{(Eq. II.1.16)}$$

II.1.3. Boundary conditions

II.1.3.1. Free surface boundary

At the free surface (the atmosphere – ocean interface), the boundary conditions of the kinetic energy and the horizontal component of current are determined in function of the wind stress τ_s (τ_{sx}, τ_{sy}). The vertical flux of turbulent kinetic energy $F_z = K_m \frac{\delta E_k}{\delta z}$ at the sea surface can be expressed, following Craig and Banner (1994), as:

$$F_z = 100\left(\frac{\tau_s}{\rho}\right)^{\frac{3}{2}} \quad \text{(Eq. II.1.17)}$$

with τ_s the wind stress computed by the bulk formula.

The surface current condition affected by the wind stress τ_s is determined as follow:

$$\rho_0 K_m \left(\frac{\delta u}{\delta z}, \frac{\delta v}{\delta z}\right) = \left(\tau_{sx}, \tau_{sy}\right) \quad \text{(Eq. II.1.18)}$$

The heat flux at the sea surface is expressed in function of the atmospheric heat flux exchanged through the air-sea interface, including the sensible heat flux Q_{SEN}, the latent heat flux Q_{LATENT}, the short waves radiative flux Q_{SR} and the long waves radiative flux Q_{LR}:

$$K_h \frac{\delta T}{\delta z} = Q_{SEN} + Q_{LATENT} + Q_{SR} + Q_{LR} \quad \text{(Eq. II.1.19)}$$

The surface salinity depends on the net freshwater budget at the sea surface, estimated from the surface boundary conditions applied to the vertical velocity W_{surf}:

$$W_{surf} = -\left(\frac{Q_{LATENT}}{\rho L_v} + Pr\right) \quad \text{(Eq. II.1.20)}$$

where L_v is the latent heat of condensation of water (L_v=2.5*10^6 J/kg) and P_r the precipitation rate. Q_{SEN}, Q_{LATENT}, and the wind stress τ_s are calculated from the turbulent fluxes at the surface using bulk formulas described in Large and Yeager (2004), while the short and long waves radiative flux (Q_{SR} and Q_{LR}) and the precipitation rate are deduced from atmospheric model dataset (see II.2 below).

II.1.3.2. Bottom

The heat and salt turbulent fluxes at the sea bottom are equal to 0.

$$K_m \left(\frac{\delta T}{\delta z}, \frac{\delta S}{\delta z}\right)_{z=-h} = 0 \quad \text{(Eq. II.1.21)}$$

The boundary condition approximation for turbulent energy kinetic at the sea bottom corresponds to the equilibrium between energy production and dissipation. The latter is generated by the friction of currents on the sea bed, related to the bottom stress τ_b:

$$E_{k_{z=-h}} = \frac{\|\tau_b\|}{\rho_0 \sqrt{2^{0.5} c_0^3 S_m}} \quad \text{(Eq. II.1.22)}$$

where τ_b is determined by a quadratic relation of the bottom velocity $\overrightarrow{V_b}$, calculated at the first layer of the model grid of height z_1

$$\overrightarrow{\tau_b} = \rho_0 C_D \|\overrightarrow{V_b}\| \overrightarrow{V_b} = \rho_0 u_*^2 \quad \text{(Eq. II.1.23)}$$

In which $\overrightarrow{V_b}$ the bottom velocity, u_* the friction velocity and C_D the non-dimensional bottom drag coefficient. C_D is related to the bottom roughness z_0 through a relation based on a logarithmic form of the bottom current:

$$C_D = \left(\frac{\kappa}{log\left(\frac{z_1}{z_0}\right)} \right)^2 \quad \text{(Eq. II.1.24)}$$

with κ = 0.41 is the Von Karman's constant.

II.1.3.2. Lateral boundaries

At closed lateral boundaries such as continents or islands, the normal velocity components are equal to 0. At the open sea borders, the boundary conditions play two roles: the radiation of outgoing waves and the forcing elements at every time step issued from a larger scale model. Following Marsaleix et al. (2006), the open boundary conditions scheme applied in the SYMPHONIE model is the difference between the modeled variables and the forcing variables. Given the open ocean boundaries at x=0 and x=m, we distinguish the barotropic and baroclinic currents.

For the barotropic current $(\bar{u}, \bar{v})$, the Flather type condition is applied to the surface elevation η:

$$\eta - \eta_f = -\sqrt{\frac{H}{g}} \left(\bar{u} - \bar{u_f} \right) \text{ at x =0} \quad \text{(Eq. II.1.25a)}$$

$$\eta - \eta_f = \sqrt{\frac{H}{g}} \left(\bar{u} - \bar{u_f} \right) \text{ at x = m} \quad \text{(Eq. II.1.25b)}$$

where the f index indicates the forcing (large scale circulation and tidal circulation).

The tangential transport at the boundaries is computed using the Neumann condition:

$$\frac{\delta H(\bar{v}-\bar{v_f})}{\delta x} = 0 \text{ at x = 0 and x = m} \qquad \text{(Eq. II.1.26)}$$

For the baroclinic currents (u, v), the radiative condition of Sommerfeld type is applied on the difference between the SYMPHONIE variables (Φ) and the forcing variables (Φ_f):

$$\frac{\delta(\phi-\phi_f)}{\delta t} + C_c \frac{\delta(\phi-\phi_t)}{\delta x} = 0 \text{ at x = 0} \qquad \text{(Eq. II.1.27a)}$$

$$\frac{\delta(\phi-\phi_f)}{\delta t} - C_c \frac{\delta(\phi-\phi_t)}{\delta x} = 0 \text{ at x = m} \qquad \text{(Eq. II.1.27b)}$$

where C_c is the phase velocity of baroclinic waves.

Regarding the scalar variables (T, S), the open boundary conditions of the advection scheme are applied using a hybrid scheme composed of an upstream scheme and a centered scheme. In case of incoming flow, the temperature and salinity (T_f, S_f) are deduced from the forcing of a larger scale model. In case of outgoing flow, these variables are issued from the simulated domain.

In combination with equations 25, 26, 27, correction terms (recall terms) are applied and at the open boundary x=0, this term is written as:

$$e^{\frac{-x}{d}} \frac{\phi-\phi_f}{\tau_r} \qquad \text{(Eq. II.1.28)}$$

where Φ stands for velocity, T or S depending on the equation considered; d corresponds to a distance of exponential decrease depending on the domain size; τ_r corresponds to the recall time addressed by the user.

II.1.3.3. Tide

Variables u, v and η also include the tidal circulation. For coastal boundary, tidal forcing consists mainly of tidal surface elevations and currents, written as follow:

$$\eta(\lambda,\varphi,t) = \sum_k f_k \eta_{0,k}(\lambda,\varphi) cos\left(\omega_k(t-t_0) + V_{0,k} + u_k - G_{\eta,k}(\lambda,\varphi)\right) \qquad \text{(Eq. II.1.29a)}$$

$$u(\lambda,\varphi,t) = \sum_k f_k u_{0,k}(\lambda,\varphi) cos\left(\omega_k(t-t_0) + V_{0,k} + u_k - G_{u,k}(\lambda,\varphi)\right) \qquad \text{(Eq. II.1.29b)}$$

$$v(\lambda,\varphi,t) = \sum_k f_k v_{0,k}(\lambda,\varphi) cos\left(\omega_k(t-t_0) + V_{0,k} + u_k - G_{v,k}(\lambda,\varphi)\right) \qquad \text{(Eq. II.1.29c)}$$

where η_0, u_0, v_0 and G_η, G_u, G_v are the amplitudes and phase lags for sea surface elevations and currents depending on the longitude λ and the latitude φ; the subscript k represents the tidal components considered in the configuration. The nodal factors f_k and u_k are considered as constants (Doodson, 1927), ω is the tidal frequency and V_0 a constant related to the reference time t_0.

The tidal forcing also consists of astronomical and loading potential (respectively Π_A and Π_L), providing a barotropic force added to the momentum equation, through the horizontal components of their gradients. The tidal potential due to astronomical effects Π_A (Hendershott, 1972) is taken into account as follow:

$$\Pi_A = (1 + k_2 + h_2) fa * \left(v_0 \frac{1-3sin^2(\varphi)}{2} + v_1 sin(2\varphi) + v_2 cos^2(\varphi)\right) * cos\big(\omega(t-t_0)\big) + v\lambda + + V_0 + u$$

(Eq. II.1.30)

where k_2, h_2 are the Love numbers, *a* the equilibrium amplitude of the tidal constituents considered, the term (v_0, v_1, v_2) and v vary with the type of tide. In case of long period tide $v_0 = 1$ and $v = 0$, of diurnal tide $v_1 = 1$ and $v = 1$, of semi diurnal tide $v_2 = 1$ and $v = 2$.

The loading potential Π_L (LSA potential) is expressed as:

$$\Pi_L = f\Pi_0(\lambda,\varphi) cos(\omega(t-t_0) + G_\Pi(\lambda,\varphi) + V_0 + u) \qquad \text{(Eq. II.1.31)}$$

The horizontal momentum equation for the hydrostatic pressure force is determined as:

$$-\frac{\nabla p}{\rho_0} = -\frac{g}{\rho_0}\nabla \int_z^\eta (\rho - \rho_0) dz' - g\nabla(\eta - \Pi_A - \Pi_L) \qquad \text{(Eq. II.1.32)}$$

II.1.3.4. Rivers

At the river mouths, the salinity value is considered equal to 0 and the temperature varies in a cosinusoidal function with a one-year period between at minimum and a maximum value. The barotropic velocity U is calculated based on the river runoff flux F following the relationship:

$$U = \frac{F}{l} \qquad \text{(Eq. II.1.33)}$$

where l is the horizontal grid spacing. More details on the river mouth open boundaries in SYMPHONIE is described in Reffray et al. (2004).

II.1.4. Discretization of equations

II.1.4.1. Spatial discretization

The SYMPHONIE model equations are solved using the finite difference method on the Arakawa staggered C-grid (Arakawa and Suarez 1983) scheme, as illustrated in Figure II.1. Horizontal velocity components u, v are defined in the middle of the edges of the grid volume at each half level, whereas the tracers (temperature, salinity, surface elevation) are defined at the center of the grid cell. The vertical velocity and kinetic energy are calculated at the center of the grid edges at each vertical level.

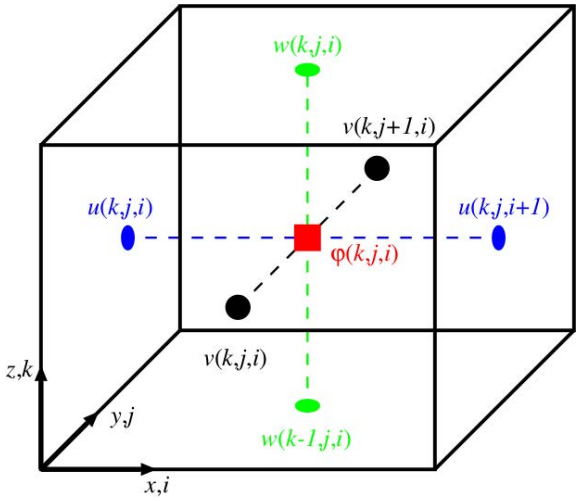

Figure II.1: The Arakawa staggered C-grid (Piton, 2019). The i, j, k indices respectively correspond to x, y, z direction; φ the scalar quantities (tracers). Turbulent fields are defined at green points (the same position as vertical components of velocity).

Regarding the vertical grid, SYMPHONIE employs a system of vanishing quasi-sigma (VQS) vertical coordinate concept described in Dukhovskoy et al. 2009. An example of the vertical grid of SYMPHONIE is presented in Figure II.2. This original choice of this "hybrid" grid allows to take advantage of the generalized sigma coordinate grid: providing a good representation of the bathymetry and avoiding hydrostatic inconsistencies in calculation of pressure gradient for strong slopes. The VQS coordinate also helps to limit the number of vertical levels at very shallow zones, while maintaining an accurate description in deep regions and to reduce the truncation errors associated with the sigma coordinate (Siddorn et al, 2013).

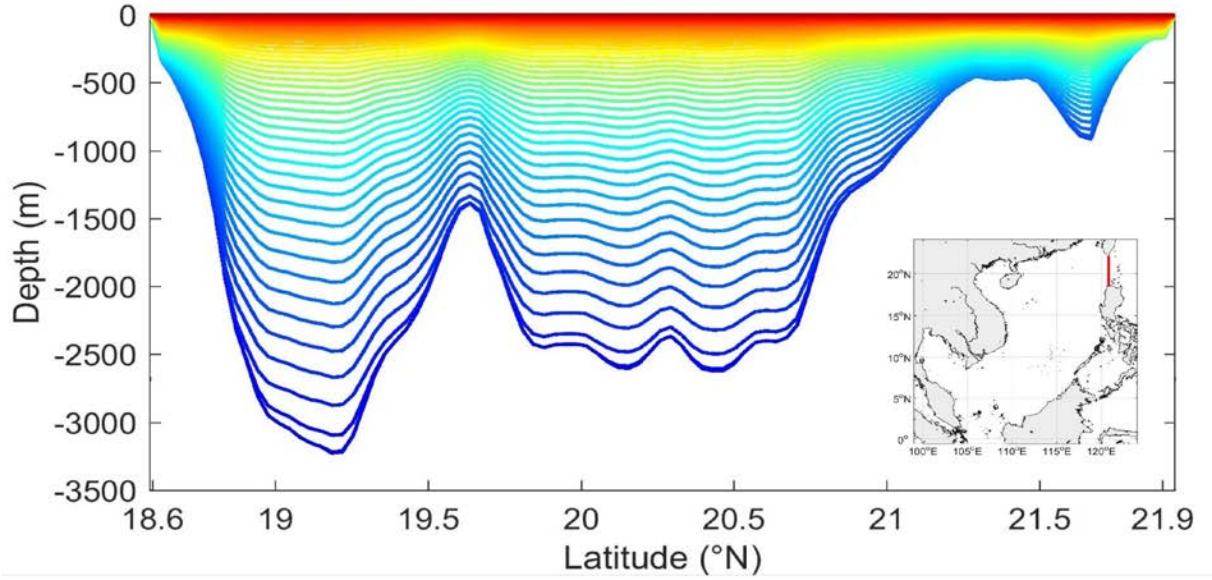

Figure II.2: The VQS vertical coordinate at the Luzon Strait (red line in the map).

The vertical advection is computed using a centered scheme. The QUICKEST scheme (Leonard, 1979) is used for horizontal advection and diffusion of temperature and salinity. Horizontal advection and diffusion of momentum are each computed with a fourth order centered biharmonic scheme. The biharmonic viscosity of momentum is calculated according to a Smagorinsky-like formulation derived from Griffies and Hallberg (2000).

II.1.4.2. Temporal discretization

The forward-backward (FB) time stepping scheme is used for the temporal discretization of the equations. In this explicit time stepping methods, the variable value at time t+1 is deduced by the variable value at time t:

$$F' = F^t + \Delta t f(F^t) \quad \text{(Eq. II.1.34a)}$$

$$F^{t+1} = F^t + \Delta t f(F') \quad \text{(Eq. II.1.34b)}$$

More details of the FB time stepping application and chronology of variables in SYMPHONIE are further described in Marsaleix et al. (2019).

II.2. The South China Sea configuration

Simulations in this study are performed using the SYMPHONIE model on a regular grid mesh covering the whole SCS area, expanding from 99°E to 124°E and from -0.6°N to 24°N (Figure II.3). The horizontal resolution of the grid is 4 km, including 690 x 700 (in x and y axes respectively) horizontal points. There are 50 vertical layers with a bathymetry ranging from 3 m to more than 5000 m (Figure II.3). Simulations run from 1st January 2009 to 31st December 2018.

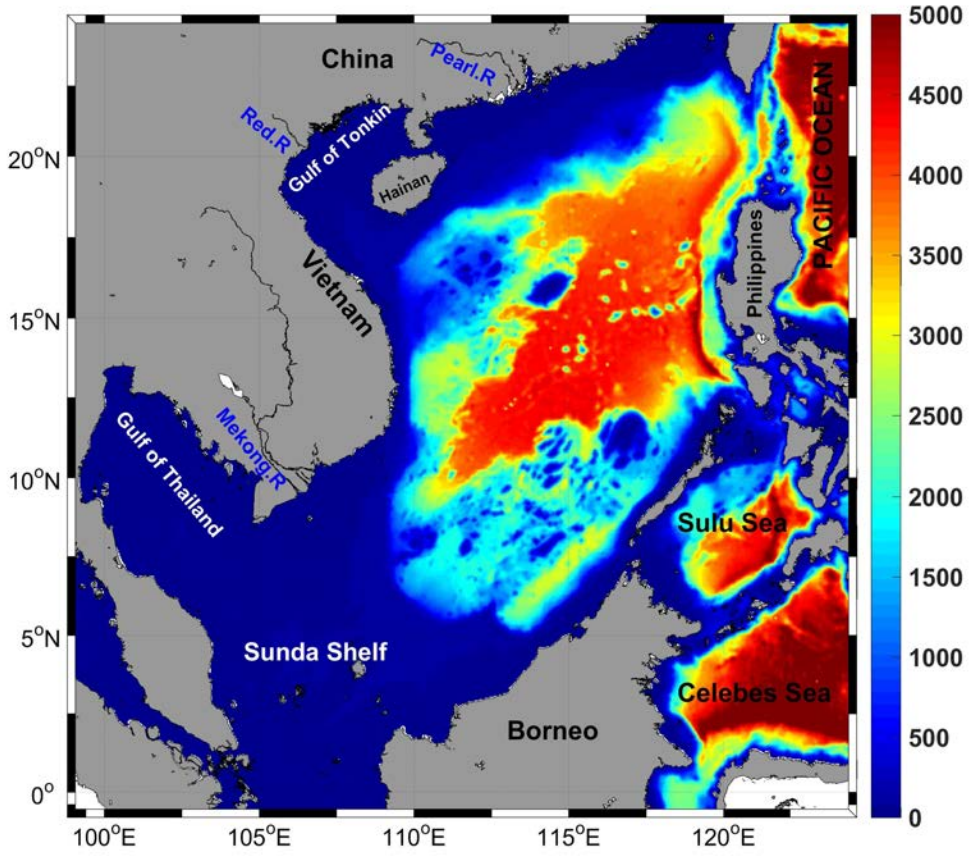

Figure II.3: Bathymetry and domain of the SCS configuration

To build the computation grid over our SCS domain, we used the bathymetry product obtained by merging the topographic dataset GEBCO 2014 (https://www.gebco.net/data_and_products/historical_data_sets/) and the digitalized nautical chart CM93, collected via OpenCPM (https://opencpn.org/). The 30 arc-second interval grid GEBCO 2014 is mainly built from the ship-track sounding database and is provided at 1 km of resolution. This global bathymetry dataset is appropriate in representing the SCS topography at large scale, but its resolution is too low to represent coastal areas as well as the interocean straits of the basin, which are mostly narrow and situated in shallow zones. To improve the bathymetric resolution at these areas, the nautical chart CM93 in the coastal shallow zone has been merged with the large-scale dataset GEBCO 2014. Details of the construction of this new bathymetry dataset are provided in Piton et al. (2020).

The initial and open lateral boundary conditions for temperature, salinity, current velocities and sea level over the simulation period are issued from the daily dataset of the Global

Ocean 1/12° physics analysis and forecast Copernicus CMEMS: Global_Analysis_Forecast_Phy_001_024 Global Ocean, available at: https://resources.marine.copernicus.eu/. The Copernicus dataset is displayed with a 0.083° (1/12°) horizontal resolution with regular longitude/latitude equirectangular projection and 50 regular depth levels (ranging from 0 to 5500 m).

The air-sea interface forcing conditions come from the European Center for Medium Range weather forecast (ECMWF). This product – a forecast CF-10 – provides 3 hourly analyses at 1/8° horizontal resolution in atmospheric pressure, potential temperature, wind intensity, relative humidity, precipitation, short and long wave radiation fluxes.

In order to prescribe the most realistically possible river fluxes, a collection work in river discharges has been carried out. Our configuration included 63 river mouths, with 45 rivers flowing into the SCS (see Figure II.4). Among them, 11 rivers (including the Red river) in the Northern and Center of Vietnam are real – time daily data provided by the National Hydro-Meteological Service (NHMS) of Vietnam. The other river runoff is monthly climatology data issued from the coastal runoff database of the CLS – INDESO project (Tranchant et al., 2006), including the Mekong river and Pearl river.

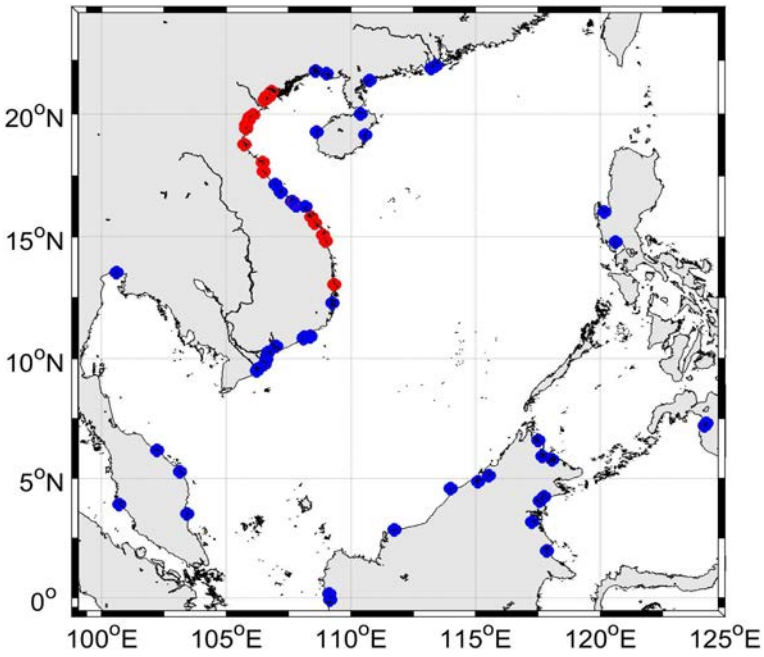

Figure II.4: Positions of river mouths in the SCS configuration. Red point = real-time river runoff; blue point = monthly climatology river runoff.

We use the tidal atlas FES2014b for open boundary tidal forcing. This is the latest product of the global tide model FES (Finite Element Solution), described in Carrère et al. (2012). Nine barotropic tidal components are taken into account, including semi-diurnal tides (M2, S2, N2, K2), diurnal tides (K1, P1, O1, Q1), and a compound tide (M4). The model is also forced by the astronomical plus the loading and self-attraction potentials (Lyard et al., 2006). Details and numerical issues can be found in Pairaud et al. (2008, 2010).

II.3. Observation data for model evaluation

II.3.1. Satellite observations

II.3.1.1. OSTIA sea surface temperature (SST)

Daily data of the Operational Sea Surface Temperature and Sea Ice Analysis (OSTIA) are used to evaluate the SST of SYMPHONIE simulation outputs over the simulated period 2009-2018. OSTIA is a Level 4 sea surface temperature daily product, with a high resolution of 0.054 degree. The OSTIA analysis assimilates satellite data from sensors from the GHRSST (Group for High Resolution Sea Surface Temperature) project, including the Advanced Very High Resolution Radiometer (AVHRR), the Advanced Along Track Scanning Radiometer (AATSR), the Spinning Enhanced Visible and Infrared Imager (SEVIRI), the Advanced Microwave Scanning Radiometer-EOS (AMSRE), the Tropical Rainfall Measuring Mission Microwave Imager (TMI), together with in situ data from drifting and moored buoys to determine the SST. The analysis is carried out using a variant of optimal interpolation (OI) as described in study of Martin et al. (2007). More details on OSTIA system descriptions are found in Donlon et al. (2011). OSTIA data is provided every day in netCDF format at: https://data.nodc.noaa.gov/ghrsst/L4/GLOB/UKMO/OSTIA/

II.3.1.2. SMOS sea surface salinity (SSS)

For SSS evaluation, we use the 9-day-averaged de-biased SMOS (Soil Moisture and Ocean Salinity) SSS Level 3 version 3, a product of SMOS earth observation mission of the European Space Agency. Launched in 2009, the SMOS satellite use a novel interferometric radiometer instrument called Microwave Imaging Radiometer with

Aperture Synthesis (MIRAS) that measures changes in land moisture and in SSS by observing variations in the microwave L – band (1.4 kHz) emission from the surface of the planet.

This version of SMOS observations, developed by Boutin et al. (2018), has a resolution of 25 km and is available for the period 2010 – 2017. The L3_DEBIAS_LOCEAN_v3 Sea Surface Salinity maps have been produced by LOCEAN/IPSL (UMR CNRS/UPMC/IRD/MNHN) laboratory and ACRI-st company that participate to the Ocean Salinity Expertise Center (CECOS) of Centre Aval de Traitement des Donnees SMOS (CATDS). This product is distributed by the Ocean Salinity Expertise Center (CECOS) of the CNES-IFREMER Centre Aval de Traitement des Donnees SMOS (CATDS), at IFREMER, Plouzane (France) via: ftp://ext-catds-cecos-locean:catds2010@ftp.ifremer.fr.

II.3.1.3. CTOH/CMEMS sea level anomaly (SLA)

The modeled SLA and surface geostrophic currents are evaluated by comparison with the daily 1/4° global ocean gridded L4 sea surface heights and derived variables in delayed – time of Copernicus Marine Environment Monitoring Service (CMEMS), available from:

http://marine.copernicus.eu/services-portfolio/access-to-products/?option=com_csw&view=details&product_id=SEALEVEL_GLO_PHY_L4_REP_OBSERVATIONS_008_047

This altimetry product (hereafter called ALTI) is generated using data from different altimeter missions (Jason-3, Sentinel-3A, HY-2A, Saral/AltiKa, Cryosat-2, Jason-2, Jason-1, T/P, ENVISAT, GFO, ERS1/2) and covers the period from 1993 up to present (Ablain et al. 2015, Ray and Zaron 2015). The altimeter satellite gridded sea surface heights is computed with respect to a twenty – year mean.

For the comparison with model outputs, we extract the daily altimetry SLA on the period of simulation (2009 – 2018), and remove for each grid point of dataset (model and altimetry) the mean dynamic topography over 2009 – 2018 from the absolute dynamic topography.

II.3.2. In – situ observations

For water masses characteristics evaluation, we compare the simulated temperature and salinity profiles with daily Argo floats (2009 - 2018) profiles over the period 2009 - 2018 and with the dataset collected from the Vietnam – USA joined glider campaign performed in winter – spring 2017. Continuous SST and SSS in-situ data issued from the ALIS measurement campaign in Southern Vietnam in summer 2014 are used for surface characteristic evaluations. Measurement stations of Argo floats, and glider and ALIS campaigns are presented in Figure II.5.

II.3.2.1. ARGO floats

A large number of Argo profiles found in the SCS (more than 12 600 profiles over the studied period 2009 – 2018) has allowed us to better understand and characterize the water masses characteristics in our zone, where the in-situ measurements stay scarce until now. However, certain zones have not been covered yet by Argo floats, such as coastal zones, the Gulf of Tonkin and Gulf of Thailand. The daily Argo temperature and salinity profiles are collected from the Ifremer website (ftp://ftp.ifremer.fr/ifremer/argo/geo/pacific_ocean/) in the studied SCS zone (99°E – 124°E; -0.6°N – 24°N).

II.3.2.2. Alis campaign 2014

In the framework of the VITEL (VIetnam TELedetection) project (program TOSCA, CNES, P. I. S. Ouillon), a field campaign was organized in May – July 2014 on the French scientific vessel ALIS, gathering a multi-disciplinary team on board. Two principal campaigns were held in the coastal zone of Northern and Southern Vietnam respectively, in order to study the optical properties of coastal water masses and to develop a new bio-optical algorithm for water quality parameters. During the trajectory of ALIS vessel in the South China Sea, the temperature and salinity of surface water were measured and registered every 6 seconds, from 10 May 2014 to 28 July 2014 by the sensor thermosalinometer Seabird SBE21, fixed on the board and took measurements permanently (hereafter called TSG data). Information of ALIS equipment (in french) is found at:

https://www.flotteoceanographique.fr/La-Flotte/Navires-semi-hauturiers/Alis/Caracteristiques-detaillees

II.3.2.3. Sea glider campaign 2017

Under the framework of a cooperative international research program, including Vietnamese and U.S. scientific institutions (Rogowski et al. 2019), a glider-based observational program was initiated. Seaglider sg206 was deployed on 22 Jan 2017 and crossed the strong southward currents near the shelf break approximately 4 times before the steering mechanism malfunctioned on 21 Apr 2017. Ultimately, the mission ended on 16 May 2017 without recovery. The glider collected 555 vertical profiles over the 114 days of deployment.

Seagliders measure temperature and pressure, using an unpumped Sea-Bird Electronics CTD (SBE 41CP). Temperature and depth are sampled at 5 s intervals in the upper 150 m and between 55 – 100 s below. Optical measurements are sampled at 5 – 10 s intervals in the upper 150 m, between 110 – 200 s down to 600 m, and not at all below. All sensors are factory calibrated. Salinity is estimated correcting for the thermal lag error using a variable flow rate (Garau et al. 2011). Seagliders sample from the surface down to about 5 m above the bottom or to a maximum depth of 1000 m with a vertical speed of about 10 cm/s (full depth dives take approximately 6 hours) and a horizontal speed of about 25 cm/s. At 5 s sampling intervals, vertical resolution is less than 1 m, and the along-track distance between surfacings is about 5 km. In addition to the *in situ* measurements, the dive-averaged velocity can be estimated from the dead-reckoned and measured glider surface positions.

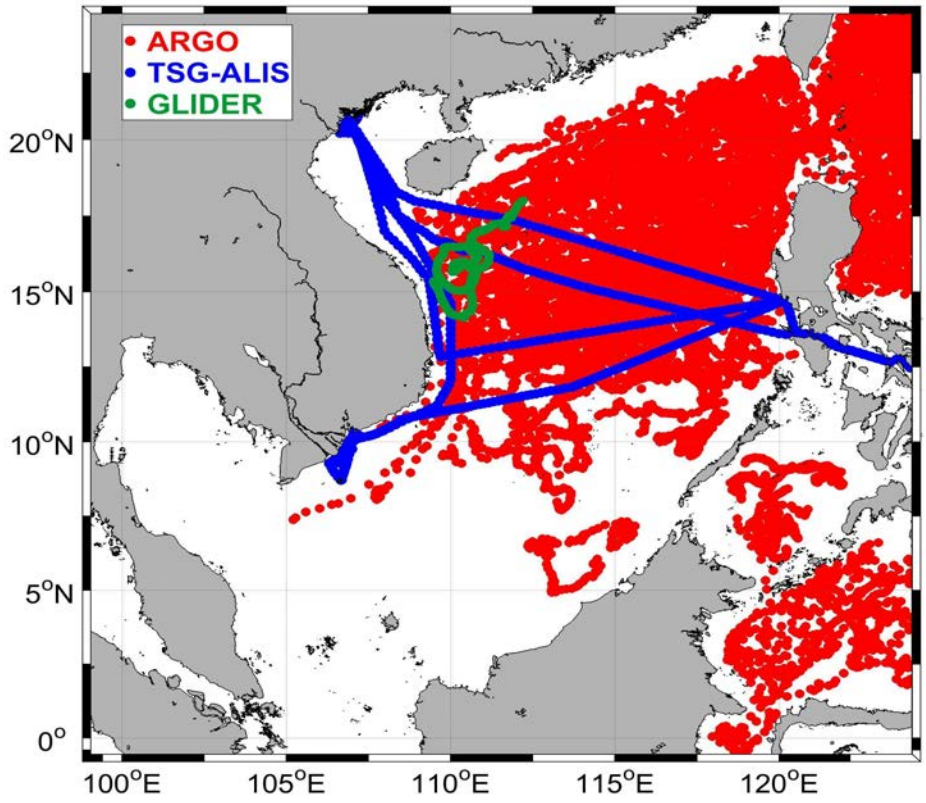

Figure II.5: Locations of Argo buoys over the period 2009 – 2018 (red), ALIS TSG in 2014 (blue) and GLIDER in 2017 (green) measurements.

To perform comparisons between in-situ measurements and modeled outputs in terms of surface (TSG) and vertical distributions (Argo and Glider) of water masses, we extract the simulated results at the nearest point (both in time and position) to the real-time data.

II.3.3. Climate indices

To study the effect of large – scale climate phenomena such as ENSO and PDO on the interannual simulated parameters, we use the ONI and the PDO index.

The ONI index, calculated by averaging the SST anomalies in the Nino 3.4 region (situated in the Central equatorial Pacific Ocean, from 5°S to 5°N, 170°W to 120°W), is one of the primary indices monitoring the ENSO. The ONI is calculated every three consecutive months in order to extract the variability closely related to the ENSO phenomenon. This index is provided by NOAA:

https://origin.cpc.ncep.noaa.gov/products/analysis_monitoring/ensostuff/ONI_v5.php

The monthly PDO index is the leading empirical orthogonal function (EOF) of monthly SST anomalies over the North Pacific (poleward of 20°N). In this study the PDO index computed by the Japan Meteorological agency (https://ds.data.jma.go.jp) is used.

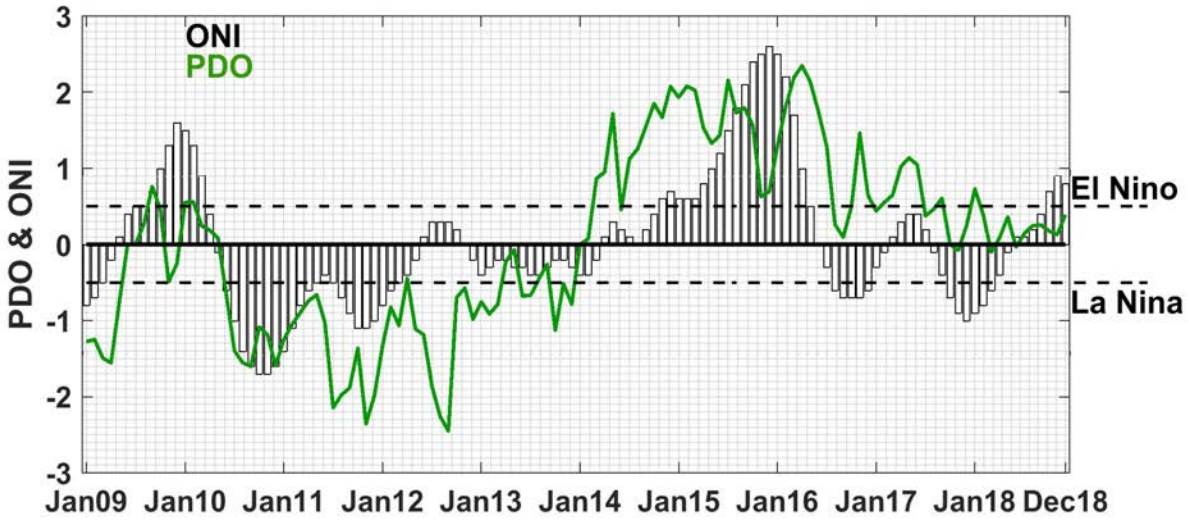

Figure II.6: The time series of ONI (black) and PDO (green) indexes over 2009 - 2018.

Figure II.6 presents the time series time series of ONI and PDO indexes over 2009 - 2018. During this period, moderate El Niño events occurred in 2009 - 2010 and a very strong El Niño event in 2015 - 2016. A strong La Niña event occured in 2010 - 2011, while moderate and weak La Niña events took place in late 2016 and winter 2017 - 2018. At the beginning of 2014, the PDO phase changed from a globally negative phase (2009 - 2013) into a positive phase (2014 - 2018).

II.4. Analysis and statistical methods

II.4.1. Flux and budget calculations

In this part we detail the calculation methods of water, heat and salt budgets over the SCS zone, and of the lateral fluxes passing through the six interocean straits: Luzon, Taiwan, Mindoro, Balabac, Karimata, Malacca, discussed in Chapters IV and V.

II.4.1.1. Water, heat and salt budgets

Our goal is to quantify volume, heat and salt budgets over the whole SCS and to assess the contributions of the different terms of the budget equations: internal contents variations and atmospheric, lateral and river fluxes.

Water volume balance

The internal variation of water volume V over the SCS area between times t_1 and t_2 (ΔV) is equal to the integral between t_1 and t_2 of all water fluxes into (out of) the SCS domain, taken as the sea zone limited by the 6 interocean straits shown in Figure 1a:

$$\Delta V = V_{t2} - V_{t1} = \int_{t_1}^{t_2} \left(F_{w,lat} + F_{w,atmo} + F_{w,riv} \right) \delta t \qquad \text{(Eq. II.4.1)}$$

where $F_{w,lat}$, $F_{w,atmo}$ and $F_{w,riv}$ are the net lateral, atmospheric and river water fluxes respectively. Here and in the following, positive lateral fluxes correspond to inflow, and negative fluxes to (outflow).

Heat balance

The variation of heat content *HC* between times t_1 and t_2 (ΔHC) is equal to the sum of all heat fluxes exchanged within the SCS domain between t_1 and t_2:

$$\Delta HC = HC_{t2} - HC_{t1} = \int_{t_1}^{t_2} \left(F_{T,lat} + F_{T,atmo} + F_{T,riv} \right) \delta t \qquad \text{(Eq. II.4.2)}$$

where $F_{T,lat}$, $F_{T,atmo}$ and $F_{T,riv}$ are the net lateral, atmospheric and river heat fluxes respectively, and HC is computed from:

$$HC = \rho_0 C_p \iiint_{x,y,z} T(x,y,z,t) dx dy dz \qquad \text{(Eq. II.4.3)}$$

With T the temperature (in °C), ρ_0 a seawater density constant (1028 kg.m^{-3}), C_p a seawater specific heat constant (3900 J.kg^{-1}°C^{-1}) and the triple integral symbol represents the integral over the volume of the region under consideration, the SCS here.

Salt balance

We assume that there is no salt input from atmospheric fluxes and river runoff and that the only source/sink of salt is from the lateral boundaries, so that the variation of salt

content between t_1 and t_2 (ΔSC) is simply equal to the sum of salt fluxes exchanged at the lateral boundaries of the SCS domain between t_1 and t_2 :

$$\Delta SC = SC_{t2} - SC_{t1} = \int_{t_1}^{t_2} F_{S,lat}\delta t \quad \text{(Eq. II.4.4)}$$

where $F_{S,lat}$ is the net salt flux at the lateral boundaries and SC is computed from:

$SC = \iiint_{x,y,z} S(x,y,z,t)dxdydz$ with S the salinity. (Eq. II.4.5)

II.4.1.2. Lateral volume, heat and salt fluxes

The lateral volume flux $F_{w,lat}$ in Sv (Sv =10^6 m^3s^{-1}) through the vertical section A is computed from:

$$F_{w,lat} = \int_A v_t \delta A \quad \text{(Eq. II.4.6)}$$

with v_t the current velocity normal to the transect (m^3s^{-1}), A the area of the section from the surface to bottom.

The lateral heat flux $F_{T,lat}$ in PW (PW =10^{15} W) is computed from:

$$F_{T,lat} = \rho_0 C_p \int_A T v_t \delta A \quad \text{(Eq. II.4.7)}$$

The lateral salt flux $F_{S,lat}$ in Ggs^{-1} is computed from:

$$F_{S,lat} = \rho_0 \int_A S v_t \delta A \quad \text{(Eq. II.4.8)}$$

II.4.1.3. Atmospheric fluxes

The atmospheric freshwater flux is computed in Sv (1 Sv = 10^6 m^3 s^{-1}) from:

$$F_{w,atmo} = \int_{Surf} (P - E)\delta Surf \quad \text{(Eq. II.4.9)}$$

where P stands for the precipitation in ms^{-1}, E the evaporation in ms^{-1}, Surf is the surface area. Atmospheric fluxes are computed over the SCS area limited by the 6 interocean straits shown in Figure 1a.

The net atmospheric heat flux ($F_{T,atmo}$), in PW, is the sum over the SCS of the short-wave radiation flux (F_{SR}), long-wave radiation flux (F_{LR}), sensible heat flux (F_{SEN}) and latent heat flux (F_{LATENT}):

$$F_{T,atmo} = \int_{Surf}(F_{SR} + F_{LR} + F_{SEN} + F_{LATENT})\delta Surf \quad \text{(Eq. II.4.10)}$$

II.4.1.4. River fluxes

The river flux $F_{w,riv}$ is calculated as the sum over all the rivers of the product of the velocity of river flow at the river mouth, v_{riv}:

$$F_{w,riv} = \sum_{rivers} \int_A v_{riv}\delta A \quad \text{(Eq. II.4.11)}$$

where A is the area of the river mouth section from the surface to bottom.

The river heat flux $F_{T,riv}$, in PW, is computed from:

$$F_{T,riv} = \sum_{rivers} \rho_0 C_p \int_A T_{riv} v_{riv}\delta A \quad \text{(Eq. II.4.12)}$$

where T_{riv} is the temperature (in °C) at the river mouth.

II.4.2. Statistical methods

The relationship between the simulated dataset S and observational dataset O (of the same element number N) is investigated using three statistical parameters: the bias, Normalized Root Mean Square Error (NRMSE) and the Pearson correlation coefficient R. We keep the same convention for the three statistic formula:

Si, Oi: the simulation series and observation series

$\bar{S}, \bar{O}$: the mean value of respectively the simulation series and observation series.

II.4.2.1. Bias

The bias between two time series S and O is equal to the difference between the two mean value of the two time series:

$$bias = \bar{S} - \bar{O} \quad \text{(Eq. II.4.13)}$$

II.4.2.2. Normalized root means square error (NRMSE)

The NRMSE between two dataset S and O is computed as follow:

$$NRMSE = \frac{\sqrt{\frac{1}{N}\sum_{i=1}^{n}(Si-Oi)^2}}{(O_{max}-O_{min})} \quad \text{(Eq.II.4.14)}$$

II.4.2.3. Pearson correlation coefficient R

The Pearson correlation coefficient R is a statistical parameter which measures the strength of a linear association between two variables S and O.

$$R = \frac{\sum_{i=1}^{N}(O_i-\bar{O})(S_i-\bar{S})}{\sum_{i=1}^{N}(O_i-\bar{O})^2 \sum_{i=1}^{N}(S_i-\bar{S})^2} \quad \text{(Eq. II.4.15)}$$

The calculation of R gives as result a number between -1 and 1. Positive correlation means that if one variable increases, the other also increases. Negative correlation indicates that if one variable increases, the other decreases. To quantify the statistical significance of a correlation, we moreover compute for each correlation coefficient the associated p-value, defined as the probability that the null hypothesis (there is no relationship between the two variables being studied) is true. The p-value is calculated using a t-distribution with (n - 2) degrees of freedom (n = number of pairs of scores). In practice, a table of critical values for Pearson correlation is used for the determination of p-value. The smaller the p-value, the stronger the evidence that the null hypothesis is rejected. If p-value < 0.05, resp 0.01, the correlation coefficient is called statistically significant at 95% (significant), resp. 99% (highly significant).

Chapter III: Model evaluation

This chapter details the evaluation of the modeled dynamical and water masses characteristics at the seasonal and interannual scales over the period 2009 - 2018. Surface characteristics (SST, SSS, SLA) and vertical temperature and salinity profiles are evaluated by comparison with satellite and in-situ data. This chapter is a part of the article "*Volume, heat and salt budgets for the South China Sea: new estimates from a high-resolution closed budget model*" submitted in journal *Progress in Oceanography*.

III.1. Surface characteristics

For each evaluation of sea surface characteristics, we present below the comparison of the seasonal cycle, the interannual variations and the summer/winter spatial average 2D maps between model outputs and corresponding satellite observations. The time series of climatological monthly average over 2009-2018 and of yearly averages between 2009 and 2018 of the averaged SST, SSS, SLA on the whole computational domain shown on Figure II.3 (Chapter II) and the corresponding satellite observations are shown in Figure III.1.

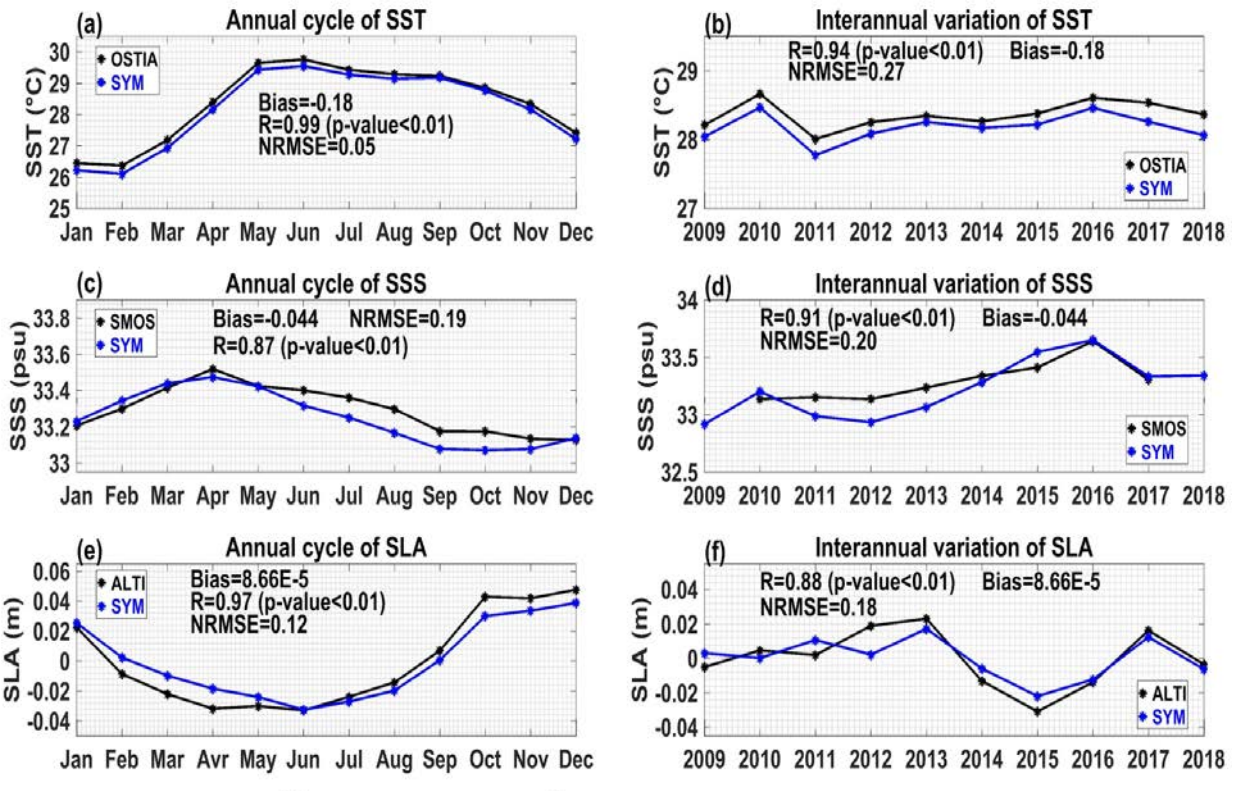

Figure III.1: Averaged annual cycle (left) and interannual variations (right) of SST (°C, a, b), SSS (psu, c, d) and SLA (m, e, f) computed from the model (blue) and from satellite observations (black). R stands for the correlation coefficient value and p-value for the associated p-value, and NRMSE for Normalized Root Mean Square Error.

III.1.1. Annual cycle

The SST annual cycle (Figure III.1a) computed from OSTIA observations is very well represented by the model, with a highly significant correlation (R=0.99 and p-value $p < 0.01$, corresponding to a significant level higher than 99%), and a small value of NRMSE (0.05) between the model outputs and satellite observations. The model shows a slight negative bias of 0.18°C. In both datasets, the monthly climatological cycle of SST reaches its maximum value in May/June (summer) and decreases to its minimum in January/February (winter). This monthly climatological SST is in agreement with the study of Kumar et al. (2010), who observed the same SST annual cycle by analysing hydrographic WOA data (World Ocean Atlas, 2005).

The SSS seasonal cycle (Figure III.1c) also shows a good agreement between the model and SMOS data, with a highly significant correlation of 0.89 ($p < 0.01$) and a low NRMSE

equal to 0.19. Our model shows a slight negative bias (-0.04) compared to SMOS. In both model and satellite data, the average SSS is maximum in April (spring) with values of 33.47 psu in the model and 33.52 psu in SMOS, and minimum in September and October (autumn) with 33.07 psu in the model and 33.17 psu in SMOS. This significant seasonal variation of SSS in the SCS, with high salinity in winter-spring and low salinity in summer-autumn was also obtained by Kumar et al. (2010) and Zeng et al. (2014).

The annual cycle of SLA obtained with the model and ALTI data during the period 2009 - 2018 shows a minimum value in summer (June) with -0.033 m both for our model and ALTI. The SLA reaches its highest value in winter (December) with 0.039 m and 0.049 m respectively for the model and ALTI. The model outputs and the altimeter measurements have a highly significant correlation ($R=0.97$, $p<0.01$), and a small NRMSE value (0.12). The monthly climatological SLA issued from model outputs is also in agreement with Shaw et al. (1999) and Ho et al. (2000): using TOPEX/Poseidon altimeter data, they both concluded on a higher SLA in winter and lower SLA in summer over the SCS.

III.1.2. Interannual variations

We obtain a highly significant correlation coefficient between our model and OSTIA ($R=0.94$, $p<0.01$) regarding yearly SST interannual variations. The yearly SST bias (0.18°C in average) in SYMPHONIE is rather constant over the period (Figure. III.1b) and the NRMSE is 0.27. From 2009 to 2018, the average yearly SST over the basin reached its highest values in 2010 and 2016 (28.47°C and 28.46°C respectively). This observation is consistent with the study of Yu et al. (2019), who found a co-occurrence between those SST positive anomalies peaks and El-Niño events in 2009-2010 and 2015-2016 (see the ONI time series from NOAA available at: https://origin.cpc.ncep.noaa.gov/products/analysis_monitoring/ensostuff/ONI_v5.php).

The minimum of averaged SST (27.77°C) is observed in 2011, corresponding to the La Niña event that occurred in 2011-2012. Yu et al. (2019) obtained the same interannual time-series by analysing MODIS satellite-derived SST data for the period 2003 - 2017.

The interannual variations of yearly SSS (Figure III.1d) show a highly significant correlation ($R=0.91$, $p<0.01$) and a rather low NRMSE value (0.20) between the model results and satellite data. There is a significant increase of the annual averaged SSS over

the SCS between 2012 to 2016, both in the model outputs and SMOS data. Over the period 2010 - 2017, the SSS reached a low value in 2012 (32.93 for the model, 33.14 for SMOS), then increased continuously until a maximum value in 2016 (33.65 psu for the model, 33.64 psu for SMOS). The freshening until 2012 and strong salinification over the SCS domain during the following 4 years are in agreement with observations of Zeng et al. (2014, 2018), who revealed that 2012 was the year with the lowest recorded value of SSS in the SCS over a 50-year period, and that the SSS then increased from late 2012 to 2016 over the SCS.

In terms of SLA interannual variations, our model and ALTI show strong similarities with a NRMSE equal to 0.18 (Figure III.1f) and a highly significant correlation ($R=0.88$, $p< 0.01$). During the studied period, the overall averaged SLA was maximum in 2013 (0.017 m in model outputs and 0.023 m in ALTI), and minimum in 2015 (-0.02 m in the model and -0.03 m in ALTI).

Those comparisons between modeled and observed SST, SSS and SLA thus show that our model reproduces realistically the annual cycle and interannual variations of the sea surface hydrological characteristics and circulation in the SCS.

III.1.3 Spatial seasonal surface patterns

In this section we compare the 2D maps of SST, SSS and SLA averaged over the boreal winter (December, January and February, DJF) and summer (June, July and August, JJA) and over the 2009-2018 period, in the model and in the corresponding satellite dataset (Figure III.2).

In both summer and winter, the modeled SST is very close to observations, with highly significant spatial correlation (respectively $R=0.98$ and 0.84 in winter and summer, $p<0.01$) compared to OSTIA, and similar temperature ranges in observations and model outputs (Figure III.2a, b). In winter, the model shows a negative bias of -0.27°C on average, and cold zones offshore southern Vietnam and in the northern basin, near the Taiwan strait. In summer (Figure III.2c, d), the average negative bias is reduced to -0.18°C, and the simulation produces a SST lower than OSTIA in the northern SCS near Taiwan, in the South Vietnam upwelling zone (off southern Vietnam coast, Da et al. 2019), along the Mekong delta, and in the Sulu and Celebes Seas (see Figure. II.3). On the other

hand, modeled SST is warmer in the Gulf of Tonkin, Gulf of Thailand and the southern basin.

The spatial distribution of SSS in the model also shows a highly significant spatial correlation with SMOS for both seasons (R=0.88 and 0.84 in winter and summer, respectively, $p<0.01$). Our model has a positive bias in winter (0.05 psu), and a negative bias in summer (-0.1 psu). In winter (Figure III.2 e,f), the coastal zone and the Gulf of Thailand are fresher in the model than in SMOS data, whereas the center of the basin and the southern Gulf of Tonkin are saltier. In summer (Figure III.2 g,h), we obtain a significantly lower SSS at the big river mouths (Pearl River, Red River, Mekong River), in the Gulf of Thailand and in the Malacca strait in model outputs compared to SMOS. SMOS, with a low resolution of 25 km, might not be able to capture these changes in SSS at the coastal zone.

We examine the performance of SYMPHONIE in simulating the SLA and geostrophic currents (Fig 3 i,j,k,l). Both in winter and summer, the seasonal mean spatial distribution of SLA is quite similar in model outputs and ALTI, with a highly significant correlation ($R=0.97$, $p<0.01$). The model shows very weak negative seasonal biases in SLA compared to ALTI, of -0.006 m in winter and -0.004 m in summer. In the Gulf of Thailand, the SLA issued from model outputs are lower in winter and higher in summer as compared to ALTI. Regarding the geostrophic currents, we obtain great similarities between the model and ALTI. In winter when the northeastern monsoon dominates, two cells of cyclonic gyre cover the whole basin, one near Luzon and another at the Sunda Shelf. In summer, with the southwest monsoon, most of the SCS geostrophic currents reverse and flow northeast. The geostrophic currents are most intense at the Sunda Shelf zone (see Figure II.3) in winter. In summer, we observe strong geostrophic flows at the southern Vietnam coast, and at the east of Malaysian coast. The intensity and direction of those seasonal geostrophic currents are consistent with previous studies (e.g. Da et al. 2019, Wang.Y et al. 2006).

Those comparisons of SST, SSS and SLA spatial fields in winter and summer therefore show that our simulation reproduces realistically the seasonal spatial distributions of sea surface characteristics and circulation.

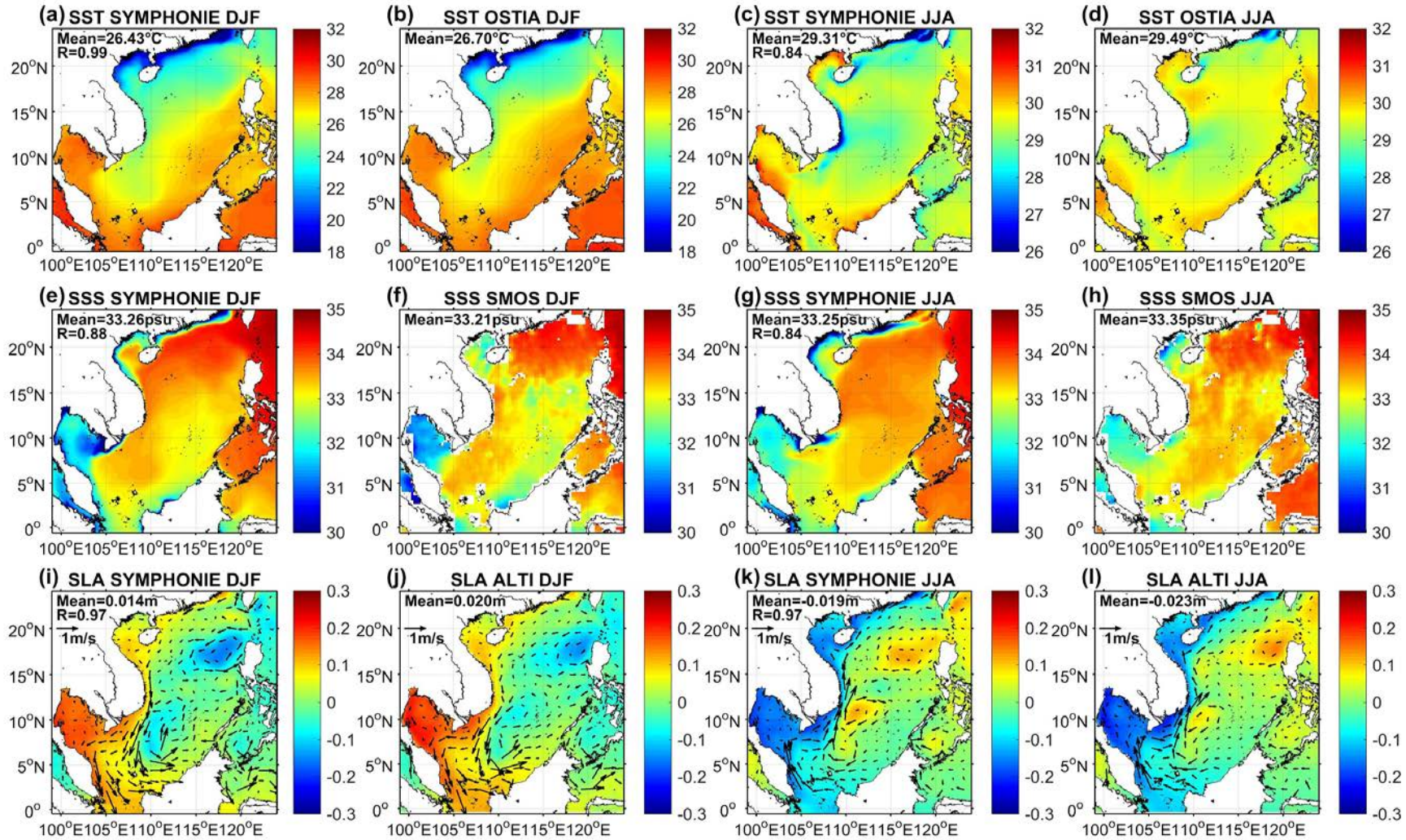

Figure III.2: Spatial distribution in winter (DJF) and summer (JJA) of climatological SST (°C, a, b, c, d), SSS (psu, e, f, g, h), SLA (m) and geostrophic current (m/s, i, j, k, l) in model outputs and corresponding satellite observations. R stands for the spatial correlation coefficient (here p-value is always smaller than 0.01).

III.2. Water masses characteristics

We hereafter examine the performance of the model in reproducing the surface and vertical water properties. Figure III.3 illustrates the comparisons between model results and observations from Argo floats that crossed the study area over the period 2009-2018 (Figure III.3a-c), glider measurements in 2017 (Figure III.3e-h) and ALIS vessel's TSG sea surface data in 2014 (Figure III.3i, j).

III.2.1. Comparison with Argo, glider and in situ profiles

First, the simulation shows a high performance in the representation of surface water characteristics, with a strong similarity compared to TSG-Alis data during summer 2014 (Figure III.3i, j) and correlation coefficients of 0.70 and 0.82 ($p<0.01$), for SST and SSS respectively. Second, we obtain a great agreement between the vertical profiles from Argo floats and model outputs, both in temperature and salinity (Figure III.3a-d). The simulated profiles are in the same range as observations. In particular the maximum salinity observed in the intermediate water mass is well reproduced by the model. Third, the comparison between Glider measurements collected in winter-spring 2017 and model outputs also shows that the modeled vertical profiles of temperature and salinity are realistic (Figure III.3e, g).

The temperature and salinity averaged profiles of the model therefore show a good agreement with the in-situ dataset. In general, modeled temperatures are cooler than measurements from Argo floats and gliders, with a negative bias in the whole water column (Figure III.3b, f). The highest differences between our simulation and in-situ observations are located at the subsurface layer (50-200 m), with maximum bias values of -1.2°C compared to Argo data and of -1.5°C compared to glider data. Underneath 200 m, the temperature bias is stable, with values varying around 0.2-0.5°C compared to Argo floats and 0.7-1°C compared to glider data. In terms of salinity profiles, model results have a positive bias in general. Below 200 m, our model presents a very low salinity bias, both compared to Argo and Glider data. The highest bias is obtained in the subsurface layer, with value of 0.2 psu (model-Argo, Figure III.3d) and 0.3 psu (model-glider, Figure III.3h).

These comparisons with in-situ observations confirm the realism of our simulation. The negative bias in temperature profiles and a positive bias in salinity profiles in the model

might be explained by a stronger vertical mixing in the model than reality. These weak biases are however acceptable and our simulation can legitimately be used to study water mass dynamics in the SCS.

III.2.2. Representation of SCS water masses

The temperature and salinity profiles collected from Argo floats and Glider project allow us to confirm the water mass characteristics of the SCS (Fig. III.3a-h). We obtain the same characteristics of water masses in the zone as previous studies on SCS (Uu and Brankart 1997, Rojana-anawat et al. 2000, 2001, Saadon et al. 1999 a,b) and on Pacific (Pickard and Emery, 1990). In the upper layer (0-50 m), we observe both the Open Sea Water (OSW, characterized by salinity of 33-34 psu and temperature of 25-30°C) and the Continental Shelf Waters (CSW) with low salinity (less than 33 psu) and a temperature between 20 and 30°C (depending on the season).

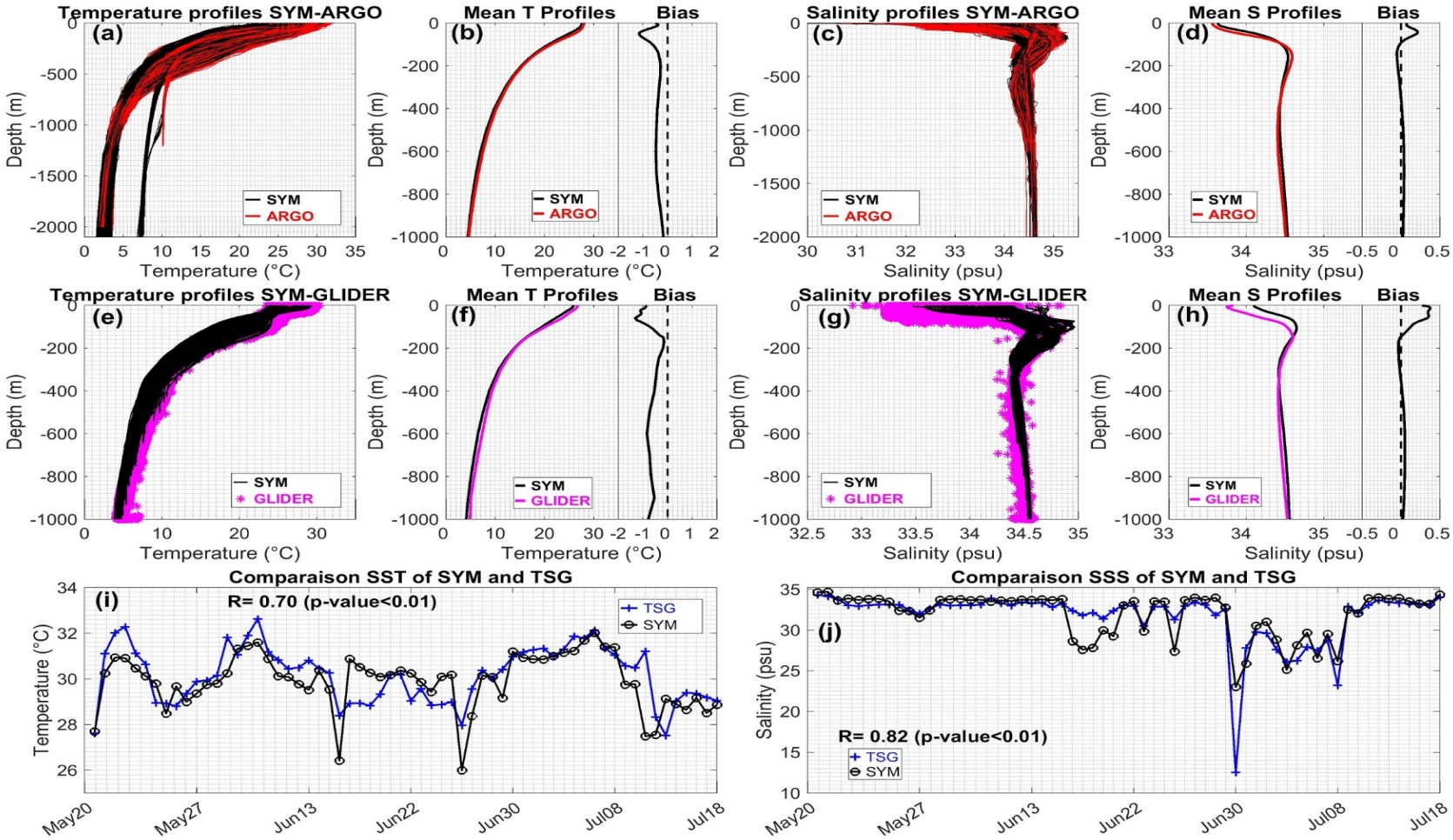

Figure III.3: (a to h) Temperature (°C) and salinity vertical profiles (all profiles, mean profiles and mean bias between model and observations) comparison between model outputs, Argo floats (a,b,c,d) and Glider measurements (e,f,g,h). (i,j) SST (°C) and SSS comparison between the model and TSG-Alis data.

The 50-100 m layer is characterized by the mixing between the Northern Open Sea Water (NOSW) and the Pacific Ocean Water (POW) during winter. The NOSW has salinities of 34-34.5 psu and temperatures of 23-25°C, while the POW is saltier with salinities of 34-35 psu and temperatures of 25-27°C. Deeper, at 100-200 m, the Maximum Salinity Water (MSW) is characterized by temperatures between 15-17°C and salinities between 34.5 and 35 psu and is a property of the equatorial regions (Rojana-Anawat et al. 2000). Below the MSW, from 200-1000 m, the North Pacific Intermediate Water (NPIW) and Pacific Equatorial Water (PEW) are flowing with temperatures and salinities between 5-13°C and 34-35 psu, respectively. The Deep Water (DW), below 1000 m, is identified by temperatures of 2-5°C, and salinities of 34.3 - 34.7 psu.

We observe some temperature profiles not following those DW characteristics both in Argo and model outputs, with temperature varying from 7-10°C below 700 m: they are located in the Sulu Sea. This marginal sea, nearly isothermal, possedes unique water characteristics, with potential temperature varying around 9.8°C below 1000 m, as confirmed by observations of Wyrtki (1961), Chen et al. (2006) and Gordon et al. (2011), much higher than those of neighbouring seas such as the SCS, the Celebes Sea as well as the Western Pacific (Qu and Song. 2009).

Conclusion of the chapter

The three-dimensional hydrodynamic model SYMPHONIE was used to simulate ocean circulation in the SCS for a recent 10-year period (2009 – 2018). A configuration with high horizontal resolution (4 km) and 50 layers depth was built with 3 hourly atmospheric forcing, daily lateral oceanic boundary forcing, 9 tidal forcing components, and real-time or climatology data for 63 river discharge points. The model shows great performance with high similarity between model results and surface satellite data and in-situ observations, in terms of seasonal cycle and interannual variability of surface characteristics (SST, SSS, SLA) as well as vertical distributions of temperature and salinity. Low biases and high spatial and temporal correlations between the model outputs and observation data show the realism of the representation of the spatial and temporal (seasonal to interannual) variability of the SCS circulation and water masses. We then use this model configuration

to provide a new quantitative insight of SCSTF and SCS budgets at the climatological, seasonal and interannual scales, which will be detailed in Chapter IV and V.

Chapter IV: Climatological average and seasonal cycle of water, heat and salt budgets

In this chapter we analyse the volume, heat and salt budgets over the SCS obtained from our simulation at the climatological and seasonal scales, and quantify the contributions of each term of those budgets (Equations II.4.1, II.4.2, II.4.4, Chapter II) to the internal variations of volume and heat and salt contents in the SCS : lateral fluxes flowing through the SCS interocean straits, air-sea fluxes and continental inputs from rivers. Figure IV.1 shows the climatological average and standard deviation of yearly averages over the simulated period (2009-2018) for all those terms. These results are presented in the article "*Volume, heat and salt budgets for the South China Sea: new estimates from a high-resolution closed budget model*" submitted in *Progress in Oceanography*.

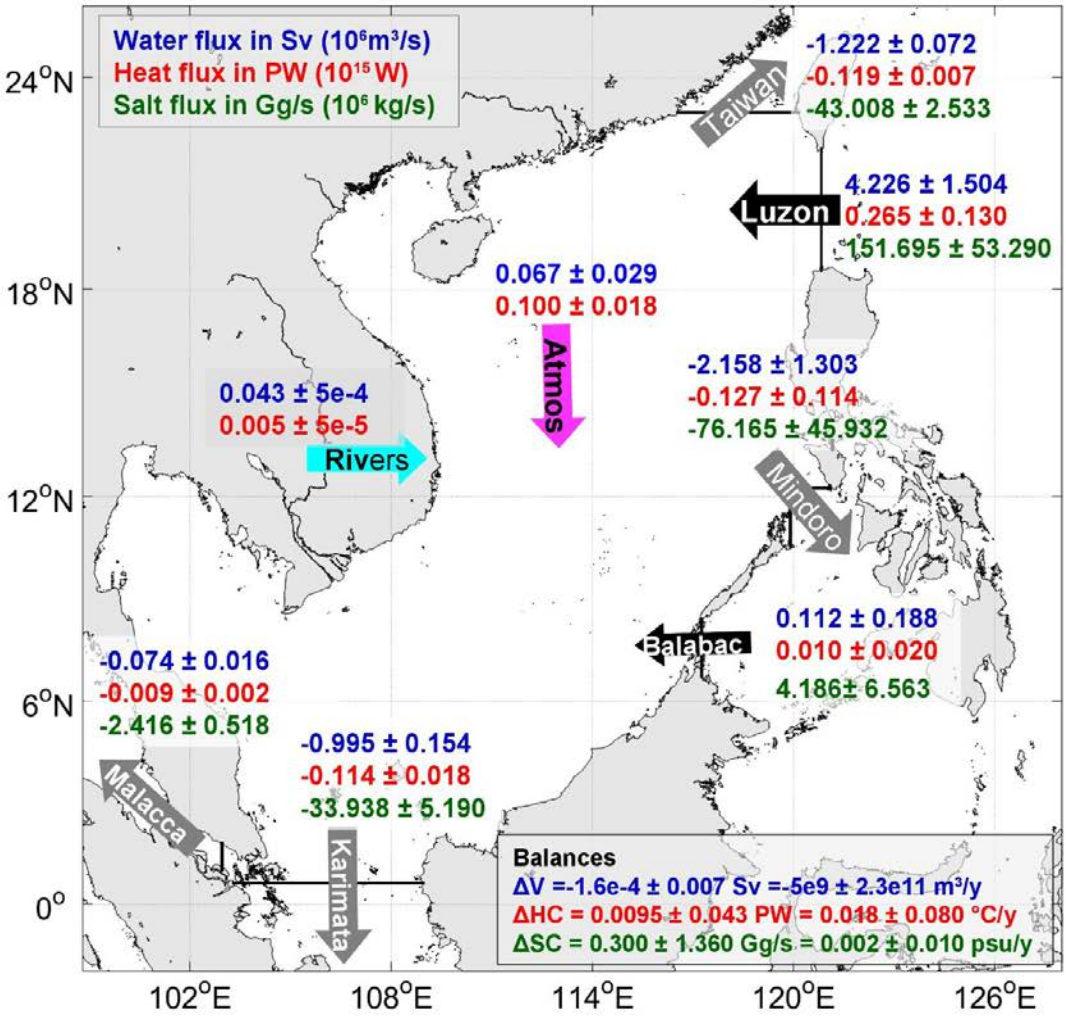

Figure IV.1: 2009-2018 averages and standard deviations of volume, heat and salt yearly fluxes at the straits (black arrow = inflow, gray arrow = outflow), and of volume, and heat yearly fluxes from the atmosphere (magenta arrow) and from rivers (cyan arrow). Positive and negative values correspond to inflow and outflow, respectively. The averages and standard deviations of the yearly volume and of the heat and salt yearly contents in the whole SCS over period 2009 - 2018 are provided on the bottom right corner.

IV.1. Volume fluxes

IV.1.1. Lateral fluxes through the interocean straits

Overall in our simulation, water masses enter the SCS through the Luzon and Balabac straits and flow out of the basin via the Taiwan strait in the north, the Mindoro strait in the west and the Karimata and Malacca straits in the south, forming the SCSTF identified by Qu et al. (2005) (Figure IV.1).

Simulation results show that the main inflow into the SCS is from the Pacific Ocean through the Luzon strait, with an average water inflow of 4.23±1.50 Sv. Calculations of LST and other straits' volume transports based on previous numerical and observational studies are presented in Table I.3 (Chapter I). Our value is in the range of the LST estimations from previous numerical studies, that vary between 2.4 and 4.8 Sv (Metzger and Hurlburt 1996, Qu et al. 2004, Xue et al. 2004, Tozuka et al. 2007, 2009, 2014, Fang et al. 2005, 2009, Liu et al. 2011, Hsin et al. 2012, Xu and Malanotte-Rizzoli 2013, Wei et al. 2016, Wang Yan et al. 2019) and from previous observational studies, that vary between 3.0 and 6.5 Sv (Qu 2000, Chu and Li 2000).

Figure IV.2a illustrates the seasonal cycles of volume transport at different transects issued from our model. The LST (black line) is positive (westward) all over the year, with a maximum intrusion in winter (in December, 6.60 Sv) and a minimum intrusion in summer (in June, 1.17 Sv), in agreement with previous numerical studies (Metzger and Hurlburt 1996, Qu 2000, Qu et al. 2004, Chu and Li 2000, Fang et al. 2005, Yaremchuk et al. 2009, Liu et al. 2011, Yu and Qu 2013, Xu and Malanotte-Rizzoli 2013, Wang Yan et al. 2019). Our model averaged LST in January (6.21 Sv), August (3.18 Sv) and October (5.68 Sv) is also close to observations of respectively Qu (2000, 5.3 Sv in January - climatology value), Yuan et al. (2008, 3.5 Sv in August 1994), Tian et al. (2006, 6±3 Sv in October 2005).

The simulated volume outflow through the Taiwan strait is 1.22±0.07 Sv. This result is consistent with numerical studies that produced outflow estimates varying from 0.45 to 2.6 Sv (Wu and Hsin 2005, Fang et al. 2005, 2009, Tozuka et al. 2007, 2014, Yaremchuk et al. 2009, Wang et al. 2009, Liu et al. 2011, Hsin et al. 2012, Zhang et al. 2014, Wei et al. 2016, Wang Yan et al. 2019, Table I.3), as well as with observational studies who produced estimates of 1.8 - 2.0 Sv (Fang et al. 1999, Wang et al. 2003 - Table I.3, Chapter I). The seasonal cycle of volume transport at the Taiwan strait (Figure IV.2a, red line) shows that this transport is negative (outflow) the whole year. This outflow reaches its maximum value in July (2.50 Sv) and decreases in autumn - winter until the minimum value of 0.16 Sv in December. These results are consistent with numerical estimations of Xue et al. (2004), Fang et al. (2005, 2009), Yaremchuk et al. (2009), Liu et al. (2011),

Zhang et al. (2014), Wang Yan et al. (2019) and close to measurements of Wang et al. (2003) and of Rong et al. (2007) who found a maximum outflow of 1.5 - 2.7 Sv in summer and a minimum outflow of 0.4 - 0.9 Sv in winter. Our model's volume outflow through Taiwan strait in May and August is respectively 1.93 Sv and 2.13 Sv, consistent with observations of Chung et al. 2001 (2.0 Sv in May, 2.2 Sv in August 1999).

At the Mindoro strait, our model simulates a lateral seawater outflow of 2.16 ±1.30 Sv, in agreement with estimates from previous modelling studies varying from 0.1 to 2.6 Sv (Liu et al. 2011, Wang Yan et al. 2019, Fang et al. 2009, Yaremchuk et al. 2009, Xu and Malanotte-Rizzoli 2013, Tozuka et al. 2007, 2014). The simulated outflow is also quite close to observations (2.4 Sv) analysed by Qu and Song (2009), and stronger than in-situ estimates (0.07 Sv) of Sprintall et al. (2012). The seawater at the Mindoro strait flows out of the SCS basin for most of the year, except in June (Figure IV.2a, green line). The strongest outflow occurs in December (4.00 Sv) and flow becomes weaker in summer (0.003 Sv inflow in June). This seasonal cycle of volume transport at the Mindoro strait is quite similar to results of Fang et al. (2005, 2009), Yaremchuk et al. (2009), Liu et al. (2011), Xu and Malanotte-Rizzoli (2013) and Wang Yan et al. (2019) who found a year-round outflow at this channel, intense in winter, and reduced in spring-summer.

In the south of the SCS, the seawater flows out of the basin through the Karimata strait at a rate of 1.00±0.15 Sv following our simulated outputs. This result is in agreement with previous estimates of Karimata outflow by numerical methods, ranging from 0.3 to 2.3 Sv (Fang et al. 2005, 2009, Yaremchuk et al. 2009, Tozuka et al. 2007, 2009, 2014, Wang et al. 2009, Metzger et al. 2010, Liu et al. 2011, Xu and Malanotte-Rizzoli 2013, He et al. 2015, Daryaboy et al. 2016, Wei et al. 2016, Wang Yan et al. 2019), and slightly greater than estimates from measurements (0.50 to 0.74 Sv) recorded during the period 2007 - 2008 (Susanto et al. 2013) and 2008-2015 (Wang Yan et al., 2019). The modeled annual cycle of the Karimata volume transport (Figure IV.2a, magenta line) shows a southward outflow from September to April, and a northward inflow from May to August. Values range from -2.68 Sv in January to 0.94 Sv in June. Previous numerical studies (Fang et al. 2005, 2009, Xue et al. 2004, Yaremchuk et al. 2009, Liu et al. 2011, Xu and Malanotte-Rizzoli 2013, He et al. 2015, Wei et al. 2016, Wang Yan et al. 2019), as well as observational

analysis (Rong et al. 2007, Daryaboy et al. 2016, Susanto et al. 2013, Wang Yan et al. 2019) produced a similar seasonal cycle.

Compared to the four main straits of the SCS, the other two channels of the SCS - Balabac and Malacca straits - have volume transports one order of magnitude smaller than the other straits (Figure IV.1). In the present simulation, water from the Sulu Sea enters the SCS at the Balabac strait, with an annual mean westward flow of 0.11±0.19 Sv. Our estimation is in agreement with the one of 0.1 Sv by Hsin et al. (2012), while Wang et al. (2009) and Liu et al. (2011) estimated very small inflows (0.01 Sv) and Tozuka et al. (2014) suggested a much stronger inflow (0.8 Sv) at this strait. Fang et al. (2005, 2009), in contrast, proposed an eastward (outflow) of respectively 0.061 Sv and 0.41 Sv at this channel. Throughout the year, the flow simulated at Balabac enters into the basin from January to May, and exits the SCS from June to December (Figure IV.2a, blue line). The maximum inflow through Balabac occurs in March (0.88 Sv) and the maximum outflow in October (0.66 Sv). Fang et al. (2005, 2009), on the other hand, obtained an outflow the whole year at this channel. Although there are differences in the direction of Balabac flows following studies, it should be noted that the volume transport at Balabac is at least one order of magnitude smaller than the other interocean transports. Moreover, we obtain a strong interannual variability of transport at this channel, with a standard deviation equal to 167% of the average (Figure IV.1), which can explain those discrepancies.

At the narrowest interocean strait of the SCS, Malacca, water flows out of the SCS toward the Andaman Sea (Indian Ocean) at a rate of 0.07±0.02 Sv in our simulation, which is at the low end of the range of previous estimates (from 0.08 to 0.27 Sv - Metzger et al. 2010, Fang et al. 2009, Liu et al. 2011, Daryaboy et al. 2016). The seasonal cycle at this strait (Figure IV.2a, cyan line) shows that the Andaman Sea receives water from the SCS all over the year (maximum 0.16 Sv in February, minimum 0.02 Sv in May and June) (Figure IV.2a, yellow line), consistently with observations of Fang et al. (2005, 2009).

In a yearly cycle, the volume transport at Balabac strait shows the strongest relative annual variability (Figure IV.2a), with a very high standard deviation relative to the average (0.51 Sv, 421%), followed by Karimata (1.40 Sv, 137%), Taiwan (0.86 Sv, 71%), Mindoro (1.42 Sv, 65 %), Malacca (0.05 Sv, 61%), and Luzon (1.84 Sv, 43%) strait.

IV.1.2 Contributions of atmospheric, river and lateral water fluxes to the SCS budget

The average of net seawater lateral flux exchanged through SCS interocean channels over the period 2009 - 2018 in our simulation is estimated at -0.11±0.03 Sv: the domain overall loses water through these straits. This loss balances the two other input terms: the SCS receives water from rivers and atmosphere, evaluated respectively at 0.04±5e-4 Sv and 0.07±0.03 Sv, i.e. a total freshwater input of 0.11±0.03 Sv. The negative difference between the gain from atmosphere and rivers and the loss from straits, equal to the volume variation, is -1.6e-4±0.007 Sv, equivalent to a decrease of sea level of 1.5e-3±0.07 m $year^{-1}$ over the 2009-2018 period (Figure IV.1). This variation is negligible compared to the total volume input (0.004%) and also to the interannual variability of this variation itself (2%, Figure IV.1). The change of seawater volume and average surface height in our study area during the simulated period is therefore negligible and not significant.

Our value of atmospheric freshwater flux is slightly smaller than estimates of Qu et al. 2006 (0.1 - 0.2 Sv) performed from precipitation and evaporation datasets. Fang et al. (2009) deduced from the land discharges relation of Perry et al. (1996) an annual river flux of 0.05 Sv, close to our yearly river water flux. Using numerical models, Qu et al. (2006), Fang et al. (2009) and Wang Yan et al. (2019) obtained a yearly average of total freshwater flux over the whole SCS respectively of 0.08 Sv (period 1950 - 2003), 0.11 Sv (period 1982 - 2003) and 0.11 Sv (period 2008 - 2015), quite close to our model result. These previous studies assumed a null total lateral volume flux and calculated the total freshwater flux based on the lateral salt budget and the mean salinity of the whole basin.

Figure IV.2b illustrates the 10-year climatological monthly averages of all the water fluxes exchanged between the SCS and surrounding environment in our simulation: the total interocean lateral flux, the total river runoff, the atmospheric flux, and the sum of all three fluxes, which equals the internal water volume variation (Eq. II.4.1). The total lateral flux is positive (lateral inflows > lateral outflows) from January to May and negative (lateral inflows < lateral outflows) the rest of the year. The strongest lateral inflow occurs in March (0.24 Sv) and the strongest outflow in September (-0.41 Sv). On the other hand, atmospheric fluxes are negative during the winter - spring dry season (with a maximum

atmospheric loss in February, -0.06 Sv) when evaporation dominates precipitation. During the summer - autumn rainy season, precipitation becomes abundant, the atmospheric fluxes become positive (maximum value in September 0.18 Sv). The freshwater river flux also increases from May to October during the rainy boreal summer season. The strongest total river runoff occurs in August, with a value equal to 0.09 Sv.

To better understand the role of the SCS in the global and regional water cycle, we analyse the sum of the water fluxes (Figure IV.2b, black curve) exchanged yearly over the domain, equal to the volume variation. In overall, the SCS stores water from January to June (sum of water fluxes, i.e., monthly internal variation, positive, maximum in March and April with 0.21 Sv) and releases water from July to December (sum of water fluxes negative, minimum in October with -0.17 Sv). The correlations between monthly lateral, atmospheric and river fluxes and the total water monthly flux are respectively 0.95 ($p<0.01$), -0.76 ($p<0.01$) and -0.68 ($p=0.02$). Moreover, the standard deviation of the climatological monthly total lateral flux (0.24 Sv) is about 3 times higher than the standard deviation of atmospheric fluxes (0.09 Sv) and 10 times higher than the standard deviation of river fluxes (0.03 Sv). This suggests that over an annual cycle, the monthly variability of the lateral flux dominates the variability of the 2 other fluxes (atmospheric and river) and drives the annual cycle of the SCS water storage. The low variability of river flux compared to lateral and atmospheric fluxes can be partly explained by the use of monthly climatology river runoff for most of rivers in our simulation, especially for huge rivers such as Mekong and Pearl rivers.

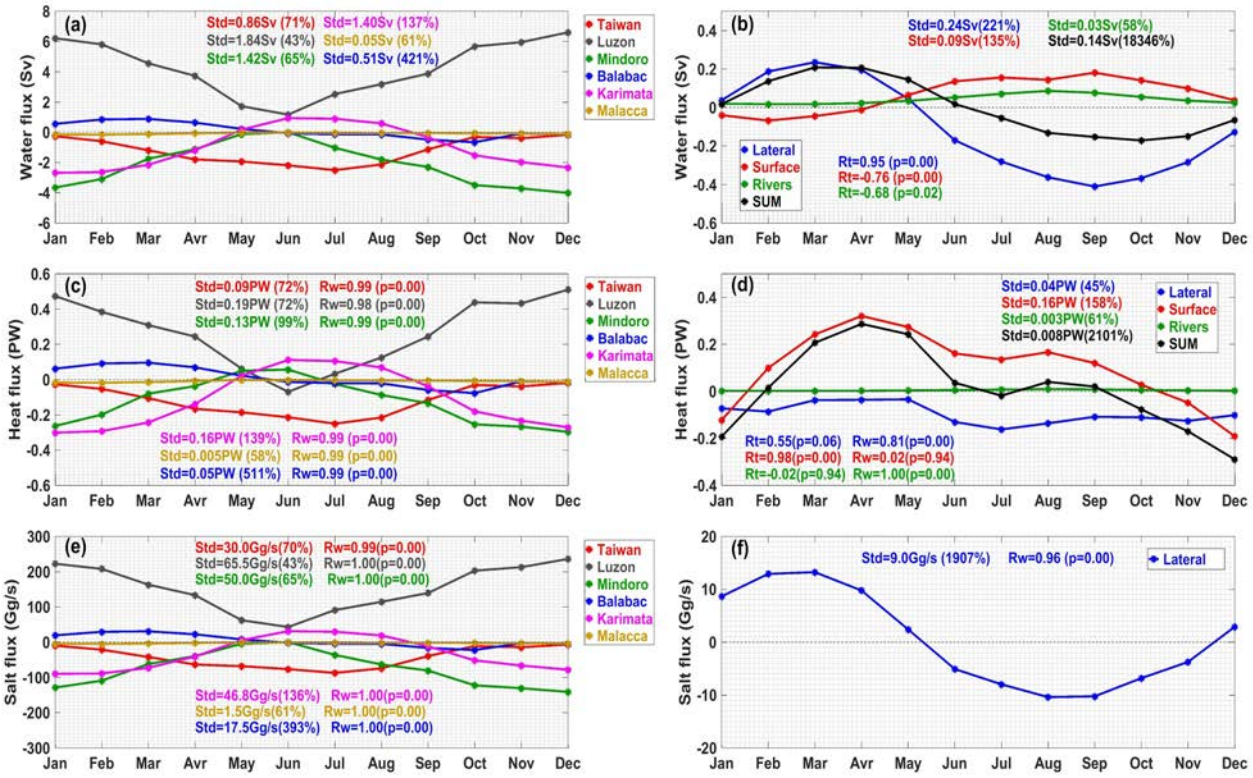

Figure IV.2: 10-year (2009-2018) monthly averages of (a) lateral water transport through each strait, (b) total lateral, river and atmospheric water fluxes and their sum (equal to the monthly internal variation, Eq.1) over the SCS domain, (c) heat fluxes through each strait, (d) total lateral, river and atmosphere fluxes and their sum over the domain, (e) salt fluxes through each strait, (f) total lateral salt flux over the domain. Std, Rt and Rw stand for standard deviation, correlation with the sum of fluxes, correlation with corresponding water fluxes, respectively.

IV.2 Heat fluxes

The simulated yearly averaged heat fluxes exchanged through each strait, through river discharges and at the sea surface, as well as the yearly variations of the heat content, are indicated on Figure IV.1 (in red).

IV.2.1 Lateral heat fluxes at interocean straits

In our simulation, the SCS laterally receives heat from the Pacific Ocean via the Luzon strait (0.265±0.130 PW) and from the Sulu Sea via the Balabac strait (0.010±0.020 PW), and loses heat through the other straits: Taiwan (-0.119±0.007 PW), Mindoro (-0.127±0.114 PW), Karimata (-0.114±0.018 PW) and Malacca (-0.009±0.002 PW). Those results are in agreement with previous results, even if values can differ. Compared to Fang et al. (2005, 2009), Tozuka et al. (2009), Liu et al. (2010), Susanto et al. (2013), Daryaboy

et al. (2016), Wang Yan et al. (2019), our simulated values are quite close to the lower range (0.261-0.373 PW) of their estimates for Luzon heat inflow, slightly smaller than their outflow estimates for Taiwan strait (-0.148-0.2 PW) and Malacca strait (-0.014-0.016 PW), and in their range of estimates for Mindoro (-0.111-0.135 PW) and Karimata (-0.018-0.19 PW) heat outflows. The model simulates an opposite direction of Balabac heat flow compared to Fang et al. (2009, -0.039 PW).

The annual cycle of lateral heat fluxes through different straits, presented in Figure IV.2c, is highly correlated with lateral volume transports cycle (Figure IV.2a), with correlation values of 0.98 ($p<0.01$) for the Luzon strait, and 0.99 ($p<0.01$) for the other straits: for each strait, the seasonal variability of heat flux is strongly related to the variability of volume flux.

Heat flux at the Luzon strait (black line) is westward most of the year except in June: the Pacific Ocean represents a source of heat for the SCS most of the year, with a maximum heat inflow simulated in December (0.51 PW), and a weak flux in spring-summer (in June, the Luzon heat flux becomes an outflow, with value estimated at -0.07 PW). Fang et al. (2005) and Wang Yan et al. (2019) obtained a similar seasonal cycle of heat flux at the Luzon strait.

At the Taiwan strait, the heat flux is negative (northward) all year round (Figure IV.2c, red line), with the strongest intensity in July (-0.25 PW) and a decrease in winter (minimum -0.02 PW in December), in agreement with Liu et al. (2010) and Wang Yan et al. (2019).

Through the southern Karimata border (Figure IV.2c, magenta line), the heat flows out of the basin in autumn, winter and spring, with maximum heat outflow in January and February (-0.30 PW), in agreement with observation of Fang et al. (2010, -0.36±0.08 PW in January - February 2008). In summer, Java sea water mass brings heat to the SCS with a maximum heat inflow in June (0.11 PW). The Karimata seasonal variability of heat flux simulated in our model is consistent with in-situ observations of Susanto et al. (2013), as well as with the numerical studies of Fang et al. (2005), Daryaboy et al. (2016) and Wang Yan et al. (2019).

Heat flux behavior at the Mindoro strait is similar to the one at the Karimata strait: the SCS loses heat in autumn, winter and spring, and gains heat in May and June (Figure IV.2c, green line). The maximum heat outflow at the Mindoro strait is obtained in December (-0.30 PW) and the strongest heat inflow in May (0.06 PW). Wang Yan et al. (2019) obtained a similar heat flux annual cycle, while Fang et al. (2005) obtained an all year-round heat outflow.

At the Balabac strait, heat flux from our simulation is westward from January to May (most intense in March, 0.10 PW), and eastward the rest of the year (maximum outflow in October, 0.08 PW), as presented in Figure IV.2c (blue line).

The SCS releases heat to the Indian Ocean via Malacca strait all year round (Figure IV.2c, orange line) according to our simulation, with strongest intensity in January and February (-0.02 PW) and smallest in June (-0.002 PW), in agreement with Fang et al. (2005), except in July when they obtained a small heat inflow.

Like the water lateral fluxes, the monthly climatological heat fluxes at Balabac channel have the strongest relative seasonal variability (standard deviation = 0.05 PW, i.e 511% of the mean value), followed by Karimata strait (standard deviation = 0.16 PW, 139%), Mindoro (standard deviation = 0.13 PW, 99%), Luzon (standard deviation = 0.19 PW, 72%), Taiwan (standard deviation = 0.09 PW, 72%), and Malacca (standard deviation = 0.005 PW, 58%)

IV.2.2. Atmospheric, river and lateral heat fluxes

Figure IV.2d presents the seasonal cycle of atmospheric heat flux (red line), river heat flux (green line), the total lateral heat flux (blue line) and the sum of these three heat fluxes, equal to the monthly internal variation of SCS heat content (black line and Eq. II.4.2).

In our simulation, the total net lateral flux is negative (-0.095 ± 0.039 PW): the SCS exports heat toward the neighbouring ocean. This loss for the SCS is compensated by a heat gain from the atmosphere (0.100±0.018 PW) and to a much lesser extent (~20 times less) from rivers ($0.005 \pm 5 \times 10^{-5}$ PW). If we consider the sea surface area (3.32×10^{12} m^2), over the period 2009 - 2018, the SCS receives an annual mean heat flux of 30.07±5.42 W m^{-2} from the atmosphere. This estimate is in the range of atmospheric heat flux estimates produced

by models (from 17 to 51 W m^{-2}, Qu et al. 2004, Fang et al. 2009, Wang Yan et al. 2019) or from observations (from 23 to 49 W m^{-2}, Oberhuber 1988, Yang et al. 1999, Yu and Weller 2007). Our results show that the SCS receives heat from the atmosphere almost year-round, except from November to January (Figure IV.2d), consistent with observations of Yang et al. (1999). The intensity of atmospheric heat gain reaches its maximum in spring (0.32 PW) and decreases in summer - autumn. In late autumn/beginning of winter, the SCS releases heat to the atmosphere, with a maximum loss in December (-0.19 PW). The river heat flux is highly correlated to the river freshwater flux (correlation coefficient R=1.00, p-value<0.01), and is maximum in August (0.010 PW) and minimum in February and March (0.002 PW). The seasonal cycle of total lateral heat fluxes is also partly driven by the lateral water fluxes: the correlation between both times series is highly significant (0.81, p-value <0.01).

Finally, over the period 2009 - 2018, in our simulation, atmosphere (and to much lesser extent rivers) bring a total heat flux of 0.105±0.018 PW to the SCS, and 0.096 PW of this heat is released laterally to the East China Sea, the Sulu Sea, the Java and Andaman seas all year round (Figure IV.2d): interocean lateral fluxes therefore contribute to “cool” the SCS area, in agreement with previous conclusions by Fang et al. (2009) and Tozuka et al. (2009). The difference between the “cooling” lateral fluxes and “heating” atmospheric and river fluxes is equal to 0.0095±0.043 PW, corresponding to the average yearly storage of heat in the SCS for the simulated period (2009 - 2018).

The correlation coefficients between the climatological monthly time series of each kind of heat flux (lateral, atmospheric, river) and the time series of the total heat flux are 0.55 (p=0.06), 0.98 (p<0.01) and -0.02 (p=0.94) respectively, with monthly standard deviation of those times series of respectively 0.04 PW, 0.16 PW and 0.00 PW, and 0.18 PW for the sum. These results show that the atmospheric heat flux, and not the lateral and river heat fluxes, drives the seasonal variability of the SCS internal heat content.

IV.3. Salt fluxes

The annual mean of simulated salt fluxes flowing into and out of the SCS basin through interocean straits are illustrated in Figure IV.1 (in green). Salt is brought into the SCS through the Luzon (151.7±53.3 Gg/s) and Balabac (4.2±6.6 Gg/s) straits, and flows out of

the domain through the straits of Taiwan (-43.0±2.5 Gg/s), Mindoro (-76.2±45.9 Gg/s), Karimata (-33.9±5.2 Gg/s) and Malacca (-2.4±0.5 Gg/s). Those results are in agreement with previous studies, even if values can differ: our Luzon inflow and Taiwan and Malacca outflows are slightly smaller than estimates by Fang et al. (2009), Daryaboy et al. (2016) and Wang Yan et al. (2019) (165.0-169.9 Gg/s at Luzon, - 54.4-60.2 Gg/s at Taiwan, - 4.1-5.3 Gg/s at Malacca), while our Mindoro and Karimata outflows are in the upper range of their estimates (- 47.2-74.4 Gg/s at Mindoro, - 5.7-39.3 Gg/s at Karimata) and we obtain an inflow at Balabac while Fang et al. (2009) obtained a 14.1 Gg/s outflow.

For each interocean strait, the simulated seasonal variation of salt fluxes (Figure IV.2e) is completely correlated to the seasonal cycle of volume transport (Figure IV.2a, correlation coefficients of 1.00, $p<0.01$). Salt flows year round into the domain through the Luzon strait (black line). This flux is maximum in winter (236.1 Gg/s in December) and decreases in intensity in summer (43.0 Gg/s in June). In the northern basin, at the Taiwan strait, salt flux exits the basin year round, with a maximum flow rate in summer (-87.1 Gg/s in July) and minimum in winter (-6.5 Gg/s in December). The situation is reversed at the Mindoro strait where the year round outflow becomes maximum in winter (-143.1 Gg/s in December) and reduces in summer (close to zero in June). At the southern gate Karimata, salt flux enters the SCS in summer (maximum inflow 31.1 Gg/s in June) and flows out of the basin in winter (strongest outflow -90.0 Gg/s in January). This later is lower than observations of Fang et al. (2010) at Karimata who obtained a salt flux of -120±30 Gg/s for January - February 2008. At the Balabac channel, salt flux is westward (inflow) the first part of the year (January to May, maximum 29.4 Gg/s in February) and eastward (outflow) the rest of the year (June to December, maximum -22.4 Gg/s in October). Salt flux passing through the Malacca strait is one order of magnitude smaller compared to other straits, and eastward (outflow) all year round. This salt outflow is stronger in winter (maximum -5.1 Gg/s in February) and weaker in summer (minimum -0.6 Gg/s in June).

There is no salt input from the atmosphere and rivers. The time series total monthly salt flux, equal to the monthly variation of SCS internal salt content (Eq. II.4.4), derives only from interocean lateral salt fluxes and is illustrated in Figure IV.2f. From December to May, the total salt flux over the domain is positive (maximum total inflow 13.2 Gg/s in March):

the SCS stores salt during the winter-spring period. From June to November, the total net salt flux becomes negative (maximum total outflow -10.4 Gg/s in August), the SCS is a net source of salt during the summer-autumn period. The seasonal variability of total lateral salt flux / internal SCS salt content is strongly driven by the lateral water flux, with a highly significant correlation (0.96, $p<0.01$, Figure IV.2b).

IV.4. Vertical structure of strait fluxes

We perform an analysis of the vertical distribution of water, heat and salt fluxes at the straits to better characterize those interocean exchanges. Figure IV.3 shows the simulated yearly and seasonal (summer, June to August, and winter, January to March) means climatologically averaged over the period 2009 - 2018 of vertical profiles of volume, heat and salt fluxes at the 6 channels of the SCS.

At the largest and deepest strait of the SCS, the Luzon strait, we simulate a strong seasonal variability of fluxes in the surface and subsurface layers, from 0 to 400 m (Figures IV.3 a,b,c). In the first 50 m, the winter lateral seawater flux is westward (inflow), and the summer one is eastward (outflow), in phase with the atmospheric wind forcing: with northeast monsoon winds in winter and southwest monsoon winds in summer, respectively. This seasonal variability of the surface flow is consistent with observations of Centurioni et al. (2004) obtained from Argo floats data showing an inflow in the upper 15 m from the Pacific to the SCS in winter (October to January), but no inflow in summer. The yearly averaged flux is eastward (outflow) for the upper 50 m. In the 50-700 m layer, summer, winter, and yearly mean fluxes are all westward, with a maximum inflow between 100 and 300 m. Until 400 m depth, inflow is stronger in winter, and weaker in summer. Below 400 m depth, we do not obtain any significant seasonal variability. Our simulation produces an outflow (at each season) between 700 and 1900 m (slightly stronger in winter), then a weak inflow in the deep layer (slightly stronger in summer), from 1900 m until the bottom. Qu et al. (2004), Hsin et al. (2012), Nan et al. (2013, 2015), Liu and Gan (2017) found the same vertical structure of volume transport crossing the Luzon strait, using numerical methods. Li and Qu (2006), using dissolved oxygen distribution data from the World Ocean Atlas (WOA, 2001), also confirmed this sandwiched structure in vertical transports at Luzon. We obtain exactly the same vertical structure for salt flux. The

distribution of heat flux along the water column also follows this “sandwich” structure, but with negligible magnitudes of inflow and outflow in the deep layers below 500 m.

For all other straits, salt and heat fluxes also follow the same vertical structure as the water fluxes.

Through the Taiwan section (Figures IV.3d,e,f) in the northern basin, the yearly mean water, heat and salt fluxes are negative along the whole water column: fluxes flow northward out of the basin from the surface to the bottom. We simulate a strong seasonal variability on vertical distribution of fluxes at this shallow strait, again triggered by the atmospheric forcing. In winter, under the northeast monsoon wind, fluxes flow southward (inflow) in the surface layer (0-10 m), then underneath this depth, fluxes become northwards (outflow). In summer, under the southwest monsoon wind, fluxes are northwards from the surface to the bottom, and particularly strong between 0 and 15 m.

Regarding the strait of Mindoro (Figure IV.3j,k,l) in the east, we simulate a strong seasonal variability of fluxes crossing this transect for the upper 300 m. At layers deeper than 300 m, we observe no significant seasonal variability, vertical distribution is identical for all fluxes, which are negligible below 400 m. In winter, fluxes flow inward in the layer 0-20 m, then outward between 20 and 400 m, with a maximum outflow at around 120 m. In summer, we obtain a “sandwich” vertical distribution like at the Luzon strait, with outflows in the upper layer (0-30 m, maximum at the surface) and in the subsurface layer (130-400 m, maximum near 200-250 m) and an inflow between these two layers (30-130 m, maximum near 60 m). Again, winter westward inflow and summer estward outflow in the surface layer follow the monsoon wind direction. Below 130 m, both winter and summer fluxes flow outward, but with different intensity: the winter outflow is much stronger than the summer one. The annual mean flux is between these two seasonal fluxes, with a small inflow in the first 10 m and an outflow below 10 m, with local maxima at 30 and 180 m depths.

At the shallow Karimata strait, in the southern basin (Figure IV.3g,h,i), the yearly climatological fluxes are southwards (outflow) all depth long. Like for the Taiwan strait, fluxes through the Karimata strait strongly vary with the seasonal monsoon. In summer, under the influence of southwest monsoon winds, fluxes enter the basin above 30 m

depth, then slightly flow out in the deepest layer until 55 m depth. In winter, fluxes are southwards all along the water column, taking seawater, heat and salt out of the SCS. This simulated seasonal variability of vertical fluxes is in agreement with *in-situ* measurements of Fang et al. (2010), who found that the monsoon was the main factor influencing the fluxes at the Karimata strait.

The vertical structure of fluxes across the shallow Balabac strait also connecting the SCS with the Sulu sea also varies strongly with the seasonal cycle (Figure IV.3m,n,o). In winter, the (westward) inflow is maximum at the surface then decreases with depth. From 60 m depth to the bottom, the winter flux becomes slightly negative. The situation is opposite in summer: fluxes flow eastward (outflow) in the surface layer with a decrease with depth until 30 m, then flow westward (inflow) from 30 m depth until the bottom. The annual mean fluxes are negative (outflow) for the upper 20 m, then into the basin until the bottom (with a maximum inflow at 40 m depth).

Fluxes crossing the Malacca strait in the south flow westward (outflow) all year round along the whole water column, with stronger values near the surface, and a decrease with depth, and stronger fluxes in winter (Figure IV.3q,r,s). As the section is very shallow (40 m depth), the monsoon wind again plays an important role in the difference of seasonal fluxes intensity: the northeast wind reinforces the outflow at the Malacca strait in winter, and the southwest monsoon reduces these fluxes in summer.

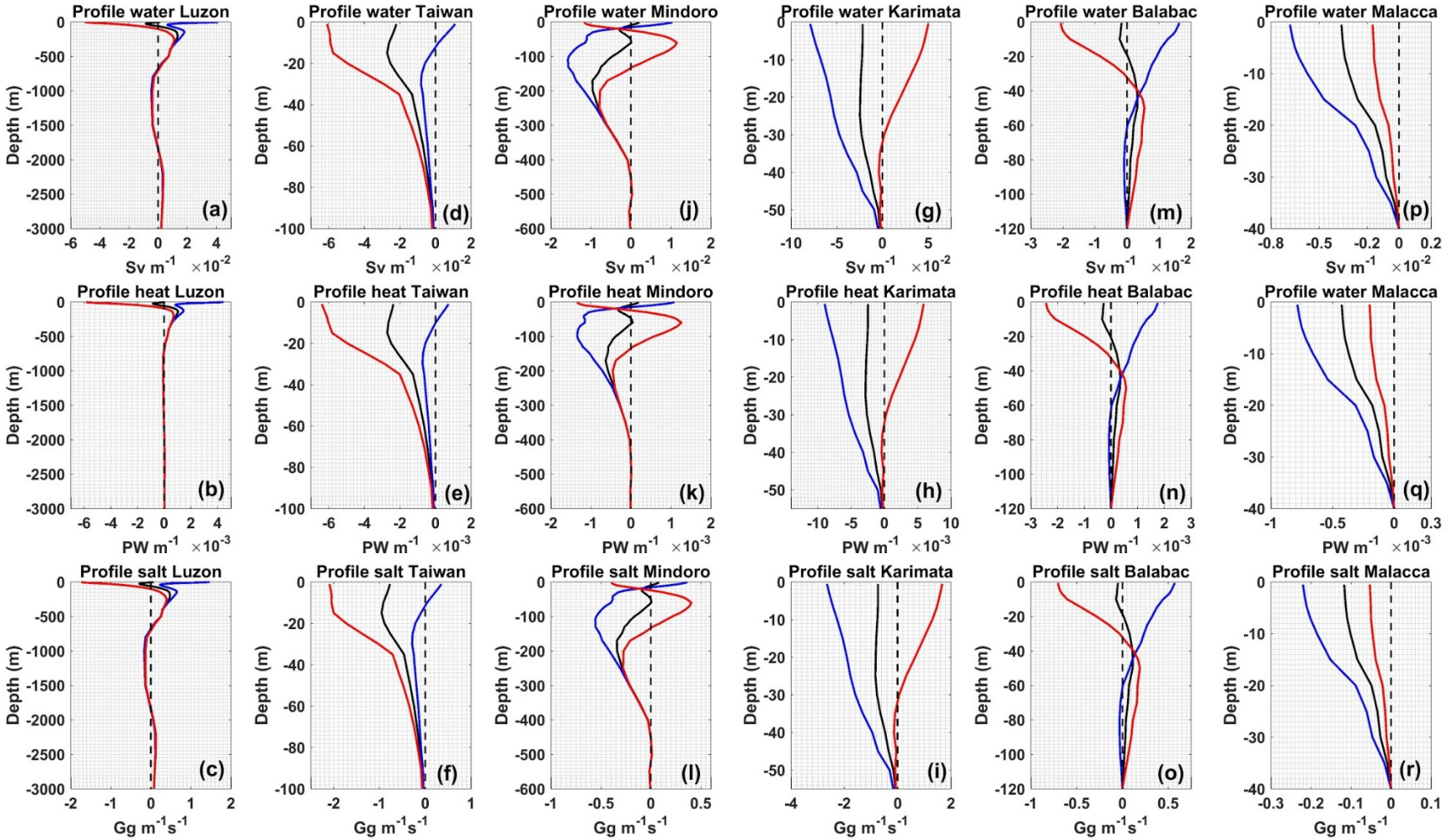

Figure IV.3: Yearly (in black) and seasonal (winter: December, January and February, in blue and summer: June, July, August, in red) climatological averages over 2009-2018 of vertical profiles of water, heat and salt fluxes via the 6 interocean straits. Positive, resp. negative values indicate inflow, resp. outflow. Note that the depth axis varies and is adapted to the depth of the strait.

IV.5. Summary and discussion

The objective of this study was to quantify the contributions of all the terms involved in the volume, heat and salt budget of the SCS (lateral, atmospheric and river fluxes, internal variations) and to characterize their seasonal variability. To our knowledge, this study is the first to produce a consistent, completely closed water, heat and salt budgets analysis based on a high-resolution model. New estimates of the volume, heat and salt transports through interocean straits of the SCS over the 2009-2018 period were established, as well as a quantification of each term of the volume, heat and salt budgets over the whole domain (atmospheric, lateral and river fluxes as well as internal variations) and of their seasonal cycle and vertical distributions. Our study, based on a high-resolution model where water, heat and salt budgets are rigorously closed, therefore provides updated and consistent estimates of all those terms over the 2009-2018 period. Those estimates of atmospheric, river and interocean lateral fluxes of water, heat and salt are in the range of numbers produced by previous numerical and observational studies.

According to our simulation over the period 2009 – 2018, the SCS receives an annual average water input of 4.45±1.35 Sv that mainly flows from the Western Pacific through the Luzon strait (4.23±1.50 Sv, 95%). The contributions from the Sulu Sea through the Balabac strait (0.11±0.19 Sv, 3%), from the atmosphere (0.07±0.03 Sv, 1%) and from river discharges (0.04±0.00 Sv, 1%) represent less than 5% of the total water input. The SCS then releases all of this water (4.45±1.35 Sv) through the other straits: almost half of the water flows to the Sulu Sea through the Mindoro strait (2.16±1.30 Sv, 49%), about one quarter flows northward to the East China Sea via the Taiwan strait (1.22±0.07 Sv, 27%), and another quarter flows southwestward to the Java Sea through the Karimata strait (1.00±0.15 Sv, 22%) and to the Andaman Sea through the Malacca strait (0.07±0.02 Sv, 2%). Following Fang et al. (2009), He et al. (2015), Wei et al. (2016), we take the sum of fluxes through the Mindoro, Balabac, Karimata and Malacca straits to provide an estimate for the volume transport from the SCS into the Indian Ocean, obtaining 3.11±1.48 Sv, i.e. suggesting that 70% of the total water input to the SCS is transferred toward the Indian Ocean.

We then used this simulation to better understand the seasonal cycle of SCSTF and SCS water budgets (Figure IV.2). From February to July, the SCS stores water, with a maximum storage from February to April. This water gain first comes from lateral fluxes (from February to April), mainly through the Luzon strait, then to a lesser extent from rivers and atmospheric freshwater fluxes (from May to July). From August to January, the SCS receives water from the atmosphere and rivers but releases a larger amount of water through lateral fluxes, mostly through the Taiwan, Mindoro and Karimata straits, with a peak outlow in August-September. Except for the Taiwan strait, interocean exchanges for the main inflows and outflows (Luzon, Mindoro and Karimata) are enhanced during the autumn-winter period, from October to February. This SCSTF strengthening can be attributed to the effect of the winter northeast monsoon winds that favor the eastward Luzon inflow and the southward outflows at the Karimata and Mindoro straits. Conversely, fluxes at those straits are weakened from April to September (and even reversed for Karimata between May and August), under the opposite influence of southwest monsoon winds. The situation is the opposite at the Taiwan strait, where the winter northeast monsoon weakens the northward outflow whereas the summer southwest monsoon enhances it. Finally, seasonal variations of SCS water content are completely driven by the lateral water fluxes, and not by rivers and atmospheric freshwater fluxes, which show out of phase and weaker seasonal cycles compared to lateral fluxes. The SCS is indeed a source of water to the atmosphere from January to April (evaporation exceeds precipitation), and a sink from May to December (precipitation exceeds evaporation).

Regarding the salt fluxes, over the 2009-2018 period, the SCS receives in total 155.9±48.4 Gg/s of salt in annual average, mostly from the Western Pacific through the Luzon strait (151.7±53.3 Gg/s, 97%). A very small amount of salt comes from the Sulu Sea through the Balabac strait (4.2±6.6 Gg/s, 3%). More than 99.8% of this salt input (155.5±47.9 Gg/s) is released through the other straits, following the same distribution as for the water fluxes: half of this salt flows through the Mindoro strait into the Sulu Sea (76.2±45.9 Gg/s, 49%), one quarter to the East China Sea via the Taiwan strait (43.0±2.5 Gg/s, 28%), and another quarter to the Java Sea through the Karimata strait (33.9±5.2 Gg/s, 22%) and to a much lesser extent to the Indian Ocean through the Malacca strait (2.4±0.5 Gg/s, 1%). The salt transport from the SCS to the Indian Ocean is thus evaluated at 108.3±52.5 Gg/s, i.e. 70%

of the total salt input. The seasonal cycle of the salt transport is completely correlated with the seasonal cycle of lateral volume transport described above, suggesting that the seasonal variability of salt fluxes and salt content is driven by variations in water volume lateral fluxes rather than by variations in the salinity of the inflowing and outflowing waters.

Over the simulated period 2009-2018 the SCS receives a total heat input of 0.378±0.121 PW annually, mostly from the Western Pacific through Luzon strait (0.265±0.130 PW, 70%) and from the atmosphere (0.100±0.018 PW, 26%), the remaining 4% coming from the Sulu Sea via the Balabac strait (0.010±0.020 PW, 3%) and from river runoff (0.005±0.000 PW, 1%). 98% of this heat gain (0.370±0.118 PW) is released through other interocean straits: about one third flows northward to the East China Sea through the Taiwan strait (0.119±0.007 PW, 32%), another third to the Sulu Sea through the Mindoro strait (0.127±0.114 PW, 35%) and the last third to the Java Sea through the Karimata strait (0.114±0.018 PW, 31%) and to the Andaman Sea via the Malacca strait (0.009±0.002 PW, 2%). Our study therefore confirms the conclusion of Fang et al. (2009) that the SCS plays a “cooling” role in the regional climate by absorbing heat from the Western Pacific, atmosphere and land and releasing it to the Indian Ocean and East China Sea through interocean channels. The heat transport from the SCS toward the Indian Ocean is estimated at 0.240±0.133 PW, i.e. 64% of the total heat input, for the period 2009 – 2018, quite close to the estimation of Fang et al. 2009 (0.279 PW, period 1982 - 2003).

The total lateral heat flux remains negative year round. The SCS stores heat from March to May from atmospheric heat flux. This heat is released from October to January by atmospheric heat loss and via lateral heat outflow, mostly through Mindoro and Karimata straits. During the intermediate season atmospheric heat gain is compensated by lateral heat loss through the Taiwan strait (in February), and the Mindoro and Karimata straits (from June to September). The SCS plays an important role in terms of climate regulating: it is a sink for heat for the atmosphere in spring – summer and a source in winter. We observed for the heat budget seasonal cycle the same influence of seasonal monsoon winds described above for water budget, with a winter strengthening of Luzon heat inflow, and Mindoro and Karimata heat outflows, and a summer weakening (and even a reversal

in June) in summer, and an opposite effect at Taiwan. Finally, differently to what obtained for the water and salt budgets, the seasonal variations of heat content over the SCS is driven by the seasonal cycle of atmospheric fluxes.

The analysis of vertical distributions of annual and seasonal water, heat and salt transport at the different straits provides important information on the circulation in different layers of the SCS and on the effect of seasonal monsoon on these interocean transports. The northeast winter monsoon winds and southwest summer monsoon winds are the main factors driving the direction of lateral fluxes in the upper layer. The winter monsoon reinforces the outflow at Karimata and Malacca straits, strengthens the inflow at Balabac strait and reduces the outflow at Taiwan strait, even inducing a surface inflow in the first 10 m. The situation reverses in summer, when the southwesterly monsoon governs, strengthening the Taiwan outflow, inducing an inflow at Karimata and a surface outflow at Balabac and weakening the Malacca outflow. For deep straits such as Luzon and Mindoro, fluxes in the upper layer are also driven by the reversing monsoonal winds, with a surface summer outflow and a surface winter inflow. But in the deeper layer, monsoon winds are no longer the dominant factor and we obtain an alternance of inflow and outflow along the water column at Luzon all year round and at Mindoro in summer. These results reinforce the conclusions of Gan et al. (2016), Liu and Gan (2017) and Zhu et al. (2017, 2019) about a “sandwiched” circulation in the SCS, with a cyclonic – anticyclonic – cyclonic circulation for the upper – intermediate – deep layers, independent of the season, corresponding to the vertical distribution of the simulated transport at the Luzon strait in our study.

Finally, our simulation suggests that over the period 2009-2018, the SCS does not store water, but stores heat (0.010±0.048 PW, 2.5% of the total input) and salt (0.4±1.1 Gg/s, 0.3% of the total input), equivalent respectively to atmospheric fluxes of 2.9±14.4 W m^{-2} and 3.8±10.6 kg m^{-2} $year^{-1}$, and to temperature and salinity increases of 0.02±0.09 °C $year^{-1}$ and 0.003±0.008 psu $year^{-1}$. Moreover, the annual standard deviation of water, heat and salt variations is very strong, much larger than the climatological average (more than 40 times for water, 5 for heat and 3 times for salt, Figure IV.1), showing that the water, heat and salt cycles in the SCS and the associated SCSTF show a strong interannual variability. This interannual variability of the SCS water, heat and salt contents and sea

surface elevation, temperature and salinity during the 2009-2018 period will be examined more into detail in the next chapter.

Chapter V: Interannual variability of the water, heat and salt budgets

Following the study on the climatological average and seasonal cycle of water, heat and salt budgets over the SCS carried out in Chapter IV, which revealed a strong interannual variability of those budgets, we examine in this chapter this interannual variability by quantifying and investigating the contribution of each term: internal variations, atmospheric, river and lateral fluxes. We analyse in detail the interannual variability of water, heat and salt fluxes through the 6 interocean straits (Taiwan, Luzon, Mindoro, Balabac, Karimata, Malacca) shown on Figure IV.1, Chapter (IV). We also investigate the answer of those different terms of the SCS water, heat and salt budgets to ENSO and PDO climate influences.

V.1. Interocean straits fluxes

Figure V.1a, c, e presents the annual time series of net water, heat and salt fluxes through the 6 interocean straits. Table V.1 summarizes the average, standard deviation and minimum and maximum values of those fluxes for each strait. The vertical distribution of those net annual volume, heat and salt fluxes through the 6 interocean straits from 2009 to 2018 is presented in Figure V.2.

Strait	Average (Figure IV.1 of Chapter IV)	Std (and % of the average value)	Min (corresponding year)	Max (corresponding year)
Luzon	4.2 Sv 0.27 PW 152 Gg/s	1.5 Sv (36%) 0.13 PW (49%) 53 Gg/s (35%)	1.94 Sv (2013) 0.07 PW (2013) 71 Gg/s (2013)	6.45 Sv (2015) 0.47 PW (2015) 231 Gg/s (2015)
Mindoro	-2.2 Sv -0.13 PW -76 Gg/s	1.3 Sv (60%) 0.11 PW (89%) 46 Gg/s (60%)	-0.2 Sv (2013) 0.04 PW (2010) -6 Gg/s (2013)	-1.0 Sv (2015) -0.28 PW (2015) -142 Gg/s (2015)
Taiwan	-1.2 Sv -0.12 PW	0.07 Sv (6%) 0.01 PW (6%)	-1.1 Sv (2011) -0.11 PW (2011)	-1.3 Sv (2009) -0.13 PW (2009)

	-43 Gg/s	2.5 Gg/s (6%)	-39 Gg/s (2011)	-47 Gg/s (2009)
Karimata	-1.0 Sv -0.11 PW -34 Gg/s	0.15 Sv (16%) 0.02 PW (15%) 5.2 Gg/s (16%)	-0.7 Sv (2016) -0.08 PW (2016) -24 Gg/s (2016)	-1.2 Sv (2011) -0.13 PW (2011) -40 Gg/s (2011)
Malacca	-0.1 Sv -0.01 PW -2 Gg/s	0.02 Sv (22%) 0.002 PW (22%) 0.52 Gg/s (22%)	-0.04 Sv (2016) -0.005 PW (2016) -1.3 Gg/s (2016)	-0.09 Sv (2011) -0.01 PW (2011) -3.0 Gg/s (2011)
Balabac	0.1 Sv 0.01 PW 4 Gg/s	0.2 Sv (167%) 0.02 PW (209%) 7 Gg/s (157%)	0.4 Sv (2010) 0.04 PW (2010) 14 Gg/s (2010)	-0.3 Sv (2016) -0.03 PW (2016) -10 Gg/s (2016)

Table V.1: Average values, standard deviations, minimum and maximum values of water, heat and salt net fluxes at 6 interocean straits. Positive values indicate inflows, negative values indicate outflows.

For each strait, the interannual chronology of net heat and salt fluxes over the modeled period is almost identical to the chronology of net water flux, and those time series are highly significantly correlated (significance level higher than 99%, corresponding to a p-value p smaller than 0.01): the correlation with the annual water flux varies between 0.96 and 1.00 ($p<0.01$) for the annual heat flux (Figure V.1c), and between 0.99 and 1.00 ($p<0.01$) for the annual salt flux (Figure V.1e). The interannual variability of net heat and salt fluxes through each interocean strait is therefore mostly driven by the interannual variability of the net water flux.

As obtained at the climatological scale (Chapter IV, Yaremchuk et al. 2009), water, heat and salt mostly flow into the SCS through the Luzon strait and out of the SCS through the Mindoro, Karimata and Taiwan straits (Figure V.1a, c, e). Fluxes through Malacca and Balabac straits are one order of magnitude smaller. Fluxes at Luzon and Mindoro show the higher standard deviation, with absolute values one order of magnitude higher than at the 4 other straits (Table V.1).

Annual net fluxes of water, heat and salt through Luzon strait are always positive (Figure V.1a,c,e). Those inflows have high standard deviations (respectively 1.5 Sv, 0.13 PW and 53 Gg/s, i.e 36%, 49 and 35% of the average values). They vary between minimum values in 2013 (1.94 Sv, 0.07 PW and 71 Gg/s) and maximum values in 2015 (6.45 Sv, 0.47 PW and 231 Gg/s), and are about twice higher on average over 2014 - 2018 (5.44 Sv, 0.37 PW, 195 Gg/s) than over 2009 - 2013 (3.01 Sv, 0.16 PW, 107 Gg/s). The vertical distribution of lateral fluxes through the Luzon strait reflects the same interannual variability as the total vertically integrated flux, especially in the upper layer (~0-700 m depth, Figure V.2a,b,c). Salt flux vertical profiles are extremely similar to water flux profiles, following an alternatively inflow-outflow-inflow sandwiched structure, as already discussed in Chapter IV. Heat flux profiles follow the same structure, though their variability is strong in the 0-700 m layer but much weaker below. Water, heat and salt fluxes in the first 50 m are highly variable, negative (outflow) during years of minimum total inflow (2009, 2010, 2012, 2013, Figure V.1a,c,e), positive (inflow) during years of maximum total inflow (2015, 2016) and alternatively positive in the first meters and negative below for the other years. Between 100 and 700 m depth, fluxes are positive for all years, showing the same variability as the total vertically integrated flux. In the 800 - 1900 m layer, fluxes are negative (outflow) for all years, and in the deep layer below, they are positive for all years. In those layers the variability of water and salt fluxes is weaker than in the upper layer, but non negligible.

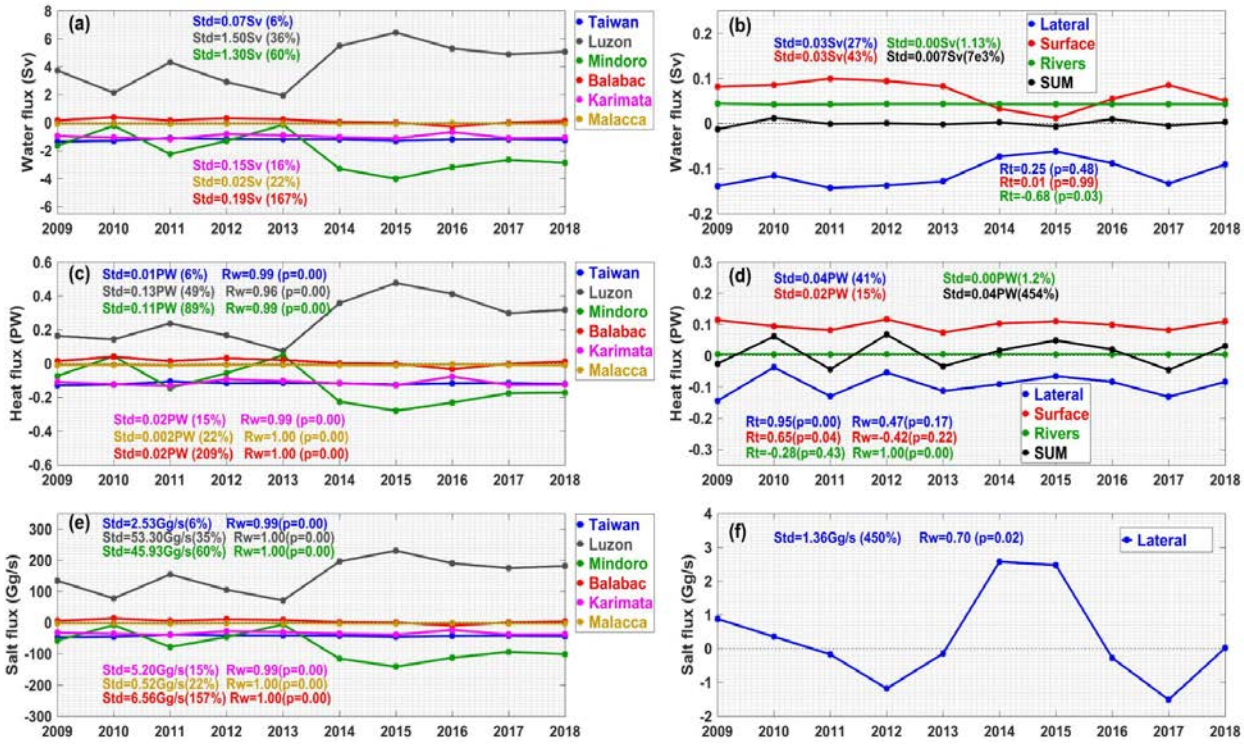

Figure V.1: Time series of the yearly net lateral fluxes of water (a), heat (c) and salt (d) through the six SCS interocean straits, and of the yearly total lateral total lateral, atmospheric and river fluxes of water (b), heat (d) and salt (f) and of their sum over the SCS domain. A positive / negative value corresponds to an inflow /outflow. Std stands for the standard deviation of the time series. Rw stands for the correlation between a time series of heat or salt flux and the time series of the corresponding water flux. Rt stands for the correlation between a time series of total atmospheric, river or lateral flux and the time series of the sum of all fluxes.

At Mindoro, the net depth-integrated water and salt fluxes are always negative (outflow, Figure V.1a, c, e). The net heat flux is however positive in 2010 and 2013, though those net annual heat inflows are one order of magnitude smaller than the heat outflow values obtained for the other years. Outflows at Mindoro strait show a very similar variability to the inflows at Luzon, with standard deviations of 1.3 Sv, 0.11 PW and 46 Gg/s (i.e 60%, 89%, 60% of the average), values varying between a minimum in 2010 and 2013 (0.2 Sv, -0.04 PW (slight inflow), 6 Gg/s) and a maximum in 2015 (4.0 Sv, 0.28 PW, 142 Gg/s), and averages over 2014 - 2018 (3.2 Sv, PW, 113 Gg/s) about three time larger than over 2009 - 2013 (1.1 Sv, PW, 39 Gg/s). For Mindoro strait, as for the 4 other straits (Taiwan, Malaca, Balabac and Karimata), heat and salt fluxes have the same vertical structure as water fluxes (Figure V.2d-o). The vertical distribution of fluxes through the Mindoro strait

in the upper 400m follows the same interannual variability as the total integrated fluxes (Figure V.2g,h,i, Figure V.1a,c,d). In the 0 - 100 m layer this variability is very strong, with entirely inflowing fluxes during years of weaker total outflow (2010, 2012, 2013), entirely outflowing fluxes during years of stronger total outflow (2011, 2014, 2015, 2016), surface (0-30 m) inflow above outflow during two years (2017, 2018), and surface outflow (0 - 40 m) above inflow during 2009. Under 150 m fluxes are negative all the years, with strongest fluxes in 2015 and weakest fluxes in 2010 and 2013. Below 400 m, net fluxes as well as their variability are close to zero.

Total net fluxes at Luzon and Mindoro are almost completely anti-correlated over the studied period (-0.99, $p<0.01$ for water and salt, -0.96, $p<0.01$ for heat, Fig. V.1a,c,e). The variability of the lateral fluxes in or out of the SCS is therefore dominated by the variability of Luzon and Mindoro transports, and the variability of inflows at Luzon are mainly compensated by the variability of outflows at Mindoro.

Transports at Taiwan, Karimata and Malacca straits are always negative (outflows, Figure V.1a,c,e) and their interannual variability is weaker, with standard deviations respectively equal for those 3 straits to ~6%, 15% and 22% of the average values for all fluxes (water, heat and salt). Fluxes through those straits are negative over the whole depth for all years (Figures V.2d,e,f for Taiwan strait; V.2j,k,l for Karimata strait and V.2p,q,r for Malacca strait). Fluxes at Balabac are negligible on average compared to fluxes at Luzon, Mindoro, Taiwan and Karimata straits, but they show a strong relative interannual variability with standard deviations equal respectively to 167%, 209% and 157% of the average values for water, heat and salt fluxes. Moreover, they are alternatively positive (inflow, maximum in 2010 : 0.4 Sv, 0.04 PW, 14 Gg/s, Table V.1) and negative (outflow, maximum in 2016 : -0.3 Sv, -0.03 PW, -10 Gg/s,) with comparable magnitudes (maximal values in 2010 and 2016 (-0.3 Sv, -0.03 PW, -10 Gg/s, Table V.1). Their vertical distribution also shows a strong interannual variability, with alternating positive or negative fluxes depending on layers and years (from completely negative in 2016 to completely positive in 2010, 2012, 2018).

V.2. Interannual variability of water, heat and salt budgets over the SCS

Figure V.1b, d, f shows the annual time series of the internal variations of the SCS water, heat and salt contents, of the total lateral net fluxes of water, heat and salt and of atmospheric and river net fluxes of water and heat. Note that the interannual variability of river freshwater and heat fluxes is negligible (their standard deviation over 2009-2018 is respectively equal to 0.005 Sv and 0.0005 PW, ~1% of the mean value) since most of the river discharges are prescribed from monthly climatological data. Rivers fluxes therefore do not contribute to the interannual variability of water and heat budgets in our study and will not be discussed in the following.

V.2.1. Water budget

On average over the modeled period but also for each year, the SCS receives water from the surface: annual freshwater river and atmospheric fluxes are always positive (Figure V.1b). Most of this water gain is released laterally through the interocean straits (annual water lateral fluxes are always negative), and annual atmospheric and lateral fluxes are highly significantly correlated (0.97, $p<0.01$). The internal variation of SCS water volume, equal to the sum of those fluxes (Eq.II.4.1, Chapter II), remains nearly equal to zero over the studied period, with a standard deviation of 0.007 Sv (less than 1% of the average value, Figure V.1b) negligible compared to the standard deviation of atmospheric and lateral fluxes (0.03 Sv, respectively 43% and 27% of the average value). The total lateral water flux is significantly correlated with Luzon annual inflow and Mindoro annual outflow (respectively 0.67 and -0.67, $p=0.03$), while it is not correlated with fluxes through the 4 other straits ($p>0.13$). The interannual variations of surface water inputs due to atmospheric variability of precipitations and evaporation are therefore compensated by the interannual variations of the total lateral outflow, so that the resulting SCS volume remains nearly constant. A decrease (or increase) in freshwater atmospheric input therefore induces a corresponding decrease (increase) in lateral net outflow, resulting in the conservation of SCS water volume. The variability of this net lateral outflow is mainly associated with the variability of Luzon and Mindoro net fluxes.

From 2009 to 2013, the atmospheric and net lateral water fluxes vary weakly, and are respectively around 0.10 Sv and 0.13 Sv. Their variability is stronger between 2013 and 2018: atmospheric inputs and lateral outputs decrease until a minimum in 2015 (0.01 Sv and 0.06 Sv respectively), increase until 2017 (0.08 Sv and 0.14 Sv) and decrease again (0.05 Sv and 0.08 Sv in 2018). This reduction of total lateral outflow between 2013 and 2017 is associated with an increase of the net Luzon inflow and of the net Mindoro outflow (Figure V.1a). The deficit of surface water input induced by the decrease of precipitation during this period therefore induces an increase of lateral net water inflow at Luzon, which then induces an increase of lateral net water outflow at Mindoro.

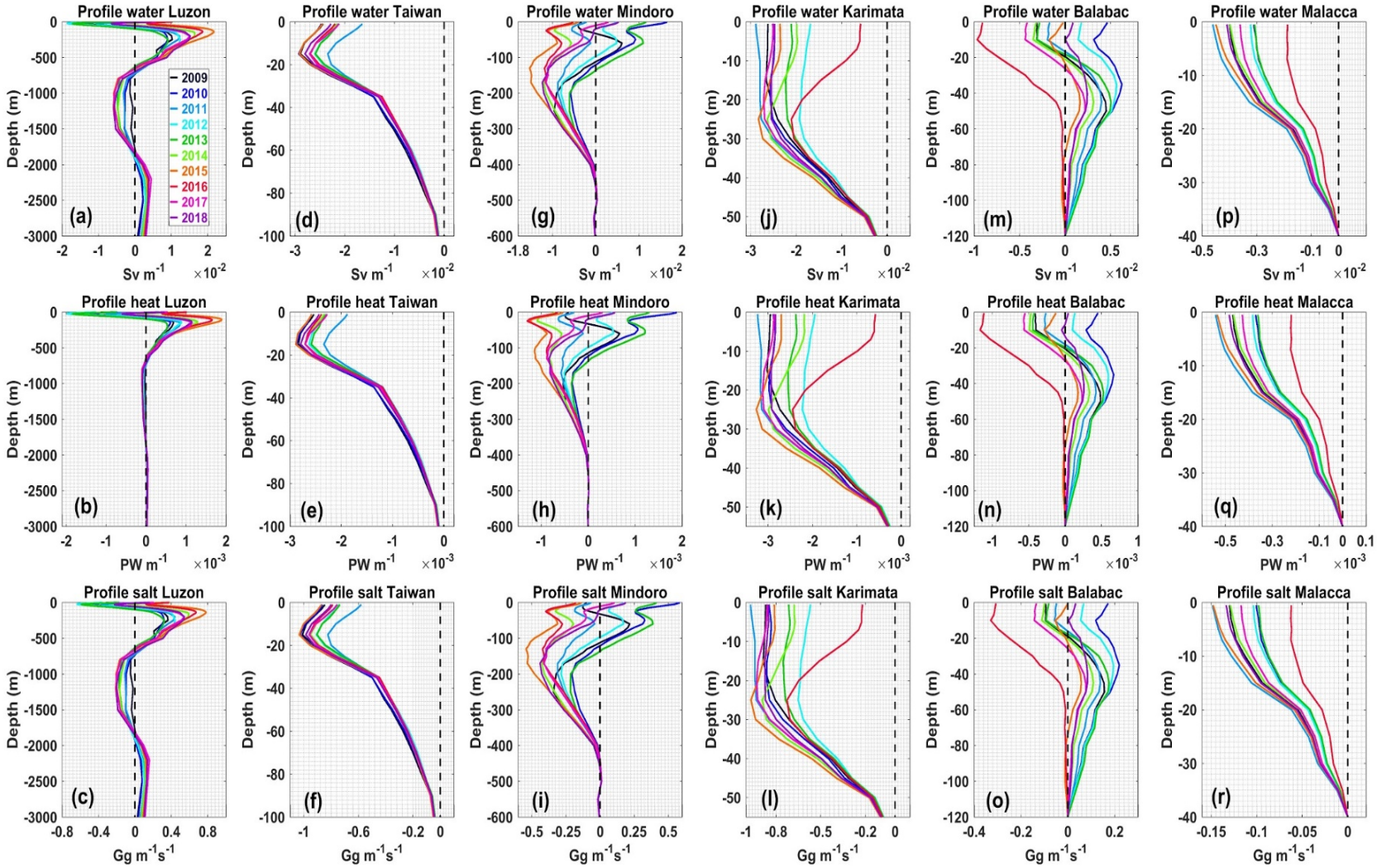

Figure V.2: Annual average of vertical distribution of lateral water, heat and salt fluxes through different straits of the domain over period 2009 - 2018. Positive value = inflow, negative value = outflow. Note that the range of y-axis varies with strait depth.

V.2.2. Heat Budget

Figure V.1d shows the time series of the annual atmospheric, river and total lateral heat fluxes over the SCS and of their sum (equal to the annual internal variation of heat content, Eq.II.4.2, Chapter II). As obtained for the water fluxes, the annual lateral heat flux is always negative over the simulated period while the annual surface (atmosphere + river) flux is always positive: interocean fluxes play a “cooling” role for the SCS, laterally “evacuating” the surface heat gain to neighboring basins. The lateral heat flux varies between a minimum of 0.03 PW in 2010 and a maximum of 0.15 PW in 2011, and has a high interannual variability (its standard deviation over the period is equal to 0.04 PW, i.e. 41% of the mean value). The atmospheric heat flux has a weaker variability (0.02 PW, i.e 15% of the mean value) and varies between a minimum of 0.07 Sv in 2013 and a maximum of 0.13 Sv in 2012.

Contrary to what is observed for the water budget, the annual internal variations of heat content are not negligible (Figure V.1d) and vary between -0.05 PW and +0.06 PW, with a standard deviation of 0.04 PW (454% of the average value), i.e. of the same order as the 0.04 PW and 0.02 PW standard deviation of lateral and atmospheric heat flux respectively. The SCS alternatively stores (in 2010, 2012, 2014 – 2016 and 2018) or releases (in 2009, 2011, 2012, 2017) heat. On average over the period the SCS stores a small amount of heat (0.01 PW, 2.5% of the total input, Chapter IV), but at the annual scale the heat storage or release can be larger. Annual internal variations of SCS heat content are highly significantly correlated with the annual lateral heat flux (0.92, $p<0.01$, Figure V.1d), and not with the atmospheric heat flux ($p=0.13$). The net interocean heat exchange therefore governs the interannual variability of the heat budget of the SCS. Moreover, the annual lateral heat flux is not significantly correlated with the annual lateral water flux ($p=0.17$, Figure V.1d): this suggests that the interannual variability of lateral heat flux through interocean strait is not primarily driven by the variability of lateral water flux, but by the variability of the temperature of lateral outflows and inflows.

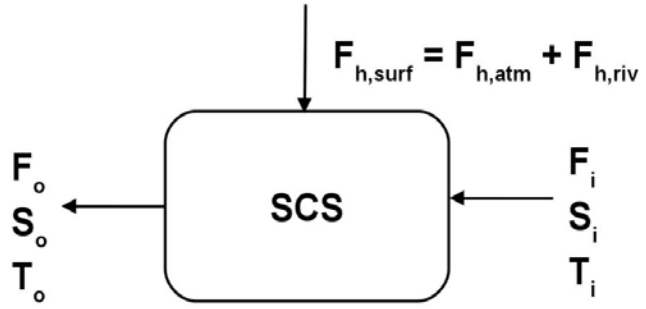

Figure V.3: Schematic representation of box heat and salt budgets over the SCS.

To confirm this hypothesis and better identify which factors drive the variability of the heat and salt budget over the SCS, we perform an analysis based on the time derivative of box budgets (Figure V.3). The heat and salt budgets over the SCS domain during a given period can be written as:

$$\Delta HC = F_i * T_i - F_o * T_o + F_{h,surf} \quad \text{(Eq.V.1)}$$

$$\Delta SC = F_i * S_i - F_o * S_o \quad \text{(Eq.V.2)}$$

where ΔHC and ΔSC are respectively the variations of heat and salt contents of the SCS domain during this period; F_i and F_o the lateral water total inflow and total outflow integrated over this period; S_i, S_o, T_i, T_o the average salinity and temperature of those inflow and outflow; and the surface water and heat fluxes $F_{w,surf}$ and $F_{h,surf}$ are the sum of the atmospheric and river fluxes integrated during this period.

These two equations above could be expressed as follow:

$$\Delta HC = \underbrace{\frac{1}{2}(T_i - T_o)(F_i + F_o)}_{A_H} + \underbrace{\frac{1}{2}(T_i + T_o)(F_i - F_o)}_{B_H} + \underbrace{F_{h,surf}}_{C_H} \quad \text{(Eq.V.3)}$$

$$\Delta SC = \underbrace{\frac{1}{2}(S_i - S_o)(F_i + F_o)}_{A_S} + \underbrace{\frac{1}{2}(S_i + S_o)(F_i - F_o)}_{B_S} \quad \text{(Eq.V.4)}$$

In Eq.V.3 (respectively Eq.V.4), the sum of the 1st (A), 2nd (B) and 3rd (C) terms of the right hand side corresponds to the contribution of the variation of lateral water fluxes to the variation of heat (respectively salt) content internal variation. The term A (A_H for heat and A_S for salt fluxes) corresponds to the contribution of the variation of the temperature (respectively salinity) of lateral inflowing and outflowing water. The term B (B_H for heat and B_S for salt fluxes) stands for the contribution of the variation of the volume of net lateral inflow. The 3rd term (C_H) corresponds to the contribution of the variation of surface heat flux.

To identify which terms drive the interannual variability of the heat budget, we compute the correlation coefficient between each term and the variation of heat budget ΔHC (Figure V.4a). The variation of heat budget is mostly driven by A_H (correlation coefficient R(A_H, ΔHC)=0.94, p<0.01) and the surface heat flux C_H (correlation coefficient R(C_H, ΔHC)=0.65, p<0.05) plays a second order role. B_H does not present a significant correlation with ΔHC. We also plot $\frac{1}{2}\overline{(T_i - T_o)}(F_i + F_o)$, $\frac{1}{2}\overline{(F_i + F_o)}(T_i - T_o)$, $\frac{1}{2}\overline{(F_i - F_o)}(T_i + T_o)$, and $\frac{1}{2}\overline{(T_i + T_O)}(F_i - F_o)$ (Figure V.4a). Results show that $A_H = (T_i - T_o)(F_i + F_o) \simeq (T_i - T_o)\,\overline{(F_i + F_o)}$.

The variability of temperature of lateral inflowing and outflowing water is thus the main driver of A_H. The interannual variability of the heat budget over the studied period is thus mainly driven by the variations of temperature of inflowing/outflowing water, and not by the variations of lateral seawater fluxes.

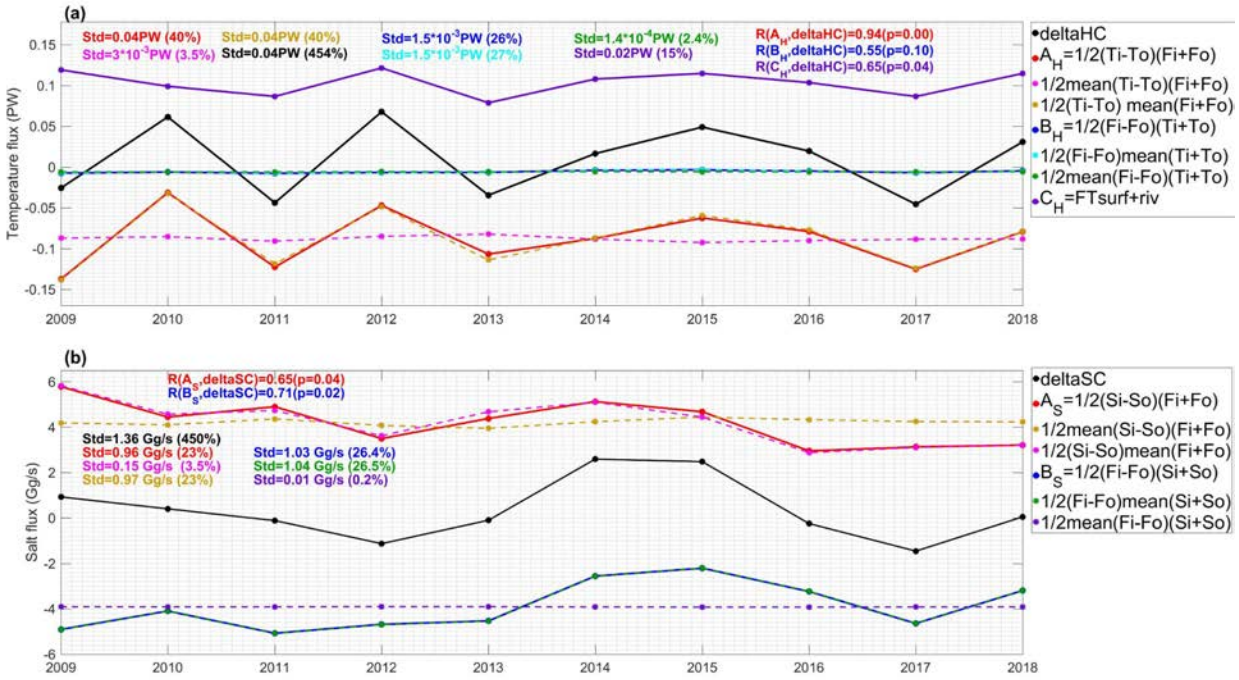

Figure V.4: Internal variations of (a) heat budgets and (b) salt budgets and contributing terms over the whole SCS for the period 2009 - 2018. Std = standard deviation, in the bracket the % of the average value. R= correlation coefficient.

V.2.3. Salt budget

The time series over 2009 - 2018 of the total annual lateral interocean salt fluxes over the SCS, equal to the annual variation of salt content (Eq.II.4.4, Chapter II, no surface salt fluxes) is shown in Figure V.1f. The internal variation of SCS salt content varies much interannually (standard deviation = 1.36 Gg/s i.e. 450% of the mean value), between a minimum negative value of -1.18 Gg/s in 2012 and a maximum positive value of 2.57 Gg/s in 2014. In other words, the basin stores salt in certain years and releases it in other years, though this salt content internal variation is negligible on the climatological average scale (0.4 Gg/s, 0.3% of the total input, Chapter IV). The annual lateral salt flux, equal to the annual salt content variation, is significantly correlated with the annual total lateral water flux (0.70, p=0.02, Figure V.1f). The interannual variability of salt content variation is therefore completely driven by the interannual variability of total lateral salt flux, itself strongly driven by the interannual variability of total lateral water flux. The latter directly results from the interannual variability of surface water flux (section V.2.1). To better

identify which part of the lateral flux drives the interannual variability of the salt content variation, we perform the same box budget analysis as done for the heat (Eq.V.3, V.4).

The correlation coefficients between each term of Eq.V.4 and the annual variation of salt budget ΔSC over the period 2009 - 2018 are $R(A_S,\Delta SC)=0.65$ ($p<0.05$) and $R(B_S,\Delta SC)=0.71$ ($p<0.05$). Those results show that the interannual variability of salt content variation is mainly driven by the variations of B_S and that the variations A_S plays a slightly weaker but non negligible role. We moreover plot $\frac{1}{2}\overline{(S_i - S_o)}(F_i + F_o)$, $\frac{1}{2}\overline{(F_i + F_o)}(S_i - S_o)$, $\frac{1}{2}\overline{(F_i - F_o)}(S_i + S_o)$, and $\frac{1}{2}\overline{(S_i + S_o)}(F_i - F_o)$ (Figure V.4b) : $A_S \simeq (S_i - S_o)\,\overline{(F_i + F_o)}$ and $B_S \simeq (F_i - F_o)\,\overline{(S_i + S_o)}$. A_S is thus driven by the variability of lateral inflowing and outflowing salinity difference. B_S is governed by the variability of net lateral water inflow. Over the period 2009 - 2018, salt content variations over the SCS are therefore driven firstly by the variations of the net lateral water flux (itself compensating variations of the net atmospheric freshwater flux), and second by the variations of difference between inflowing and outflowing water salinities.

We then compute the variations of terms of Eq. V.4 between 2012 and 2015 (period of strong increase of salt content variation, Figure V.1f) and 2015 and 2017 (period of strong decrease):

- $\Delta SC_{2012\text{-}2015}$=3.66 Gg/s, $A_{S,2012\text{-}2015}$=1.18 Gg/s (32%), $B_{S,2012\text{-}2015}$=2.48 Gg/s (68%)
- $\Delta SC_{2015\text{-}2017}$=-3.98 Gg/s, $A_{S,2015\text{-}2017}$=-1.55 Gg/s (39%), $B_{S,2015\text{-}2017}$=-2.43 Gg/s (61%).

The increase of SCS salinity between 2012 and 2015 (Figure V.5a,b) is thus mainly driven by the increase in net lateral sea water inflow (that compensates the atmospheric freshwater flux deficit), and second by the increase in salinity of inflowing water. The decrease between 2015 and 2017 is equivalently related to the decrease in net lateral sea water inflow (related to the atmospheric freshwater flux excedent) and the decrease in inflowing water salinity.

V.4. ENSO/ PDO

Here we study the relationship between interannual variability of volume, heat and salt fluxes and the large-scale climate phenomena ENSO/PDO. For that, we compute the lagged correlation between the yearly fluxes time series and the monthly ONI/PDO indexes over the studied period (Tables V.2, V.3). It is important to note that although our study period is relatively short compared to the PDO periods, it includes a transition period between a cool phase and a warm phase of PDO and this makes it possible to study the link between interannual variability and PDO.

As explained above, river fluxes show a weak (<1%) interannual variability and are therefore never significantly correlated with ENSO or PDO.

For each interocean strait, lateral heat and salt fluxes are highly correlated with the lateral water flux (see section V.1), their response to climate indexes is therefore extremely similar (Table V.2). We obtain significant correlations ($p < 0.05$) between ONI and the net annual water, heat and salt fluxes through Luzon, Mindoro, Balabac, Karimata and Malacca straits. Fluxes through Luzon and Mindoro straits (both strongly related, see section V.1) both show maximum correlations with ONI with a +5 months lag, i.e. ONI in June of the same year (respectively 0.72 and -0.71, $p<0.05$, Table V.2). Fluxes through Balabac, Karimata and Malacca straits show maximum correlations with ONI of respectively previous May (-0.67, $p<0.05$), August (0.65, $p<0.05$) and August (0.81, $p<0.01$). Taiwan fluxes are not significantly correlated with ONI.

The annual atmospheric water flux and the annual lateral water flux (which are strongly related, see 3.2.1) are respectively highly significantly (-0.78, $p<0.01$) and significantly (0.71, $p<0.05$) correlated with ONI in May of the same year. The resulting annual internal volume variation is significantly correlated with ONI in July of the same year (-0.68, $p<0.05$). Lateral heat fluxes and the sum of heat fluxes (equal to internal heat content variations), which are actually related (see 3.2.2), present respectively highly significant (0.79, $p<0.01$) and significant (0.65, $p<0.05$) correlations with ONI of previous December. Atmospheric heat fluxes are only significantly correlated with ONI of December one year before (-0.63, $p<0.05$). The annual lateral salt fluxes, equal to the internal variation of salt

content shows a significant correlation (0.64, p<0.05) with ONI in December of the same year.

Table V.2: Correlation coefficients and time lags between ONI and water, heat, salt fluxes. In the bracket the time lags corresponding in month. The 0 time lag corresponds to January of the same year. Positive / negative time lags indicate correlations with ONI/PDO monthly indexes after / before January of the same year. For a 10 element timeseries the threshold of 95% (p<0.05), respectively 99% significance level (p<0.01) significance level is equal to 0.632 and 0.765.

	Corr Volume flux / ONI			**Corr Heat flux / ONI**			**Corr Salt flux / ONI**		
	Max	***p<0.01***	***p<0.05***	***Max***	***p<0.01***	***p<0.05***	***Max***	***p<0.01***	***p<0.05***
Luzon	0.72 (+4)	-	(+4, +5)	**0.80 (+4)**	(+4)	(+5)	**0.80 (+4)**	-	(+4, +5)
Taiwan	0.57 (-11)	-	-	0.57 (-11)	-	-	0.57 (-11)	-	-
Mindoro	-0.71 (+4)	-	(+4, +5)	-0.70 (+4)	-	(+4, +5)	-0.70 (+4)	-	(+4, +5)
Balabac	-0.67 (-8)	-	(-9, -8, +4)	-0.66 (-8)	-	(-9, -8, +4)	-0.66 (-8)	-	(-9, -8, +4)
Karimata	0.65 (-5)	-	(-5)	0.63 (-5)	-	(-5)	0.63 (-5)	-	(-5)
Malacca	**0.81 (-5)**	(-6 to -4)	(-7, -3 to +2)	**0.81 (-5)**	(-6 to -4)	(-7, -3 to +2)	**0.80 (-5)**	(-6 to -4)	(-7, -3 to +2)
Lateral	0.71 (+4)	-	(+4)	**0.79 (-1)**	(-2 to +1)	(-7 to -3, +2)	0.64 (+11)	-	(+11)
Atmos	**-0.78 (+4)**	**(+4)**	(+5, +8 to +11)	-0.63 (-12)	-	(-12, -11, +9, +10)	-	-	-
Rivers	-0.56 (-9)	-	-	0.50 (+10)	-	-	-	-	-
Sum flux	-0.68 (+6)	-	(+6 to +8)	0.65 (-1)	-	(-1, 0)	0.64 (+11)	-	(+11)

Water, heat and salt fluxes through Luzon, Mindoro, Balabac strait are all highly correlated with PDO, with (highly) significant correlations for lags between -12 and +11 (Table V.3): the PDO conditions of the ongoing years strongly influences annual fluxes through those straits. Fluxes through the other straits are not significantly correlated with PDO.

Both the atmospheric and the total lateral water fluxes are highly significantly correlated with PDO of the same year ($p<0.01$ from January to September for lateral and from July to November for atmospheric). There is no significant correlation between PDO and the other components of the water budget. None of the components of the heat budget are significantly correlated with PDO. The total annual lateral salt flux, equal to the internal variation of salt content, is only significantly correlated with PDO in August (0.77, $p<0.01$).

Table V.3: The same with Table V.2 for PDO.

	Corr Volume flux / PDO			Corr Heat flux / PDO			Corr Salt flux / PDO		
	Max	p<0.01	p<0.05	Max	p<0.01	p<0.05	Max	p<0.01	p<0.05
Luz	**0.81 (-8, +6)**	(-8, +5 to +7)	(-12, -10, -9, -1, 0, +2, +8, +9, +11)	**0.84 (+5)**	(-8, +1, +2, +5, +6)	(-12, -10, -9, -7, -6 to 0, +3, +4, +7, +9, +11)	**0.81 (-8, +6)**	(-8, +5 to +7)	(-12, -10, -9, -1, +2, +8, +9, +11)
Tai	-0.44 (-4, +8)	-	-	-0.47 (-4)	-	-	-0.53 (-4)	-	-
Min	**-0.81 (-8)**	(-8, +6, +7)	(-12, -10, -9, +2, +5, +8, +9, +11)	**-0.82 (-8)**	(-8, +6)	(-12, -10, -9, +2, +5, +7, +9, +11)	**-0.81 (-8**)	(-8, +6, +7)	(-12, -10, -9, +2, +4, +5, +9, +11)
Bal	**-0.84 (-12)**	(-12 to -10, +5)	(-9, -7 to -5, +2 to +4, +6,	**-0.83** (-12)	(-12 to -10, +5)	(-9, -6, -5, +2 to +4, +6, +11)	**-0.85** (-12)	(-12 to -10, +5)	(-9, -7 to -5, +2 to +4, +6,

			+11)						+11)
Kar	0.43 (+10)	-	-	0.43 (+10)	-	-	0.39 (+10)	-	-
Mal	0.39 (+3)	-	-	0.39 (+3)	-	-	0.36 (+3)	-	-
Lateral	**0.83 (+6)**	(0 to +2, +6 to +8)	(-5 to -1, +3 to +5, +9, +10)	0.58 (+1)	-	-	**0.77 (+9)**	(+9)	(+7)
Atmos	**-0.90 (+6)**	(+6 to +9, +11)	(-4, -1 to +2, +5, +10)	0.42 (+9)	-	-	-	-	-
Rivers	-0.50 (+1)	-	-	-0.50 (+1)	-	-	-	-	-
Sum flux	-0.46 (+8)	-	-	0.52 (-4, +1)	-	-	**0.77 (+9)**	(+9)	(+7)

V.5. Discussion and conclusion

In this chapter, we have examined from a rigorously closed-budget simulation performed over the period 2009-2018 with a high-resolution ocean model (4 km, 50 depth layers) the interannual variability of the volume, heat and salt budgets over the SCS. For that we have studied and quantified the contribution of each term to those budgets: internal variations, surface fluxes and lateral interocean fluxes.

For each interocean strait, the interannual variability of lateral net heat and salt fluxes is completely driven by the interannual variability of lateral net water fluxes. Annual inflow at Luzon and outflow Mindoro are highly anti-correlated and dominate the total net lateral transport over the SCS, both in terms of climatological mean and interannual variability.

Average and standard deviation of transports through Karimata, Malacca and Balabac straits over 2009-2018 are one order of magnitude weaker, however the relative interannual variability of fluxes through Balabac is high, with a standard deviation larger than the average value. The high interannual variability also affects the vertical structure of interocean fluxes, through Luzon, Mindoro and Balabac straits. This variability is stronger in the upper part of the water column, and fluxes through those straits can even alternatively be positive or negative in the surface layer (above 100 m) depending on the years. This suggests the difficulty to estimate those fluxes from spatially and/or temporally punctual in-situ observations, but also the need to develop and strengthen long-term in-situ measurements to improve our estimates of those interocean fluxes. Over the period 2009 - 2018, vertical annual fluxes at Luzon strait all follow the alternating inflow-outflow-inflow sandwiched structure for the respectively upper (100 - 700 m), intermediate (700 - 1900 m) and deep (> 2000 m) layers, as discussed in several studies (Qu et al. 2004, Hsin et al. 2012, Nan et al. 2015), and the standard deviation of those fluxes relative to their average is significant even in the deep part of the water column.

Inflow through Luzon and outflow through Mindoro are about twice weaker during the 2009-2013 period than during the 2014-18 period. Using HYCOM reanalysis, Zeng et al. (2018) also observed this positive trend of water intrusion through the Luzon strait during the period 2012 - 2017. This evolution is in phase with the PDO, which shifts from a negative cool phase to a positive warm phase in the beginning of 2014. Conversely, fluxes exchanged (inflow) through Balabac channel reinforce over the PDO negative phase, and reduce under PDO positive phase. Inflow at Luzon and outflow at Mindoro are highly significantly correlated with the PDO while inflow at Balabac is highly significantly anti-correlated with the PDO, with correlation coefficients higher than 0.81 ($p<0.01$). The influence of PDO on interocean fluxes at Karimata and Malacca straits is not significant. Studies on the relationship between PDO and different interocean transport of the SCS are scarce, however Yu and Qu (2013) also found significant correlation between LST and PDO (higher than 0.60, $p<0.05$) by analysing a 62-years (1950-2010) hindcast global ocean circulation model. ENSO, with a marked La Niña period in 2011-2012 and a strong El Niño period in 2015-2016, also impacts interocean fluxes. Annual net water, heat and salt Luzon inflow and Mindoro outflow are indeed significantly ($p<0.05$, coefficients higher

than 0.70) correlated with ONI of the same year. In other words, inflow at Luzon and outflow at Mindoro strait are stronger during El Niño and during the PDO warm phase and weaker right after La Niña events and during the PDO cool phase. This agrees with conclusions from numerical studies of Wang.Y et al. (2006) and Qu et al. (2004) and from wind data and ocean assimilation data analyses of Wang.D et al. (2006) that cover the periods 1981 - 2004, 1982 - 1998, and 1958 - 2004 respectively. They also suggested a close connection between LST and ENSO with stronger LST during El Niño years and weaker LST during La Niña years. ENSO conditions also affect Malacca and Karimata outflows and Balabac inflow, which are significantly anti-correlated with ONI of the previous summer: during the El Niño 2015 - 2016 period, fluxes at Balabac flux change into outflow, and Karimata and Malacca outflows are minimum, while Balabac inflows and Karimata and Malacca outflows are maximum during La Niña 2010 - 2012. Fluxes through Taiwan show a weak interannual variability and no significant answer to ENSO or PDO.

Over the SCS, the interannual variability of the water budget is governed by the annual atmospheric water flux, which is always positive over the SCS (precipitation exceeds evaporation). Variations of atmospheric freshwater input are directly compensated by the variations of lateral outflow, so that the internal SCS water volume hardly varies interannually. The annual time series of modeled SSH over the SCS closely follows observed SSH (Figure III.1e, Chapter III) which confirms the robustness of this result.

Between 2009 and 2013, under the PDO cool phase, the precipitation rate over the SCS is high and reaches its maximum during the 2011 - 2012 La Niña period. It strongly decreases between 2013 and 2015, and during 2014 - 2018, under the PDO warm phase, rainfall is about twice weaker than during 2009 - 2013 and reaches its minimum in 2015 under the additional effect of the strong 2015 - 2016 El Niño event. This rainfall decrease between the negative and positive PDO phases is in agreement with results from Krishnamurthy and Krishnamurthy (2014). This variability of the atmospheric water flux was also observed by Zeng et al. (2018) who observed a decrease of precipitations (shown to be the main factor modulating the atmospheric water flux) from 2014 to the beginning of 2016 by analysing evaporation and precipitation monthly anomalies from OAFluxes and TRMM from 2012 to 2017. The decrease of surface water input between

2013 and 2015 induces a mirror decrease of the net lateral outflow, associated with an increase of Luzon inflow and a decrease of Karimata and Malacca outflows. This suggests a strong combined influence of ENSO and PDO, who are in phase over the studied period (correlation coefficient of 0.60, $p<0.05$), on those components of the water budget. This result is in agreement with conclusions of Krishnamurthy and Krishnamurthy (2014), who showed that the co-occurrence of warm PDO phase and El Niño induces weaker rainfall and the co-occurrence of cold PDO phase and La Niña favors stronger precipitation over southern Asia. Both lateral and atmospheric annual water fluxes are indeed significantly correlated with ONI (correlation coefficient higher than 0.70) and highly significantly correlated with PDO (correlation coefficient higher than 0.80).

The annual internal variation of SCS salt content, equal to the net lateral salt flux, varies much interannually, and the SCS alternatively stores or releases salt over the 2009 - 2018 period. The interannual variability of the salt budget is mainly driven by the variability of the net lateral water flux, itself driven by the variability of atmospheric water input as seen above. The variability of in/outflowing seawater salinity plays a significant but weaker role in modulating the salt budget over 2009 - 2018. ENSO and PDO therefore impact the SCS salinity through their effect on the rainfall in the SCS region: the significant correlation between the SCS salt content variations and the ONI (0.64, $p<0.01$) and PDO (0.77, $p<0.01$) indexes reflects the fact that the variations of SCS salt content are strongly driven by the atmospheric freshwater flux.

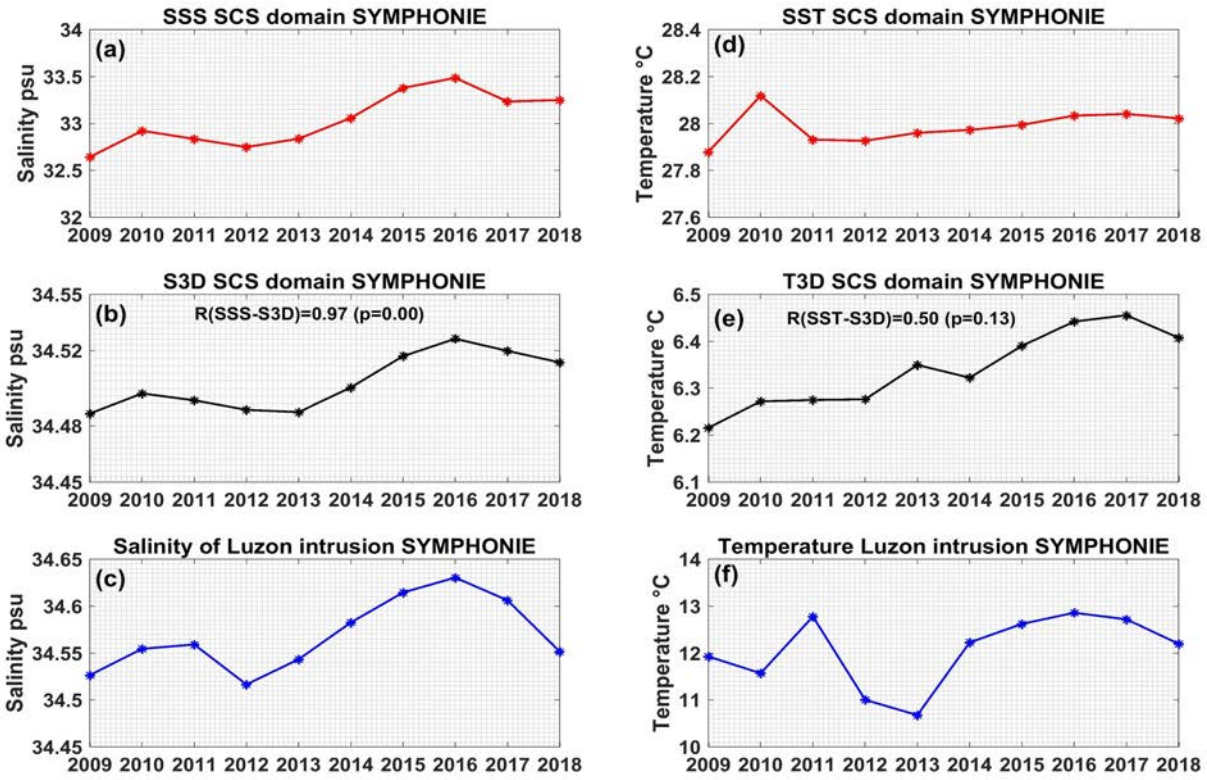

Figure V.5: The model interannual time series (2009 - 2018) over the SCS domain of (a) SSS, (b) Salinity in the whole depth S3D, (c) Salinity of the intrusion at Luzon strait, (d) SST, (e) Temperature in the whole depth T3D, (f) Temperature of the intrusion at Luzon strait.

Analysing satellite and ARGO floats data, Zeng et al. (2018) observed an increase of the SCS SSS between 2012 and 2017. Our simulation is in agreement with those observations, with a strong increase of the annual SSS and whole depth salinity of the SCS between 2012 and 2016 in our model (Figure V.5a, b). The simulated annual SSS and depth-integrated salinity are almost completely correlated (0.97, $p<0.01$), suggesting that the surface and whole depth salinity variations are induced by the same mechanisms. Zeng et al. (2018) pointed out that the combination of a decrease in surface freshwater and an increase in LST with saltier incoming water were the main factors explaining this salinification of the SCS surface. Li et al. (2019) indeed observed an increase of salinity in the upper Western Pacific from 2005 to 2015 attributed to the reduction of precipitation. In agreement with those observations, our simulation takes into account first a decrease of rainfall between 2011 and 2015 that induces a decrease of the total lateral outflow and an increase of Luzon inflow, and second an increase between 2012 and 2016 of the

salinity of water flowing through Luzon strait from the Western Pacific (Figure V.5c). Our budget analysis enables us to confirm and quantify the hypothesis of Zeng et al. (2018): it shows first that the saltening of the SCS between 2012 and 2016 mainly results from the reduction in rainfall freshwater input that was compensated by an increase of salt seawater transport through Luzon from the Western Pacific Ocean, and second that the saltening of the inflowing seawater slightly reinforced this effect but played a secondary role. Moreover, it shows that the decrease of salinity (over the whole depth and the surface) after 2016 was equivalently due to the decrease of net lateral water flux and to the decrease of salinity of the inflowing water.

Over the studied period, the interannual variability of the SCS annual variation of internal heat content is high, and the SCS alternatively stores or releases heat. Contrary to what we obtain for salinity, sea surface temperature (SST) and depth-averaged temperature are not significantly correlated over the studied period (Figure V.5d, e), suggesting that their interannual variability is related to different mechanisms. This is in agreement with results of Xiao et al. (2019) who showed that SCS SST and upper ocean heat content (0 - 300m) computed from SODA during the 1975-2010 period experienced contrasting changes during the 1975-2010 period. They highlighted the role of the SCS ocean circulation in the upper ocean heat content variation, and hypothesized that the Kuroshio intrusion, hence the SCSTF, could also play a role in those variations. Our results on the variability of SCS heat budget over 2009-2018 indeed show that the SCS heat budget is primarily driven by the variability of the total lateral heat flux through interocean straits, itself driven first by the variability of the temperature of the out/inflowing waters. The variability of lateral water flux and surface heat flux plays a weaker though non negligible role. This finding differs from conclusions obtained in Chapter IV regarding the seasonal variability of heat content, which was shown to be driven first by the seasonal variability of the atmospheric heat flux.

The SCS heat budget is affected by ENSO, with a highly significant correlation (0.79, $p<0.01$) between net lateral heat flux (which drives the variability of the SCS heat budget) and ONI and a significant correlation (0.65, $p<0.05$) between the heat content annual variation and ONI, but is not significantly related to PDO. During the 2015 - 2016 El Niño

event, the increase of heat inflow at Luzon strait and the decrease of heat outflow at Karimata and Malacca straits contributed to decrease the SCS lateral heat loss. The modeled ocean heat content becomes positive: the SCS stores heat (Figure V.1d) and the temperature over the whole depth increases over these years (Figure V.5d). This further illustrates the leading role that the SCSTF plays in regulating the heat budget of the SCS. Those results confirm previous conclusions of He et al. (1997) and Qu et al. (2004) who revealed a close relationship between the SCSTF and the upper ocean heat content, as well as the impact of ENSO on the heat budget.

Finally, we obtain a warming trend of the whole water column over the studied period (Figure V.5d). Though this trend does not affect our results about the interannual variability of heat content annual variations (a constant trend disappears in Eq.II.4.2, Chapter II), it will be explored in a future study.

Our numerical analysis of the interannual variability of water, heat salt budgets shows that the atmospheric water fluxes is the dominant governing factor for the water and salt budgets variability over the SCS and more extensively over the Southeast Asia during the 2009-2018 period, while the heat budget variability is driven by the variability lateral heat flux, which is related first to the temperature of the laterally inflowing and outflowing water. Water and salt budgets are strongly influenced by PDO, but also by ENSO, due to their impact on atmospheric rainfall in the area. The heat budget is not related to PDO, but significantly impacted by ENSO.

Chapter VI: Conclusion & Perspectives

The interactions between the SCS ocean dynamics and the surrounding environment (atmosphere, continent, ecosystems, …) have attracted a growing attention of scientists over the last decades, and were the central scientific question of this thesis.

Understanding those interactions requires in particular to better know the role of the SCS in the regional cycle of water, heat and salt. This thesis therefore focused on estimating and understanding the contributions of the different components of the regional climate system (interocean, atmospheric and continental exchanges) to the water, heat and salt budgets of the SCS. Several studies attempted to quantify those components, in particular the interocean fluxes participating into the SCSTF, by both in-situ and satellite observations and numerical methods. The complexity of the SCS topography and the difficulty to implement long-term monitoring data make it difficult to achieve an accurate and exhaustive understanding on these issues using only observations. Numerical approaches can valuably complement that information and are also widely used, but most of the previous studies did not rigorously close the water budget and assumed an equilibrium state. In addition, the contribution of river discharges and atmospheric fluxes into the SCS water, heat and salt budgets were not detailed. This thesis therefore aimed to provide new estimates over a recent period 2009 - 2018 of the SCSTF interocean fluxes, as well as to examine consistently the role of each component the water, heat and salt budgets over the SCS, in climatological averages, seasonal cycle and interannual variability, through a rigorously closed-budget and high-resolution model. Here, we resume the principal results obtained, discuss the limitations of our method and present avenues for future works that should be carried out.

VI.1. Conclusion

VI.1.1. Numerical methods and model evaluation

We have built a high-resolution configuration (4 km in horizontal resolution, 50 depth layers) covering the SCS domain (99-121°E, -0.6-24°N) with an updated bathymetry (fusion of Gebco dataset and the CM93 chart of topography), daily open boundary

conditions from CMEMS-Copernicus and 3-hourly atmospheric forcing ECMWF. The river runoff (63 river mouths) is also taken into account, with daily real-time river discharges for rivers in northern Vietnam and monthly climatological data for the rest. The model also includes tidal forcing (nine barotropic tidal components) issued from FES2014. To our knowledge, this is the first numerical study on the SCS water, heat and salt budgets that takes into consideration such numbers of river mouths, and represents ocean dynamics and tidal impacts at a very high resolution. In addition, the calculation of fluxes and budgets are carried out based on a rigorously-closed budget model, which allows to study consistently the contribution of each component of those budgets.

The simulation performed over the period 2009-2018 is first evaluated by comparing the modeled outputs with satellite and in-situ observations of water masses hydrological characteristics and surface circulation and characteristics. The realism of the simulation outputs in representing the spatial and temporal variability of the SCS circulation and water masses is confirmed quantitatively, revealing weak biases and high spatial and temporal correlations between the model and observations. In terms of seasonal cycle and interannual variability of surface characteristics (SST, SSS, SLA), as well as vertical distribution of temperature and salinity, we obtain high similarity between the model and observational dataset. Under the influences of the alternating monsoon winds, the surface characteristics show a strong seasonal cycle: minimum SST and maximum SLA are observed in winter; maximum SST and minimum SLA are observed in summer; while the SSS reaches its maximum in spring and minimum value in autumn. Interannually, we observe a sea surface warming from 2011 to 2017, a salinification of the annual SSS over 2012 - 2016 and a decrease of SLA in 2014 - 2016, both in the model and in observations.

VI.1.2. Water, heat and salt fluxes and budgets: climatological averages

Flux and budget calculations are carried out using simulation outputs, knowing that all budgets (in water, heat and salt) are rigorously closed. Estimates of surface, river and interocean fluxes of water, heat and salt are in the range of results issued from previous numerical and observational studies. Connecting the SCS with the Pacific Ocean, the Luzon strait is the biggest interocean channel of the SCS and is the main strait conveying fluxes from the Western Pacific into the SCS : it represents 95% of the total 4.45±1.35 Sv

water input to the SCS, 97% of the 155.9±48.4 Gg/s salt input and 70% of the 0.378±0.121 PW heat input. Other sources of water, salt and heat are the Sulu Sea (through the Balabac strait: 3% of the total inputs), the atmosphere (1% of water input and 26% of heat input) and rivers (1% of water and heat inputs). Most of those inputs of water, heat and salt are then released through other interocean straits. The Mindoro strait is the biggest channel of interocean outflow in water and salt (49% of the outputs), then Taiwan (28%) and Karimata (22%). The lateral heat outflow is distributed equally between Mindoro (35%), Taiwan (32%) and Karimata (31%) straits. Less than 2% of the outputs flow through the Malacca strait. As a result, 70% of the total water and salt inputs and 64% of the heat input to the SCS are transferred into the Indian Ocean.

As revealed by Qu et al. (2006), the SCS therefore plays a “conveyor” role in heat and freshwater: it absorbs heat and water inputs from the atmosphere, rivers and the Pacific Ocean then releases these gains through its interocean straits to the other surrounding seas and the Indian Ocean. In particular, the total interocean heat fluxes contribute to “cool” the SCS area, laterally evacuating the 26% of heat gained at the surface from the atmosphere. Over 2009-2018, the SCS does not store water, but stored respectively 0.3% and 2.5% of the total salt and heat inputs, equivalent respectively to net surface fluxes of 3.8±10.6 kg m^{-2} $year^{-1}$ and 2.9±14.4 $W.m^{-2}$, and to salinity and temperature increases of 0.003±0.008 psu $year^{-1}$ and 0.02±0.09°C $year^{-1}$.

VI.1.3. Water, heat and salt budgets: seasonal cycle

The SCSTF as well as the water, heat and salt budgets of the SCS present a strong seasonal cycle, mostly driven by the alternating monsoon winds. Eastward and southward interocean water, heat and salt fluxes exchanged through the straits of Luzon (inflow), Mindoro and Karimata (outflow) are strengthened in autumn-winter (October to February) under the effect of northeast winter monsoon and weakened in spring-summer (April to September) under the effect of southwest summer monsoon. We observe the opposite situation at the Taiwan strait, where the seasonal monsoon winds weaken the northward outflow fluxes weaker in winter and strengthen it in summer. The vertical distributions of seasonal water, heat and salt transports show that the interocean fluxes passing through shallow straits (Taiwan, Karimata, Balabac, Malacca) and the vertical fluxes in the upper

layer of deep channels (Luzon and Mindoro straits) are driven by the monsoon winds, following the mechanism explained above for the vertically average fluxes. In the deeper layer (below 400 m), the monsoon winds are however no longer the dominant factor and we obtain an alternance of inflow and outflow along the water column at Luzon all year round and at Mindoro in summer. These results confirm previous studies of Qu et al. (2004), Hsin et al. (2012), Nan et al. (2013, 2015), Liu and Gan (2017) about a "sandwiched" vertical distribution of the LST: an alternating inflow - outflow - inflow in respectively the upper, intermediate and deep layers.

The SCS gains water from the atmosphere (precipitation exceeds evaporation) from May to November, and loses water (evaporation exceeds precipitation) to the atmosphere from December to April. Overall, the SCS stores water from February to July (maximum storage in spring), and releases water from August to January (outflow peak at August - September). The seasonal variation of water content over the SCS is completely driven by the lateral water fluxes. Similarly, the SCS stores salt from January to May, and releases salt the rest of the year. We obtain a very high correlation between the salt content and the total lateral volume transport, suggesting that the seasonal cycle of salt budget is mainly driven by the lateral volume transport. Unlike the water and salt content, the annual cycle of heat content is mainly modulated by the atmospheric heat flux and not by the lateral volume transport, as revealed by Qu et al. (2004). The SCS stores heat gained from atmospheric heat flux from March to May and releases heat from October to January through atmospheric heat loss and lateral heat outflow. The SCS thus plays an important role in terms of climate regulating: it is a sink for heat for the atmosphere in spring – summer and a heat source in winter.

VI.1.4. Water, heat and salt budgets: interannual variability

At each interocean strait, the interannual variability of lateral net heat and salt fluxes is completely driven by the interannual variability of lateral net water flux. Annual fluxes at the two biggest straits, Luzon (inflow) and Mindoro (outflow), are highly anti-correlated and dominate the total net lateral transports over the domain. Over 2009 - 2018, fluxes through Luzon and Mindoro straits present a high interannual variability. These strong variations are also observed vertically, especially in the upper part of the water column,

where fluxes vary strongly from one year to another. At Luzon strait, under 100 m of depth, the interannual variability is still significant, but in general, fluxes follow the alternating inflow-outflow-inflow sandwiched structure as described above. Transports through Karimata and Malacca straits show weaker interannual variations, both in water column average and over the column, whereas at Taiwan strait, fluxes do not vary much within the years. At Balabac, fluxes are negligible compared to the other straits, however they show a high interannual variability relative to their average value, and can alternatively be positive or negative. Large scale climate phenomena, namely ENSO and PDO, have strong impacts on the interocean fluxes of the SCS. Water, heat and salt fluxes at the two biggest straits (Luzon and Mindoro) show high correlations with ONI (higher than 0.70, $p<0.05$) and PDO (0.81, $p<0.01$) of the same year. Inflow at Luzon and outflow at Mindoro strengthen during El Niño 2015 - 2016 and during PDO warm phase (2014 - 2018). These fluxes weaken right after La Niña 2010 - 2012 and during PDO cool phase (2009 - 2013). The Balabac inflow shows a highly significantly anti-correlated variation with PDO and ENSO: the flow reduces during El Niño/PDO positive phase, and reinforces during La Niña/PDO negative phase. The Karimata and Malacca outflows are not significantly correlated with PDO, but present a high anti-correlated connection with ENSO of the previous summer. These outflows become minimum during El Niño 2015 - 2016 and maximum during La Niña 2010 - 2012. ENSO and PDO have no impacts on Taiwan outflow fluxes.

Concerning the budgets, over the period 2009 - 2018, the SCS does not store or release water but alternatively stores or releases heat and salt. The interannual variability of the water budget is governed by the annual atmospheric water flux (always positive). The increase (decrease) of atmospheric water gain (i.e. of precipitations) is compensated by the increase (decrease) of the total volume lateral loss, so that the internal SCS water volume hardly varies interannually. Both lateral and atmospheric annual water fluxes are significantly correlated with ONI (correlation coefficient higher than 0.70, $p<0.05$) and highly significantly correlated with PDO (correlation coefficient higher than 0.80, $p<0.01$). Over the period 2009 - 2018, the combined effect of ENSO and PDO induces a strong variation of annual atmospheric water gain hence net lateral volume outflow. From 2009 - 2013, under the influence of PDO negative (cool) phase, the precipitation rate over the

SCS is high and reaches its maximum during the 2011 - 2012 La Niña period. The net lateral water outflow is high to compensate for the high atmospheric freshwater gain. During the period 2014 - 2018, under the PDO warm phase, precipitations over the SCS decrease and reach their minimum during the strong 2015 - 2016 El Niño event. To compensate for this deficit of atmospheric freshwater input, the net lateral water outflow decreases, via a strengthened inflow at Luzon strait and reduced outflows at Karimata and Malacca straits.

The interannual variability of the salt budget is driven mainly by the variations of annual net lateral water flux (itself driven by the variability of atmospheric water input), then by the salinity variations of the lateral inflow and outflows. The SCS salt budgets and salt content variations show a significant correlation with ENSO (0.64, $p<0.05$) and PDO (0.77, $p<0.01$) indexes, due to the fact that they are strongly driven by the atmospheric freshwater flux, itself correlated with ENSO and PDO indexes (see above). The modeled SSS shows a salinification of the SCS surface during 2012 - 2016, in accordance with observation of Zeng et al. (2018). The modeled whole depth salinity and the SSS varies very similarly at the interannual scale (correlation value 0.97, $p<0.01$), suggesting that their variations are induced by the same mechanisms. Our analysis of factors contributing to the SCS salt content first confirms the hypothesis proposed by Zeng et al. (2018): the saltening of the SCS between 2012 and 2016 mainly results from the reduction in rainfall freshwater input over the SCS that was compensated by an increase of salt seawater transport through Luzon from the Western Pacific Ocean. Calculations from model outputs moreover allowed us to go deeper in this analysis, showing that this salinification was firstly governed by the increase of inflowing water volume. The saltening of this inflowing seawater slightly reinforced the effect but played a secondary role.

The interannual variability of the SCS heat budget is primarily driven by the variability of the total lateral heat flux through interocean straits, itself driven first by the variability of the temperature of the out/inflowing waters, then by the lateral water flux and the surface heat flux. Contrary to what we obtain for the salinity, the SST and whole depth temperature are not significantly correlated, suggesting that their interannual variability is related to different mechanisms. Unlike the water and salt budgets which are all impacted by ENSO

and PDO, the SCS heat budget is affected only by ENSO. During the 2015 - 2016 El Niño event, the increase of heat inflow at Luzon strait and the decrease of heat outflow at Karimata and Malacca straits contributed to decrease the SCS lateral heat loss, the SCS thus stored heat, its temperature increased. Those results confirm the leading role of the SCSTF in regulating the heat budget of the SCS, in agreement with previous studies of He et al. (1997) and Qu et al. (2004).

To sum up, from a realistic high resolution and rigorously closed-budget modeling, new estimates over a recent period of water, heat and salt fluxes participating into the SCSTF, of the fluxes exchanged through air-sea and continent-sea interactions and of the internal variations are provided. An exhaustive analysis of the climatological averages, seasonal cycle and interannual variations of SCS fluxes and budgets is performed. The SCSTF, strongly affected by the monsoon systems at the annual scale and ENSO/PDO at the interannual scale, plays an essential role in the SCS circulation and climate. By absorbing the water and heat gains from the atmosphere and the Pacific Ocean and releasing them through interocean straits to the surrounding seas and Indian Ocean, the SCSTF participates not only in driving the dynamical characteristics (sea level, temperature and salinity) of the SCS but also in water, heat and salt cycles of the surrounding regional seas and oceans climate. Over a seasonal cycle, the SCSTF volume transport is the main factor driving the seasonal variations of SCS water and salt budgets, whereas the seasonal heat budget is governed by the atmospheric heat gain. On the interannual time scale over the period 2009 - 2018, the atmospheric freshwater net gain (which induces the variability of SCSTF) is the dominant factor governing the water and salt budgets variability over the SCS, while the heat budget variability is driven first by the variability of lateral heat flux, itself driven first by the temperature of in/outflowing water, then of lateral water flux.

VI.2. Limitations and Perspectives

The present study has contributed to improve the knowledge and understanding of the role of SCS ocean dynamics in the Southeast Asian climate in terms of water, heat and salt cycles, at the climatological, seasonal and interannual scales. However, our work shows some limitations that will have to be accounted for in future studies. In this section, we discuss those limitations and the improvements that could/should be undertaken. We

eventually present the perspectives for future works that will/could be developed from this study.

VI.2.1. Long-term in-situ measurements

Although our estimates of SCS interocean fluxes and budgets are computed with a well closed-budget model and all results are in the range of previous studies, it is still difficult to compare in detail those values of the SCS fluxes and budgets with observational data. Previous estimates vary indeed much from one study to another (see section I.4.2.2) in particular due to the fact that those fluxes present a high spatial, seasonal and interannual variability: in-situ measurements performed at punctual stations over limited periods or at low frequency cannot capture this strong temporal and spatial variability. Unfortunately, until present, no long-term monitoring observations have been performed for SCS interocean fluxes, due to the complexity of the climate, topography but also in geopolitical situations of the region. Our study highlights the importance and needs of internationally coordinated long-term and high frequency in-situ measurements of fluxes through interocean straits over the SCS- the only robust way to provide robust estimates that can be used for studying the interaction between the SCS and surrounding regions and validating numerical results.

VI.2.2. Sensitivity studies

Each numerical study provides different estimates of SCS water, heat, salt fluxes and budgets (see section I.4.2.2), both in climatological averages and seasonal cycles. This is due to the differences in methodological choices, in forcing conditions, numerical configurations, studied period, etc. In particular, investigating the sensitivity of our results to the choice of atmospheric, river and lateral boundary forcing will allow us to explore and quantify those different sources of uncertainties in our estimates, to understand the divergences from previous studies, and to examine the robustness of our results to the methodological choice.

VI.2.2.1. Choice of the forcing dataset used

The atmospheric fluxes play a crucial role in the water, heat and salt budget of the SCS. In a seasonal cycle, the atmospheric heat flux modulates the internal variation of heat budget, while in interannual time scale, the net atmospheric water flux governs the water and salt budgets. Estimates of atmospheric net freshwater and heat fluxes vary much from one dataset to another (see section I.2.2). Therefore, the choice of atmospheric forcing might strongly affect the estimate of water, heat and salt budgets over the SCS. It is thus important to evaluate the sensitivity of the model outputs to the use of different atmospheric forcing datasets, e.g. JRA-55 reanalysis (Kobayashi et al. 2015) or NCEP-CFSR (Kalnay et al. 1996, Saha et al. 2010).

The seasonal cycles and interannual variabilities of water and salt budgets are strongly driven by the lateral water flux. In our configuration, the positions of Karimata and Taiwan straits in particular (Figure II.3, Chapter II) are close to the boundary of the models, whereas it is not the case for other key straits (Luzon, Mindoro). The boundary conditions thus might influence the computation of fluxes participating into the SCSTF. Sensitivity tests should be performed using different open boundary conditions, e.g. SODA (Simple Ocean Data Assimilation) reanalysis (Jackett et al. 2006), INDESO (Tranchant et al. 2016), etc.

VI.2.2.2. Improvement in real-time river discharges

The configuration used in this study includes 63 river mouths, with only 11 rivers using daily real-time discharges, the others using monthly climatology data, including major rivers such as Mekong and Pearl rivers. In addition, the river heat flux is deduced from the river temperature, which is taken into account by a cosinusoidal function with a one-year period between at minimum and a maximum value, not by the real-time temperature value. This makes it difficult to precisely clarify the role of river fluxes in the SCS water, heat and salt budgets and in their variability. Simulations performed using long-term real time dataset of river runoff and nutrient concentration, that would provide a global view on the changes of regional river runoff in recent years under impacts of anthropogenic activities (dam construction, freshwater overexploitation, pollution, etc) and climate change (floods, droughts, tropical cyclones, etc), would help to evaluate the effects of these changes.

It is noteworthy that the collection work on real-time river discharges in this region is cumbersome, due to the limited sharing of information between institutes from different countries and the lack of long-term monitoring measurements, especially in nutrient concentrations.

VI.2.2.3. Impact of tides on the SCSTF and SCS budgets

Tidal forcing is particularly important in the SCS, both in the coastal zone and in the deep sea (Li et al. 2006). In shallow shelf, the amplified tidal mixing can strongly impact the mixing in the river mouths (Piton et al. 2020). In the deep basin, following Wang et al. (2017), the dissipation of the well-known internal waves (baroclinic tides) in Luzon strait and SCS modulates the water mass properties and deep circulation features in the SCS, thus impacts the SCSTF. Despite this important role, most of the previous studies on the SCSTF and SCS budgets did not take into account the tidal forcing. The present work is one of the first numerical studies including this important forcing, but we haven't explored its influence during this thesis. It will be interesting to study the effect of tides on the SCSTF and SCS budgets, by comparing the simulation analysed here with a twin simulation performed without tidal forcing, exploring the role of each tidal component.

VI.2.3 Studies of other temporal scales and regions

VI.2.3.1. Impact of short-term extreme events

As discussed in Chapter I, the SCS and Western Pacific are regions most frequented by TCs in the world. On average, 10 TCs pass through the SCS from 1965 to 2005 (Goh and Chan 2010). Analysis of decadal frequency and intensity of the TCs landing in the southern China of Liu and Chan (2020) during the period 1975 - 2018 showed an increase of intense TCs frequency passing through the SCS over period 2012 - 2018. Herrmann et al (2019), on the other hand, have shown, based on forced atmospheric model outputs, that climate change could lead to a decrease in the frequency and intensity of TCs in the region. Heavy winds and rainfall from TCs lead not only to severe disasters but also strongly affect the momentum, heat and water exchanges between the ocean and the atmosphere, thus the water, heat and salt budgets over the whole SCS area. Piton (2019), while analysing the impact of typhoons in the Gulf of Tonkin, has revealed that the TCs

could inverse the summer anticyclonic circulation and reinforce the winter cyclonic circulation over the Gulf, generating daily water fluxes of the same order as the average monthly fluxes. Therefore, it would be highly interesting to evaluate the impacts of short-term extreme events such as TCs on the SCS circulation and on interocean fluxes and budgets.

VI.2.3.2. Decadal variability and climate change

Simulations over the 10-year period (2009 - 2018) showed a close connection between the SCSTF and the water, salt and heat budgets and large-scale interannual (ENSO) and decadal (PDO) climate variabilities. Investigating the answer of SCS budgets to decadal variability and climate change by longer simulations are interesting perspectives to be developed. Long simulations will in particular allow to examine the contribution of SCS interocean fluxes and other components of the budgets on the variability and trends (warming/cooling, saltening/freshening) at larger scale of the SCS and to study the long-term evolution of the role of the SCS in the regional climate system and its answer to climate change.

Besides ENSO and PDO, the SCS is also under the influence of another large-scale phenomenon: the Indian Ocean Dipole (IOD, see Chapter 1). IOD has a major impact on the Indian Ocean monsoon onset and precipitation rate over India, eastern South Africa, southern Australia and Indonesia (Saji et al. 1999, Ashok et al. 2001). This phenomenon also influences the onset of the SCS summer monsoon in neutral ENSO years (Yuan et al. 2008a) and the interannual variation of SLA in the southern SCS (Soumya et al. 2015). It is therefore an interesting future work, to evaluate the impact of IOD as well as its combined effects with ENSO and PDO, not only on the water, heat and salt budgets over the SCS basin, but also on the planktonic pelagic ecosystems.

VI.2.3.3. Study at the whole SEA scale

Our high resolution and closed-budget model could be used over a broader region to study the water, heat and salt budgets of the whole SEA scale, including all the Indonesian straits that play a key role in the transfer of water masses between the Pacific and Indian Oceans (the Indonesian Throughflow, ITF, Gordon et al. 2010). In particular it will be

interesting to explore the interactions between the SCSTF and the ITF, as these two currents are closely related (Tozuka et al. 2007). The study could provide new insights into the connection between the SCSTF and ITF and more generally, the interaction between the Pacific and Indian Oceans. Using a coupled ocean-atmosphere model over the SEA region would furthermore allow to explore more into details, and taking into account air-sea interactions, the cycles of water, heat and salt in the regional SEA climate system. This is an on-going work performed in the framework of the LOTUS International Joint Laboratory and CORDEX-SEA project.

VI.2.4. Impact on ecosystems: coupled physical/biogeochemical model studies

The second objective of this work was to develop a high resolution coupled physical - biogeochemical configuration over the SCS, in order to study the response of the pelagic planktonic ecosystem under the variability of ocean dynamics in different scales. This work was technically implemented during this PhD, but the calibration of the model and analysis of the simulations still require a significant amount of work that will be continued after the framework of this PhD. The description of the biogeochemical model Eco3M-S and of the configuration used for the coupling with the SYMPHONIE hydrodynamic model are detailed in the following Appendix. Results issued from a preliminarily one-year (2016 - 2017) simulation are also discussed. Despite the improvements needed to be made in terms of Chla and nutrient concentrations, the model successfully reproduces the seasonal cycle of biogeochemical characteristics and of planktonic elements in the open sea. This coupled model, after a rigorous calibration and validation, will be used to estimate the interocean fluxes and budgets of nutrients, oxygen and carbon over the SCS, and to study the evolution of SCS planktonic ecosystems under influences of ocean dynamics and of their variability, from the short-term to the long-term time scales (TCs, seasonal cycle, interannual variability, decadal and interdecadal variability).

Conclusion Générale

Les interactions entre la dynamique océanique en SCS et les milieux environnants (atmosphère, continent, écosystèmes, ...) ont attiré un intérêt croissant des scientifiques au cours des dernières décennies, et ont constitué la question scientifique centrale de cette thèse.

La compréhension de ces interactions nécessite en particulier de mieux connaître le rôle de la SCS dans le cycle régional de l'eau, de la chaleur et du sel. Cette thèse s'est donc focalisée sur l'estimation et la compréhension des contributions des différentes composantes du système climatique régional (échanges interocéaniques, atmosphériques et continentaux) aux bilans océaniques d'eau, de la chaleur et du sel en SCS. Plusieurs études ont porté sur l'étude et l'estimation de ces composantes, en particulier des flux interocéaniques participant au SCSTF, à partir des observations in-situ et satellitaires et de méthodes numériques. La topographie complexe de la SCS et la difficulté de mettre en œuvre des programmes de mesures à long terme rendent cependant difficile l'étude précise et exhaustive de cette question à partir uniquement d'observations. Les approches numériques peuvent compléter utilement les observations et ont été largement utilisées, mais la plupart des études précédentes ne fermaient pas rigoureusement le bilan hydrique et faisaient l'hypothèse que l'état était à l'équilibre. En outre, la contribution des rejets fluviaux et des flux atmosphériques dans les bilans hydrique, thermique et halin de la SCS SCS n'a pas été détaillée. Cette thèse visait donc à dresser de nouvelles estimations sur une période récente (2009 - 2018) des flux interocéaniques impliqués dans le SCSTF, ainsi qu'à examiner de manière cohérente le rôle de chaque composante des bilans d'eau, de la chaleur et du sel en SCS, aux échelles climatologique, saisonnière et interannuelle, en mettant en place une configuration à haute résolution d'un modèle océanique où les bilans ont été rigoureusement fermés. Nous résumons ici les principaux résultats obtenus, discutons des limites de ce travail et présentons des pistes pour nos travaux futurs.

Conclusion

Méthodes numériques et évaluation du modèle

Nous avons construit une configuration à haute résolution (4 km en résolution horizontale, 50 niveaux de profondeur) couvrant le domaine SCS (99-121°E, -0,6-24°N) avec une bathymétrie mise à jour (intégrant des données Gebco et des données de cartes topographiques CM93). Le modèle a été forcé aux conditions aux limites ouvertes par les sorties quotidiennes fournies de CMEMS-Copernicus et à la surface atmosphérique par les sorties à 3 heures des analyses ECMWF. Le ruissellement fluvial (63 embouchures de rivières) a également été pris en compte, avec les débits quotidiens réels pour les rivières du nord du Vietnam et des données climatologiques mensuelles pour le reste. Le modèle prend également en compte le forçage de la marée (neuf composantes barotropes de la marée) issu de FES2014. À notre connaissance, il s'agit de la première étude numérique sur les bilans hydrique, thermique et halin de la SCS prenant en compte un tel nombre d'embouchures de rivières, et qui représente la dynamique océanique à très haute résolution. En outre, le calcul des flux et des bilans est effectué sur la base d'un modèle de budget rigoureusement fermé, ce qui permet d'étudier de manière cohérente la contribution de chaque composante de ces budgets.

La simulation, réalisée sur la période 2009-2018, a d'abord été évaluée en comparant les sorties du modèle avec les observations satellitaires et in-situ des caractéristiques hydrologiques des masses d'eau et de la circulation et des caractéristiques de surface. Le réalisme de la simulation en termes de représentation de la variabilité spatiale et temporelle de la circulation et des masses d'eau en SCS est ainsi confirmé quantitativement, révélant de faibles biais et des corrélations spatiales et temporelles élevées entre le modèle et les observations. En termes de cycle saisonnier et de variabilité interannuelle des caractéristiques de surface (SST, SSS, SLA), ainsi que de distribution verticale de la température et de la salinité, nous obtenons une grande similitude entre le modèle et l'ensemble des données d'observation. Sous l'influence des vents de mousson, les caractéristiques de surface présentent un cycle saisonnier fort : les SST maximale and SLA minimale sont observées en été, et vice versa, les SST minimale and SLA maximale sont observées en hiver ; tandis que la SSS atteint son maximum au printemps et sa

valeur minimale en automne. Chaque année, on observe un réchauffement de la surface de la mer entre 2011 et 2017, une salinisation de la SSS annuelle entre 2012 et 2016 et une diminution de la SLA entre 2014 et 2016, tant dans le modèle que dans les observations.

Flux et bilans d'eau, de chaleur et de sel : moyennes climatologiques

Les calculs de flux et de budgets sont effectués de cette simulation, sachant que tous les bilans (en eau, chaleur et sel) sont rigoureusement fermés. Les estimations des flux d'eau, de chaleur et de sel à la surface, dans les rivières et entre les océans se situent dans la fourchette des résultats issus d'études numériques et d'observations précédentes. Reliant la SCS à l'Océan Pacifique, le détroit de Luzon est le plus grand détroit interocéanique de la SCS et est le principal détroit transportant les flux du Pacifique Occidental vers le SCS : il représente 95 % de l'apport total d'eau de 4,45±1,35 Sv, 97 % de l'apport de sel de 155,9±48,4 Gg/s et 70 % de l'apport de chaleur de 0,378±0,121 PW. Les autres sources d'eau, de sel et de chaleur sont la mer de Sulu (par le détroit de Balabac : 3 % des apports totaux), l'atmosphère (1 % de l'apport en eau et 26 % de l'apport en chaleur) et les rivières (1 % des apports en eau et en chaleur). La plupart de ces apports d'eau, de chaleur et de sel sont ensuite libérés par d'autres détroits interocéaniques. Le détroit de Mindoro est le plus grand canal de sortie interocéanique d'eau et de sel (49% des sorties), suivi de Taïwan (28%) et de Karimata (22%). L'écoulement latéral de chaleur est réparti à parts égales entre Mindoro (35 %), Taïwan (32 %) et Karimata (31 %). Moins de 2 % des flux sortants passent par le détroit de Malacca. Au final, 70 % des apports totaux d'eau et de sel et 64 % des apports de chaleur à la SCS sont transférés vers l'Océan Indien.

Comme l'ont révélé Qu et al. (2006), la SCS joue donc un rôle de "transporteur" de chaleur et d'eau douce : elle absorbe la chaleur et les apports d'eau de l'atmosphère, des rivières et de l'Océan Pacifique puis les libère par les détroits interocéaniques vers les autres mers environnantes et l'Océan Indien. En particulier, les flux thermiques interocéaniques totaux contribuent à "refroidir" la région de la SCS, en évacuant latéralement les 26 % de chaleur gagnés à la surface à l'atmosphère. Sur la période 2009-2018, la SCS n'a pas stocké d'eau, mais a stocké respectivement 0,3 % et 2,5 % des apports totaux de sel et de chaleur, ce qui équivaut respectivement à des flux nets en surface de 3,8±10,6 kg m^{-2}

an^{-1} et 2,9±14,4 $W.m^{-2}$, et à une augmentation de salinité et de température de 0,003±0,008 psu an^{-1} et 0,02±0,09°C an^{-1}.

Bilans d'eau, de la chaleur et du sel : cycle saisonnier

Le SCSTF ainsi que les bilans hydrique, thermique et salin de la SCS présentent un fort cycle saisonnier, principalement dû à l'alternance des vents de mousson. Les flux interocéaniques d'eau, de chaleur et de sel échangés par les détroits de Luzon (entrée), Mindoro et Karimata (sortie) vers l'est et le sud sont renforcés en automne-hiver (octobre à février) sous l'effet de la mousson d'hiver du nord-est et affaiblis au printemps-été (avril à septembre) sous l'effet de la mousson d'été du sud-ouest. On observe la situation inverse au niveau du détroit de Taïwan, où les vents de mousson saisonniers affaiblissent les flux sortants vers le nord en hiver et les renforcent en été. Les distributions verticales des transports saisonniers d'eau, de chaleur et de sel montrent que les flux interocéaniques passant par les détroits peu profonds (Taïwan, Karimata, Balabac, Malacca) et les flux verticaux dans la couche supérieure des canaux profonds (détroits de Luzon et de Mindoro) sont pilotés par les vents de mousson, suivant le mécanisme expliqué ci-dessus pour les flux verticaux moyens. Dans la couche plus profonde (en dessous de 400 m), les vents de mousson ne sont cependant plus le facteur dominant et nous obtenons une alternance d'entrées et de sorties le long de la colonne d'eau à Luzon toute l'année et à Mindoro en été. Ces résultats confirment les études précédentes de Qu et al. (2004), Hsin et al. (2012), Nan et al. (2013, 2015), Liu et Gan (2017) qui révèlaient une distribution verticale "en sandwich" du LST : une alternance flux entrants - flux sortants - flux entrants respectivement dans les couches supérieures, intermédiaire et profonde.

La SCS gagne de l'eau provenant de l'atmosphère (les précipitations dépassent l'évaporation) de mai à novembre, et en perd (l'évaporation dépasse les précipitations) de décembre à avril. Dans l'ensemble, la SCS stocke de l'eau de février à juillet (stockage maximum au printemps), et en libère d'août à janvier (pic en août - septembre). La variation saisonnière du contenu en eau de la SCS est entièrement déterminée par les flux d'eau latéraux. De même, le SCS stocke du sel de janvier à mai et en libère le reste de l'année. Nous obtenons une corrélation très élevée entre le contenu en sel et le

transport volumique latéral total, ce qui suggère que le cycle saisonnier du bilan en sel est principalement déterminé par le transport volumique latéral. Contrairement au contenu en eau et en sel, le cycle annuel du contenu thermique est principalement modulé par le flux de chaleur atmosphérique et non par le transport volumique latéral, comme l'ont aussi suggéré Qu et al. (2004). La SCS stocke la chaleur obtenue à partir du flux de chaleur atmosphérique de mars à mai et libère de la chaleur d'octobre à janvier via la perte de chaleur atmosphérique et le transport de chaleur latéral. La SCS joue donc un rôle important en termes de régulation du climat : c'est un puits de chaleur pour l'atmosphère au printemps - été et une source de chaleur en hiver.

Bilans d'eau, de la chaleur et du sel : variabilité interannuelle

A chaque détroit, la variabilité interannuelle des flux nets latéraux de chaleur et de sel est entièrement pilotée par la variabilité interannuelle des flux nets latéraux d'eau. Les flux annuels des deux plus grands détroits, Luzon (entrée) et Mindoro (sortie), sont fortement anti-corrélés et dominent le total des transports latéraux nets sur le domaine. Sur la période 2009 - 2018, les flux à travers les détroits de Luzon et de Mindoro présentent une forte variabilité interannuelle. Ces fortes variations sont également observées verticalement, en particulier dans la partie supérieure de la colonne d'eau, où les flux varient fortement d'une année à l'autre. Dans le détroit de Luzon, en dessous de 100 m de profondeur, la variabilité interannuelle est toujours importante, mais en général, les flux suivent la structure en sandwich décrite ci-dessus. Les transports par les détroits de Karimata et de Malacca présentent des variations interannuelles plus faibles, à la fois le long de la colonne d'eau et en valeur intégrée, et au détroit de Taïwan, les flux varient très peu. À Balabac, les flux sont négligeables par rapport aux autres détroits, mais ils présentent une forte variabilité interannuelle par rapport à leur valeur moyenne, et peuvent être positifs ou négatifs. Les phénomènes climatiques à grande échelle, à savoir ENSO et la PDO, ont une forte influence sur les flux interocéaniques en SCS. Les flux d'eau, de chaleur et de sel dans les deux plus grands détroits (Luzon et Mindoro) présentent une forte corrélation avec ENSO (supérieure à 0.70, $p<0.05$) et la PDO (0.81, $p<0.01$) de la même année. Les flux entrants à Luzon et les flux sortants à Mindoro s'affaiblissent pendant la phase froide de PDO (2009 - 2013) et en particulier juste après

La Niña 2010 - 2012, et se renforcent pendant la phase chaude de la PDO (2014-2018) et en particulier pendant le El Niño 2015-2016. Le flux à Balabac présente est très significativement anticorrélé avec la PDO et ENSO : il diminue pendant les périodes El Niño et phase positive de PDO et se renforce pendant les périodes La Niña et phase négative de PDO. Les flux sortants à Karimata et Malacca ne sont pas significativement corrélés avec la PDO, mais présentent une forte anti-corrélation avec l'indice ENSO de l'été précédent. Ces sorties sont minimales pendant El Niño 2015 - 2016 et maximales pendant La Niña 2010 - 2012. L'ENSO et la PDO n'ont aucun impact sur les flux sortants à Taïwan.

En ce qui concerne les budgets, sur la période 2009-2018, la SCS ne stocke ou ne libère pas d'eau d'une année à l'autre, mais stocke ou libère de la chaleur et du sel. La variabilité interannuelle du budget d'eau est régie par le flux d'eau atmosphérique annuel, toujours positive (gain). L'augmentation (la diminution) du gain d'eau atmosphérique (c'est-à-dire des précipitations) est compensée par l'augmentation (la diminution) de la perte latérale totale, de sorte que le volume d'eau interne d'eau en SCS ne varie pratiquement pas d'une année à l'autre. Les flux annuels d'eau latéraux et atmosphériques sont corrélés de manière significative avec ENSO (coefficient de corrélation supérieur à 0.70, $p<0.05$) et de manière très significative avec la PDO (coefficient de corrélation supérieur à 0.80, $p<0.01$). Sur la période 2009 - 2018, l'effet combiné d'ENSO et de la PDO induit une forte variation du gain atmosphérique annuel d'eau, donc de la perte latérale d'eau. De 2009 à 2013, sous l'influence de la phase négative (froide) de la PDO, le taux de précipitation en SCS est élevé et atteint son maximum durant la période La Niña 2011 - 2012. La perte latérale nette d'eau est élevée pour compenser le gain élevé atmosphérique d'eau douce. Pendant la période 2014-2018, lors de la phase chaude de la PDO, les précipitations en SCS diminuent et atteignent leur minimum pendant le fort épisode El Niño de 2015-2016. Pour compenser ce déficit d'apport atmosphérique d'eau douce, la perte latérale nette d'eau diminue, via un renforcement de l'apport dans le détroit de Luzon et une réduction du débit sortant dans les détroits de Karimata et de Malacca.

La variabilité interannuelle du bilan salin est principalement pilotée par les variations de la perte latérale nette annuelle d'eau (elle-même déterminée par la variabilité du gain d'eau atmosphérique), puis par les variations de salinité des eaux entrantes et sortantes. Les bilans salins et les variations du contenu en sel en SCS présentent une corrélation significative avec les indices ENSO (0.64, $p<0.05$) et PDO (0.77, $p<0.01$), du fait qu'ils sont fortement influencés par le flux d'eau douce atmosphérique, lui-même corrélé avec les indices ENSO et PDO (voir ci-dessus). La SSS modélisée montre une salinisation de la surface de la SCS entre 2012 et 2016, en accord avec les observations de Zeng et al. (2018). Dans le modèle, le contenu salin et la SSS varient de manière très similaire à l'échelle interannuelle (valeur de corrélation 0.97, $p<0.01$), ce qui suggère que leurs variations sont induites par les mêmes mécanismes. Notre analyse des facteurs contribuant à la variabilité du contenu en sel de la SCS confirme tout d'abord l'hypothèse proposée par Zeng et al. (2018) : la salinisation de la SCS entre 2012 et 2016 résulte principalement du fait que la réduction de l'apport d'eau douce pluviale sur la SCS pendant cette période a été compensée par une augmentation d'entrée d'eau de mer salée par Luzon depuis le Pacifique Ouest. Les calculs effectués à partir des sorties du modèle nous ont de plus permis d'approfondir cette analyse : ils montrent que cette salinisation est d'abord régie par l'augmentation du volume d'eau entrant, et que l'augmentation de la salinité de l'eau entrante à Luzon renforce légèrement cet effet mais au second ordre.

La variabilité interannuelle du bilan thermique de la SCS est principalement due à la variabilité du flux thermique latéral total (toujours négatif) à travers les détroits interocéaniques, lui-même déterminé d'abord par la variabilité de la température des eaux sortantes/entrantes, puis dans une moindre mesure par le flux d'eau latéral et le flux thermique de surface. Contrairement à ce que nous obtenons pour la salinité, le contenu thermique total et la SST ne sont pas significativement corrélées, ce qui suggère que leur variabilité interannuelle est régie par des mécanismes différents. Contrairement aux bilans d'eau et de salinité, tous deux influencés par ENSO et la PDO, le bilan thermique de la SCS n'est influencé que par ENSO. Pendant l'épisode El Niño de 2015-2016, l'augmentation de l'apport de chaleur dans le détroit de Luzon et la diminution de l'évacuation de chaleur dans les détroits de Karimata et de Malacca ont contribué à diminuer la perte de chaleur latérale en SCS, la SCS a donc stocké de la chaleur, sa

température a augmenté. Ces résultats confirment le rôle prépondérant du SCSTF dans la régulation du bilan thermique du SCS, en accord avec les études précédentes de He et al. (1997) et Qu et al. (2004).

En résumé, à partir d'un modèle réaliste à haute résolution et à bilans rigoureusement fermés, de nouvelles estimations sur une période récente des flux d'eau, de chaleur et de sel participant au SCSTF, des flux échangés par les interactions air-mer et continent-mer, et des variations internes sont fournies. Une analyse exhaustive des moyennes climatologiques, du cycle saisonnier et des variations interannuelles des flux et des budgets est effectuée à l'échelle de la SCS. Le SCSTF, fortement affecté par les systèmes de mousson à l'échelle annuelle et l'ENSO/PDO à l'échelle interannuelle, joue un rôle essentiel dans la circulation et le climat de la SCS. En absorbant les gains dl'eau et de chaleur de l'atmosphère et de l'Océan Pacifique, puis en les libérant par les détroits interocéaniques vers les mers environnantes et l'Océan Indien, le SCSTF participe non seulement à la détermination des caractéristiques dynamiques (niveau de la mer, température et salinité) de la SCS, mais aussi aux cycles de l'eau, de la chaleur et du sel des mers et océans et du climat régional environnants. Sur un cycle saisonnier, le transport lateral de volume d'eau (donc le SCSTF) est le principal facteur qui détermine les variations saisonnières des bilans hydrique et salin de la SCS, alors que le bilan thermique saisonnier est régi par le flux de chaleur atmosphérique. A l'échelle interannuelle pour la période 2009-2018, le gain net d'eau douce atmosphérique (qui induit la variabilité du SCSTF) est le facteur dominant qui régit la variabilité des bilans d'eau et de sel en SCS, tandis que la variabilité du bilan thermique est d'abord déterminée par la variabilité du flux thermique latéral, elle-même déterminée d'abord par la température de l'eau entrante et sortante, puis par le flux latéral d'eau.

Limites et perspectives

Cette étude a contribué à améliorer la connaissance et la compréhension du rôle de la dynamique océanique en SCS dans le climat d'Asie du Sud-Est en termes de cycles de l'eau, de chaleur et de, aux échelles climatologique, saisonnière et interannuelle. Cependant, notre travail présente certaines limites dont il faudra tenir compte. Dans cette section, nous discutons ces limites et les améliorations qui pourraient ou devraient être

apportées. Enfin, nous présentons les perspectives des travaux futurs qui seront ou pourraient être développés à partir de cette étude.

Mesures in-situ à long terme

Bien que nos estimations des flux et des bilans interocéaniques en SCS soient calculées avec un modèle à budget rigoureusement fermé et que tous les résultats se situent dans la gamme des études précédentes, il est encore difficile d'évaluer en détail ces valeurs des flux et des bilans de la SCS à partir des données d'observation. Les estimations précédentes varient en effet beaucoup d'une étude à l'autre (voir section I.4.2.2), notamment parce que ces flux présentent une forte variabilité spatiale, saisonnière et interannuelle : les mesures in situ effectuées à des stations ponctuelles sur des périodes limitées ou à basse fréquence ne peuvent pas rendre compte de cette forte variabilité temporelle et spatiale. Malheureusement, jusqu'à présent, aucu suivi à long terme n'a été effectué pour les flux interocéaniques en SCS, en raison de la complexité du climat, de la topographie mais aussi de la situation géopolitique de la région. Notre étude souligne l'importance et les besoins de mesures in situ à long terme et à haute fréquence, coordonnées au niveau international, des flux à travers les détroits de la SCS - le seul moyen de fournir des estimations robustes pouvant être utilisées pour étudier l'interaction entre la SCS et les régions environnantes et valider les résultats numériques.

Études de sensibilité

Chaque étude numérique fournit différentes estimations des flux et des bilans d'eau, de chaleur et de sel en SCS (voir section I.4.2.2), tant en termes de moyennes climatologiques que de cycles saisonniers. Ceci est dû aux différences dans les choix méthodologiques, dans les conditions de forçage, les configurations numériques, la période étudiée, etc. L'étude de la sensibilité de nos résultats au choix des forçages atmosphériques, fluviaux et aux frontières latérales nous permettra d'explorer et de quantifier les différentes sources d'incertitudes de nos estimations, de comprendre les divergences par rapport aux études précédentes, et d'examiner la robustesse des résultats à ces choix méthodologiques.

Choix de l'ensemble de données de forçage utilisé

Les flux atmosphériques jouent un rôle crucial dans le bilan hydrique, thermique et salin de la SCS. Dans un cycle saisonnier, le flux de chaleur atmosphérique module la variation interne du bilan thermique, tandis que dans une échelle de temps interannuelle, le flux d'eau atmosphérique net régit les bilans de l'eau et du sel. Les estimations des flux atmosphériques nets d'eau douce et de chaleur varient beaucoup d'un ensemble de données à l'autre (voir section I.2.2). Par conséquent, le choix du forçage atmosphérique peut fortement affecter l'estimation des bilans d'eau, de chaleur et de sel sur la SCS. Il est donc important d'évaluer la sensibilité des sorties du modèle au forçage atmosphérique en utilisant différents ensembles de, comme les réanalyses JRA-55 (Kobayashi et al. 2015) ou NCEP-CFSR (Kalnay et al. 1996, Saha et al. 2010).

Les cycles saisonniers et les variabilités interannuelles des bilans hydriques et salins sont fortement influencés par le flux latéral de l'eau. Dans notre configuration, les positions des détroits de Karimata et de Taiwan (Figure II.3, Chapitre II) sont proches de la limite des modèles, alors que ce n'est pas le cas pour d'autres détroits clés (Luzon, Mindoro). Les conditions aux limites pourraient donc influencer le calcul des flux participant au SCSTF. Le même type de tests de sensibilité que pour le forçage atmosphérique doit être effectué avec des conditions aux limites ouvertes différentes : CMEM-Copernicus, les réanalyses SODA (Simple Ocean Data Assimilation) (Jackett et al. 2006), INDESO (Tranchant et al. 2016), etc. Ces tests de sensibilité sur les données de forçage utilisés nous permettront d'évaluer dans quelle mesure les résultats dépendent des produits atmosphériques et océaniques utilisés.

Amélioration des rejets en temps réel dans les rivières

La configuration utilisée dans cette étude comprend 63 embouchures de rivières, dont seulement 11 utilisent des débits quotidiens en temps réel, les autres utilisant des données climatologiques mensuelles, y compris les grands fleuves comme le Mékong et la rivière de Pearl. En outre, le flux de chaleur du fleuve est déduit de la température du fleuve, qui est prise en compte par une fonction cosinusoïdale avec une période d'un an entre une valeur minimale et une valeur maximale, et non par la valeur de la température en temps réel. Il est donc difficile de clarifier avec précision le rôle des flux fluviaux dans

les bilans hydrique, thermique et salin de la SCS et dans leur variabilité. Des simulations réalisées à l'aide d'un ensemble de données à long terme et en temps réel sur le ruissellement fluvial et la concentration en nutriments, qui fourniraient une vue globale des changements du ruissellement fluvial régional au cours des dernières années sous l'effet des activités anthropiques (construction de barrages, surexploitation de l'eau douce, pollution, etc) et du changement climatique (inondations, sécheresses, cyclones tropicaux, etc), aideraient à évaluer les effets de ces changements.

Il convient de noter que le travail de collecte des données sur les rejets fluviaux en temps réel dans cette région est lourd, en raison du partage limité des informations entre les instituts des différents pays et du manque de mesures de surveillance à long terme, notamment en ce qui concerne les concentrations en nutriments.

Impact des marées

L'influence de la marée est particulièrement importante en SCS, tant dans la zone côtière qu'en haute mer (Li et al. 2006). Dans les zones peu profondes du plateau continental, le mélange amplifié par les marées peut avoir un impact important au niveau des embouchures des rivières (Piton et al. 2020). Au large, selon Wang et al. (2017), la dissipation des vagues internes (marées baroclines) dans le détroit de Luzon et en SCS module les propriétés des masses d'eau et les caractéristiques de la circulation profonde en SCS, ce qui impacte le SCSTF. Malgré ce rôle important de la marée, la plupart des études précédentes sur le SCSTF et les bilans en SCS ne l'ont pas pris en compte. Le présent travail est l'une des premières études numériques incluant l'effet des marées. Il sera intéressant d'étudier précisement cet effet sur le SCSTF et les budgets en, en comparant la simulation analysée ici avec une simulation jumelle réalisée sans forçage des marées, et en explorant le rôle de chaque composante des marées.

Études d'autres échelles temporelles et régions

Impact des événements extrêmes à court terme

Comme nous l'avons vu au chapitre I, la SCS et le Pacifique occidental sont les régions les plus touchées par les TCs dans le monde. En moyenne, 10 TCs ont traversé annuellement la SCS entre 1965 et 2005 (Goh et Chan 2010). L'analyse de la fréquence

et de l'intensité décennales des TCs affectant le sud de la Chine de Liu et Chan (2020) au cours de la période 1975 - 2018 a montré une augmentation de la fréquence des TCs intenses passant par la SCS au cours de la période 2012 - 2018. Herrmann et al. (2019) ont en revanche montré, à partir de sorties de modèles atmosphériques forcés, que le changement climatique pourrait conduire à une diminution de la fréquence et l'intensité des TCs dans la région. Les vents violents et les pluies abondantes des TCs ne provoquent pas seulement de graves catastrophes, mais affectent aussi fortement la dynamique, les échanges de chaleur et d'eau entre l'océan et l'atmosphère, et donc les bilans d'eau, de chaleur et de sel sur l'ensemble de la zone SCS. Piton (2019), en analysant l'impact des typhons dans le Golfe du Tonkin, a révélé que les TCs pourraient inverser la circulation anticyclonique estivale et renforcer la circulation cyclonique hivernale sur le Golfe, en générant des flux d'eau quotidiens du même ordre que les flux mensuels moyens. Il serait donc très intéressant d'évaluer l'impact des événements extrêmes tels que les TCs sur la circulation en SCS et sur les flux et les bilans interocéaniques.

Variabilité décennale et changement climatique

Notre simulation sur la période 2009 - 2018 a montré un lien étroit entre le SCSTF et les budgets d'eau, de sel et de chaleur et les variations climatiques interannuelles (ENSO) et décennales (PDO) à grande échelle. L'étude de la réponse des budgets et du SCSTF à la variabilité décennale et au changement climatique par des simulations plus longues sera un travail à développer. Les simulations longues permettront notamment d'examiner la contribution des flux interocéaniques de la SCS et d'autres composantes des bilans sur la variabilité et les tendances (réchauffement/refroidissement, salinité/fraîcheur) sur une plus grande échelle temporelle en SCS et d'étudier l'évolution à long terme du rôle de la SCS dans le système climatique régional et sa réponse au changement climatique.

Outre l'ENSO et la PDO, la SCS est également sous l'influence d'un autre phénomène à grande échelle : le Dipôle de l'Océan Indien (IOD, voir Chapitre I). L'IOD a un impact majeur sur le début de la mousson de l'océan Indien et sur le taux de précipitation en Inde, dans l'est de l'Afrique du Sud, dans le sud de l'Australie et en Indonésie (Saji et al. 1999, Ashok et al. 2001). Ce phénomène influence également le début de la mousson

d'été de la SCS lors des années neutres de l'ENSO (Yuan et al. 2008) et la variation interannuelle de SLA dans le sud de la SCS (Soumya et al. 2015). Il sera donc intéressant d'évaluer l'impact de l'IOD ainsi que ses effets combinés avec ENSO et la PDO, non seulement sur les bilans hydrique, thermique et halin de la SCS, mais aussi sur les écosystèmes pélagiques planctoniques.

Étude à l'échelle régionale

Notre modèle à haute résolution et à budget fermé pourrait être utilisé sur une région plus large à l'échelle de toute l'Asie du Sud-Est, englobant les détroits indonésiens qui jouent un rôle majeur dans le transfert des masses d'eau entre les Océans Pacifique et Indien (l'Indonesian Throughflow, ITF, Gordon et al. 2010), pour étudier les budgets d'eau, de la chaleur et du sel. Il sera en particulier intéressant d'étudier les interactions entre le SCSTF et l'ITF (ITF), étant donnée la relation étroite entre ces deux systèmes de courants (Tozuka et al. 2007), afin d'apporter de nouveaux éclairages sur le lien entre SCSTF et ITF et, plus généralement, sur l'interaction entre les océans Pacifique et Indien. L'utilisation d'un modèle couplé océan-atmosphère sur la région d'Asie du Sud-Est permettrait en outre d'explorer plus en détail, et considérant les interactions air-mer, les cycles de l'eau, de la chaleur et du sel dans le système climatique régional. Il s'agit d'un travail en cours effectué dans le cadre du LMI LOTUS et du projet CORDEX-SEA.

Impact sur les écosystèmes : études de modèles physiques-biogéochimiques couplés

Le second objectif de ce travail était de développer une configuration couplée physique - biogéochimique à haute résolution sur le SCS, afin d'étudier la réponse de l'écosystème planctonique pélagique sous la variabilité de la dynamique océanique à différentes échelles. Ce travail a été techniquement mis en œuvre au cours de ce doctorat, mais la calibration du modèle et l'analyse des simulations nécessitent encore un travail important qui sera poursuivi au-delà de ce doctorat. La description du modèle biogéochimique Eco3M-S et de la configuration utilisée pour le couplage avec le modèle hydrodynamique SYMPHONIE sont détaillées dans l'annexe suivante. Les résultats issus de la simulation préliminaire sur l'étude d'un an (2016 - 2017) sont également discutés. Malgré les

améliorations à apporter en termes de Chla et de concentrations de nutriments, le modèle reproduit correctement le cycle saisonnier des caractéristiques biogéochimiques et des éléments planctoniques. Ce modèle couplé, après une calibration et une validation rigoureuse, sera utilisé pour estimer les flux interocéaniques et les bilans de nutriment en SCS, la réponse des écosystèmes planctoniques en SCS à la dynamique océanique et sa variabilité, des échelles évènementielles à climatique (TCs, cycle saisonnier, variabilité interannuelle, variabilité décennale et interdécennale).

Appendix

To study the biogeochemical characteristics of the SCS, we use the coupled model physical/biogeochemical SYMPHONIE/Eco3M-S. In the following, we describe first the biogeochemical model and its implementation for this study, second comparisons of the coupled model outputs with observations, and finally the modelled seasonal cycles of the biogeochemical variables for year 2016/2017.

A.1. The biogeochemical model (Eco3M-S)

The Eco3M-S model is a multi-nutrient and multi-plankton functional type model that simulates the dynamics of the biogeochemical decoupled cycles of several biogenic elements (carbon, nitrogen, phosphorus, silicon and oxygen) and of non-redfieldian plankton groups. The model structure used in this study is based on the same pelagic plankton ecosystem model as the one fully described and used by Auger et al. (2011, 2014), Herrmann et al. (2013, 2014, 2017), Ulses et al. (2016, 2020) and Kessouri et al. (2017, 2018). The model includes 7 interconnected compartments (Figure A.1) with a total of 35 state variables.

+ 1 compartment of phytoplankton including 3 types classified by size (pico-phytoplankton [0.7–2 µm], nanophytoplankton [2–20µm] and micro-phytoplankton [20–200 µm])
+ 1 compartment of zooplankton including 3 types classified by size (nano-zooplankton [5–20 µm], micro-zooplankton [20–200 µm] and meso-zooplankton [>200 µm])
+ 1 compartment for bacteria.
+ 4 compartments of respectively dissolved organic matter (DOM), particulate organic matter (POM, light and heavy, differentiated by the settling speed and origin), inorganic nutrients (DIM, nitrate, ammonium, phosphate and silicate) and dissolved oxygen.

All the state variables are summarized in the table A.1 below.

State Variables	Description	Unit
Nut_1 (NO_3), Nut_2 (NH_4), Nut_3 (PO_4), Nut_4 (SiO_4)	Nitrate, Ammonium, Phosphate, Silicate	mmol m^{-3}
O_2	Dissolved oxygen	mmol m^{-3}
$XPhy_1$, $XPhy_2$, $XPhy_3$	Pico-, nano-, micro-phytoplankton in X, X = C (carbon), N (nitrogen), P (phosphorus) or Si (silica) for Phy_3 only	mmolX m^{-3}
$ChlPhy_1$, $ChlPhy_2$, $ChlPhy_3$	Pico-, nano- micro-phytoplankton in chlorophyll	mgChl m^{-3}
$CZoo_1$, $CZoo_2$, $CZoo_3$	Nano-, micro- and meso-zooplankton	mmolC m^{-3}
CBac	Bacteria	mmolC m^{-3}
DOX	Dissolved organic X, X=carbon, nitrogen, and phosphorus	mmolX m^{-3}
$XDet_Y$	Heavy (Y=H) and light (Y=L) particulate organic X, X= carbon, nitrogen, phosphorus, silica and chlorophyll	mmolX m^{-3}

Table A.1: Lists of the state variables.

This model is a newly calibrated and completed version of the model version presented by (Hermann et al. 2013; Auger et al. 2014). The food-web structure of the model and the biogeochemical processes interacting between compartments are schematically represented in the following Figure A.1.

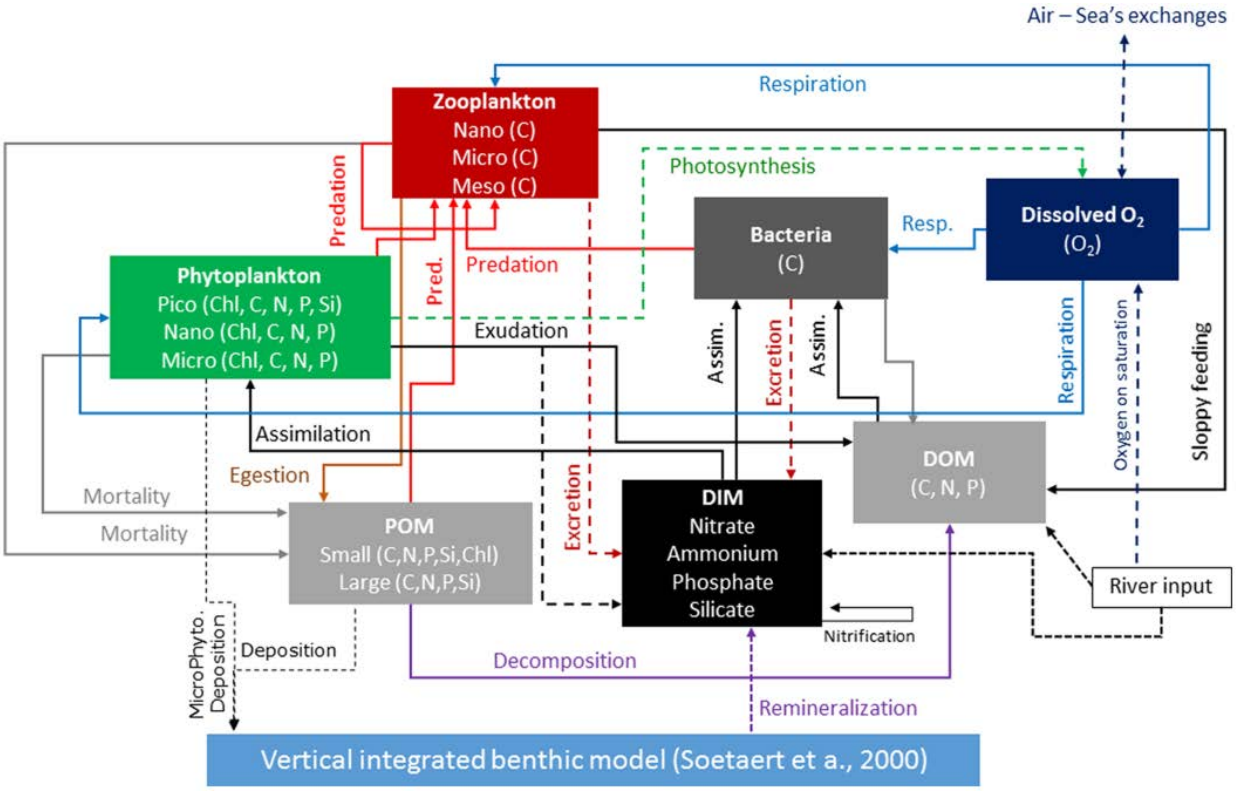

Figure A.1. The block diagram of Eco3M-S biogechemical model. Image source: Kessouri (2015)

All chemical fluxes and functions used for representing equations of states of the model are summarized in Table A.2.

Symbol	Definition	Unit
GPP_i	Phytoplankton i gross primary production	mmolC m^{-3} d^{-1}
$\mu^{NR}_{Phy_i}$	Phytoplankton i maximal growth rate in nutrient-replete (NR) conditions	d^{-1}
μ_{Phy_i}	Phytoplankton i growth rate	d^{-1}
gml_i	Growth multi-nutrient limitation function for phytoplankton i	-
$f^{Q}_{Phy_i,Xlim}$	Phytoplankton i growth quota function, Xlim = N, P, Si	-
$f^{Q}_{Upt\,Phy_i,X}$	Phytoplankton i quota function for uptake of nutrient XNut, X = N, P, Si	-
$RespPhy_i$	Phytoplankton i respiration rate	mmolC m^{-3} d^{-1}
$UptPhy_{i,Nut_j}$	Phytoplankton i uptake rate of nutrient Nut_j, where $Nut_1 = NO_3$, $Nut_2 = NH_4$, $Nut_3 = PO_4$, $Nut_4 = SiO_4$	mmol m^{-3} d^{-1}
$V^{max}_{Phy_i,X}$	Phytoplankton i maximum carbon specific gross uptake rate of XNut, where X = N, P, Si	molX $molC^{-1}$ m^{-3} d^{-1}
$(X/C)_{Phy_i}$	Phytoplankton I internal X/C quota, X = C, N, P, Si, Chl	molX $molC^{-1}$
$Exu_{i,X}$	Phytoplankton i exudation rate of DOX, where X = C, N, P, or SiO_4	mmolX m^{-3} d^{-1}
$SynthChl_i$	Phytoplankton i chlorophyll synthesis rate	mgChl m^{-3} d^{-1}

$\rho_{Phy_i,Chl}$	Phytoplankton i chlorophyll synthesis regulation term	gChl molN^{-1}
$MortPhy_{i,X}$	Phytoplankton i mortality rate in X, where X = C, N, P, Si or Chl	mmolX m^{-3} d^{-1} or mgChl m^{-3} d^{-1}
$Graz_{i,XPrey}$	Zooplankton i grazing rate on XPrey, where Prey = Phy_i, Zoo_i, Bac, $Det_{L,H}$ and X = C, N, P, Si or Chl	mmolX m^{-3} d^{-1} or mgChl m^{-3} d^{-1}
$(X/C)_{Prey}$	X/C quota in zooplankton prey, where Prey = Phy_i, Zoo_i, Bac, $Det_{L,H}$	molX molC^{-1}
$MessyFeed_{i,X}$	Zooplankton i messy feeding rate, X = C, N, P	mmolX m^{-3} d^{-1}
$Eges_{i,X}$	Zooplankton i egestion rate in X, X = C, N, P, Si or Chl	mmolX m^{-3} d^{-1}
$GrowthZoo_{i,C}$	Zooplankton i net growth rate in carbon	mmolC m^{-3} d^{-1}
$RespZoo_i$	Zooplankton i respiration rate	mmolC m^{-3} d^{-1}
$FoodZoo_{i,X}$	Zooplankton i food flux in X, where X = C, N, P	mmolX m^{-3} d^{-1}
$(X/C)_{FoodZoo_i}$	Zooplankton i food X/C quota, where X = C, N, P	molX molC^{-1}
$ExcZoo_{i,XNut}$	Zooplankton i excretion of dissolved inorganic nutrient XNut, where XNut = NH_4, PO_4	mmolX m^{-3} d^{-1}
$RespZoo_i^{add}$	Zooplankton i additional respiration rate	mmolC m^{-3} d^{-1}
$MortZoo_{i,X}$	Zooplankton i mortality rate in X, X = C, N, P	mmolX m^{-3} d^{-1}
$PredZoo_{3,X}$	Mortality of zooplankton 3 through predation by higher trophic level rate in X, X = C, N, P	mmolX m^{-3} d^{-1}
$UptBac_{DOX}$	Bacteria uptake of dissolved organic X, where X = C, N, P	mmolX m^{-3} d^{-1}
$UptBac_{XNut}$	Bacteria uptake of dissolved inorganic nutrient XNut, XNut = NH_4, PO_4	mmolX m^{-3} d^{-1}
$UptBac_{XNut}^{max}$	Bacteria maximal uptake of dissolved inorganic nutrient XNut, XNut = NH_4, PO_4	mmolX m^{-3} d^{-1}
$GrowthBac$	Net bacterial production	mmolC m^{-3} d^{-1}
$GrowthBac^*$	Potential net bacterial production	mmolC m^{-3} d^{-1}
$(X/C)_{FoodBac}$	Bacteria food X/C quota, where X = C, N, P	molX molC^{-1}
$(X/C)_{DOM}$	Dissolved organic matter X/C quota, where X = C, N, P	molX molC^{-1}
$FoodBac_X$	Bacteria food flux in X, X = C, N, P	mmolX m^{-3} d^{-1}
$ExcBac_{XNut}$	Bacteria excretion of dissolved inorganic nutrient XNut, XNut = NH_4, PO_4	mmolX m^{-3} d^{-1}
$RespBac$	Bacteria respiration rate	mmolC m^{-3} d^{-1}
$MortBac_X$	Bacteria mortality rate in X, X = C, N, P	mmolX m^{-3} d^{-1}
$Nitrif$	Nitrification flux	mmolN m^{-3} d^{-1}
Rem_{XDet_Y}	Remineralisation of XDetY, X = C, N, P, Si, Chl and Y= L (light), H (heavy)	mmolX m^{-3} d^{-1}
f^T	Temperature function for phytoplankton growth, zooplankton grazing, bacterial growth, remineralization and nitrification processes	-
$PAR(z)$	Photosynthetically active radiation at the depth z	J m^{-2} d^{-1}
PAR_{surf}	Photosynthetically active radiation at the surface: PARsurf = PAR(z=0)	J m^{-2} d^{-1}

Table A.2: List of biogeochemical fluxes and functions

A.1.1. Dissolved inorganic matter

The compartment consists of nitrate (NO_3), phosphate (PO_4), silicate ($Si(OH)_4$) and ammonium (NH_4).

Nitrate is considered to be one of the primary nutrients limiting the growth of phytoplankton and bacteria (Chen et al. 2004). It is consumed directly by phytoplankton. It is produced by nitrification.

The rate of variation of nitrate = Nitrification – The absorption by phytoplankton

$$\frac{dNO_3}{dt} = Nitrif - \sum_{i=1}^{3} UptPhy_{i,NO_3} \quad \text{(Eq. A1)}$$

Ammonium is produced by the excretion from heterotrophs (bacteria and zooplankton). It is nitrified, and consumed by bacteria and phytoplankton. The consumption by phytoplankton corresponds to the regenerated production.

The rate of variation of ammonium = The excretion by zooplankton + The excretion by bacteria - Nitrification – The absorption by phytoplankton – The absorption by bacteria

$$\frac{dNH_4}{dt} = \sum_{i=1}^{3} ExcZoo_{i,NH_4} + ExcBac_{NH_4} - Nitrif - \sum_{i=1}^{3} UptPhy_{i,NH_4} - UptBac_{NH_4} \quad \text{(Eq. A2)}$$

Phosphate is excreted by heterotrophs (bacteria and zooplankton) and consumed by bacteria and phytoplankton. The SCS ecosystem does not seem to be limited by the dissolved inorganic phosphorus (DIP), following Wu et al. (2003).

The rate of variation of phosphate = The excretion by zooplankton + The excretion by bacteria - The absorption by phytoplankton – The absorption by bacteria

$$\frac{dPO_4}{dt} = \sum_{i=1}^{3} ExcZoo_{i,PO_4} + ExcBac_{PO_4} - \sum_{i=1}^{3} UptPhy_{i,PO_4} - UptBac_{PO_4} \quad \text{(Eq. A3)}$$

Silicate is an element limiting the growth of diatoms (third size class of phytoplankton in the model). The silicate is exuded by phytoplankton and produced by the remineralization process.

The rate of variation of silicate = The exudation of organic matter + The remineralization of organic matter - The absorption by phytoplankton

$$\frac{dNH_4}{dt} = \sum_{i=1}^{3} ExcZoo_{i,NH_4} + ExcBac_{NH_4} - Nitrif - \sum_{i=1}^{3} UptPhy_{i,NH_4} - UptBac_{NH_4} \quad \text{(Eq. A4)}$$

A.1.2. Phytoplankton

Phytoplankton is represented by three groups which are classified by their sizes (as noted: i = 1 (pico), 2 (nano), 3 (micro) in the state and process equations): picophytoplankton (< 2μm) mostly dominating in the oligotrophic regions, nanophytoplankton (2-20 μm), and microphytoplankton (20-200 μm) consisting mainly of the group of diatoms. Microphytoplankton has a non-zero sinking speed unlike the first two classes of phytoplankton. The phytoplankton model is derived from the Eco3M model (Baklouti et al., 2006). The dynamics of phytoplankton is determined by the primary production, the synthesis of chlorophyll, the consumption of nutrient salts, the respiration, exudation, natural mortality and grazing. Phytoplankton has a variable internal ratio due to the fact that the ratios among the different chemical elements are not constant. The temporal evolution of phytoplankton due to biogeochemical processes is given by the following equations:

The rate of variation of phytoplankton = The primary production – RespirationN + The absorption of nutrien salts – The exudation – The mortality – The grazing by zooplankton

$$\frac{dCPhy_i}{dt} = GPP_i - RespPhy_i - Exu_{i,C} - MortPhy_{i,C} - \sum_{j=1}^{3} Graz_{j,CPhy_i} \quad \text{(Eq. A5)}$$

$$\frac{dCNhy_i}{dt} = UptPhy_{i,NH_4} + UptPhy_{i,NO_3} - Exu_{i,N} - MortPhy_{i,N} - \sum_{j=1}^{3} Graz_{j,NPhy_i} \quad \text{(Eq. A6)}$$

$$\frac{dPPhy_i}{dt} = UptPhy_{i,PO_4} - Exu_{i,P} - MortPhy_{i,N} - \sum_{j=1}^{3} Graz_{j,PPhy_i} \quad \text{(Eq. A7)}$$

$$\frac{dSiPhy_i}{dt} = UptPhy_{i,SiO_4} - Exu_{i,Si} - MortPhy_{i,Si} - \sum_{j=1}^{3} Graz_{j,SiPhy_i} \quad \text{(Eq. A8)}$$

$$\frac{dChlPhy_i}{dt} = Synth_{i,Chl} - MortPhy_{i,Chl} - \sum_{j=1}^{3} Graz_{j,ChlPhy_i} \quad \text{(Eq. A9)}$$

A.1.3. Zooplankton

Zooplankton is broadly ordered into three size classes (as noted i = 1 (nano), 2 (micro), 3 (meso) in state and process equations): nano-zooplankton [diameter <20μm], microzooplankton [20μm<diameter< 200μm] and mesozooplankton [diameter > 200μm] which consists mainly of copepods. The zooplankton model is based on the model developed by Anderson and Pondaven (2003) and Raick et al. (2005). In contrast with phytoplankton, zooplankton has a constant internal ratio. The dynamics of zooplankton is governed by the grazing, the natural mortality, the basal respiration, the excretion to maintain the constant internal ratio, the egestion, "Sloppy feeding" (loss of prey biomass

in feeding process), the predation by higher trophic levels. The evolution of zooplankton is given by the following equation :

The rate of variation of zooplankton = The grazing by phytoplankton + The predation by carnivous zooplankton - The mortality – The basal respiration – The egestion – The excretion of dissolved organic matter

$$\frac{dCZoo_i}{dt} = GrowthZoo_{i,C} - MortZoo_{i,C} - \sum_{j=1}^{3} Graz_{j,CZoo_i} - RespZoo_i^{add} \quad \text{(Eq. A10)}$$

in which: $GrowthZoo_{i,C} = k_{c,Zoo_i}(Graz_{i,CPrey} - Eges_{i,C} - MessyFeed_{i,C})$

A.1.4. Bacteria

The bacteria model is also based on the model developed by Anderson and Pondaven (2003) and Raick et al. (2005). This model has also a constant internal ratio. The consumption of dissolved organic matter (DOC) and nutrient, the respiration, excretion, natural mortality and the consumption of nano-zooplankton are the processes that govern the bacteria dynamics. The evolution of bacteria takes place in the model by the following equation:

The rate of variation of bacteria = The absorption of dissolved carbon and nutrient – The respiration - The mortality – The predation by zooplankton - The excretion of inorganic matter

$$\frac{dCBac}{dt} = UptBac_{DOC} + UptBac_{Nut} - RespBac - MortBac_C - \sum_{j=1}^{3} Graz_{j,CBac} - ExcBac_{Nut} \quad \text{(Eq. A11)}$$

In which : Nut = N, P.

A.1.5. Particulate inorganic matter

Particulate inorganic matter is a key component in biogeochemical cycles, which includes the particles characterized from low sinking speeds (0.7 $m.d^{-1}$) to high sinking speed (90 $m.d^{-1}$). Small and large detritus are produced by the mortality of phytoplankton and zooplankton, the egestion of zooplankton. They are eaten by zooplankton and remineralized.

The rate of variation of small detritus = The mortality of phytoplankton + The mortality of zooplankton + The egestion of zooplankton – The degradation – The predation – The grazing

$$\frac{dCDet_S}{dt} = \sum_{i=1}^{3} MortPhy_{i,C} + \sum_{i=1}^{3} Eges_{i,C} + \sum_{i=1}^{2} fr_{Det_S}^{MortZoo_i} MortZoo_{i,C} + fr_{Det_S}^{MortZoo_3} PredZoo_{i,C} - Deg_{CDet_S} - \sum_{i=1}^{13} Graz_{i,CDet_S}$$ (Eq. A13)

$$\frac{dPDet_S}{dt} = \sum_{i=1}^{3} MortPhy_{i,P} + \sum_{i=1}^{3} P + \sum_{i=1}^{2} fr_{Det_S}^{MortZoo_i} MortZoo_{i,P} + fr_{Det_S}^{MortZoo_3} PredZoo_{i,P} - Deg_{PDet_S} - \sum_{i=1}^{3} Graz_{i,PDet_S}$$ (Eq. A14)

$$\frac{dNDet_S}{dt} = \sum_{i=1}^{3} MortPhy_{i,N} + \sum_{i=1}^{3} Eges_{i,N} + \sum_{i=1}^{2} fr_{Det_S}^{MortZoo_i} MortZoo_{i,N} + + fr_{Det_S}^{MortZoo_3} PredZoo_{i,N} - Deg_{NDet_S} - \sum_{i=1}^{3} Graz_{i,NDet_S}$$ (Eq. A15)

$$\frac{dSiDet_S}{dt} = MortPhy_{3,Si} + fr_{Det_S}^{Eges_{Si}} . \sum_{i=2}^{3} Eges_{i,Si} - Deg_{SiDet_S}$$ (Eq. A16)

$$\frac{dChlDet_S}{dt} = \sum_{i=1}^{3} MortPhy_{i,Chl} + \sum_{i=2}^{3} Eges_{i,Chl} - Deg_{ChlDet_S}$$ (Eq. A17)

The rate of variation of large detritus = The mortality of phytoplankton + The mortality of zooplankton– The degradation –The grazing of zooplankton

$$\frac{dCDet_L}{dt} = \sum_{i=1}^{3} \left(1 - fr_{Det_S}^{MortZoo_i}\right) MortZoo_{i,C} + \left(1 - fr_{Det_S}^{MortZoo_3}\right) MortPhy_{i,C} - Deg_{C,Det_L} - - \sum_{i=1}^{3} Graz_{i,CDet_L}$$ (Eq. A18)

$$\frac{dPDet_L}{dt} = \sum_{i=1}^{3} \left(1 - fr_{Det_S}^{MortZoo_i}\right) MortZoo_{i,P} + \left(1 - fr_{Det_S}^{MortZoo_3}\right) MortPhy_{i,P} - Deg_{P,Det_L} - - \sum_{i=1}^{3} Graz_{i,PDet_L}$$ (Eq. A19)

$$\frac{dNDet_L}{dt} = \sum_{i=1}^{3} \left(1 - fr_{Det_S}^{MortZoo_i}\right) MortZoo_{i,N} + \left(1 - fr_{Det_S}^{MortZoo_3}\right) MortPhy_{i,N} - Deg_{N,Det_L} - - \sum_{i=1}^{3} Graz_{i,NDet_L}$$ (Eq. A20)

$$\frac{dSiDet_L}{dt} = \left(1 - fr_{Det_S}^{Eges_{Si}}\right) . \sum_{i=2}^{3} Eges_{i,Si} - Deg_{SiDet_L}$$ (Eq. A21)

A.1.6. Dissolved organic matter

Dissolved organic matter (DOM) is released by exudation of phytoplankton and "Messy feeding" process by zooplankton. It also stems from degradation of particulate organic matter and mortality of bacteria. It is consumed by bacteria:

The rate of variation of dissolved organic carbon = The exudation of phytoplankton + The destruction of prey before the consumption of zooplankton + The mortality of bacteria + The degradation of particulate organic matter– The consumption of bacteria

$$\frac{dDOC}{dt} = \sum_{i=1}^{3} Exu_{i,C} + \sum_{i=1}^{3} SloppyFeed_{i,C} + MortBac_C + Deg_{CDet_S} + DegRem_{CDet_L} - - UptBac_{DOC}$$ (Eq. A22)

with X ∈ (C, N, P)

A.1.7. Dissolved oxygen

Dissolved oxygen refers to the level of free, non-compound oxygen present in water. It is an important parameter in assessing water quality because of its influence on the aquatic organisms. It is exchanged at the air-sea interface, produced through primary production and consumed by respiration and nitrification. The air-sea flux of oxygen was calculated here using the parameterization of the gas transfer velocity proposed by Wanninkhof and McGillis (1999). The dissolved oxygen at saturation level is calculated using the equation of Garcia and Gordon (1992).

$$The\ surface\ oxygen\ flux = \frac{Kw}{360000} * (oxygen_{sat} - oxygen) \quad \text{(Eq. A23)}$$

With

Gas transfer velocity $Kw = (0.0283 * wind^3) * (Sc/660)^{-0.5}$ (Wanninkhof and McGillis, 1999)

Number of Schmidt $Sc = ox_A - (ox_B * T) + (ox_C * T^2) - (ox_D * T^3)$

The satured oxygen in water $oxygen_{sat} = \left(\frac{1000}{22.3916}\right) * e^{x_1}$ (Garcia and Gordon, 1992)

oxygen the oxygen air condition.

Where :

$$x_1 = (ox_{A0} + ox_{A1} * T_s + ox_{A2} * T_s^2 + ox_{A3} * T_s^3 + ox_{A4} * T_s^4 + ox_{A5} * T_s^5) + \\ +S * (ox_{B0} + ox_{B1} * T_s + ox_{B2} * T_s^2 + ox_{B3} * T_s^3) + ox_{C0} * S^2$$

In which :

ox_{Ai}, ox_{Bi}, ox_{C0}: constant coefficients (values detailed in Garcia and Gordon, 1992)

$T_s = log\left(298.5 - \frac{T}{273.15} + T\right)$ with T the water temperature and S the salinity.

The rate of variation of oxygen = PPB – Phytoplankton respiration – Zooplankton respiration – Bacteria respiration + Nitrification

$$\frac{dO_2}{dt} = (GPP_i \times C/O) - \left(RespPhy_i \times \frac{N}{O}\right) - \left(RespZoo_i^{add} \times \frac{N}{O}\right) - \left(RespBac \times \frac{N}{O}\right) - \\ -(Nitrif \times N/O) \quad \text{(Eq. A23)}$$

A.2. The implementation of the Eco3M-S model on the SCS basin

The biogeochemical model is forced offline by the outputs of the hydrodynamic SYMPHONIE model. The advection and diffusion of the biogeochemical variables were

calculated using the QUICKEST (QUICK with Estimated Streaming Terms) scheme (Leonard, 1979) on the horizontal and with a centred scheme on the vertical. For biogeochemical simulations, we use the same configuration as the hydrodynamical simulations presented in Chapter II: the grid covers the region SCS from 99°E to 124°E and from -0.6°N to 24°N with 4 km of resolution and 50 vertical sigma layers (Figure II.3). The initial conditions for nutrients (nitrate, phosphate, silicate, ammonium, oxygen) and for phytoplankton (carbon and chlorophyll) are issued from the daily dataset of the Copernicus BIOMER4V2R1 (hereafter called Bio-Copernicus). This latter is also used as open boundary conditions for nutrient parameters. The Bio-Copernicus dataset is displayed with a 0.25° horizontal resolution with regular longitude/latitude equirectangular projection and 50 z-coordinate depth levels. The air-sea interface forcing conditions of solar radiation and wind stress are issued from the 3 hourly analyses at 1/8° resolution product of ECMWF. To simplify the first simulations presented here, we neglect the input fluxes of organic and inorganic matters from the atmosphere, as well as the contributions of nutrients and organic matters resulting from the process of diagenesis and sedimentary resuspension at the sea bottom. The nutrient concentrations at the river outlets are prescribed, using observational results of previous studies (nutrient data provided from INPC, VAST for Red river, from the National Hydro-Meteological Service (NHMS) of Vietnam for Mekong river, and from Cai et al. (2004) for the Pearl river).

In the next section we present the preliminary results from biogeochemical simulations for the case study 2016 - 2017.

A.3. Case study 2016 – 2017

A.3.1. Atmospheric and hydrodynamical conditions

We firstly analyse the atmospheric and hydrodynamical conditions affecting the biogeochemical characteristics of the SCS: windstress, atmospheric heat flux, mixed layer depth (MLD) and solar radiative flux. All physical forcing conditions are computed over the period of the biogeochemical simulation (from May 2016 to end of April 2017).

Atmospheric conditions

The annual cycle of atmospheric forcing of the biogeochemical simulation are illustrated in Figure A.2. During the period May 2016 - April 2017, the atmospheric heat fluxes are positive (gain for the sea) and maximum in summer (May to August), reduce in autumn,

and reach their minimum value in winter (January), presenting negative values during strong wind events, then become positive again in spring (Figure A.2a). Regarding the solar radiative flux (Figure A.2b), most intense solar radiation (250 W/m^2) is observed in summer and weakest SSR flux (150 W/m^2) in winter. Over the whole basin, the wind stress is strongest in winter (0.10 N/m^2 in average, December to February) and reduces in summer (0.05 N/m^2 in average, May to August) (Figure A.2c).

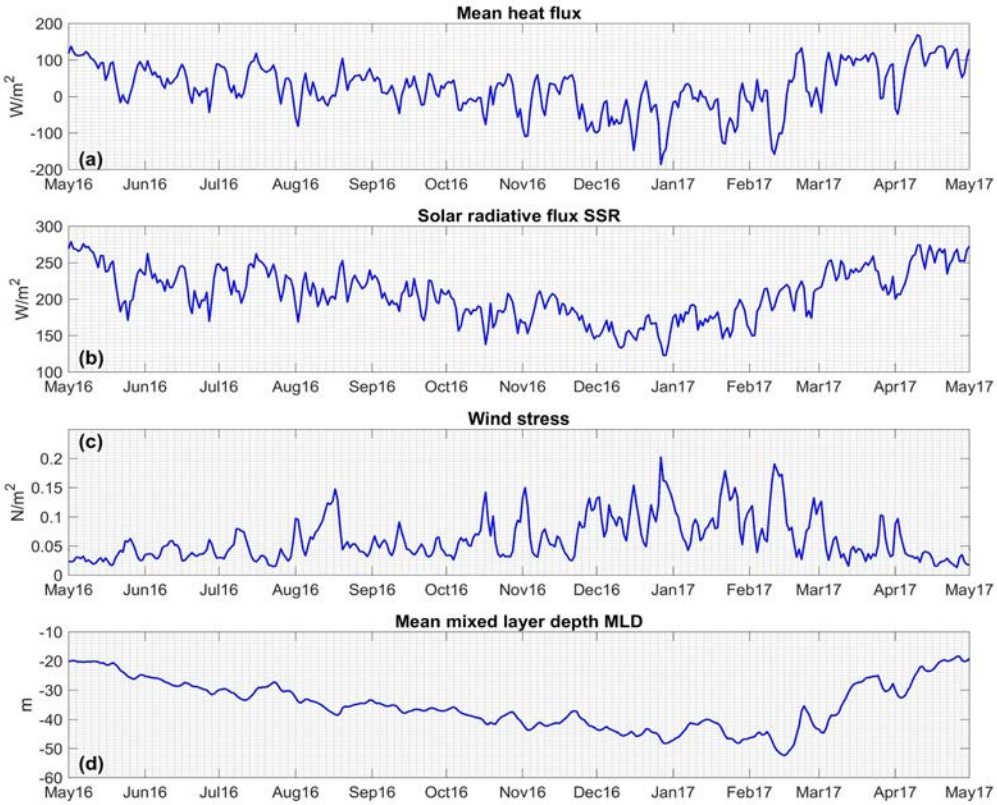

Figure A.2: Time series of model spatial average of (a) atmospheric heat flux, (b) mean solar radiative flux (SSR), (c) wind stress, (d) mixed layer depth for period 2016/2017 in average over the SCS.

The wind stress spatial distribution over the SCS presents a pronounced seasonal variation, with the alternating monsoon winds (Figure A.3a, b). In winter, the northeastern monsoon governs over the whole SCS. Highest wind stress is observed in the northwest of Luzon and over southern Vietnam coasts. In summer, the southwest monsoon flows with weaker intensity than the winter monsoon. High wind stress zone in summer is located offshore of southern Vietnam, where the SVU occurs (see I.4.1). The wind stress

spatial distribution is in accordance with previous studies of Park and Choi (2016), Da (2018), Wang et al. (2007) via satellite observations.

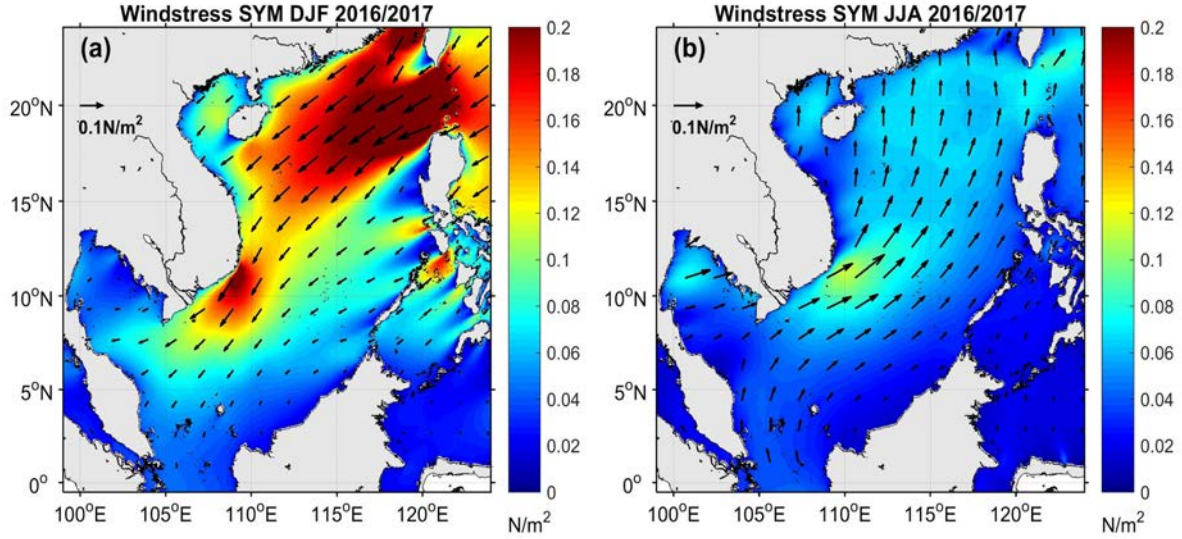

Figure A.3. Maps of average winter (a) and summer (b) modeled wind-stress.

Mixed layer depth

The monsoon system also induces a strong seasonal variability of MLD, with the spatial mean MLD over the whole SCS deeper in winter (50 m) and shallower in summer (30 m) (Figure A.2d). Figures A.4a, b show the spatial variation of the winter and summer MLD. The strong winter monsoon winds associated with heat loss enhance the vertical mixing over the entire SCS basin, especially in the northern basin (Figure A.4a). Highest values of modeled winter MLD (~80 m) are located over the China shelf, southern Gulf of Tonkin and southwest of the SCS basin. The situation changes in summer, the MLD in the northern part (~20 m) is shallower than in the southern part (~40 m) (Figure A.4b). The maximum value of modeled MLD in summer (~55 m) is observed offshore the southern Vietnam coast and over the Gulf of Thailand.

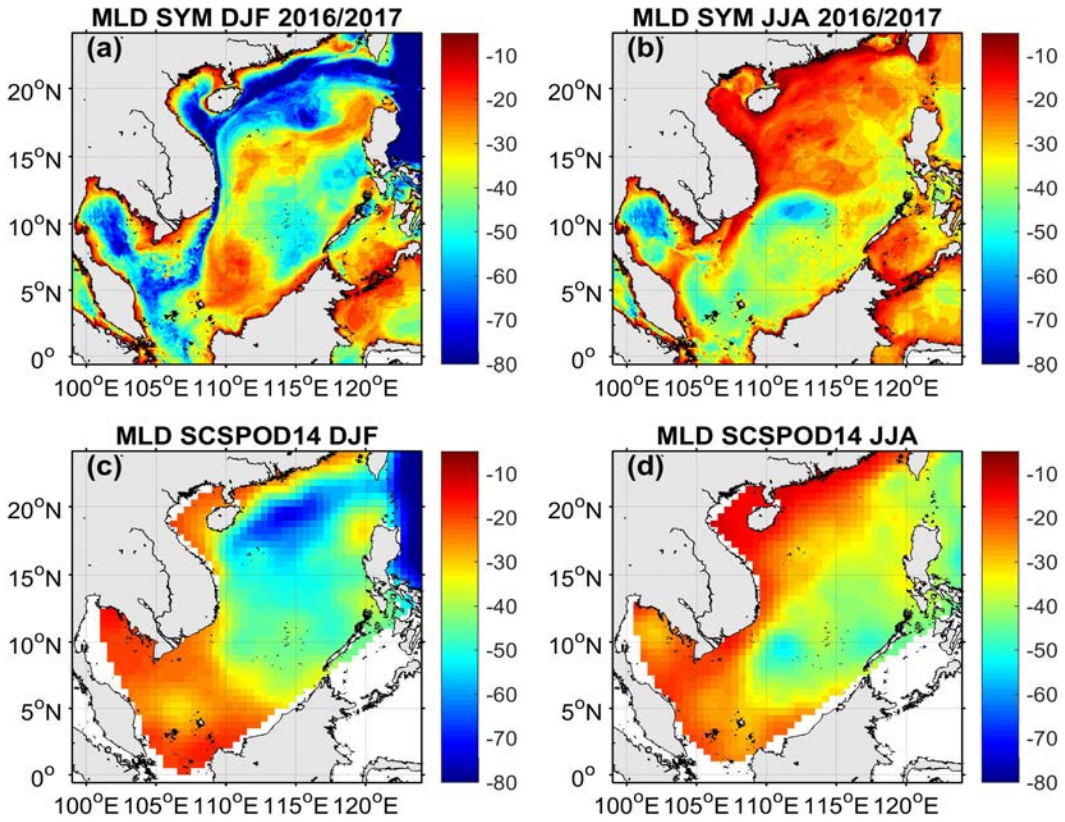

Figure A.4: Maps of mixed layer depth in winter (DJF) and summer (JJA) issued from (a, b) model in 2016-2017; (c, d) SCSPOD14 dataset (Zeng et al. 2016)

The spatial distribution of modeled MLD presents similarity with the in-situ climatological monthly dataset SCSPOD14 (Zeng et al. 2016a, Figure A.4c, d). The SCSPOD14 includes 11,774 T/S profiles collected within the SCS (100–125°E, 0–25°N) from 1919 to 2009, taken from three datasets: WOD09, Argo, and in-situ data from SCSIO (South China Sea Institute of Oceanology (SCSIO), Chinese Academy of Sciences (CAS)).

Figure A.4 shows that in both datasets, the MLD is higher in winter and lower in summer in the northern basin than in the southern basin. The model simulates deeper ML than the climatological in-situ data along coastal and slope zones in the western SCS and over the southern basin both in winter and summer. Note that the coverage of SCSPOD14 datasets decreases southward (see Zeng et al. 2016a, Fig. 3).

Under these forcing conditions, in the next part we analyze the preliminary results issued from the biogeochemical simulation. Model outputs are firstly evaluated by comparison with satellite and in-situ observations. We then investigate the seasonal cycle of principal compartments and variables of the planktonic pelagic ecosystem.

A.3.2. Comparing model results with observations: phytoplankton biomass and nutrients

In order to evaluate the performance of the biogeochemical model, we compare the simulation outputs with observations issued from climatologies, in situ measurements, satellite data and literature observations. We first examine surface characteristics and then the vertical distribution.

Surface nutrients and chlorophyll

According to Wu et al. (2003) and Chen et al. (2004), in the SCS where the ratio of nitrate to phosphate is smaller than the Redfield ratio, nitrate is the limiting nutrient in the growth of phytoplankton rather than phosphate. We examine the seasonal distribution of surface nitrate over the SCS basin by comparing the modeled results with the World Ocean Atlas WOA V2 2013 dataset (Zhang et al. 2016), in summer and winter (Figure A.5).

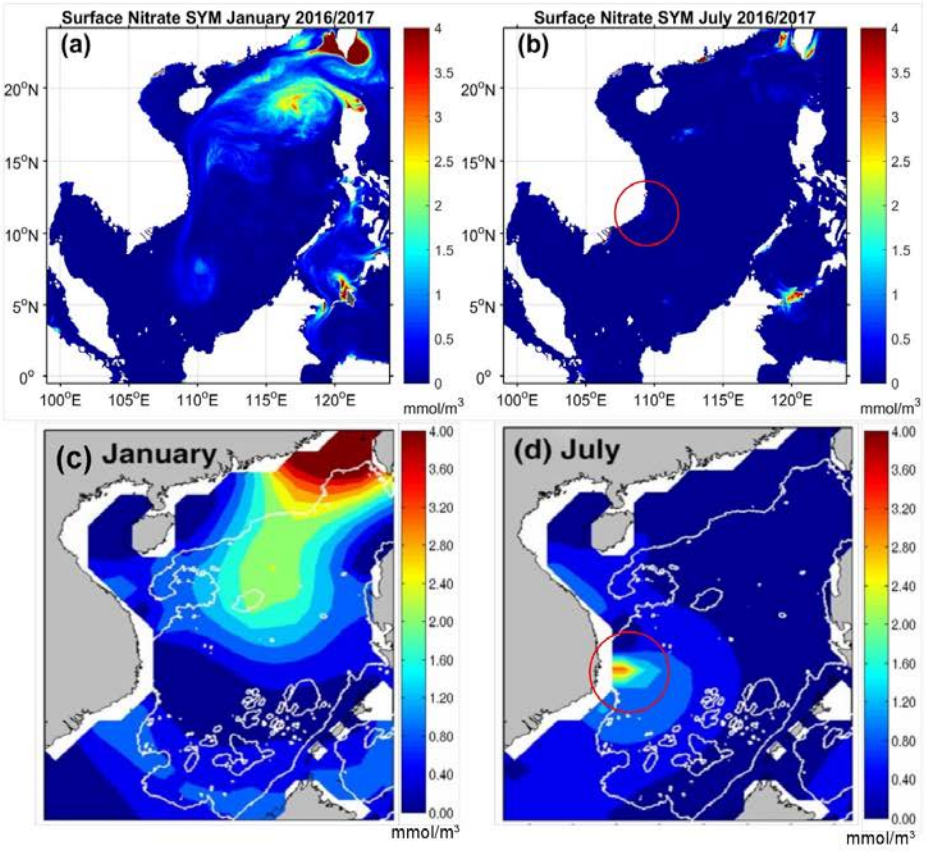

Figure A.5: Surface concentration of nitrate (mmol/m3) in winter and summer in the model (a, b) and from monthly climatological data from World Ocean Atlas WOA13 (c, d, Zhang et al. 2016).

We obtain similar seasonal distributions of surface nitrate in the model and observations. In winter, strong nitrate concentrations are visible over the northern basin. Highest values of nitrate are observed at the Taiwan strait, presumably due to the fact that northeastern winds induce a southward flux at the Taiwan strait that brings East China Sea nutrient rich waters into the SCS, according to Wu and Hsin (2005) and Zhang et al. (2014). In summer, observational data show highest nitrate surface concentrations over the SVU zone (3 $mmol/m^3$, Figure A.5d). The model also simulates a stronger nitrate concentration over the SVU zone (red circle, Figure A.5b) but 1 order of magnitude lower (0.25 $mmol/m^3$) compared to WOA13 dataset. We observe high nitrate concentrations around the Taiwan strait from model results, but not in the observational data. The model simulates lower surface nitrate in both winter and summer compared to WOA13. It could be explained by an underestimation of nutrient inputs from major rivers and a rapid consumption of nutrients by planktonic organisms.

Regarding the assessment of the surface modeled chlorophyll concentration, we use the sea surface chlorophyll-a concentration data from the Ocean Colour Climate Change Initiative (CCI) project of the European Space Agency programme. This project produced a time series of satellite-based ocean-colour products at the global scale, merging data from three sensors (Sea-viewing Wide Field-of-view Sensor (SeaWiFS), Moderate Resolution Imaging Spectroradiometer on the Aqua Earth Observing System (MODIS-Aqua), and Medium Resolution Imaging Spectrometer (MERIS)) while attempting to reduce inter-sensor biases to evaluate the model surface Chl-a outputs. Comparisons between outputs from Eco3M-S model and CCI of the monthly averaged surface Chl-a from June to October 2016 and from November 2016 to February 2017 are presented in respectively Figures A.6 and A.7.

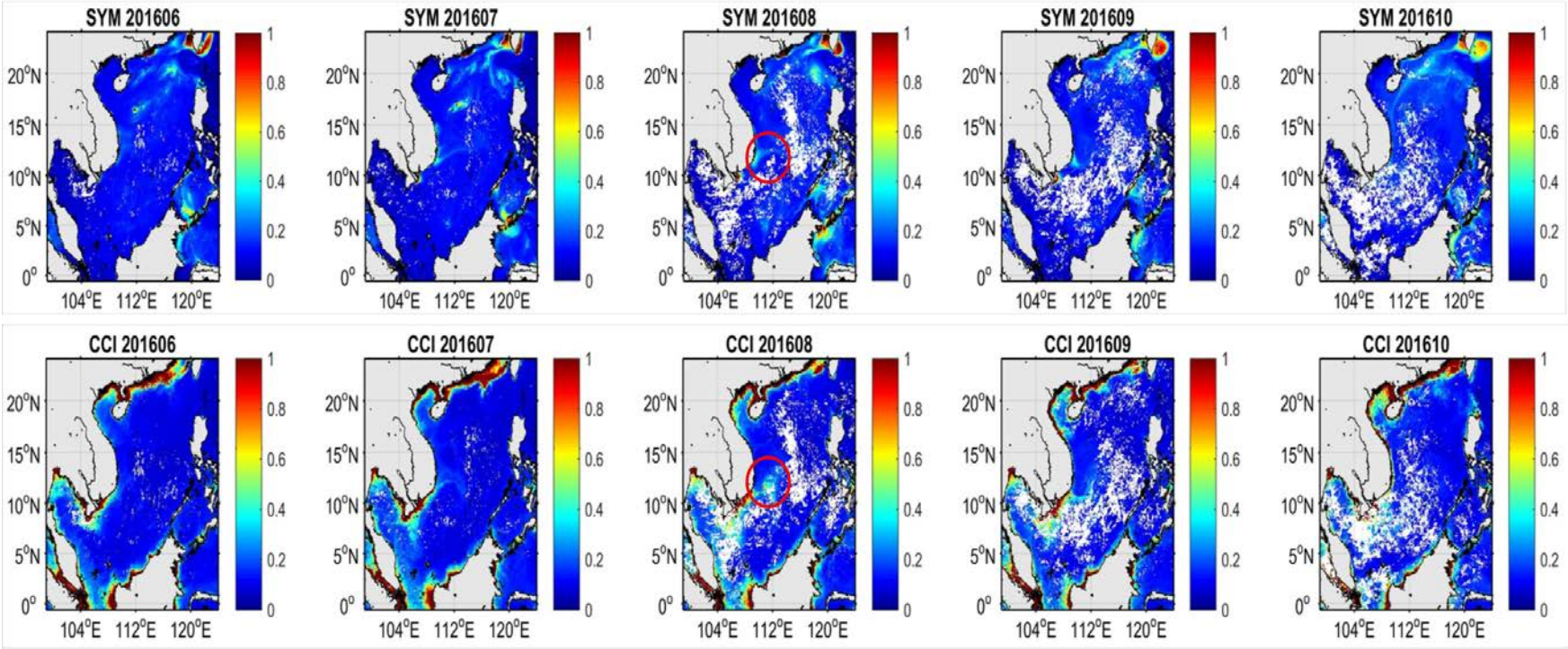

Figure A.6. Monthly mean spatial distribution of surface Chl-a (in mg/m^3) of model outputs (SYM) and satellite observation (CCI), from June to October 2016.

Following Figure A.6, in summer - autumn (June - October 2016), the model simulates weaker concentration of surface Chl-a compared to the satellite observation CCI in the coastal zones. We observe in model and observations, from July to September, the upwelling phenomenon in the southern Vietnam coasts (SVU, red circle, Figure A.6), characterized by higher value of Chl-a surface concentration. High values of surface Chl-a (1.2 - 1.5 mg/m^3) are observed from CCI in summer all along the southern China coasts, Gulf of Tonkin (northern Vietnam) and in the coastal zone of SCS southern basin, but they are not present in the model outputs. Over those coastal areas, especially at the major rivers' plumes (Pearl, Mekong and Red rivers), the concentration of surface Chl-a from the model is much weaker than the satellite observations, both in value and spatial distribution.

In winter (from November to February), the difference in surface Chl-a between the model outputs and satellite observations is even more pronounced (Figure A.7). High values of surface Chl-a are observed in CCI dataset over the southern coasts of China, the Gulf of Tonkin and the Mekong river plumes, but not in the simulations. Under the influence of the northeast winter monsoon, the vertical mixing of surface nutrient-depleted water with nutrient-rich deeper water is strengthened (Fig. A.2.d), inducing globally higher surface Chl-a concentrations over the SCS basin. We obtain, in both datasets, a Chl-a concentration increase in the upwelling area at the northwest of Luzon in winter months, stronger in the model than in CCI. This high Chl-a concentration northwest of Luzon corresponds to a strong cyclonic gyre that develops in winter and is obtained both in modeled and observed SLA (Figure III.2i,k). The modeled results show that the Chl-a surface concentration starts to increase in November, during the onset of the winter monsoon, continue to increase in December and reach a maximum in January and February, when we observe two other areas, located at ~15°N and 7°N with high Chl-a concentration. In CCI dataset, this phenomenon of high surface Chl-a is mostly observed in the northern basin and with lower intensity.

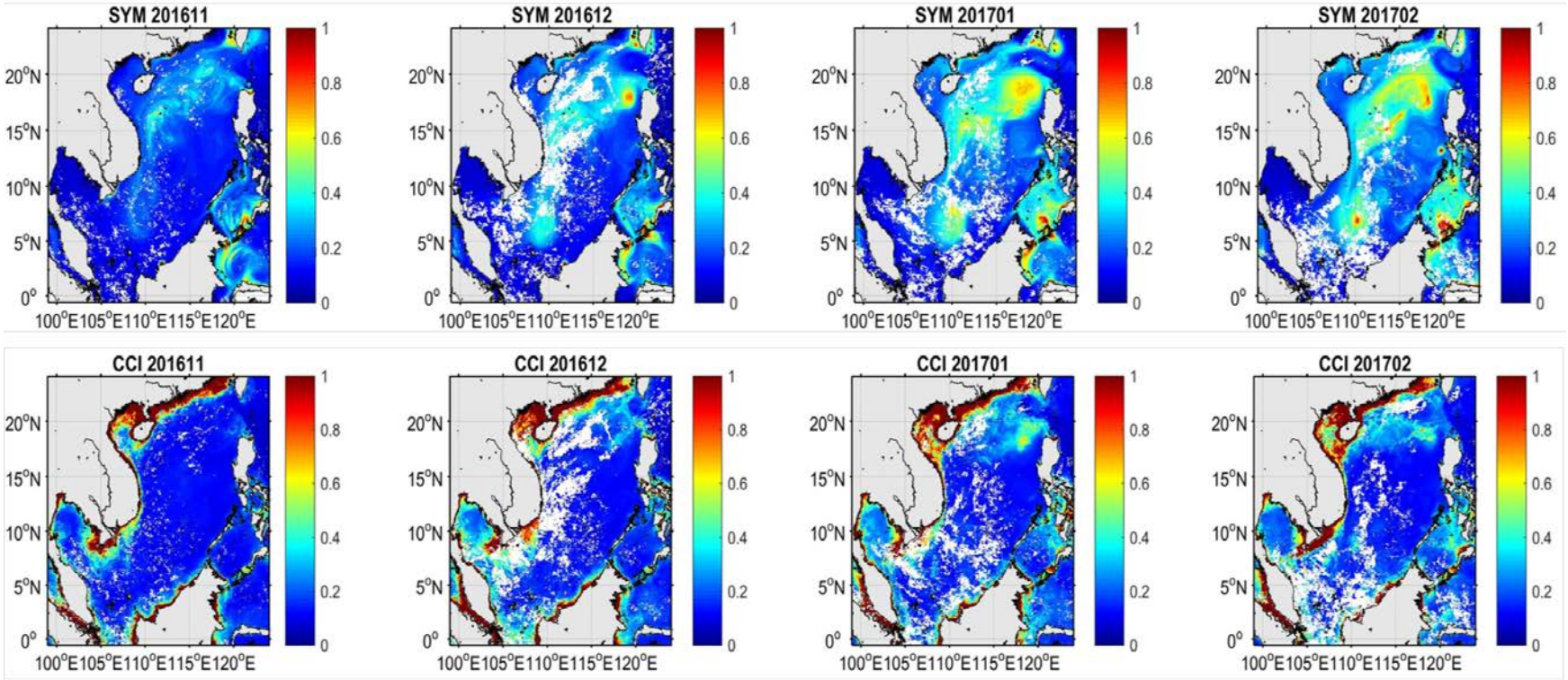

Figure A.7: Same as Figure A.6, from November 2016 to February 2017

Despite the difference between the model results and CCI observations over the coastal areas, the two datasets present similarity over the offshore SCS. The monthly means of surface Chl-a over the SCS open sea from the model and observation data show the same annual cycle, with high significant correlation (R=0.93, p<0.01) and a bias equal to 0.07 mg/m^3 (Figure A.8). Concentration of surface Chl-a reaches minimum value in summer (model 0.1 mg/m^3 in June; CCI 0.085 mg/m^3 in May) and maximum in winter (model 0.27 mg/m^3 in February; CCI 0.18 mg/m^3 in January). The model simulates higher Chl-a both in summer and winter (strongest differences are observed in January and February), compared to the satellite observations.

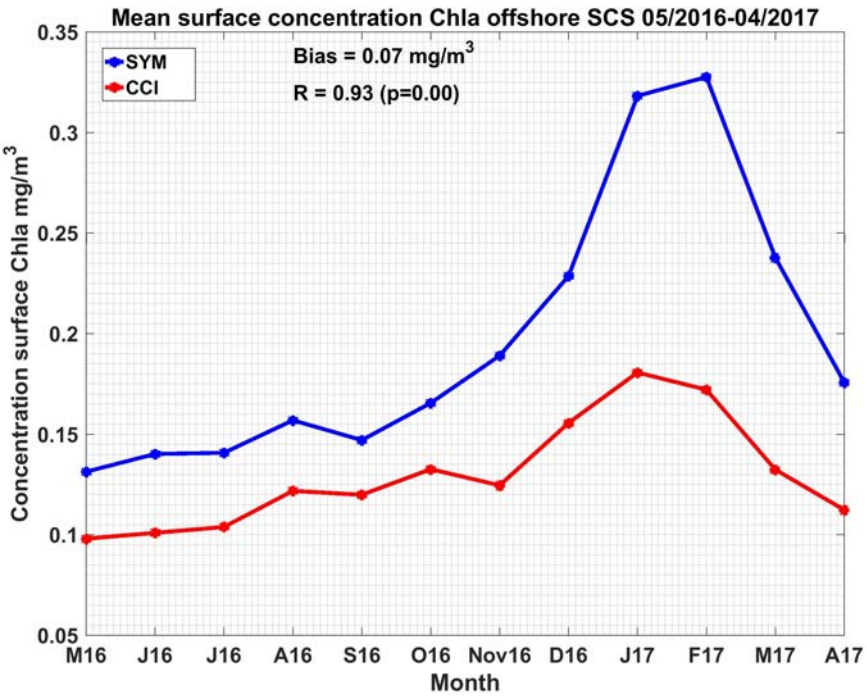

Figure A.8: Monthly time series of spatially averaged surface Chl-a of model outputs and satellite observations CCI over the offshore SCS zone (depth > 200 m).

Vertical distribution of nutrients and chlorophyll

Long-term in-situ measurements dedicated to the study of the seasonal and interannual variability of biogeochemical characteristics in the SCS zone are still limited. To evaluate the performance of the simulation in Chl-a vertical distribution in the coastal areas, we compare the model results to observational data collected from the cruise FK160603

aboard the R/V Falkor (3–19 June 2016). In total, samples from 21 stations were collected by Niskin bottle over the Mekong river plume region (Figure A.9b). The Chl-a samples were first filtered through 0.2 cellulose acetate filters and then frozen for analysis ashore. Details on this measurement campaign are provided in Weiber et al. (2019).

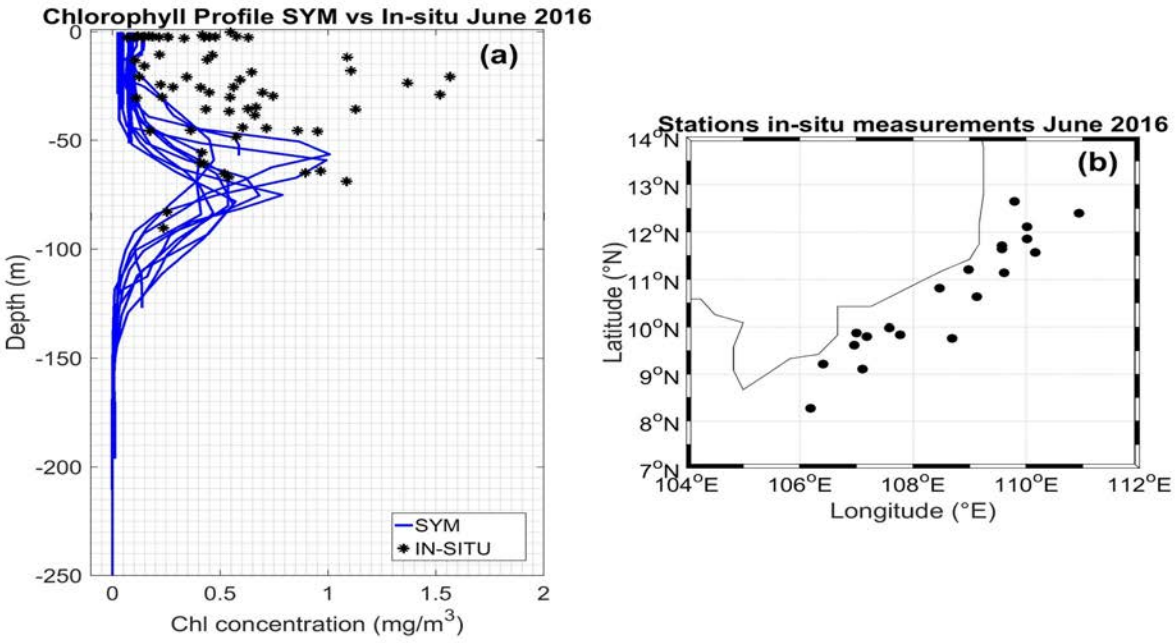

Figure A.9: (a) Comparison of modeled and in-situ Chl-a concentration profiles over the Mekong plume regions; (b) Stations of Chl-a in-situ measurements.

We compute the model Chl-a concentration profiles at the same days and same positions as the in-situ measurements. Results are shown in Figure A.9a. In the upper layer (0 - 50 m), concentrations of simulated Chl-a are weaker than in-situ observations. Underneath, from 50 - 100 m of depth, modelled values correspond well with in-situ measurements. The subsurface Chlorophyll maximum (SCM) depth is observed at about 60 m in the model, but much shallower in the in-situ dataset (30 m). This confirms the underestimation of chlorophyll concentration in the model in coastal areas deduced from the previous comparisons with satellite data.

Comparison with the ARGO-Bio dataset also allows to evaluate the vertical profiles of Chl-a. Zhang et al. (2016) deployed Argo-Bio profilers from September 2014 to August 2015 over two zones A1 (116-119°E, 17-20°N) and A2 (117-119°E, 13-16°N - locations shown in Figure A.10a) located west of Luzon island. A1 is located in the area of cyclonic gyre

that develops in winter offshore Luzon, whereas A2 is located southward of this gyre (Figure III.2i,k, Chapter III). Zone A1 is characterised by a high productivity (strong concentration of surface Chl-a) in winter, while zone A2 is a poor productivity zone. The time series of our modeled Chl-a profiles in the first 200 m over the two zones A1 and A2 (Figure A.10b, c) show a high similarity with the ones from Argo-bio presented in Zhang et al. (2016, Figure A.10d, e). Both datasets show high concentrations of Chl-a in the upper 50 m from December to March in zone A1, with maximum values of 0.7 mg/m^3 and 1.1 mg/m^3, respectively in the model and in Argo-Bio observations. Except this surface phytoplankton bloom in winter in zone A1, the Chl-a profiles in other seasons are quite stable, with a mean SCM depth around 60 m, for both model and observations. At zone A2, the Chl-a profiles show weaker seasonal variations. We observe a slight increase of modeled surface Chl-a in winter (0.25 mg/m^3, Figure A.10c) over this area, whereas Argo-bio data show low Chl-a surface concentration all year round (Figure A.10e). This could be explained by the different periods of the two datasets (2016/2017 for model, 2014/2015 for Argo-bio), or a stronger vertical mixing of the model than reality. The mean SCM depth at zone A2 is around 70 m, in both model and observation data, and is shallower in winter than in summer.

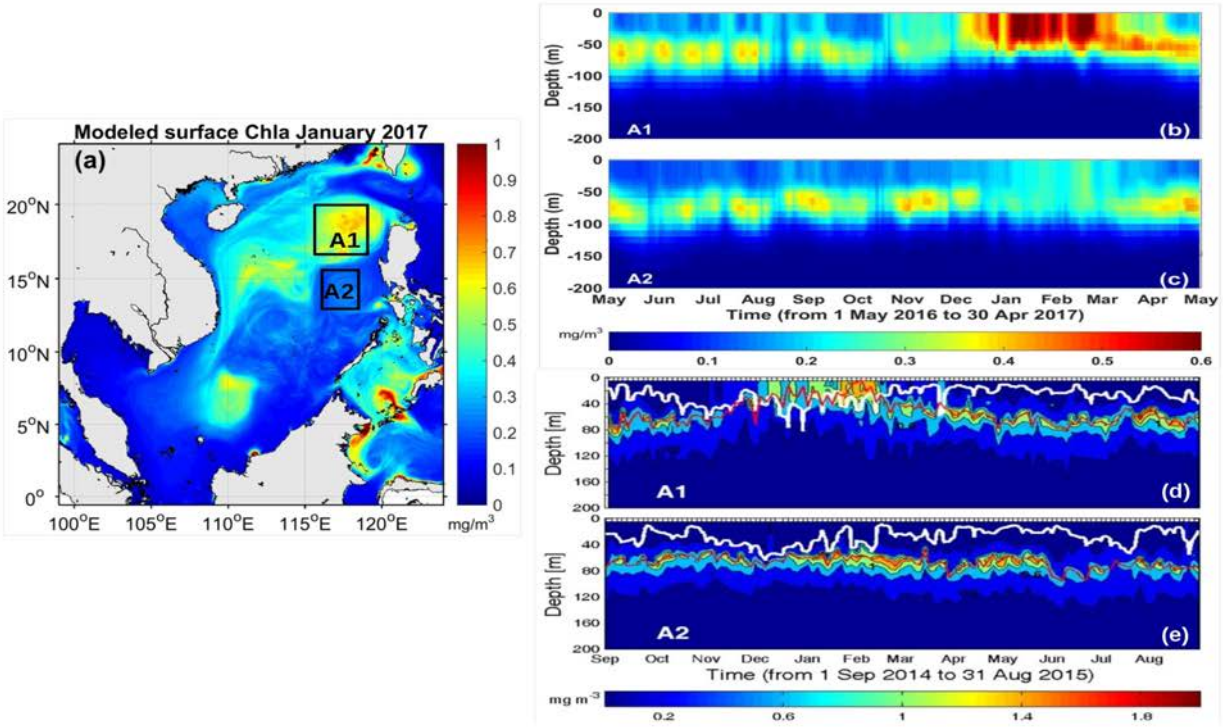

Figure A.10: (a) Positions of zones A1 (productive) and A2 (less productive) of Argo Bio floats deployed by Zhang et al. (2016), and January surface Chl-a concentration in the model; Time series of daily profiles of Chl-a concentration over A1 and A2 (b,c) from May 2016 to April 2017 in the model and (c, d) from September 2014 to August 2015 in Argo-Bio data. Note that the range of the colorbar is different for two datasets (0-0.6 mg/m^3 for model; 0-2 mg/m^3 for observation), as well as the time-axis.

One of the well-known long-term monitoring projects focusing on the SCS biogeochemistry is the SouthEast Asian Time series (SEATS) - conducted by scientists and staff from the National Center for Ocean Research (NCOR), Taipei, Taiwan. The SEATS station is located at 18°N, 116°E about 700 km southwest of Taiwan (Figure A.11e), situated in the high productivity zone A1 (Figure A.10a). Ship-based hydrographic and biogeochemical surveys are conducted every 2–3 months, from September 1998 to October 2003, then irregularly from 2007 to 2011. Details on the SEATS cruises are described in Wong et al. (2007) and Liu et al. (2013). Based on the seasonal profiles at SEATS point collected in January, March and July 2000 shown in Liu et al. (2002) and Liu and Chai (2009), we evaluate the modeled seasonal profiles in Chl-a, nitrate and silicate by comparing with the SEATS in-situ data. Results are presented in Figure A.11.

The biogeochemical model shows good performances in terms of nitrate vertical distribution at SEAT points: the modeled nitrate profiles are quite close to the in-situ measurements in January and July (Figure A.11a, c). However, we obtain a higher nitrate concentration in March over the whole upper 300 m in the model. Nitrate concentrations in winter and summer are low (close to 0) in the upper 50 m, and increase with depth. We obtain higher surface concentration of nitrate in winter than in summer.

The model simulates stronger silicate concentrations than in-situ values obtained at SEATS point, both in winter and summer (Figure A.11d, f). Further works on calibration need to be carried out in terms of silicate concentrations.

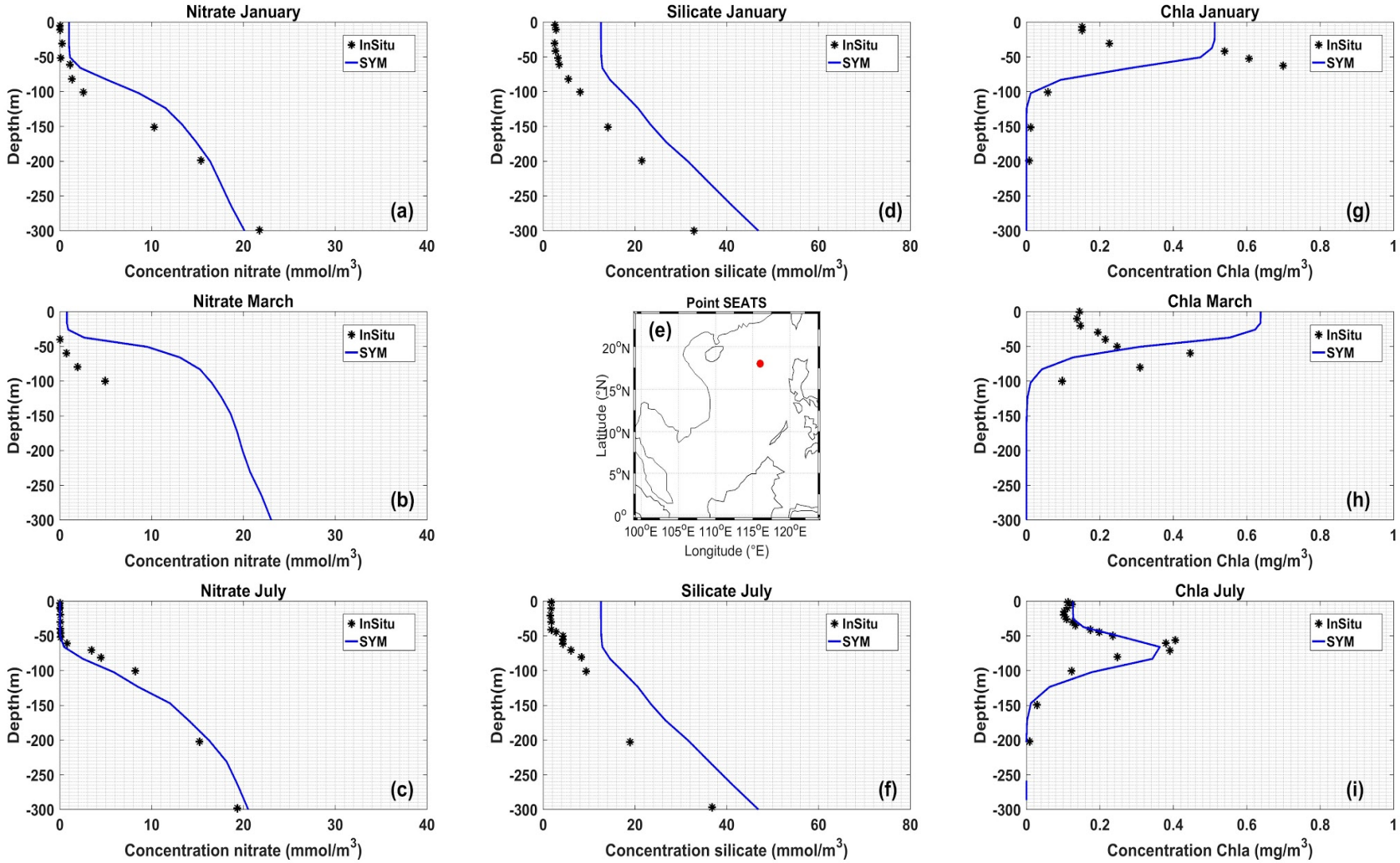

Figure A.11: Chl-a and nutrient profiles at SEATS point (116°E, 18°N) in January, March and July 2000 from in-situ measurements (black dots, Liu and Chai 2009) and in January, March and July 2016 from the model (blue line).

Concerning the Chl-a profile (Figure A.11g-i), the model simulates high Chl-a concentrations in the upper 50 m in winter and spring (January and March) but doesn't reproduce the SCM. In summer (July), the modelled Chl-a profile is highly similar to the observations (Figure A.11i), with a SCM of 0.4 mg/m^3 at around 65 m of depth. Liu et al (2013) and Xiu et al. (2019) compared vertical profiles of nitrate and chlorophyll concentrations at SEATS measured in winters under La Niña conditions and under El Niño conditions. They showed that vertical profiles present strong variability in response to ENSO influences: the nutriclines were deeper during La Niña winters than El Niño winters and a SCM was present during La Niña winters while the chlorophyll profile was homogenized over the first 60 m during El Niño winters. For the period studied here, 2016-2017, a neutral period following a strong El Niño period (see Figure II.6, Chapter II), the modeled vertical distribution may be closer than the observations of El Niño winters with shallower nutriclines and homogeneous chlorophyll concentrations in the surface layer.

A.3.2. Seasonal cycles of modeled biogeochemical characteristics

Nutrients, Zooplankton and Phytoplankton seasonal time series

We present, in this part, the preliminary results on the seasonal cycle of planktonic organisms and nutrients issued from our simulation over 2016-2017. Figure A.12 presents the monthly yearly cycle of nutrients and the 3 zooplankton and phytoplankton size-classes averaged over the upper 200 m over the SCS offshore zone (depth > 200 m).

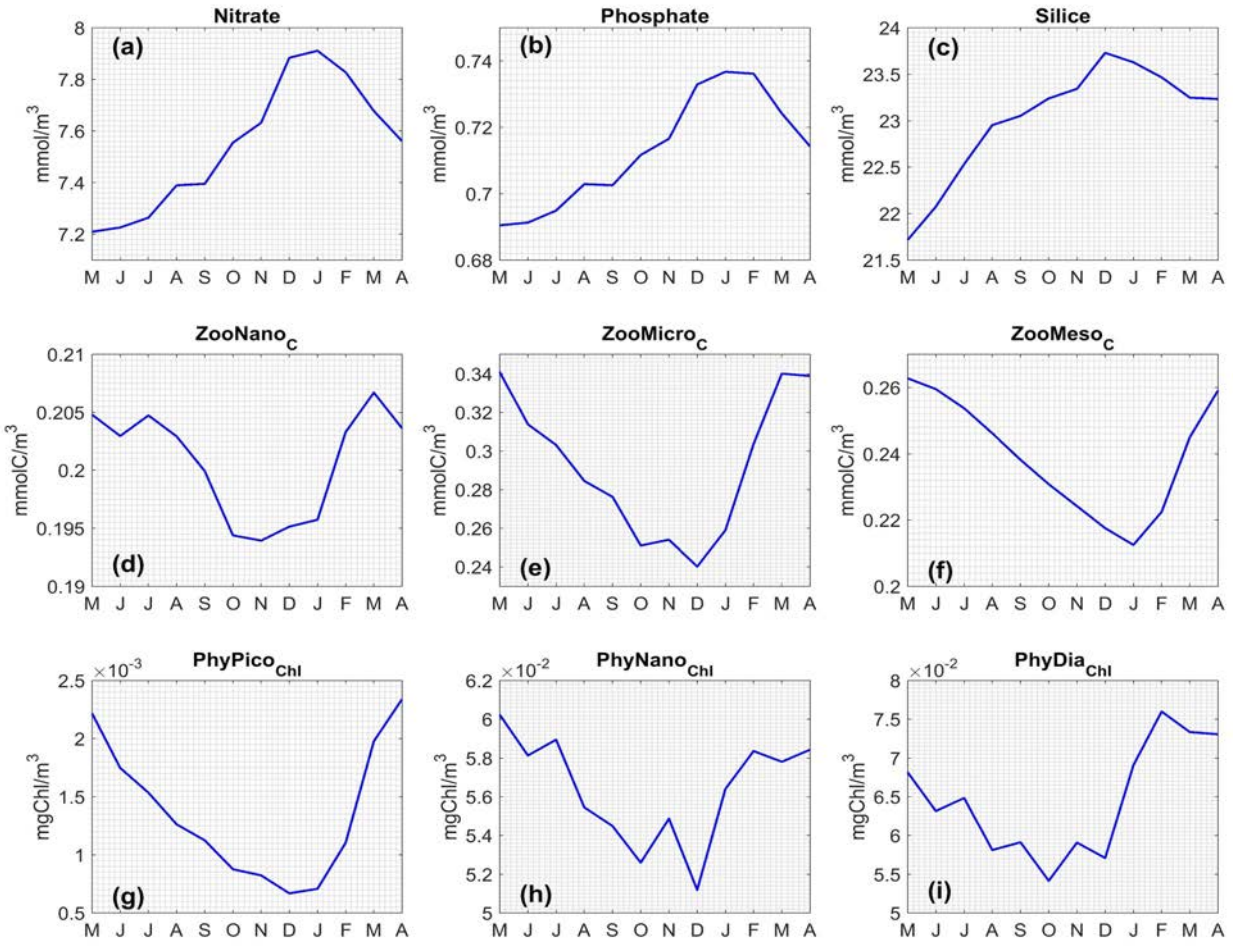

Figure A.12: Seasonal cycle of zooplankton (nano-, micro-, meso-), phytoplankton (pico-, nano-, diatoms) and nutrients (nitrate, phosphate, silicate) averaged over the upper 200 m over the SCS offshore area (depth > 200 m). Unit: mmol/m^3.

In the open sea, the nutrients are limited in summer, and more abundant in winter (Figure A.12a, b, c). Nitrate, the main limiting nutrient of phytoplankton growth in the SCS, reaches the maximum amount in January (7.9 mmol/m^3) and becomes minimum in May (7.2 mmol/m^3) in the upper 200 m. Simulated phosphate concentration in the upper 200 m shows a similar seasonal cycle, with maximum peak in January (0.74 mmol/m^3) and lowest value in May (0.69 mmol/m^3). The same seasonal tendency is observed with silicate concentrations, with a highest value in December (23.7 mmol/m^3) and a lowest value in May (21.7 mmol/m^3).

Planktonic organisms present similar seasonal cycles: high concentrations in spring-summer, and low concentrations in winter (Figure A.12 d-i). Concerning the zooplankton, the nano-, micro-, meso-zooplankton reach the maximum peak respectively at 0.21

mmolC/m^3 (March), 0.34 mmolC/m^3 (March-May), 0.26 mmolC/m^3 (Avril-May). Minimum concentrations of zooplankton are found in November (0.19 mmolC/m^3), December (0.24 mmolC/m^3), January (0.21 mmolC/m^3) for nano-, micro-, meso-zooplankton, respectively.

We obtain the same annual cycle for phytoplankton: lowest concentrations of pico-, nano-, diatoms are obtained respectively in December (0.7 10^{-3} mgChl/m^3), December (5.1 10^{-2} mgChl/m^3) and October (5.4 10^{-2} mgChl/m^3). The quantity of these organisms increases in spring and reaches its maximum quantity in April (2.3 10^{-3} mgChl/m^3), May (6.02 10^{-2} mgChl/m^3), February (7.6 10^{-2} mgChl/m^3). The modeled seasonal cycles of zooplankton and phytoplankton are in accordance with the numerical study of Liu et al. (2002).

A.4. Discussions & Conclusions

A preliminary simulation using high-resolution coupled physical/biogeochemical model (SYMPHONIE/Eco3M-S) has been performed to study the biogeochemical characteristics of the SCS for the period May 2016 to end of April 2017. Though comparisons with observations presented here show that the biogeochemical model still requires improvement, it is worth to underline that this simulation is the result from a significant work of adjustment of the biogeochemical model applied to the study area for the first time that allowed to notably reduce the initial biases and weaknesses obtained in our firsts experiments.

As presented in Chapter I, atmospheric and hydrodynamical conditions of the SCS over the period 2016/2017 present a high seasonal variability. In winter, the strong northeastern monsoon induces strong wind stress, heat loss and vertical mixing, especially in the northern basin. The MLD is deeper in the northern part than in the southern part of the basin. At the same time, the solar radiation in boreal winter reaches their minimum values. In summer when the southwest monsoon winds blow, a weaker and more homogenous wind stress occurs over the whole basin, though stronger wind stress is observed at the SVU zone. At this time, the basin receives heat from the atmosphere and the solar radiative flux is higher. Resulting from those atmospheric conditions, the mean MLD is shallower in summer than in winter, and deeper in the southern part than in the northern part of the basin.

Spatial distribution of surface nitrate concentrations presents a seasonal cycle similar as the one obtained from the climatological dataset WOA13. High concentration of nitrate is observed in winter, strongest at the strait of Taiwan then propagating further in the basin. In summer, the surface nitrate concentration is much lower in the model over the SVU area than in the observations. Vertical distribution of nitrate concentrations in winter and summer shows a high similarity between model results and observational data, whereas the concentration of nitrate in the water column in spring (March) is slightly higher than in-situ estimation. Vertical profile of silicate concentration is higher than in observations, this model parameters involved in the silice cycle thus need to be re-adjusted in the next future work. At the seasonal cycle, for the upper 200 m of the SCS offshore zone, nutrients reach their maximum concentration in winter and minimum in summer. Benefitting from the abundant nutrients and a higher solar radiation in spring, phytoplanktons and zooplanktons develop and reach their maximum in concentration in spring-begin of summer. Lowest concentrations of planktonic organisms are observed at the end of autumn-begin of winter, when both nutrients and solar radiation decrease.

The alternating monsoon and hydrodynamical conditions strongly affect the SCS ecosystem. We firstly evaluate the performance of the biogeochemical model by comparing the model outputs with satellite and in-situ observations. The modeled surface Chl-a shows a similar seasonal pattern with CCI satellite dataset in the open sea: high (low) surface concentration of Chl-a in winter (summer). In winter, strong vertical mixing brings nutrients from deep layers up to the surface, generating a phytoplankton bloom (high surface Chl-a) over the whole basin, especially in the northern part of the SCS. Zones of maximum surface Chl-a correspond to the mesoscale cyclonic eddies generated by the basin-wide cyclonic gyres in winter (Figure III.2i, k, Chapter III), situated northwest of Luzon and over the Sunda Shelf. This result confirms observation of Xiu and Chai (2011) where they showed, through a numerical study, that nutrients and chlorophyll uptake was significantly enhanced in the cyclonic eddies. In other words, the winter mesoscale cyclonic eddies are important sources of nutrients and Chl-a in the SCS basin. In summer, wind stress curl generates a strong upwelling zone at the southern Vietnam coasts (SVU), uplifting cold and rich seawater from the deep layers to the sea surface. This phenomenon generates high concentrations of Chl-a at the surface, then abundant

planktonic organisms. The model, although successfully producing higher Chl-a at upwelling zones, seems to underestimate this phenomenon in comparison to satellite Chl-a.

High differences between the modeled and observational Chl-a are observed at the coastal areas: the model simulates much lower Chl-a compared to satellite observations and in situ measurements in shallow waters, especially at the major rivers' plumes. This low modeled value of Chl-a at the river plumes could be explained by the underestimation of the nutrient concentration discharged from rivers. It is noteworthy that the nutrient discharges from Mekong river could influence the SVU, following observations in summer 2004 of Hein (2008). The nutrient discharges from major rivers therefore play an important role in modulating the biogeochemical characteristics of the SCS. Unfortunately, the nutrient concentrations over rivers are difficult to collect, since the monitoring system on biogeochemical parameters is still limited, and the policy of information sharing between institutions and countries is different. The benthic process not taken into account in this first simulation could be another reason for underestimated values of Chl-a in coastal areas. According to Liu et al. (2007), the benthic nutrient generation is important not only in the shelf region but also in the southern SCS basin: this process could enhance by 33% the overall primary production. It is then important to include the benthic processus in the biogeochemical over the SCS zone. Finally, the CCI estimation of Chl-a at coastal zones might also be overestimated, because of high turbidity at the river plumes. Satellite products with algorithms specially developed for this area by colleagues from LOG could give a better evaluation of our model results. The PLUME campaigns planned in 2022 onboard the Antea vessel in the Mekong and Red river plumes regions will allow to better characterize the composition of matter (chlorophyll, suspended sediment, organic matter…) in those regions.

Comparisons of Chl-a vertical profiles with in-situ measurements at southern Vietnam coasts and at SEATS site show that the model might underestimate these values in the upper 50 m on the shelf in summer and overestimate these values in the open sea in winter. However, comparisons with Argo-bio 2014/2015 at the SCS offshore zone show a lower modeled upper 50 m Chl-a than observations. These differences might be due to

the difference between the period of in-situ observations and of the simulation : in-situ profiles at SEATS point were collected in January 2000 - a La Niña year, the Argo-bio where deployed during 2014 - 2015 - an El Niño onset period, and our model ran from 2016 to 2017 - a neutral period (see Figure II.6, Chapter II). Studies of Liu et al. (2013) and Xiu et al. (2019) revealed a strong interannual variability of vertical distribution of nutrients and Chl-a in the SCS, especially during the ENSO periods. It is therefore essential to have real-time in-situ measurements to have a more accurate evaluation of the model performance, but also to extend our period of simulation over several years to examine the interannual variability.

With this promising preliminary study, further works have to be carried out to still improve the biogeochemical model. Longer simulations should be performed to better evaluate the model with corresponding observational data. With a well-adjusted coupled physical/biogeochemical model, we will then perform several studies on the nutrient transports, influences of physical forcings on the planktonic ecosystem, nutrients balances or carbon and nitrogen cycles, from the high frequency scale to the interannual scale.

References

Ablain. M, Cazenave. A, Larnicol. G, Balmaseda. M et al, 2015, Improved sea level record over the satellite altimetry era (1993–2010) from the Climate Change Initiative project, Ocean Sci., 11, 67-82, doi:10.5194/os-11-67-2015

Alford, M. H., Peacock, T., MacKinnon, J. A., Nash, J. D., Buijsman, M. C., Centurioni, L. R., … (David) Tang, T.-Y. (2015). The formation and fate of internal waves in the South China Sea. Nature, 521(7550), 65–69.doi:10.1038/nature14399

Anderson, T. R., and P. Pondaven. Non-redfield carbon and nitrogen cycling in the Sargasso Sea: pelagic imbalances and export flux, Deep-Sea Res., Part I, 50, 573–591, 2003

Arakawa, A., and M. J. Suarez, Vertical differencing of the primitive equations in sigma coordinates, Monthly Weather Review, 111, 34–45, 1983.

Ashok, K., Z. Guan, and T. Yamagata (2001), Impact of the Indian Ocean Dipole on the relationship between the Indian Monsoon Rainfall and ENSO. Zhaoyong Toshio Yamagata technique, Geophys. Res. Lett., 28 (23), 4499–4502, doi:10.1029/2001GL013294.

Auclair, F., Estournel, C., Floor, J.W., Herrmann, M., Nguyen, C., Marsaleix, P., 2011. A non-hydrostatic algorithm for free-surface ocean modelling. Ocean Model 36:49-70. http://dx.doi.org/10.1016/j.ocemod.2010.09.006.

Auger, P. a., Diaz, F., Ulses, C., Estournel, C., Neveux, J., Joux, F., Pujo-Pay, M. and Naudin, J. J. Functioning of the planktonic ecosystem on the Gulf of Lions shelf (NW Mediterranean) during spring and its impact on the carbon deposition: A field data and 3-D modelling combined approach, Biogeosciences, 8(11), 3231–3261, doi:10.5194/bg-8-3231-2011, 2011.

Auger, P. a., Ulses, C., Estournel, C., Stemmann, L., Somot, S. and Diaz, F. Interannual control of plankton communities by deep winter mixing and prey/predator interactions in the NW Mediterranean: Results from a 30-year

Baran E., Guerin E., Nasielski J. 2015 Fish, sediment and dams in the Mekong. Penang, Malaysia: WorldFish, and CGIAR Research Program on Water, Land and Ecosystems (WLE). 108 pp.

Boutin J., Vergely J. L., Marchand S., D'Amico F, Hasson A., Kolodziejczyk Nicolas, Reul Nicolas, Reverdin G., Vialard J. (2018). New SMOS Sea Surface Salinity with reduced systematic errors and improved variability. Remote Sensing Of Environment, 214, 115-134. https://doi.org/10.1016/j.rse.2018.05.022

Burchard H., Bolding L. (2001) Comparative analysis of four second-moment turbulence closing models for the oceanic mixed layer, J. of Physical Oceanogr.,31 (8), 1943-1968, http://journal.ametsoc.org/doi/abs/10.1175/1520-0485(2001)031%3C1943:CA0FSM%3E2.0.C0%3B2

Cai, W.-J., Dai, M., Wang, Y., Zhai, W., Huang, T., Chen, S., et al. (2004). The biogeochemistry of inorganic carbon and nutrients in the Pearl river estuary and the adjacent Northern South China sea. Cont. Shelf Res. 24, 1301–1319. doi: 10.1016/j.csr.2004.04.005.

Camargo, S. J., and A. H. Sobel, 2005: Western North Pacifictropical cyclone intensity and ENSO.J. Climate,18,2996–3006

Carrère, L., F. Lyard, M. Cancet, A. Guillot, and L. Roblou (2012), FES 2012: A new global tidal model taking advantage of nearly 20 years of altimetry, paper presented at The Symposium 20 Years of Progress in Radar Altimetry, Venice.

Canuto, V., Howard, A., Cheng, Y., Dubovikov, M., 2001. Ocean turbulence.C Part I: One-point closure model momentum and heat vertical diffusivities. J. Phys. Oceanogr. 31, 1413–1426.

Centurioni, L.R., Niiler, P.P., Lee, D.-K., 2004. Observations of Inflow of Philippine Sea Surface Water into the South China Sea through the Luzon Strait. Journal of Physical Oceanography 34, 113–121.

Chen, C.-T., and M. H. Huang, 1996: A mid-depth front separating the South China Sea water and the Philippine Sea water. J.Oceanogr., 52, 17–25.

Chen, Y. L. L., H. Y. Chen, D. M. Karl, and M. Takahashi (2004), Nitrogen modulates phytoplankton growth in spring in the South China Sea, Cont. Shelf Res., 24, 527–541.

Chen, C.-T.A., Hou, W.-P., Gamo, T., Wang, S.L., 2006. Carbonate-related parameters of subsurface waters in the West Philippine, South China and Sulu Seas. Marine Chemistry 99, 151–161.

Chen Y-L, Chen H-Y, Lin II, Lee M-A, Chang J (2007) Effects of cold eddy on phytoplankton production and assemblages in Luzon strait bordering the South China Sea. J Oceanogr 63:671–683. doi:10.1007/s10872-007-0059-9

Chen, G., Y. Hou, and X. Chu (2011), Mesoscale eddies in the South China Sea: Mean properties, spatiotemporal variability, and impact on thermohaline structure, J. Geophys. Res. Ocean. , 116 (6), 1–19, doi:10.1029/2010JC006716.

Chen, C., Z. Lai, R. C. Beardsley, Q. Xu, H. Lin, and N. T. Viet (2012), Current separation and upwelling over the southeast shelf of Vietnam in the South China Sea, J. Geophys. Res. , 117 (3), C03033, doi:10.1029/2011JC007150.

Chou C, Tu JY, Yu JY (2003) Interannual variability of the western North Pacific summer monsoon: differences between ENSO and non-ENSO years. J Clim 16:2275–2287

Chou, Wen-Chen, Sheu, David D., Chen, C. T. Arthur, Wen, Liang-Saw, Yang, Yih, Wei, Ching-Ling, 2007. Transport of the South China Sea subsurface water outflow and its influence on carbon chemistry of Kuroshio waters off southeastern Taiwan. J. Geophys. Res. 112 (C12). https://doi.org/10.1029/2007JC004087.

Chow, C. H., and Q. Liu (2012), Eddy effects on sea surface temperature and sea surface wind in the continental slope region of the northern South China Sea, Geophys. Res. Lett., 39, L02601, doi:10.1029/2011GL050230.

Chu, P., Y. Chen, and S. Lu (1998), Wind-driven South China Sea deep basin warm-core/cool-core eddies, J. Oceanogr. , 54 (1997), 347–360, doi:10.1007/BF02742619.

Chu P. C. and Li R., 2000. South China Sea isopycnal-surface circulation. Journal of Physical Oceanography, 30(9): 2419–2438.

Chung, S.W., Jan, S., Liu, K.K., 2001. Nutrient fluxes through the Taiwan Strait in spring and summer 1999. J. Oceanogr. 57, 47–53.

Craig P. D., Banner M. L. (1994) Modeling wave-enhanced turbulence in the ocean surface layer. J. of Phys. Oceanogr., 24(12), 2546-2559, doi:10.1175/1520-0485(1994)024<2546:MWETIT>2.0CO;2.

Doodson A. T. (1927) The analysis of tidal observations. Philosophical Transactions of the Royal Society of London, 227, 223-279.

Cullen, J. J. (2015). Subsurface Chlorophyll Maximum Layers: Enduring Enigma or Mystery Solved? Annual Review of Marine Science, 7(1), 207–239. doi:10.1146/annurev-marine-010213-135111

Da Nguyen Dac (2018), Variabilité interannuelle de l'upwelling du Sud Vietnam, PhD manuscrit, Université de Toulouse.

Da, N. D., Herrmann, M., Morrow, R., Niño, F., Huan, N. M., & Trinh, N. Q. (2019). Contributions of wind, ocean intrinsic variability and ENSO to the interannual variability of the South Vietnam Upwelling: A modeling study. Journal of Geophysical Research: Oceans, 124. https://doi.org/10.1029/2018JC014647.

Daryabor F, Ooi SH, Samah AA, Akbari A (2016) Dynamics of the Water Circulations in the Southern South China Sea and Its Seasonal Transports. PLoS ONE 11(7): e0158415. doi:10.1371/journal.pone.0158415

Donlon, C. J., M. Martin, J. D. Stark, J. Roberts-Jones, E. Fiedler and W. Wimmer, 2011. The Operational Sea Surface Temperature and Sea Ice analysis (OSTIA). Remote Sensing of the Environment. doi: 10.1016/j.rse.2010.10.017 2011.

Dippner, J. J. W., K. K. V. Nguyen, H. Hein, T. Ohde, and N. Loick (2007), Monsoon-induced upwelling off the Vietnamese coast, Ocean Dyn. , 57 (1), 46–62, doi:10.1007/s10236-006-0091-0.

Du, C., Liu, Z., Dai, M., Kao, S. J., Cao, Z., Zhang, Y., Huang, T., Wang, L., and Li, Y.: Impact of the Kuroshio intrusion on the nutrient inventory in the upper northern South China Sea: insights from an isopycnal mixing model, Biogeosciences, 10, 6419–6432, doi:10.5194/bg-10-6419-2013, 2013.

Duan, R., K. Yang, Y. Ma, and T. Hu (2012), A study of the mixed layer of the South China Sea based on the multiple linear regression, Acta Oceanol. Sin., 31, 19–31

Dukhovskoy, D.S., Morey, S.L., Martin, P.J., O'Brien, J.J., Cooper, C., 2009. Application of a vanishing, quasi-sigma, vertical coordinate for simulation of high-speed, deep currents over the Sigsbee Escarpment in the Gulf of Mexico. Ocean Modelling 28, 250–265.

Estournel, C., et al. (2012), Assessment of the amount of cesium-137 released into the Pacific Ocean after the Fukushima accident and analysis of its dispersion in Japanese coastal waters, J. Geophys. Res., 117, C11014, doi:10.1029/2012JC007933.

Estournel, C., et al. (2016), High resolution modeling of dense water formation in the north-western Mediterranean during winter 2012–2013: Processes and budget, J. Geophys. Res. Oceans, 121, 5367–5392, doi:10.1002/2016JC011935.

Fang, G., Zhao, B., Zhu, Y., 1991. Water volume transport through the Taiwan Strait and the continental shelf of the East China Sea measured with current meters. In: Takano, K. (Ed.), Oceanography of Asian Marginal Seas. Elsevier, New York, pp. 345–358.

Fang, G., Kwok, Y. K., Yu, K., and Zhu, Y.: Numerical simulation of principal tidal constituents in the South China Sea, Gulf of Tonkin and Gulf of Thailand, Cont. Shelf Res., 19, 845–869, 1999.

Fang W, Fang G, Shi P, Huang Q, Xie Q. (2002). Seasonal structures of upper layer circulation in the South China Sea from in situ observations. J. Geophys. Res., 107(C11): 3 202.

Fang Guohong, Wei Zexun, B. H. Choi, Wang Kai, Fang Yue, and Li Wei, 2003: Interbasin freshwater, heat and salt transport through the boundaries of the East and South China Seas from a variable-grid global ocean circulation model. Science in China (D), 46(2), 149–161.

Fang, G., Susanto, D., Soesilo, I., Zheng, Q., Qiao, F., Wei, Z., 2005. A note on the South China Sea shallow interocean circulation. Adv. Atmos. Sci. 22, 946–954.

Fang Guohong, Chen Haiying, Wei Zexun, et al. 2006. Trends and interannual variability of the South China Sea surface winds, surface height, and surface temperature in the recent decade. Journal of Geophysical Research: Oceans, 111(C11): C11S16

Fang G., Wang Y., Wei Z., Fang Y., Qiao F., and Hu X., 2009. Interocean circulation and heat and freshwater budgets of the South China Sea based on a numerical model. Dynam. Atmos. Oceans, 47, 55–72.

Fang Guohong, Susanto R D, Wirasantosa S, et al. 2010. Volume, heat and freshwater transports from the South China Sea to Indonesian seas in the boreal winter of 2007–2008. J Geophys Res, 115: C12020, doi:10.1029/2010JC006225

Fortes, M. (2006). Seas of East Asia, p 177 -192 in: UNEP/GPA (2006), The State of the Marine Environment: Regional Assessments. UNEP/GPA, The Hague.

Gan, J., H. Li, E. N. Curchitser, and D. B. Haidvogel (2006), Modeling South China Sea circulation: Response to seasonal forcing regimes, J. Geophys. Res., 111, C06034, doi:10.1029/2005JC003298.

Gan, J., L. Li, D. Wang, and X. Guo (2009), Interaction of a river plume with coastal upwelling in the northeastern South China Sea, Cont. Shelf Res., 29(4), 728–740, doi:10.1016/j.csr.2008.12.002.

Gan, J., Z. Liu, and C. Hui, 2016: A three-layer alternating spinning circulation in the South China Sea. J. Phys. Oceanogr. doi:10.1175/JPO-D-16-0044.1, in press.

Garau, B., S. Ruiz, W.G. Zhang, A. Pascual, E. Heslop, J. Kerfoot, and J. Tintoré, 2011: Thermal Lag Correction on Slocum CTD Glider Data. J. Atmos. Oceanic Technol., **28**, 1065–1071, https://doi.org/10.1175/JTECH-D-10-05030.1

Garcia, H. E., & Gordon, L. I. (1992). Oxygen solubility in seawater: Better fitting equations. Limnology and Oceanography, 37(6), 1307–1312. doi:10.4319/lo.1992.37.6.1307

Gaspar P., Gregoris Y., Lefevre J.M. (1990) A simple eddy kinetic energy model for simulations of the oceanic vertical mixing: tests at station Papa and long-term upper ocean study site. J.of Geophys. Res., 95,16179–16193.

Goh, A. Z. C., and J. C. L. Chan (2010), Interannual and interdecadal variations of tropical cyclone activity in the South China Sea, Int. J. Climatol., 30(6), 827–843, doi:10.1002/joc.1943.

Godfrey, J. S. (1989), A Sverdrup model of the depth-integrated flow for the world ocean allowing for island circulations, Geophys. Astrophys. Fluid Dyn., 45, 89 – 112.

Gordon, A. L., Sprintall, J., Van Aken, H. M., Susanto, D., Wijffels, S., Molcard, R., … Wirasantosa, S. (2010). The Indonesian throughflow during 2004–2006 as observed by the INSTANT program. Dynamics of Atmospheres and Oceans, 50(2), 115–128.doi:10.1016/j.dynatmoce.2009.12.002

Gong, X., Shi, J., & Gao, H. (2014). Modeling seasonal variations of subsurface chlorophyll maximum in South China Sea. Journal of Ocean University of China, 13(4), 561–571.doi:10.1007/s11802-014-2060-4

Gordon, A. L., Z. D. Tessler, and C. Villanoy (2011), Dual overflows into the deep Sulu Sea, Geophys. Res. Lett., 38, L18606, doi:10.1029/2011GL048878.

Guo, M., Chai, F., Xiu, P., Li, S., & Rao, S. (2015). Impacts of mesoscale eddies in the South China Sea on biogeochemical cycles. Ocean Dynamics, 65(9-10), 1335–1352. doi:10.1007/s10236-015-0867-1

Griffies, S., and R. Hallberg (2000), Biharmonic friction with a Smagorinsky-like viscosity for use in large-scale eddy-permitting ocean models, Mon. Weather Rev., 128(8), 2935–2946, doi:10.1175/1520-0493(2000)128 < 2935:BFWASL>2.0.CO;2.

Han, G., Huang, W., 2008. Pacific decadal oscillation and sea level variability in the Bohai, Yellow, and East China Seas. J. Phys. Oceanogr. 38 (12).

He Y, Guan C, Gan Z (1997) Interannual and interdecadal variations in heat content of the upper ocean of the South China Sea. Adv Atmos Sci 14:271–276

He Zhigang, Feng Ming, Wang Dongxiao, et al. 2015. Contribution of the Karimata Strait transport to the Indonesian Throughflow as seen from a data assimilation model. Continental Shelf Research, 92: 16–22, doi: 10.1016/j.csr.2014.10.007

He, Q., Zhan, H., Cai, S., & Li, Z. (2016). Eddy effects on surface chlorophyll in the northern South China Sea: Mechanism investigation and temporal variability analysis. Deep Sea Research Part I: Oceanographic Research Papers, 112, 25– 36. https://doi.org/10.1016/j.dsr.2016.03.004

Heileman, S., 2009. VIII-15 South China Sea: LME #36. Semantic scholar. Corpus ID: 150379332.

Hein, H. (2008), Vietnam Upwelling, Hamburg.

Herrmann, M. J., and S. Somot (2008), Relevance of ERA40 dynamical downscaling for modeling deep convection in the Mediterranean Sea, Geophys. Res. Lett., 35, L04607, doi:10.1029/2007GL032442.

Herrmann, M., S. Somot, F. Sevault, C. Estournel, and M. Déqué (2008), Modeling the deep convection in the northwestern Mediterranean Sea using an eddy-permitting and an eddy-resolving model: Case study of winter 1986 – 1987, J. Geophys. Res., 113,C04011, doi:10.1029/2006JC003991.

Herrmann, M., Diaz, F., Estournel, C., Marsaleix, P., Ulses, C (2013). Impact of atmospheric and oceanic interannual variability on the Northwestern Mediterranean Sea pelagic planktonic ecosystem and associated carbon cycle. Journal of Geophysical Research – Oceans 118, 5792–5813

M. Herrmann, C. Estournel, F. Adloff, F. Diaz (2014). Impact of climate change on the northwestern Mediterranean Sea pelagic planktonic ecosystem and associated carbon cycle. J. Geophys. Res., 119, 5815-5836, doi:10.1002/2014JC010016.

Herrmann, M., Auger, P.-A., Ulses, C. and Estournel, C. (2017), Long-term monitoring of ocean deep convection using multisensors altimetry and ocean color satellite data. J. Geophys. Res. Oceans. doi:10.1002/2016JC011833

Herrmann, M., Ngo-Duc, T., & Trinh-Tuan, L. (2019). Impact of climate change on sea surface wind in Southeast Asia, from climatological average to extreme events: results from a dynamical downscaling. Climate Dynamics. doi:10.1007/s00382-019-05103-6

Ho, C.-R., Q. Zheng, Y. S. Soong, N.-J. Kuo, and J.-H. Hu (2000), Seasonal variability of sea surface height in the South China Sea observed with TOPEX/POSEIDON altimeter data, J. Geophys. Res., 105, 13,981-13,990.

Hsin, Y.-C., C.-R. Wu, and S.-Y. Chao (2012), An updated examination of the Luzon Strait transport, J. Geophys. Res., 117, C03022, doi:10.1029/2011JC007714.

Hu, J., Kawamura, H., Hongi, H., Qi, Y., 2000. A review on the currents in the South China Sea: Seasonal circulation, South China Sea Warm Current and Kuroshio intrusion. Journal of Oceanography 56, 607–624.

Hu, J., and X. H. Wang (2016), Progress on upwelling studies in the China seas, Rev. Geophys., 54, 653–673, doi:10.1002/2015RG000505.

Hung, B.V., 2017. Identify the major reasons to cause vulnerability to Mekong delta under the impacts of drought and climate change. In: Trends in Asian Water Environmental Science and Technology. Springer International Publishing, Cham, pp. 211–222. http://dx.doi.org/10.1007/978-3-319-39259-2_18

Huynh, H.-N.T.; Alvera-Azcárate, A.; Barth, A.; Beckers, J.-M. Reconstruction and Analysis of Long-Term Satellite-Derived Sea Surface Temperature for the South China Sea. J. Oceanogr. **2016**, 72, 707–726.

Isoguchi, O.; Kawamura, H. MJO-related summer cooling and phytoplankton blooms in the South China Sea in recent years. Geophys. Res. Lett. **2006**, 33.

Jackett, D.R., McDougall, T.J., Feistel, R., Wright, D.G., Griffies, S.M., 2006. Algorithms for density, potential temperature, conservative temperature, and the freezing temperature of seawater. J. Atmos. Ocean. Technol. 23, 1709–1728.

Jan, S., Chern, C.-S., Wang, J., Chao, S.-Y., 2007. Generation of diurnal K1 internal tide in the Luzon Strait and its influence on surface tide in the South China Sea, Journal of Geophysical Research 112, C06019, doi:10.1029/2006JC004003.

Jickells, T. D., et al. (2017), A reevaluation of the magnitude and impacts of anthropogenic atmospheric nitrogen inputs on the ocean, Global Biogeochem. Cycles, 31, 289–305, doi:10.1002/2016GB005586

Jing, Z. Y., Qi, Y. Q., and Du, Y.: Upwelling in the continental shelf of northern South China Sea in recent years, J. Geophys. Res., 116, C02033, doi:10.1029/2010JC006598, 2011.

Juneng, L. and Tangang, F.: Evolution of ENSO-related rainfall anomalies in Southeast Asia region and its relationship with atmosphere–ocean variations in Indo-Pacific sector, Clim. Dynam., 25, 337–350, 2005.

Kalnay, E. et al. (1996), The NCEP/NCAR 40-Year Reanalysis Project, Bull. Am. Meteorol. Soc., 77 (3), 437–471, doi:10.1175/1520-0477(1996)077<0437:TNYRP>2.0.CO;2.

Kessouri F (2015). Cycles biogéochimiques de la Mer Méditerranée : Processus et bilans. PhD thesis. Université de Toulouse 3.

Kessouri F. et al., Nitrogen and Phosphorus Budgets in the Northwestern Mediterranean Deep Convection Region. Journal of Geophysical Research – Oceans 122 (12), 9429-9454. 2017

Kessouri, F., Ulses, C., Estournel, C., Marsaleix, P., D'Ortenzio, F., Severin, T., … Conan, P. (2018). Vertical Mixing Effects on Phytoplankton Dynamics and Organic Carbon Export in the Western Mediterranean Sea. Journal of Geophysical Research: Oceans, 123(3), 1647-1669. doi:10.1002/2016jc012669

Klein, S. A., B. J. Soden, and N. C. Lau, 1999: Remote sea surface temperature variations during ENSO: Evidence for a tropical Atmospheric bridge. J. Clim., 12, 917-932.

Kobayashi, S., Y. Ota, Y. Harada, A. Ebita, M. Moriya, H. Onoda, K. Onogi, H. Kamahori, C. Kobayashi, H. Endo, K. Miyaoka, and K. Takahashi, 2015: The JRA-55 Reanalysis: General Specifications and Basic Characteristics. J. Met. Soc. Jap., **93(1)**, 5-48 (DOI: 10.2151/jmsj.2015-001).

Krishnamurthy, L., & Krishnamurthy, V. (2014). Influence of PDO on South Asian summer monsoon and monsoon–ENSO relation. Climate Dynamics, 42(9–10), 2397–2410. https://doi.org/10.1007/s00382-013-1856-z.

Kumar, A., B. Jha, and M. L'Heureux (2010), Are tropical SST trends changing the global teleconnection during La Niña?, Geophys. Res. Lett., 37, L12702, doi:10.1029/2010GL043394.

Kuo, N.-J., Q. Zheng, and C.-R. Ho, Satellite observation of upwelling along the western coast of the South China Sea, Remote Sens. Environ., 74, 463–470, 2000.

Lan J., Wang Y., Cui F. and Zhang N., 2015. Seasonal variation in the South China Sea deep circulation. J Geophys Res, 120: 1682–1690.

Large W., Yeager S. (2004) Diurnal to decadal global forcing for ocean and sea-ice models: The data sets and flux climatologies, UCAR/NCAR, https://doi.org/10.5065/D6KK98Q6

Lawrence, D. M., and Webster, P. J. (2002). The boreal summer intra-seasonal oscillation: Relationship between northward and eastward movement of convection. J. Atmos. Sci. 59, 1593–1606. doi: 10.1175/1520-04692002059<1593:TBSIOR<2.0.CO;2

Lau, K. M., and S. Yang (1997), Climatology and interannual variability of the southeast asian summer monsoon, Adv. Atmos. Sci., 14 (2), 141–162, doi:10.1007/s00376-997-0016-y.

Le, T. P. Q., Garnier, J., Billen, G., Thery, S., & Chau, V. M. (2007). The changing flow regime and sediment load of the Red River, Vietnam. Journal of Hydrology, 334, 199–214.

Leonard, B.P. (1979). A stable and accurate convection modelling procedure based on quadratic upstream interpolation, Comput. Meth. Appl. Mech. Eng. 19, 59 (1979).

Li, L., W. D. Nowlin, and S. Jilan (1998), Anticyclonic rings from the Kuroshio in the South China Sea, Deep. Res. Part I Oceanogr. Res. Pap. , 45 (9), 1469–1482, doi:10.1016/S0967-0637(98)00026-0.

Li, Z., Y. Saito, E. Matsumoto, Y. Wang, S. Tanabe, and Q. L. Vu (2006), Climate change and human impact on the Song Hong (Red River) Delta, Vietnam, during the Holocene, Quat. Int., 144 (1), 4–28, doi:10.1016/j.quaint.2005.05.008.

Li L. and T. Qu, 2006. Thermohaline circulation in the deep South China Sea basin inferred from oxygen distributions. J. Geophys. Res., 111, C05017, doi:10.1029/2005JC003164.

Li, G., Y. Zhang, J. Xiao, et al. 2019. Examining the salinity change in the upper Pacific Ocean during the Argo period. Clim. Dyn. 53: 6055– 6074.

Lin, I-I, C.-C. Lien,C.-R. Wu, G. T. F. Wong, C.-W. Huang, and T.-L. Chiang(2010), Enhanced primary production in the oligotrophic SouthChina Sea by eddy injection in spring, Geophys. Res. Lett., 37,L16602, doi:10.1029/2010GL043872.

Lin, I.-I. (2012). Typhoon-induced phytoplankton blooms and primary productivity increase in the western North Pacific subtropical ocean. Journal of Geophysical Research: Oceans, 117(C3), n/a–n/a. doi:10.1029/2011jc007626

Liu, K.-K., Chao, S.-Y., Shaw, P.-T., Gong, G.-C., Chen, C.-C., & Tang, T. Y. (2002). Monsoon-forced chlorophyll distribution and primary production in the South China Sea: observations and a numerical study. Deep Sea Research Part I: Oceanographic Research Papers, 49(8), 1387–1412.doi:10.1016/s0967-0637(02)00035-3

Liu, K.-K., Chen, Y.-J., Tseng, C.-M., Lin, I.-I., Liu, H.-B., & Snidvongs, A. (2007). The significance of phytoplankton photo-adaptation and benthic–pelagic coupling to primary production in the South China Sea: Observations and numerical investigations. Deep Sea Research Part II: Topical Studies in Oceanography, 54(14-15), 1546–1574.doi:10.1016/j.dsr2.2007.05.009

Liu, Y., R. H. Weisberg, and Y. Yuan (2008), Patterns of upper layer circulation variability in the South China Sea from satellite altimetry using the self-organizing map, Acta Oceanol. Sin., 27(suppl.), 129–144.

Liu, J. P., Liu, C. S., Xu, K. H., Milliman, J. D., Chiu, J. K., Kao, S. J., et al. (2008). Flux and fate of small mountainous rivers derived sediments into the Taiwan Strait. Marine Geology, 256, 65–76.

Liu, G., and Chai, F. 2009. Seasonal and interannual variability of primary and export production in the South China Sea: a three-dimensional physical – biogeochemical model study. – ICES Journal of Marine Science, 66: 420– 431.

Liu, K.-K., Wang, L.-W., Dai, M., Tseng, C.-M., Yang, Y., Sui, C.-H., … Huang, S.-M. (2013). Inter-annual variation of chlorophyll in the northern South China Sea observed at the SEATS Station and its asymmetric responses to climate oscillation. Biogeosciences, 10(11), 7449–7462. doi:10.5194/bg-10-7449-2013

Liu, N., C. Eden, H. Dietze, D. Wu, and X. Lin (2010), Model-based estimate of the heat budget in the East China Sea, J. Geophys. Res., 115, C08026, doi:10.1029/2009JC005869.

Liu, Q., Feng, M., & Wang, D. (2011). ENSO-induced interannual variability in the southeastern South China Sea.Journal of Oceanography. 67(1), 127–133. https://doi.org/10.1007/s10872-011-0002-y

Liu, Q. Y., R. X. Huang, and D. X. Wang, 2012: Implication of the South China Sea throughflow for the interannual variability of the regional upper-ocean heat content. Adv. Atmos. Sci., 29(1), 54–62, doi: 10.1007/s00376-011-0068-x.

Liu, X., Wang, J., Cheng, X., and Du, Y.: Abnormal upwelling and chlorophyll-a concentration off South Vietnam in summer 2007, J. Geophys. Res., 117, C07021, doi:10.1029/2012JC008052, 2012.

Liu JY (2013) Status of Marine Biodiversity of the China Seas. PLoSONE 8(1): e50719. doi:10.1371/journal.pone.0050719

Liu, Q.-Y., D. Wang, X. Wang, Y. Shu, Q. Xie, and J. Chen (2014), Thermal variations in the South China Sea associated with the eastern and central Pacific El Niño events and their mechanisms, J. Geophys. Res. Oceans, 119, 8955–8972, doi:10.1002/2014JC010429.

Liu, K.-K., Kang, C.-K., Kobari, T., Liu, H., Rabouille, C., & Fennel, K. (2014). Biogeochemistry and ecosystems of continental margins in the western North Pacific Ocean and their interactions and responses to external forcing - an overview and synthesis. Biogeosciences, 11(23), 7061–7075. doi:10.5194/bg-11-7061-2014

Liu, Z. and J. Gan (2017), Three-dimensional pathways of water masses in the South China Sea: A modeling study, J. Geophys. Res. Oceans, 122, 6039–6054, doi:10.1002/ 2016JC012511.

Liu, F., Ouyang, Y., Wang, B., Yang, J., Ling, J., and Hsu, P.-C. (2020). Seasonal evolution of the intraseasonal variability of China summer precipitation. Clim. Dyn. 54, 4641–4655. doi: 10.1007/s00382-020-05251-0

Liu, K.S., Chan, J.C.L. Recent increase in extreme intensity of tropical cyclones making landfall in South China. Clim Dyn 55, 1059–1074 (2020). https://doi.org/10.1007/s00382-020-05311-5

Loick, N., J. Dippner, H. N. Doan, I. Liskow, and M. Voss (2007a), Pelagic nitrogen dynamics in the Vietnamese upwelling area according to stable nitrogen and carbon isotope data, Deep. Res. Part I Oceanogr. Res. Pap. , 54 (4), 596–607, doi:10.1016/j.dsr.2006.12.009.

Lu FH, Ni HG, Liu F, Zeng EY (2009) Occurrence of nutrients in riverine runoff of the Pearl River Delta, South China. J Hydrol 376:107–115

Lukas, R., T. Yamagata, and J.P. McCreary, Pacific low-latitude western boundary currents and the Indonesian throughflow, J. Geophys. Res., 101 (C5), 12209-12216, 1996

Lyard, F., Lefevre, F., Letellier, T. et al. Modelling the global ocean tides: modern insights from FES2004.Ocean Dynamics 56, 394–415 (2006). https://doi.org/10.1007/s10236-006-0086-x

Madden, R. a., and P. R. Julian (1972), Description of Global-Scale Circulation Cells in the Tropics with a 40–50 Day Period, J. Atmos. Sci. 29, (6), 1109–1123, doi:10.1175/1520-0469(1972)029<1109:DOGSCC>2.0.CO;2.

Madden, R. A., and P. R. Julian (1971), Detection of a 40–50 Day Oscillation in the Zonal Wind in the Tropical Pacific, J. Atmos. Sci., 28 (5), 702–708, doi:10.1175/1520-0469(1971)028<0702:DOADOI>2.0.CO;2.

Madden, R. A., and P. R. Julian (1994), Observations of the 40–50-Day Tropical Oscillation A

Review, Mon. Weather Rev. 122 (5), 814–837, doi:10.1175/1520-0493(1994)122<0814:OOTDTO>2.0.CO;2.

Marsaleix P., Auclair F., Estournel C., 2006, Considerations on Open Boundary Conditions for Regional and Coastal Ocean Models. Journal of Atmospheric and Oceanic Technology, 23,1604-1603, http://dx.doi.org/10.1175/JTECH1930.1

Marsaleix P., Auclair F., Floor J. W., Herrmann M. J., Estournel C., Pairaud I., Ulses C., 2008. Energy conservation issues in sigma-coordinate free-surface ocean models. Ocean Modelling. 20, 61-89. http://dx.doi.org/10.1016/j.ocemod.2007.07.005

Marsaleix P., Auclair F., Estournel C., 2009. Low-order pressure gradient schemes in sigma coordinate models: The seamount test revisited. Ocean Modelling, 30, 169-177. http://dx.doi.org/10.1016/j.ocemod.2009.06.011

Marsaleix P., Auclair F., Duhaut T., Estournel C., Nguyen C., Ulses C. (2012) Alternatives to the Robert-Asselin filter. Oc. Modell., 41, 53-66, doi: 10.1016/j.ocemod.2011.11.002.

Marsaleix, P., Michaud, H., Estournel, C., 2019. 3D phase-resolved wave modelling with a non-hydrostatic ocean circulation model. Ocean Modelling, 136, 28-50. https://doi.org/10.1016/j.ocemod.2019.02.002

Mao, Q., P. Shi, K. Yin, J. Gan, and Y. Qi (2004), Tides and tidal currents in the Pearl River Estuary, Cont. Shelf Res. , 24 (16), 1797–1808, doi:10.1016/j.csr.2004.06.008.

Martin, M.J., A. Hines and M.J. Bell, 2007. Data assimilation in the FOAM operational short-range ocean forecasting system: a description of the scheme and its impact. Q.J.R. Meteorol. Soc., **133**:981-995.

Masumoto, Y., Miyazawa, Y., Tsumune, D., Tsubono, T., Kobayashi, T., Kawamura, H., Estournel, C., Marsaleix, P., Lanerolle, L., Mehra, A., Garraffo, Z.D., 2012. Oceanic dispersion simulations of 137Cs released from the Fukushima Daiichi nuclear power plant. Elements 8, 207–212.

McGregor, H.V., Dima, M., Fischer, H.W. and Mulitza, S. 2007. Rapid 20th-century increase in coastal upwelling off northwest Africa. Science **315**: 637-639.

Menkes, C. E., Lengaigne, M., Lévy, M., Ethé, C., Bopp, L., Aumont, O., … Jullien, S. (2016). Global impact of tropical cyclones on primary production. Global Biogeochemical Cycles, 30(5), 767–786. doi:10.1002/2015gb005214

Metzger E J, Hurlburt H E, Xu X, et al. 2010. Simulated and observed circulation in the Indonesian seas: 1/12° Global HYCOM and the INSTANT observations. Dyn Atmos Oceans, 50: 275–300. doi:10.1016/j.dynatmoce.2010.04.002

Michaud, H., Marsaleix, P., Leredde, Y., Estournel, C., Bourrin, F., Lyard, F., Mayet, C.,Ardhuin, F., 2011. Three-dimensional modelling of wave-induced current from the surf zone to the inner shelf. Ocean Sci. Discuss. 8:2417–2478.http://dx.doi.org/10.5194/osd-8-2417-2011.

Michaud H., Marsaleix P., Leredde Y., Estournel C., Bourrin F., Lyard F., Mayet C., Ardhuin F., 2012. Three-dimensional modelling of wave-induced current from the surf zone to the inner shelf. Ocean Science, 8, 657-681, http://dx.doi.org/10.5194/os-8-657-2

Naess, T. (1999). Environment and Security in the South China Sea Region: The Role of Experts, Non-government Actors and Governments in Regime Building Processes. Ph.D. Thesis, University of Oslo, Oslo, Norway.

Nan, F., Xue, H., Chai, F., Wang, D., Yu, F., Shi, M., Guo, P., 2013. Weakening of the Kuroshio intrusion into the South China Sea over the past two decades. Journal of Climate, doi: http://dx.doi.org/10.1175/JCLI-D-12-00315.1.

Nan, F., Xue, H., & Yu, F. (2015). Kuroshio intrusion into the South China Sea: A review. Progress in Oceanography, 137, 314–333.doi:10.1016/j.pocean.2014.05.012

Neelin JD, Latif M (1998) El Niño dynamics. Phys Today 51:32–36

Ning X, Peng X, Le F, Hao Q, Sun J, Liu C, Cai Y (2008) Nutrient limitation of phytoplankton in anticyclonic eddies of the northern South China Sea. Biogeosciences Discuss 5:4591–4619. doi:10.5194/bgd-5-4591-2008

Nitani, H., 1972. Beginning of the Kuroshio. In: Stommel, H., Yashida, K. (Eds.), Kuroshio: Physical Aspects of the Japan Current. University of Washington Press, pp. 129–163.

Ng, P.K.L., Tan, K.S., 2000. The state of marine biodiversity in the South China Sea. Raffles Bull. Zool. 48, 3-7.

Oberhuber, J. M., 1988: An atlas based on COADS dataset: The budget of heat, buoyancy and turbulent kinetic energy at the surface of the Global Ocean. MPI Rep. 15, 1999 pp.

Pairaud I. L., Lyard F., Auclair F., Letellier T., Marsaleix P.: Dynamics of the semi-diurnal and quarter-diurnal internal tides in the Bay of Biscay. Part 1 : barotropic tides, Cont. Shelf. Res., 28 (10-11), 1294-1315, http://dx.doi.org/10.1016/j.csr.2008.03.004 , 2008.

Pairaud I., Staquet C., Sommeria J., Mahdizadeh M.M. (2010) Generation of harmonics and subharmonics from an internal tide in a uniformly stratified fluid: numerical and laboratory experiments. In: Dritschel D. (eds) IUTAM Symposium on Turbulence in the Atmosphere and Oceans. IUTAM Book Series, vol 28. Springer, Dordrecht. https://doi.org/10.1007/978-94-007-0360-5_5

Park, Y.-G., Choi, A., Long-term changes of South China Sea surface temperatures in winter and summer. Continental Shelf Research (2016), http://dx.doi.org/10.1016/j.csr.2016.07.019i

Peng, D., Palanisamy, H., Cazenave, A., Meyssignac, B., 2013. Interannual sea level variations in the South China Sea over 1950–2009. Mar. Geod. 36 (2), 164–182.

Perry, G.D., Duffy, P.B., Miller, N.I., 1996. An extended data set of river discharges for validation of general circulation models. J. Geophys. Res. 101 (D16), 21339–21349.

Phan, H. M., Ye, Q., Reniers, A. J. H. M., & Stive, M. J. F. (2019). Tidal wave propagation along The Mekong deltaic coast. Estuarine, Coastal and Shelf Science. doi:10.1016/j.ecss.2019.01.026

Pickard G.L. and W.J. Emery. 1990. Descriptive Physical Oceanography, 5 th (SI) Enlarged\ Edition, Butterworth-Heinemann, 320 pp.

Pinxian Wang, Qianyu Li & Chun-Feng Li, 2014. Geology of the China Seas. Development in Marine Geology, Volume 6. Elsevier. ISBN: 978-0-444-59388-7

Piton, V., 2019. Du Fleuve Rouge au Golfe du Tonkin: dynamique et transport sédimentaire le long du continuum estuaire-zone côtière. Doctoral dissertation. Université de Toulouse, Toulouse, France.

Piton, V., Herrmann, M., Lyard, F., Marsaleix, P., Duhaut, T., Allain, D., & Ouillon, S. (2020). Sensitivity study on the main tidal constituents of the Gulf of Tonkin by using the frequency-domain

tidal solver in T-UGOm. Geoscientific Model Development, 13(3), 1583–1607. doi:10.5194/gmd-13-1583-2020

Polling, G.B., 2019. Illuminating the South China Sea's Dark Fishing Fleets. https://www.ocean.csis.org

Qu, T. (2000), Upper-layer circulation in the South China Sea, J. Phys. Oceanogr., 30, 1450–1460, doi:10.1175/1520-0485(2000)030<1450: ULCITS>2.0.CO;2.

Qu, T., Y. Y. Kim, M. Yaremchuk, T. Tozuka, A. Ishida, and T. Yamagata (2004), Can the Luzon Strait transport play a role in conveying the impact of ENSO to the South China Sea?, J. Clim., 17, 3644–3657, doi:10.1175/ 1520-0442(2004)017<3644:CLSTPA>2.0.CO;2.

Qu, T., Du, Y., Meyers, G., Ishida, A., Wang, D., 2005. Connecting the tropical Pacific with Indian Ocean through South China Sea. Geophys. Res. Lett. 32, L24609, doi:10.1029/2005GL024698.

Qu, T., Du, Y., Sasaki, H., 2006. South China Sea throughflow: a heat and freshwater conveyor. Geophys. Res. Lett. 33, L23617, doi:10.1029/2006GL028350.

Qu, T., and Y. T. Song (2009), Mindoro Strait and Sibutu Passage transports estimated from satellite data, Geophys. Res. Lett., 36, L09601, doi:10.1029/2009GL037314.

Qu, HJ and Kroeze, C. 2011. Nutrient export by rivers to the coastal waters of China: management strategies and future trends. Region Environ Change, doi: 10.1007/s10113-011-0248-3, published online 04 August 2011.

Raick, C., Delhez, E. J. M., Soetaert, K. and Grégoire, M. Study of the seasonal cycle of the biogeochemical processes in the Ligurian Sea using a 1D interdisciplinary model, J. Mar. Syst., 55(3-4), 177–203, doi: 10.1016/j.jmarsys.2004.09.005, 2005.

Randall,1. E. & K. K. P. Lim (eds.), 1999. A checklist of the fishes of the South China Sea. Raffles Bull. Zool., Suppl. 7: 569-667.

Räsänen, T. A. and Kummu, M.: Spatiotemporal influences of ENSO on precipitation and flood pulse in the Mekong River Basin, J. Hydrol., 476, 154–168, 2013.

Räsänen, T. A., Lindgren, V., Guillaume, J. H. A., Buckley, B. M., & Kummu, M. (2016). On the spatial and temporal variability of ENSO precipitation and drought teleconnection in mainland Southeast Asia. CLIMATE OF THE PAST, 12(9), 1889-1905. https://doi.org/10.5194/cp-12-1889-2016

Ray R.D. and Zaron E.D, 2015, M2 internal tides and their observed wavenumber spectra from satellite altimetry, J. Phys. Oceanogr., 46, doi: 10.1175/JPO-D-15-0065.1

Reffray, G., P. Fraunié, and P. Marsaleix (2004), Secondary flows induced by wind forcing in the Rhône region of freshwater influence, Ocean Dyn., 54, 179–196, doi:10.1007/s10236-003-0079-y.

Rogowski, P., J. Zavala-Garay, K. Shearman, E. Terrill, J. Wilkin, and T.H. Lam. 2019. Air-sea-land forcing in the Gulf of Tonkin: Assessing seasonal variability using modern tools. Oceanography 32(2):150–161, https://doi.org/10.5670/oceanog.2019.223.

Rojana-anawat, P., Sukramongkol, N., Pradit, S., 2000, Characteristics of water in the South China Sea, Area III: Western Philippines. Proceedings of the Third Technical Seminar on Marine Fishery Resources Survey in the South China Sea, Area III: Western Philippines, pp. 291-307.

Rojana-anawat, P., Pradit, S., Sukramongkol, N., Siriraksophon, S., 2001. Temperature, salinity, dissolved oxygen and water masses of Vietnamese waters. Proceedings of the SEAFDEC Seminar on Fisheries Resources in the South China Sea, Area 4: Vietnamese Waters, 346–355

Rong Z., Liu Y. and Zong H. et al. 2007. Interannual sea level variability in the South China Sea and its response to ENSO. Global and Planetary Change, 55: 257–272.

Saadon, M. N., P. Rojana-anawat and A. Snidvongs (1999a): Physical characteristics of water mass in the South China Sea, Area I: Gulf of Thailand and east Coast of Peninsula Malaysia. Proceedings of the 1st Technical Seminar on Marine Fishery Resources Survey in the South China Sea, Area I, 1–5.

Saadon, N., Kin, L.P., Snidvongs, A. and Rojana-Anawat, P. (1999b) Physical characteristics of water mass in the South China Sea, Area II: Sarawak, Sabah and Brunei Darussalam waters. Proceedings of the Second Technical Seminar on Marine Fishery Resources Survey in the South China Sea, Area II: West Coast of Sabah, Sarawak and Brunei Darussalam, pp. 1-22.

Saha, S. et al. (2010), The NCEP climate forecast system reanalysis, Bull. Am. Meteorol. Soc. , 91 (8), 1015–1057, doi:10.1175/2010BAMS3001.1.

Saji, N. H., P. N. Vinayachandran, and T. Yamagata (1999), A dipole in the tropical Indian Ocean, Nature, 401 (September), 360–363.

Saito, Y., Chaimanee, N., Jarupongsakul, T., & Syvitski, J. P. M. (2007). Shrinking mega-deltas in Asia: Sea-level rise and sediment reduction impacts from case study of the Chao Phraya Delta. Inprint Newsletter of the IGBP/IHDP Land Ocean Interaction in the Coastal Zone, 2007(2), 3–9.

Sasai, Y., Sasaki, H., and Richards, K. J.: Impact of physical processes on the phytoplankton blooms in the South China Sea: an eddy-resolving physical-biological model study, Biogeosciences Discuss., 10, 1577–1604, https://doi.org/10.5194/bgd-10-1577-2013, 2013.

Shah, A. A., Qadri, T., and Khwaja, S. (2018). Living with earthquake hazards in South and Southeast Asia. ASEAN J. Commun. Engage. 2, 15–37

Sharples, J., J. J. Middelburg, K. Fennel, and T. D. Jickells (2016), What proportion of riverine nutrients reaches the open ocean?, Global Biogeochem. Cycles, 31, doi:10.1002/2016GB005483, in press.

Shaw, P. T. and S. Y. Chao (1994): Surface circulation in the South China Sea. Deep-Sea Res. I, 40(11/12), 1663–1683.

Shaw, P., S.-Y. Chao, K.-K. Liu, S.-C. Pai, and C.-T. Liu (1996), Winter upwelling off Luzon in the northeastern South China Sea, J. Geophys. Res. , 101 (C7), 16435–16448, doi:10.1029/96JC01064.

Shaw, P.-T., S.-Y. Chao, and L.-L. Fu (1999), Sea surface height variations in the South China Sea from satellite altimetry, Oceanol. Acta, 22, 1-17.

Siddorn J.R., Furner R., 2013. An analytical stretching function that combines the best attributes of geopotential and terrain-following vertical coordinates. Ocean Modelling 66, 1–13

Soumya, M., P. Vethamony, and P. Tkalich (2015), Inter-annual sea level variability in the southern South China Sea, Global Planet. Change, **133**, 17– 26.

Sprintall, J., A. L. Gordon, P. Flament, and C. L. Villanoy (2012), Observations of exchange between the South China Sea and the Sulu Sea, J. Geophys. Res., 117, C05036, doi:10.1029/2011JC007610.

Stewart, R. H. (2008), Introduction to physical oceanography, Orange Grove.

Susanto R D, Wei Zexun, Adi R T, et al. 2013. Observations of the Karimata Strait throughflow from December 2007 to November 2008. Acta Oceanologica Sinica, 32(5): 1–6, doi: 10.1007/ s13131-013-0307-3

Suhung Shen, Leptoukh, G. G., Acker, J. G., Zuojun Yu, & Kempler, S. J. (2008). Seasonal Variations of Chlorophyll a Concentration in the Northern South China Sea. IEEE Geoscience and Remote Sensing Letters, 5(2), 315–319.doi:10.1109/lgrs.2008.915932

Sverdrup, H. U., M. W. Johnson, and R. H. Fleming, 1942: The Oceans, their physics, chemistry, and general biology. Printice-Hall, Inc., 1087p

Talaue-McManus, L. (2000). Transboundary Diagnostic Analysis for the South China Sea. EAS/RCU Technical Report Series 14. United Nations Environment Programme, Bangkok, Thailand.

Tan, W., X. Wang, W. Wang, C. Wang, and J. Zuo, 2016: Different responses of sea surface temperature in the South China Sea to various El Niño events during boreal autumn. J. Climate, **29**, 1127–1142, https://doi.org/10.1175/JCLI-D-15-0338.1

Tang, D. L., H. Kawamura, T. van Dien, and M. A. Lee (2004), Offshore phytoplankton biomass increase and its oceanographic causes in the South China Sea, Mar. Ecol. Prog. Ser., 268, 31–41.

Thompson B, Tkalich P, Malanotte-Rizzoli P. 2017. Regime shift of the South China Sea SST in the late 1990s. Climate Dynamics, 48(5–6): 1873–1882, doi: 10.1007/s00382-016-3178-4

Tian, J. W., Q. X. Yang, X. F. Liang et al. 2006. Observation of Luzon Strait transport. Geophys. Res. Lett. 33: L19607, doi:10.1029/2006GL026272.

Tong, Y., Zhao, Y., Zhen, G., Chi, J., Liu, X., Lu, Y., … Zhang, W. (2015). Nutrient Loads Flowing into Coastal Waters from the Main Rivers of China (2006–2012). Scientific Reports, 5(1). doi:10.1038/srep16678.

Tozuka, T., Qu, T., Yamagata, T., 2007. Dramatic impact of the South China Sea on the Indonesian Throughflow. Geophys. Res. Lett. 34, L12612, doi:10.1029/2007GL030420.

Tozuka T, Qu T, Masumoto Y, Yamagata T (2009) Impacts of the South China Sea Throughflow on seasonal and interannual variations of the Indonesian Throughflow. Dyn Atmos Oceans 47:73–85

Tozuka, T., Qu, T., Yamagata, T., 2014. Impacts of South China Sea throughflow on the mean state and El Niño/Southern Oscillation as revealed by a coupled GCM. J Oceanogr (2015) 71:105–114, doi: 10.1007/s10872-014-0265-1

Tranchant, B., Reffray, G., Greiner, E., Nugroho, D., Koch-Larrouy, A., and Gaspar, P.: Evaluation of an operational ocean model configuration at 1/12° spatial resolution for the Indonesian seas (NEMO2.3 / INDO12) - Part 1: Ocean physics, Geosci. Model Dev., 9, 1037–1064, doi:10.5194/gmd-9-1037-2016, 2016.

Ulses, C., C. Estournel, J. Bonnin, X. Durrieu de Madron, and P. Marsaleix (2008a), Impact of storms and dense water cascading on shelf-slope exchanges in the Gulf of Lion (NW Mediterranean), J. Geophys. Res., 113, C02010, doi:10.1029/2006JC003795.

Ulses, C., C. Estournel, P. Puig, X. Durrieu de Madron, and P. Marsaleix (2008b), Dense shelf water cascading in the northwestern Mediterranean during the cold winter 2005: Quantification of the export through the Gulf of Lion and the Catalan margin, Geophys. Res. Lett., 35, L07610, doi:10.1029/2008GL033257.

Ulses, C., Auger, P.-A., Soetaert, K., Marsaleix, P., Diaz, F., Coppola, L., Herrmann, M.J., Kessouri, F., Estournel, C. (2016). Budget of organic carbon in the North-Western Mediterranean Open Sea over the period 2004–2008 using 3D coupled physical biogeochemical modeling. Journal of Geophysical Research: Oceans, 121, 7026–7055. https://doi.org/10.1002/2016JC011818

Ulses, C., Estournel, C., Fourrier, M., Coppola,L., Kessouri, F., Lefèvre D., and Marsaleix, P. (2020). Oxygen budget for the North-Western Mediterranean deep convection region. Biogeosiences Discussion.

UNEP (2005). Wilkinson, C., DeVantier, L., Talaue-McManus, L., Lawrence, D. and Souter, D. South China Sea, GIWA Regional Assessment 54. University of Kalmar, Kalmar, Sweden www.giwa.net/publications/r54.phtml

Uu D.V. and J. M. Brankart. 1997. Seasonal Variation of Temperature and Salinity Fields and Water Masses in the Bien Dong (South China) Sea, Mathl. Comput. Modelling, 26 (12): 97-113.

V.D. Vinh, S. Ouillon,T.D. Thanh, L.V. Chu, 2014. Impact of the Hoa Binh dam (Vietnam) on water and sediment budgets in the Red River basin and delta, Hydrol. Earth System Science, 18, 3987–4005, doi:10.5194/hess-18-3987-2014

Vincent, E. M., Lengaigne, M., Madec, G., Vialard, J., Samson, G., Jourdain, N. C., … Jullien, S. (2012). Processes setting the characteristics of sea surface cooling induced by tropical cyclones. Journal of Geophysical Research: Oceans, 117(C2), n/a–n/a. doi:10.1029/2011jc007396

Vincent, E.M., Madec, G., Lengaigne, M. et al. Influence of tropical cyclones on sea surface temperature seasonal cycle and ocean heat transport. Clim Dyn **41,** 2019–2038 (2013). https://doi.org/10.1007/s00382-012-1556-0

Vranes, K., Gordon, A. L., & Ffield, A. (2002). The heat transport of the Indonesian Throughflow and implications for the Indian Ocean heat budget. Deep Sea Research Part II: Topical Studies in Oceanography, 49(7-8), 1391–1410. doi:10.1016/s0967-0645(01)00150-3.

Waldman, R., et al. (2016), Estimating dense water volume and its evolution for the year 2012–2013 in the Northwestern Mediterranean Sea: An observing system simulation experiment approach, J. Geophys. Res. Oceans, 121, 6696–6716, doi:10.1002/2016JC011694

Wanninkhof, R., McGillis, W.R., (1999). A cubic relationship between gas transfer and wind speed. Geophys. Res. Lett. 26:1889–93

Wang J., 1986. Observation of abyssal flows in the Northern South China Sea. Acta Oceanogr Taiwan, 16: 36– 45.

Wang, C., R. H. Weisberg, and J. I. Virmani, 1999: Western Pacific interannual variability associated with the El Niño-Southern Oscillation. J. Geophys. Res. Oceans (1978– 2012), 104(C3), 5131-5149.

Wang, B., R. Wu, X. Fu, 2000: Pacific-East Asian teleconnection: How does ENSO affect East Asian Climate? J. Clim., 13: 1517-1536.

Wang, G. (2003), Mesoscale eddies in the South China Sea observed with altimeter data, Geophys. Res. Lett., 30 (21), 2121, doi:10.1029/2003GL018532.

Wang, Y.H., Jan, S., Wang, D.P., 2003. Transports and tidal current estimates in the Taiwan Strait from shipboard ADCP observations (1999–2001). Estuarine Coastal Shelf Sci. 57, 193–199.

Wang, D., Q. Liu, R. X. Huang, Y. Du, and T. Qu (2006), Interannual variability of the South China Sea throughflow inferred from wind data and an ocean data assimilation product, Geophys. Res. Lett., 33, L14605, doi:10.1029/2006GL026316.

Wang, G., D. Chen, and J. Su (2006), Generation and life cycle of the dipole in the South China Sea summer circulation, J. Geophys. Res. Ocean., 111 (6), 1–9, doi:10.1029/2005JC003314.

Wang, Y., G. Fang, Z. Wei, F. Qiao, and H. Chen (2006), Interannual variation of the South China Sea circulation and its relation to El Nino, as seen from a variable grid global ocean model, J. Geophys.Res.Ocean., 111(11), 1–15, doi:10.1029/2005JC003269

Wang L, Lau K-H, Fung CH, Gan JP. 2007. The relative vorticity of ocean surface winds from the QuikSCAT satellite and its effects on the genesis of tropical cyclones in the South China Sea. Tellus A 59: 562–569.

Wang, Q., H. Cui, S. Zhang, and D. Hu (2009), Water transports through the four main straits around the South China Sea, Chin. J. Oceanol. Limnol., 27, 229–236, doi:10.1007/s00343-009-9142-y.

Wang, J. J., D. L. Tang, and Y. Sui (2010), Winter phytoplankton bloom induced by subsurface upwelling and mixed layer entrainment southwest of Luzon Strait, J. Mar. Syst., 83, 141–149.

Wang, H., Saito, Y., Zhang, Y., Bi, N., Sun, X., & Yang, Z. (2011). Recent changes of sediment flux to the western Pacific Ocean from major rivers in East and Southeast Asia. Earth-Science Reviews, 108, 80–100.

Wang G., Xie S. P., Qu T. and Huang R., 2011. Deep South China Sea circulation. Geophys Res Lett, 38: L05601, doi: 10.1029/2010GL046626.Wang.H, He.S. 2012. Weakening relationship between East Asian winter monsoon and ENSO after mid-1970s. Chin. Sci. Bull. (2012), pp. 1-6

Wang, Z., Yu, G. A., & Huang, H. Q. (2012). Gender of deltas and parasitizing rivers. International Journal of Sediment Research, 27, 1–19.

Wang Zhaoyun, Zhai Fangguo, Li Peiliang. 2016. A shift in the upper-ocean temperature trends in the South China Sea since the late 1990s. Acta Oceanologica Sinica, 35(11): 44–51, doi: 10.1007/s13131-016-0947-1

Wang, X., Liu, Z., & Peng, S. (2017). Impact of Tidal Mixing on Water Mass Transformation and Circulation in the South China Sea. Journal of Physical Oceanography, 47(2), 419–432. doi:10.1175/jpo-d-16-0171.1

Wang Yan, Xu Tengfei, Li Shujiang, Susanto R. Dwi, Agustiadi Teguh, Trenggono Mukti, Tan Wei, Wei Zexun. 2019. Seasonal variation of water transport through the Karimata Strait. Acta Oceanologica Sinica, 38(4): 47–57, doi: 10.1007/s13131-018-1224-2

Wang, Q., Zeng, L., Shu, Y. et al. Interannual variability of South China Sea winter circulation: response to Luzon Strait transport and El Niño wind. Clim Dyn 54, 1145–1159 (2020).

https://doi.org/10.1007/s00382-019-05050-2

Wei Z., Fang G., Xu T., Wang Y. and Lian Z., 2016. Seasonal variability of the isopycnal surface circulation in the South China Sea derived from a variable-grid global ocean circulation model. Acta Oceanologica Sinica, 35(1): 11–20, doi:10.1007/s13131-016-0791-3.

Weber SC, Subramaniam A, Montoya JP, Doan-Nhu H, Nguyen-Ngoc L, Dippner JW and Voss M (2019) Habitat Delineation in Highly Variable Marine Environments. Front. Mar. Sci. 6:112. doi: 10.3389/fmars.2019.00112

Wolanski, E., N. Huu Nhan, and S. Spagnol (1998), Sediment Dynamics during Low Flow Conditions in the Mekong River Estuary, Vietnam, J. Coast. Res. , 14 (2), 472–482.

Wong, G. T. F., Ku, T.-L., Mulholland, M., Tseng, C.-M., & Wang, D.-P. (2007). The SouthEast Asian Time-series Study (SEATS) and the biogeochemistry of the South China Sea—An overview. Deep Sea Research Part II: Topical Studies in Oceanography, 54(14-15), 1434–1447. doi:10.1016/j.dsr2.2007.05.012

World trade statistical review. (2017). Annual report of the World Trade Organization. https://www.wto.org

Wu, C.-R., Hsin, Y.-C., 2005. Volume transport through the Taiwan Strait: a numerical study. Terr. Atmos. Ocean. Sci. 16, 377–391.

Wu CR (2013) Interannual modulation of the pacific decadal oscillation (PDO) on the low-latitude western North Pacific. Prog Oceanogr 110:49–58

Wu, J., S.-W. Chung, L.-S. Wen, K.-K. Liu, Y.-L. L. Chen, H.-Y. Chen, and D. M. Karl, Dissolved inorganic phosphorus, dissolved iron, and Trichodesmium in the oligotrophic South China Sea, Global Biogeochem. Cycles, 17(1), 1008, doi:10.1029/2002GB001924, 2003

Wu, J., Ren, H. L., Xu, X. F., and Gao, L. (2018). Seasonal modulation of MJO's impact on precipitation in China and its dynamical-statistical downscaling prediction. Meteor. Mon. 44, 737–751. doi: 10.7519/j.issn.1000-0526.2018.06.002

Wu, L., H. Zhang, J.-M. Chen, and T. Feng, 2020: Characteristics of tropical cyclone activity over the South China Sea: Local and nonlocal tropical cyclones. Terr. Atmos. Ocean. Sci., 31, 261-271, doi: 10.3319/TAO.2019.07.01.02

Wyrtki K., 1961. Scientific results of marine investigations of the South China Sea and the Gulf of Thailand 1959– 1961: Physical oceanography of the Southeast Asian waters. Naga Rep. 2, 195 pp., Scripps Inst. Of Oceanogr., La Jolla, Calif.

Xiao, F., Wang, D., Zeng, L., Liu, Q.-Y., & Zhou, W. (2019). Contrasting changes in the sea surface temperature and upper ocean heat content in the South China Sea during recent decades. Climate Dynamics.doi:10.1007/s00382-019-04697-1

Xie, S.-P. (2003), Summer upwelling in the South China Sea and its role in regional climate variations, J. Geophys. Res., 108 (C8), 3261, doi:10.1029/2003JC001867.

Xie, S. P., C. H. Chang, Q. Xi, and D. Wang (2007), Intraseasonal variability in the summer South China Sea: Wind jet, cold filament, and recirculations, J. Geophys. Res. Ocean., 112 (10), C10008, doi:10.1029/2007JC004238.

Xiu, P., & Chai, F. (2011). Modeled biogeochemical responses to mesoscale eddies in the South China Sea. Journal of Geophysical Research, 116(C10).doi:10.1029/2010jc006800

Xiu, P., Dai, M., Chai, F., Zhou, K., Zeng, L., & Du, C. (2019). On contributions by wind-induced mixing and eddy pumping to interannual chlorophyll variability during different ENSO phases in the northern South China Sea. Limnology and Oceanography.doi:10.1002/lno.11055

Xu, X. (1982), The general descriptions of the horizontal circulation in the South China Sea, in Proceedings of the 1980 Symposium on Hydrometeorology, Chinese Society of Oceanology and Limnology, pp. 137–145, Science Press.

Xu D, Malanotte-Rizzoli P (2013) The seasonal variation of the upper layers of the South China Sea (SCS) circulation and the Indonesian throughflow (ITF): an ocean model study. Dyn Atmos Oceans 63:103–130. doi:10.1016/j.dynatmoce.2013.05.002

Xu F. and Oey L. Y., 2014. State analysis using the Local Ensemble Transform Kalman Filter (LETKF) and the three-layer circulation structure of the Luzon Strait and the South China Sea. Ocean Dynamics, 64:905–923doi:10.1007/s10236-014-0720-y.

Xue H., F. Chai, N. Pettigrew, D. Xu, M. Shi, and J. Xu, 2004. Kuroshio intrusion and the circulation in the South China Sea. J. Geophys. Res., 109, C02017, doi:10.1029/2002JC001724.

Yang Haijun, Liu Qinyu, and Jia Xujing, 1999: On the upper oceanic heat budget in the South China Sea: Annual cycle. Adv. Atmos. Sci., 16(4), 619–629.
Yang Q., Tian J., and Zhao W., 2010. Observation of Luzon Strait transport in summer 2007. Deep Sea Res., Part I 57:670–676.

Yaremchuk, M., J. McCreary Jr., Z. Yu, and R. Furue (2009), The South China Sea throughflow retrieved from climatological data, J. Phys. Oceanogr., 39, 753–767, doi:10.1175/2008JPO3955.1.

Yinglong J. Zhang, Eli Ateljevich, Hao-Cheng Yu, Chin H. Wu, Jason C.S. Yu, 2015 A new vertical coordinate system for a 3D unstructured-grid model, Ocean Modelling, 85, 16-31, https://doi.org/10.1016/j.ocemod.2014.10.003

Yu L, Weller RA. 2007. Objectively Analyzed air-sea heat Fluxes (OAFlux) for the global ocean. Bull. Am. Meteorol. Soc. 88:527–39

Yu, K., and T. Qu (2013), imprint of the pacific decadal oscillation on the South China Sea throughflow variability, J. Clim.,**26**(24), 9797–9805.

Yu, Z., S. Shen, J. P. McCreary, M. Yaremchuk, and R. Furue (2007), South China Sea throughflow as evidenced by satellite images and numerical experiments, Geophys. Res. Lett., 34, L01601, doi:10.1029/2006GL028103.

Yu Yi, Zhang Hao-Ran, Jin Jiangbo, Wang Yuntao. 2019. Trends of sea surface temperature and sea surface temperature fronts in the South China Sea during 2003–2017. Acta Oceanologica Sinica, 38(4): 106–115, doi: 10.1007/s13131-019-1416-4

Yu, Y., Xing, X., Liu, H., Yuan, Y., Wang, Y., & Chai, F. (2019). The variability of chlorophyll-a and its relationship with dynamic factors in the basin of the South China Sea. Journal of Marine Systems, 200, 103230.doi:10.1016/j.jmarsys.2019.103230

Yuan D., 2002. A numerical study of the South China Sea deep circulation and its relation to the Luzon Strait transport. Acta Oceanologica Sinica, 21(2):187–202.

Yuan, Y., H. Yang, W. Zhou, and C. Li (2008a), Influences of the Indian ocean dipole on the asian summer monsoon in the following year, Int. J. Climatol. , 28 (14), 1849–1859, doi:10.1002/joc.1678.

Yuan, Y., G. Liao, and C. Yang (2008b), The Kuroshio near the Luzon Strait and circulation in the northern South China Sea during August and September 1994, J. Oceanogr., 64, 777–788, doi:10.1007/s10872008-0065-6.

Zhang, W.-Z., Wang, H., Chai, F., Qiu, G., 2016. Physical drivers of chlorophyll variability in the open South China Sea. Journal of Geophysical Research: Oceans 121, 7123–7140.

Zeng, L., W. Timothy Liu, H. Xue, P. Xiu, and D. Wang (2014), Freshening in the South China Sea during 2012 revealed by Aquarius and in situ data, J. Geophys. Res. Oceans, 119, 8296–8314, doi:10.1002/2014JC010108.

Zeng, L. et al. (2016a) SCSPOD14, a South China Sea physical oceanographic dataset derived from in situ measurements during 1919–2014. Sci. Data 3:160029 doi: 10.1038/sdata.2016.29 (2016).

Zeng, L., Wang, D., Xiu, P., Shu, Y., Wang, Q., & Chen, J. (2016b). Decadal variation and trends in subsurface salinity from 1960 to 2012 in the northern South China Sea. Geophysical Research Letters, 43, 12,181–12,189. https://doi.org/10.1002/2016GL071439

Zeng, L., Chassignet, E. P., Schmitt, R. W., Xu, X., & Wang, D. (2018). Salinification in the South China Sea since late 2012: A reversal of the freshening since the 1990s. Geophysical Research Letters, 45, 2744–2751. https://doi.org/10.1002/2017GL076574

Zhao, H. and Tang, D. L.: Effects of 1998 El Niño on the distribution of phytoplankton in the South China Sea, J. Geophys. Res., 112, C02017, doi:10.1029/2006JC003536, 2007.

Zhao, R., and X.-H. Zhu (2016), Weakest winter South China Sea western boundary current caused by the 2015–2016 El Nino event, J. Geophys. Res. Oceans, 121, 7673–7682, doi:10.1002/2016JC012252.

Zhang, L., B.Wang, and Q.Zeng, 2009: Impact of the Madden–Julian oscillation on summer rainfall in southeast China. J. Climate, 22, 201–216.

Zhang, W.-Z.; Chai, F.; Hong, H.-S.; Xue, H. (2014). Volume transport through the Taiwan Strait and the effect of synoptic events. Cont. Shelf Res. 2014, 88, 117–125. doi: http://dx.doi.org/10.1016/j.csr.2014.07.010

Zhang Z., W. Zhao, J. Tian, Q. Yang, and T. Qu, 2015. Spatial structure and temporal variability of the zonal flow in the Luzon Strait. J. Geophys. Res. Oceans, 120: 759–776, doi:10.1002/ 2014JC010308.

Zhang, W.-Z., H. Wang, F. Chai, and G. Qiu (2016), Physical drivers of chlorophyll variability in the open South China Sea, J. Geophys. Res. Oceans, 121, 7123–7140, doi:10.1002/2016JC011983

Zhou, W., and J. C. L. Chan. 2007. ENSO and the South China Sea Summer Monsoon Onset. International Journal of Climatology 27: 157–167.

Zhu Y., J. Sun, Y. Wang, Z. Wei, D. Yang, and T. Qu, 2017. Effect of potential vorticity flux on the circulation in the South China Sea. J. Geophys. Res. Oceans, 122(8): 6454-6469, doi:10.1002/2016JC012375.

Zhu, Y., Sun, J., Wang, Y., Li, S., Xu, T., Wei, Z., Qu, T., 2019. Overview of the multi-layer circulation in the South China Sea, Progress in Oceanography, doi:https://doi.org/10.1016/j.pocean.2019.04.001

Zu, T., Gan, J., & Erofeeva, S. Y. (2008). Numerical study of the tide and tidal dynamics in the South China Sea. Deep Sea Research Part I: Oceanographic Research Papers, 55(2), 137–154. doi:10.1016/j.dsr.2007.10.007